Development and Demonstration of a New Non-Equilibrium Rate-Based Process Model for the Hot Potassium Carbonate Process

by

Su Ming Pamela Ooi

Thesis submitted for the degree of
Doctor of Philosophy

in

The University of Adelaide
School of Chemical Engineering
July 2008

Summary

Chemical absorption and desorption processes are two fundamental operations in the process industry. Due to the rate-controlled nature of these processes, classical equilibrium stage models are usually inadequate for describing the behaviour of chemical absorption and desorption processes. A more effective modelling method is the non-equilibrium rate-based approach, which considers the effects of the various driving forces across the vapour-liquid interface.

In this thesis, a new non-equilibrium rate-based model for chemical absorption and desorption is developed and applied to the hot potassium carbonate process CO_2 Removal Trains at the Santos Moomba Processing Facility. The rate-based process models incorporate rigorous thermodynamic and mass transfer relations for the system and detailed hydrodynamic calculations for the column internals. The enhancement factor approach was used to represent the effects of the chemical reactions.

The non-equilibrium rate-based CO_2 Removal Train process models were implemented in the Aspen Custom Modeler® simulation environment, which enabled rigorous thermodynamic and physical property calculations via the Aspen Properties® software. Literature data were used to determine the parameters for the Aspen Properties® property models and to develop empirical correlations when the default Aspen Properties® models were inadequate. Preliminary simulations indicated the need for adjustments to the absorber column models, and a sensitivity analysis identified the effective interfacial area as a suitable model parameter for adjustment. Following the application of adjustment factors to the absorber column models, the CO_2 Removal Train process models were successfully validated against steady-state plant data.

The success of the Aspen Custom Modeler® process models demonstrated the suitability of the non-equilibrium rate-based approach for modelling the hot potassium carbonate process. Unfortunately, the hot potassium carbonate process could not be modelled as such in HYSYS®, Santos's preferred simulation environment, due to the absence of electrolyte components and property models and the limitations of the HYSYS® column operations in accommodating chemical reactions and non-equilibrium column behaviour. While importation of the Aspen Custom Modeler® process models into HYSYS® was possible, it was considered impractical due to the significant associated computation time.

To overcome this problem, a novel approach involving the HYSYS® column stage efficiencies and hypothetical HYSYS® components was developed. Stage efficiency correlations, relating various operating parameters to the column performance, were derived from parametric studies performed in Aspen Custom Modeler®. Preliminary simulations indicated that the efficiency correlations were only necessary for the absorber columns; the regenerator columns were adequately represented by the default equilibrium stage models. Hypothetical components were created for the hot potassium carbonate system and the standard Peng-Robinson property package model in HYSYS® was

modified to include tabular physical property models to accommodate the hot potassium carbonate system. Relevant model parameters were determined from literature data. As for the Aspen Custom Modeler® process models, the HYSYS® CO_2 Removal Train process models were successfully validated against steady-state plant data.

To demonstrate a potential application of the HYSYS® process models, dynamic simulations of the two most dissimilarly configured trains, CO_2 Removal Trains #1 and #7, were performed. Simple first-order plus dead time (FOPDT) process transfer function models, relating the key process variables, were derived to develop a diagonal control structure for each CO_2 Removal Train. The FOPDT model is the standard process engineering approximation to higher order systems, and it effectively described most of the process response curves for the two CO_2 Removal Trains. Although a few response curves were distinctly underdamped, the quality of the validating data for the CO_2 Removal Trains did not justify the use of more complex models than the FOPDT model.

While diagonal control structures are a well established form of control for multivariable systems, their application to the hot potassium carbonate process has not been documented in literature. Using a number of controllability analysis methods, the two CO_2 Removal Trains were found to share the same optimal diagonal control structure, which suggested that the identified control scheme was independent of the CO_2 Removal Train configurations. The optimal diagonal control structure was tested in dynamic simulations using the MATLAB® numerical computing environment and was found to provide effective control. This finding confirmed the results of the controllability analyses and demonstrated how the HYSYS® process model could be used to facilitate the development of a control strategy for the Moomba CO_2 Removal Trains.

In conclusion, this work addressed the development of a new non-equilibrium rate-based model for the hot potassium carbonate process and its application to the Moomba CO_2 Removal Trains. Further work is recommended to extend the model validity over a wider range of operating conditions and to expand the dynamic HYSYS® simulations to incorporate the diagonal control structures and/or more complex control schemes.

Statement

This work contains no material which has been accepted for the award of any other degree or diploma in any university or other tertiary institution and, to the best of my knowledge and belief, contains no material previously published or written by another person, except where due reference has been made in the text.

I give consent to this copy of my thesis, when deposited in the University Library, being made available for loan and photocopying, subject to the provisions of the Copyright Act 1968.

Su Ming Pamela Ooi
Adelaide, 16/07/2008

Acknowledgements

I wish to express my sincere appreciation to all organisations and persons who have contributed council and assistance during this work.

In particular, I would like to thank Santos for providing funding and technical support for this project. Special thanks are extended to Keith Humphris, Len Cowen, Ian Smith, Ross Mullner, Claire Barber, Randall Yeates and Mark Moss for their advice and assistance with providing technical data.

I would also like to thank my academic supervisors, Associate Professor Brian O'Neill, Dr Chris Colby and Professor Keith King, for their encouragement, advice and guidance. Special thanks are extended to Dr Robin Thiele who provided invaluable advice regarding rate-based modelling.

Finally, I would like to express my deepest gratitude to my boyfriend Simon and to my parents for providing endless support and encouragement, without which I could not have completed this thesis.

Table of Contents

List of Figures

List of Tables

Nomenclature

Latin Letters

A	–	Step size or amplitude of limit cycle
A^*	–	Latini component parameter
A_{ca}	m^3/kmol	Clarke Aqueous Electrolyte Volume parameter
A_ϕ	–	Debye-Hückel parameter
AAD	%	Average absolute deviation
a	–	Activity
a	m^6·bar/$kmol^2$	Cubic equation of state mixture parameter
a	m^2/m^3	Specific surface area
a_a	W·m^2/K·kmol	Riedel anion parameter
a_c	W·m^2/K·kmol	Riedel cation parameter
a_I	m^2/m^3	Effective interfacial area
a_j	m^6·bar/$kmol^2$	Cubic equation of state parameter for species j
$a_{T,j}$	kJ/kmol·K	Criss-Cobble entropy parameter
B_{ca}	L/mol	Breslau-Miller electrolyte parameter
b	m^3/kmol	Cubic equation of state mixture parameter
b	m^3/kmol	Ion contribution factor
$b_{a,1}$	m^3/kmol	Breslau-Miller anion parameter
$b_{a,2}$	m^3/kmol·K	Breslau-Miller anion parameter
$b_{c,1}$	m^3/kmol	Breslau-Miller cation parameter
$b_{c,2}$	m^3/kmol·K	Breslau-Miller cation parameter
b_j	m^3/kmol	Cubic equation of state parameter for species j
$b_{T,j}$	–	Criss-Cobble entropy parameter
C	kmol/m^3 mol/cm^3	Molar concentration or molar density
$\hat{C}_{H_2S}$	mol/m^3	Equivalent H_2S content
C_j	–	Electrolyte NRTL parameter (z_j for ions and 1 for molecular species)
C°_{jw}	–	Reduced volume integral of species j at infinite dilution in water
C_p	kJ/kmol·K cal/mol·K kJ/kg·K Btu/lbmol·°R	Heat capacity
$\hat{C}_p$	kJ/kg·K	Mass heat capacity
$C_p\big\vert_{25}^{T}$	kJ/kmol·K	Average value of C_p between 25°C and temperature T
C_R	–	Reduced molar density
C_v	J/mol·K	Heat capacity at constant volume
CLDG	–	Closed-loop disturbance gain matrix
CN	–	Condition number
c_t	kmol/m^3	Total mole concentration
D	m	Diameter
D	cm^2/s m^2/s	Effective diffusion coefficient or diffusivity

D_{jk}	m^2/s	Binary diffusion coefficient for species pair j-k
D_w	cm^2/s	Diffusion coefficient in water
$Đ_{jk}$	m^2/s	Maxwell-Stefan diffusivity for the binary species pair j-k
DC	–	Disturbance cost
DCN	–	Disturbance condition number
DR	–	Decay ratio
DRGA	–	Dynamic relative gain array
d	–	Height of first overshoot
d	–	Process load or disturbance
d(s)	–	Vector of process disturbances
d_h	m	Hydraulic diameter
d_N	m	Nominal packing size
d_p	m	Particle diameter
df	–	Degrees of freedom
E	kW/m^2	Energy flux across the vapour-liquid interface
E_{stage}	–	HYSYS® column overall stage efficiency
E_{Murph}	–	Murphree vapour efficiency
EF	–	Enhancement factor
e	C	Charge of an electron (1.60219×10^{-19} C)
F	C/mol	Faraday's constant (96 485 C/mol)
F	kmol/s	Feed molar flow
F	kmol/s	Flow rate
F	–	F-Test result
F	–	BLT detuning factor
F_1, F_2,F_3	–	Chung functions
F_c	–	Fractional conversion of K_2CO_3 to $KHCO_3$ and KHS
F_{CO_2}	–	CO_2 loading
F_j	–	Fractional conversion of CO_3^{2-} to HCO_3^- due to species j absorption
F_{max}	m^3/min	Maximum flow through control valve
ΔF_{in}	%	Maximum percentage step change in inflow
f	atm bar Pa	Fugacity
f_o	–	Particle friction factor
f_T	–	Twu function at temperature T
$f_{x,0}$	–	Ely-Hanley function
G	–	Electrolyte NRTL parameter
G	kmol/s	Vapour phase molar flow
G	–	Transfer function
G(s)	–	Transfer function matrix
$\hat{G}$	sm^3/h	Vapour phase standard volumetric flow
$\underline{\mathbf{G}}$(s)	–	Transfer function matrix with paired elements along the diagonal
G^E	kJ/kmol	Symmetric excess Gibbs energy
G^{E*}	kJ/kmol	Un-symmetric excess Gibbs energy
G(s)	–	Process transfer function

g	m/s^2	Gravitational acceleration ($9.81 m/s^2$)
H	m	Height
H_j	$bar \cdot m^3/kmol$	Henry's Law constant for species j in solution
H_j	bar	Henry's Law constant for species j in pure water
H_j^w	$bar \cdot m^3/kmol$	Henry's Law constant for species j in water
Ha	–	Hatta number
HETP	m	Height of packing equivalent to a theoretical plate
h	kJ/kmol kJ/kg	Enthalpy
h	–	Height of relay
h	–	Twu function
$h_{x,0}$	–	Ely-Hanley function
Δh^f	kJ/kmol kJ/mol	Enthalpy or heat of formation
Δh^{vap}	kJ/kmol	Enthalpy of vaporisation
Δhfk	kJ/mol	Joback contribution for group k to the enthalpy of formation
I	–	Identity matrix
I_c	$kmol/m^3$	Molar concentration based ionic strength
I_x	–	Mole fraction based ionic strength
IAE	–	Integral of the absolute error
J	–	Objective function for the linear quadratic regulator problem
J	$kmol/m^2 \cdot s$	Diffusion flux
K	– $kmol/m^3$ $kmol^2/m^6$	Chemical equilibrium constant
K	–	Gain
K'	–	Pseudo-equilibrium constant
K'_p	–	Integrator gain
k	J/K erg/K	Boltzmann constant (1.38066×10^{-23} J/K or 1.38066×10^{-16} erg/K)
k	m/s	Mass transfer coefficient
k	1/s $m^3/kmol \cdot s$ $m^6/kmol^2 \cdot s$	Reaction rate constant
k_{jk}	–	Cubic equation of state binary interaction parameter for species pair j-k
k'	1/s	Pseudo-first-order reaction rate constant
k''	1/s	Kinetic coefficient
L	kmol/s	Liquid phase molar flow
L_c	–	Closed-loop log modulus
ΔL_{max}	%	Maximum allowable percentage deviation from setpoint
$\hat{L}$	m^3/h	Liquid phase volumetric flow
Le	–	Lewis number
M	kmol	Material holdup
MAD	%	Maximum absolute deviation
MIC	–	Morari index of integral controllability
MRI	–	Morari Resiliency Index

MW	kg/kmol g/mol	Molecular weight
m	–	Manipulated variable
m	$kmol/m^3$	Solution molarity (total K_2CO_3 concentration)
N	$kmol/m^2 \cdot s$	Molar flux across the vapour-liquid interface
N	–	Number
N	–	Order of multivariable system
N_{eqm}	–	Number of equilibrium stages
N_k	–	Number of UNIFAC groups of type k for Joback method
N_o	1/mol	Avogadro's number (6.02205×10^{23} 1/mol)
NC	–	Number of components
ND	–	Number of data points
NI	–	Niederlinski index
n	kmol	Number of moles
n	–	Number of species in the system
P	atm bar Pa psia	Pressure or partial pressure
P^s	bar	Vapour pressure
P_o	min	Period of oscillation
P_u	min	Ultimate period or limit cycle period
ΔP	Pa kPa	Pressure drop
PRGA	–	Performance relative gain array
p	–	Pitzer-Debye-Hückel closest approach parameter (14.9)
p	–	p-value
Q	–	Objective function for the data regression runs
Q	kJ/s kW	Heat flow or duty
QDR	–	Quarter decay ratio
R	kJ/kmol·K m^3·bar/K·kmol atm·cm^3/mol·K	Gas constant (8.3144 kJ/kmol·K or 0.0831447 m^3·bar/K·kmol or 82.06 atm·cm^3/mol·K)
R	$kmol/m^3 \cdot s$	Molar reaction rate
R_{SP}	–	Ratio setpoint
RGA	–	Relative gain array
RRMSQE	–	Residual root mean square error
Re	–	Reynolds number
r_j	m	Born radius of species j
S_{25}^{∞}	kJ/kmol·K	Infinite dilution entropy at 25°C
S_T^{∞}	kJ/kmol·K	Infinite dilution entropy at temperature T
SG	–	Specific gravity
SSQ	–	Sum of squared errors
ΔSG	–	Change in specific gravity
s	–	Laplace transform variable ($s = i \cdot \omega$)

T	K °C °R °F	Temperature
T_{ref}	K	Reference temperature (298.15 K)
T*	–	Dimensionless temperature
t	min	Time
U	kJ	Energy holdup
U(s)	–	Process input transfer function
u	–	Process input
V	m^3	Volume
V	cm^3/mol m^3/kmol	Molar volume
V_{ca}^{∞}	m^3/kmol	Clarke Aqueous Electrolyte Volume parameter
V_e	L/mol	Breslau-Miller effective volume
V_R^o, V_R^δ	–	COSTALD reduced volumes
v	m/s	Velocity
v^*	cm^3/mol	Characteristic volume
$\tilde{v}$	–	Reduced molar volume
$\bar{v}^{\infty}$	cm^3/mol m^3/kmol	Partial molar volume at infinite dilution in pure water
W	–	Scalar BLT function
W_i	–	Weight of data group i
WSSQ	–	Weighted sum of squares
wf	–	Weight fraction
$wf_{K_2CO_3}$	–	Equivalent weight fraction of K_2CO_3
X	–	Effective local mole fraction
x	–	Liquid phase mole fraction
x	–	Component mole fraction
Y(s)	–	Process output transfer function
y	–	Vapour phase mole fraction
y	–	Component mass fraction
y	–	Process output or response
Z	–	Compressibility
Z	–	Chung parameter
Z	cSt	Twu kinematic viscosity parameter
Z°	1/atm	Isothermal compressibility at infinite dilution in water
$Z^{(0)}$	–	Pitzer compressibility function for spherical molecules
$Z^{(1)}$	–	Pitzer compressibility deviation function
Z_{RA}	–	Rackett parameter
z	–	Charge number
z	–	Feed mole fraction
z	–	Ionic charge
z	–	Secondary process variable

Greek Letters

α	–	Chung parameter
α	–	Electrolyte NRTL non-randomness factor
α	–	Latini component parameter
α	$kW/m^2 \cdot K$	Heat transfer coefficient
α_c	–	Riedel critical point parameter
α_j	–	Cubic equation of state alpha function for species j
β	–	Chung parameter
β	–	Latini component parameter
β	–	Packing specific constant
β_{CO_2}	$m^3/kmol$	Contribution factor for CO_2 absorption
δ	m	Film thickness
δ	Debye	Dipole moment
δ_p	–	Chapman-Enskog-Brokaw polar parameter
ε	–	Error
ε	$C^2/J \cdot m$	Dielectric constant
ε	erg	Characteristic energy
ϕ	°	Phase lag
	rad	
ϕ	m^3/m^3	Phase volumetric holdup
ϕ	m^3/m^3	Packing voidage
ϕ_{jk}	–	Wilke viscosity function for species pair j-k
Γ	m·K/W	Stiel-Thodos parameter
γ	–	Activity coefficient
γ	–	Latini component parameter
γ	–	Symmetric activity coefficient
γ^*	–	Un-symmetric activity coefficient
η	–	Dimensionless film coordinate
η	–	Column stage efficiency
φ	kV	Electrical potential
φ	–	Fugacity coefficient
κ	–	Chung association factor
λ	–	Relative gain
λ	–	Eigenvalue
λ	min	IMC tuning parameter
λ	W/m·K	Thermal conductivity
$\boldsymbol{\lambda}$	–	Vector of eigenvalues
λ'	W/m·K	Ely-Hanley translational thermal conductivity contribution
λ''	W/m·K	Ely-Hanley internal thermal conductivity contribution
λ^∞	$m^2/\Omega \cdot kmol$	Ionic conductivity at infinite dilution in water
μ	kJ·m/kmol	Chemical potential

μ	cP kg/m·s Pa·s	Dynamic viscosity
$\Delta\mu_{ca}$	cP	Jones-Dole viscosity contribution term for electrolyte ca
ν	cSt m^2/s	Kinematic viscosity
θ	min	Dead time
ρ	g/m^3 kg/m^3	Mass density
σ	–	Standard error associated with a data point
$\sigma(s)$	–	Singular value
σ	Å	Characteristic length
σ_c	N/m	Critical surface tension parameter
$\Delta\sigma_{ca}$	N/m	Onsager-Samaras surface tension contribution term for electrolyte ca
σ_L	N/m dyne/cm	Surface tension
τ	–	Electrolyte NRTL binary interaction energy parameter
τ	min	Natural period of oscillation
τ	min	Time constant
υ	–	Stoichiometric coefficient
$\Omega_{D,jk}$	–	Diffusion coefficient integral for species pair j-k
ω	–	Acentricity
ω	rad/min	Frequency
ξ	$K^{1/6}\cdot kmol^{1/2}/kg^{1/2}\cdot atm^{2/3}$	Dean-Stiel parameter
Ψ	–	Chung function
ψ_b	–	Riedel parameter
ζ	–	Damping factor

Subscripts

∞	Final or at infinity or at steady-state
0	Reference fluid
Abs	Absorber
a, a’	Anion
aq	Aqueous
av	Average
B	Bandwidth
b	Normal boiling point
CL	Closed-loop
CLR	Closed-loop regulator
CLS	Closed-loop servo
Cond	Condenser
c	Column
c	Controller
c	Critical
c, c’	Cation
ca	Electrolyte consisting of cation c and anion a
co	Cross-over
D	Derivative
d	Disturbance
diag	Diagonal matrix
dry	Dry packing
eq	Equilibrium
est	Estimated
expt	Experimental
F	Feed
f	Film
f	Forward reaction
G	Vapour phase
H	High gas throughput
H_2O	Water
I	Integral
I	Vapour-liquid interface
IG	Ideal gas
i	Stage
irr	Irrigated packing
j	Component or species
j	Data point
jk	Component or species pair j-k
K_2CO_3	Potassium carbonate
k	Component or species
L	Liquid phase
L	Low gas throughput

LS	Lean solution
lc	Local composition
M	Medium gas throughput
m, m’	Molecular species
m	Measured
max	Maximum
min	Minimum
OL	Open-loop
o	Pre-loading
PV	Process variable or measured process variable
p	Process
R	Reaction
Reb	Reboiler
RG	Raw gas
r	Reverse reaction
ref	Reference
SP	Setpoint
s	Solvent
T	Temperature
T	Total or mixture
t	Total or mixture
u	Ultimate
vap	Vapour
w	Water
x	Fluid of interest

Superscripts

∞	At infinite dilution in water or in solvent
*	Un-symmetric convention
+	Adjusted matrix with positive diagonal elements
-1	Inverse
Born	Born model
Chem	Chemical
c	Molar concentration basis
E	Excess
eq	Chemical equilibrium
ex	Excess
f	Formation
H	Conjugate transpose
LP	Low pressure or atmospheric pressure
o	Reference
NRTL	Non-Random Two-Liquid model
PDH	Pitzer-Debye-Hückel model
Phys	Physical
res	Residual
s	Saturation or at vapour pressure P^s
T	Transpose
w	Water
ZN	Ziegler-Nichols

CHAPTER 1

INTRODUCTION

Chemical absorption and desorption are two fundamental process operations. Involving the selective transfer, facilitated by chemical reactions, of components between a vapour (or gas) mixture and a liquid mixture, they play a significant role in the process industry, particularly in gas treatment applications (Astarita et al., 1983).

One such gas treatment method is the widely used hot potassium carbonate process (Benson and Field, 1959) for removing acidic gas impurities, such as carbon dioxide (CO_2) and hydrogen sulfide (H_2S). A typical chemical absorption and desorption system, the hot potassium carbonate process displays complex process behaviour, which arises from the combined influence of many different driving forces, including multicomponent diffusion, chemical interactions and temperature gradients. In practice, equilibrium is rarely achieved due to the rate-controlled nature of chemical absorption and desorption (Chakravarty et al., 1985).

As a result of its assumption of thermodynamic equilibrium, the classical equilibrium stage approach is considered inadequate for describing chemical absorption and desorption processes like the hot potassium carbonate process. Instead, a more physically consistent approach is the non-equilibrium rate-based method (Kenig et al., 2001). This approach separates the material and energy balances for the two phases by only assuming equilibrium at the phase interface. It therefore enables a more thorough consideration of the mass and heat transfer relations, the chemical reaction kinetics and the column hydrodynamics.

In this thesis, a new non-equilibrium rate-based model for describing chemical absorption and desorption is developed for the hot potassium carbonate process. Unlike previous models, this model incorporates rigorous thermodynamic, heat and mass transfer relations and column hydrodynamic calculations for both the absorber and regenerator columns. It also considers both the reaction rate expression and enhancement factor approaches for representing the effects of the chemical reactions. To demonstrate this new model, it is applied to the hot potassium carbonate process CO_2 Removal Trains at the Moomba Processing Facility, one of the key operations for Santos, a major Australian oil and gas exploration and production company.

Santos does not currently have detailed process models of the Moomba CO_2 Removal Trains, despite the CO_2 Removal Trains being one of the bottlenecks of the processing facility. Consequently, the process models developed in this thesis have the potential to be particularly useful tools for Santos, provided they are implemented in HYSYS®, Santos's preferred simulation environment. Accurate and detailed process models can enable the evaluation of different operating conditions for process optimisation purposes without disrupting the operation of the actual plant. They can also save time and human resources since process simulations can be relatively quick and easy to perform compared to actual plant tests.

To demonstrate a potential application of the process models developed in this thesis, the models are used to analyse the multivariable controllability of the CO_2 Removal Trains. The results of this analysis are used to develop diagonal control structures to fully automate the control of the individual trains. Although diagonal control structures are the simplest and most widely used form of multivariable control (Luyben and Luyben, 1997), their application to the hot potassium carbonate process has not been previously published in the literature.

1.1 Project Objectives

In summary, the four objectives of this work are as follows:

1. To develop a new rigorous non-equilibrium rate-based model for the hot potassium carbonate process;

2. To apply this model to the hot potassium carbonate process CO_2 Removal Trains at the Santos Moomba Processing Facility;

3. To develop accurate and detailed process models of the CO_2 Removal Trains in HYSYS®, the preferred simulation environment for Santos; and

4. To demonstrate a potential application of the HYSYS® process models by analysing the multivariable controllability of the CO_2 Removal Trains and developing diagonal control structures for automating the control of the individual CO_2 Removal Trains.

1.2 Thesis Structure

As a guide to the reader, the overall structure of this thesis is described below.

In Chapter 2, a review of the relevant literature is presented. The hot potassium carbonate process is described and the operation of the Moomba CO_2 Removal Trains is outlined. Next, the effective simulation of the hot potassium carbonate process is explored: the non-equilibrium rate-based modelling approach is discussed; electrolyte thermodynamics are considered; and the capabilities of

Santos's preferred process simulation platform, HYSYS®, are examined. An overview of the simple diagonal control structure for multivariable process control is also provided.

Due to the limitations of HYSYS® identified in Chapter 2, the new rigorous non-equilibrium rate-based model for the hot potassium carbonate process was instead developed in the Aspen Custom Modeler simulation environment. Chapter 3 describes the physical and thermodynamic property models that were used to represent the behaviour of the hot potassium carbonate system, focussing particularly on the regression of the electrolyte thermodynamic model parameters from literature data. Chapter 4 outlines the process model equations and discusses the necessary model adjustments identified from preliminary column simulations. The benefits of increasing the model complexity and rigor are evaluated, followed by the validation of the Aspen Custom Modeler® process models against steady-state plant data.

Importation of the Aspen Custom Modeler® process models into HYSYS® was considered impractical due to the large computation times associated with these process models. Consequently, a novel approach, utilising column stage efficiencies and hypothetical components, was undertaken to compensate for HYSYS®'s restricted capabilities in simulating the hot potassium carbonate process. Chapter 5 outlines a series of parametric studies investigating the effects of various operating parameters on the performance of the Aspen Custom Modeler® process models. The results of these studies are used in Chapter 7 to develop the column stage efficiency correlations for the absorber and regenerator process models. Chapter 6 discusses the creation of the hypothetical components and the modifications to the standard HYSYS® property models to accommodate the hot potassium carbonate system. Chapter 8 outlines the development and validation of the HYSYS® process models of the Moomba CO_2 trains.

To demonstrate a potential application of the HYSYS® process models, the controllability of the two most dissimilar CO_2 Removal Trains, Trains #1 and #7, was examined using the MATLAB® numerical computing environment. Chapter 9 describes the derivation of simple first-order plus dead time (FOPDT) process transfer function models from dynamic HYSYS® simulations for the two CO_2 Removal Trains. Despite the wide use of the simple diagonal control structure for multivariable control, its application to the hot potassium carbonate process has not been previously documented. Consequently, the development and evaluation of an optimal diagonal control structure for CO_2 Removal Trains #1 and #7 are presented in Chapter 10.

Finally, Chapter 11 outlines the conclusions for this thesis and the recommendations for future work.

CHAPTER 2

LITERATURE REVIEW

The relevant literature for this thesis is reviewed in this chapter. To introduce the reader to the hot potassium carbonate process and its application in the Santos Moomba Processing Facility, the process background is briefly described and the operation and configuration of the Moomba CO_2 Removal Trains is outlined. An overview of the process chemistry is also provided.

The next parts of the literature review consider the various aspects of developing an effective process model for the hot potassium carbonate process. The non-equilibrium rate-based approach and its application to chemical absorption and desorption processes, like the hot potassium carbonate process, are reviewed. In this section, the relevant model equations are presented for the material and energy balances, the mass and heat transfer relations and resistances, the column hydrodynamic calculations and the chemical reaction kinetics. The following section briefly discusses electrolyte thermodynamic models, which are necessary for the accurate representation of the non-ideal behaviour of the electrolyte system governing the hot potassium carbonate process. It is noted that rigorous electrolyte thermodynamics have only been previously implemented in modelling the absorber column for the hot potassium carbonate process. Finally, the capabilities of HYSYS®, Santos' preferred simulation environment, are examined and a novel approach is considered for simulating the hot potassium carbonate process in HYSYS®.

To complete the literature review, an overview of the simple diagonal control structure for multivariable process control is provided. This includes a review of the various controllability analysis tools associated with this form of multivariable control and a brief description of a simple method of tuning such control structures. A survey of the available literature highlights the absence of any previous research concerning the multivariable control of the hot potassium carbonate process.

2.1 The Hot Potassium Carbonate Process

2.1.1 Process Background

The acidic nature of CO_2 and H_2S enables their removal through contact with alkaline solutions, such as aqueous monoethanolamine (MEA), aqueous diethanolamine (DEA) and aqueous potassium carbonate (K_2CO_3) solutions (Astarita et al., 1983). In 1959, U.S. Bureau of Mines researchers H. E. Benson and J. H. Field invented a process which utilised these alkaline solutions to remove CO_2 and H_2S from gas mixtures (Benson and Field, 1959). It was noted that this process performed best with concentrated potassium carbonate solution, which became the preferred absorbent solution. A simple process flowsheet for the hot potassium carbonate process is depicted in Figure 2.1.1.

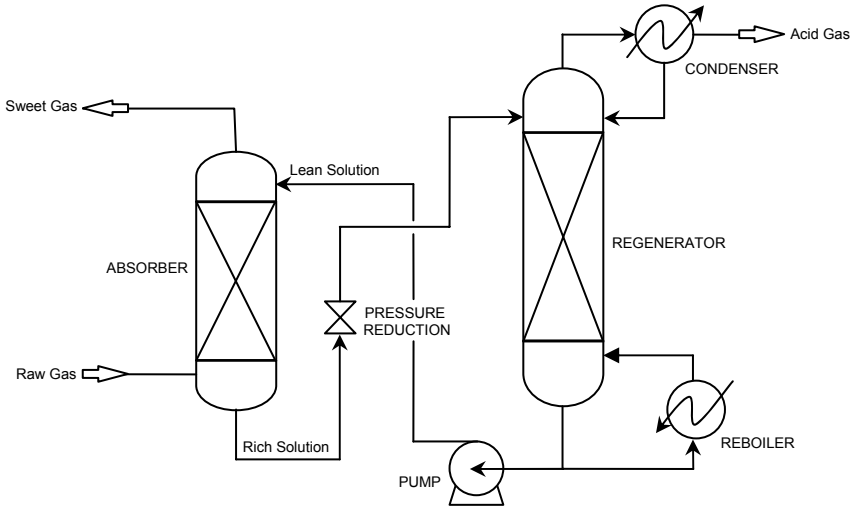

Figure 2.1.1: A simple form of the hot potassium carbonate process.

The raw gas, containing the acid gas impurities, enters the bottom of the high pressure (>8 atm) absorber countercurrent to the lean hot potassium carbonate solution which is fed to the top of the absorber. Within the column, contact between the two phases results in the transfer of the acid gases from the gas phase into the liquid phase. The sweet gas leaves through the top of the absorber while the rich potassium carbonate solution, containing the absorbed acid gases, leaves from the bottom. The rich solution is depressurised, causing some of the absorbed acid gas to flash off, before entering the low pressure (1 – 3 atm) regenerator. The remaining acid gas is then removed in the regenerator through reboil stripping. The removed acid gas is vented from the top of the regenerator while the regenerated potassium carbonate solution is pumped back to the absorber.

The high pressure in the absorber is required to ensure that the acid gas partial pressure in the raw gas exceeds the equilibrium pressure of the acid gas over the potassium carbonate solution (Benson and Field, 1959). This is necessary for the absorption of the acid gas to take place. The high operating pressure also enables the absorber to be run at temperatures close to the atmospheric boiling point of the potassium carbonate solution (100° – 140°C) without excessive evaporation of the

solution, thereby eliminating the need to heat the rich solution before it enters the regenerator. Another advantage of the elevated absorber temperature is the increased solubility of potassium carbonate and potassium bicarbonate. This enables the use of concentrated solutions between 20 to 40 wt% potassium carbonate, which facilitates greater acid gas removal. Kohl and Nielson (1997) recommend a solution concentration of 30 wt% potassium carbonate as a suitable design value for most applications.

Further research and development work has introduced many enhancements that have substantially improved the process economics and extended the applicability of the hot potassium carbonate process. One such enhancement is the addition of small quantities of amine or inorganic activators to the potassium carbonate solution to increase the rate of acid gas absorption (Bartoo, 1984; Kohl and Nielson, 1997). Other improvements involve modifications to the process flow scheme, such as the inclusion of more complex split-flow absorbers and two-stage regenerators to increase the sweet gas purity (Field et al., 1962; Benson and Parrish, 1984), and energy conservation features to improve the process economy (Benson and McCrea, 1979; Grover, 1987).

To date, there are over 700 commercial installations of the hot potassium carbonate process worldwide (UOP Gas Processing, 2000). Seven of these comprise the Raw Gas Conditioning (RGC) Plant at the Santos Moomba Processing Facility. Located in the Central Australian desert, the Moomba facility processes raw natural gas to reduce its CO_2 and water content and to recover ethane and heavier hydrocarbons. The removal of CO_2 occurs in the RGC Plant, which consists of seven parallel hot potassium carbonate process trains known as the CO_2 Removal Trains (CO_2 trains). The configuration and operation of these CO_2 trains are outlined in the following section.

2.1.2 The Santos Moomba CO_2 Trains

The seven parallel Moomba CO_2 trains are not identical, but share similar layouts, which are depicted in Figure 2.1.2. The CO_2 trains are based on a simple single-stage packed absorber and single-stage packed regenerator configuration, similar to the flow scheme in Figure 2.1.1. Some energy conservation features have been incorporated: power recovery turbines are coupled to the main solution pumps for all seven trains, while gas-gas heat exchangers have been included for heat recovery in CO_2 trains #3 to #7. A proprietary amine activator, ACT-1, was previously added to the potassium carbonate solutions for CO_2 trains #1 to #5, but Santos has since discontinued its use.

The purpose of the Moomba CO_2 trains is to remove sufficient CO_2 to prevent the formation of dry ice (solid CO_2) in the cold sections of the downstream Liquids Recovery Plant (LRP) and to meet the quality specification for sales gas, the final gas product from the Moomba Processing Facility. H_2S removal also occurs within the CO_2 trains, but this is of minor consequence due to the relatively insignificant levels of H_2S in the raw gas.

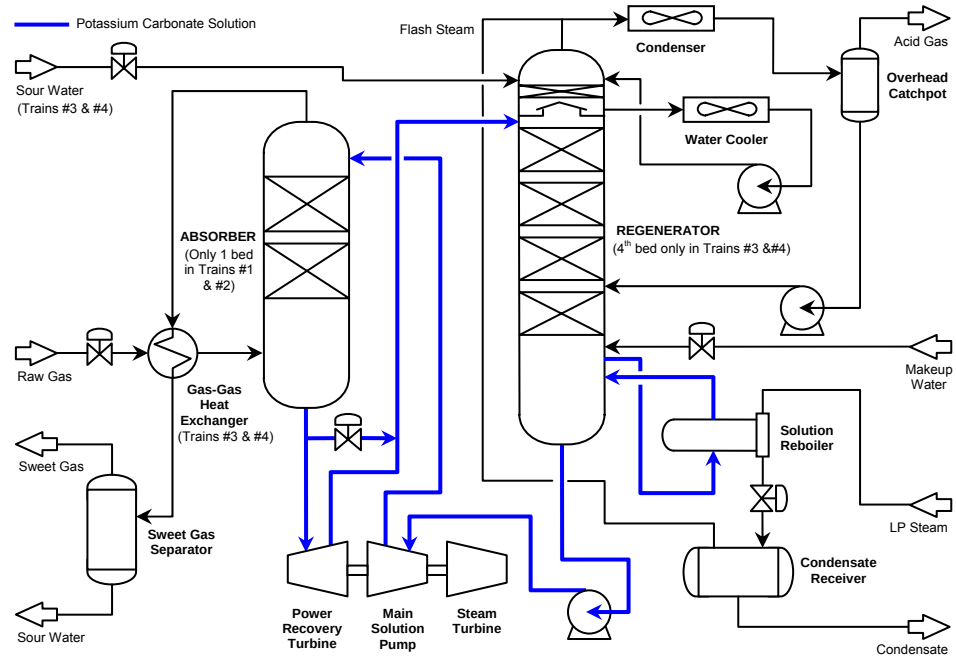

(a)

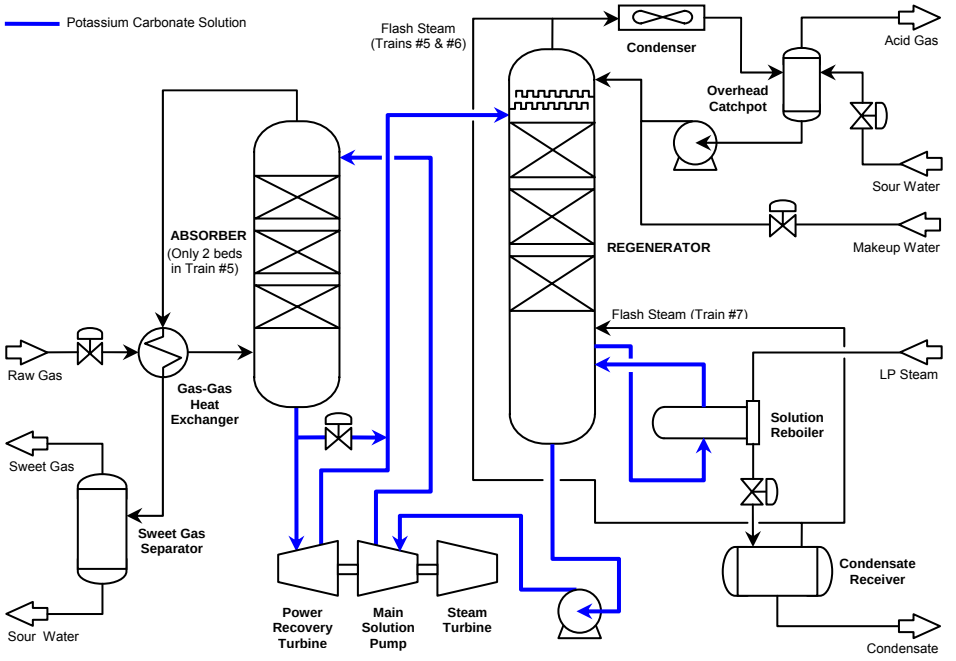

(b)

Figure 2.1.2: Basic CO_2 train process flow diagrams. (a) CO_2 trains #1 to #4. (b) CO_2 trains #5 to #7.

The raw gas entering the RGC Plant typically contains 16 to 20 mol% CO_2 and 5 to 20 ppm H_2S. This variation is due to changes in the proportions of the raw gas supplied to Moomba from various gas fields, whose individual CO_2 content range from 5 to 45 mol%. The sweet gas leaving the RGC Plant typically contains 2.5 to 3 mol% CO_2 and 0.5 to 1 ppm H_2S. However, due to the different absorber designs, the CO_2 content of sweet gas streams produced by the individual trains can vary between 0.1

and 8 mol% depending on the operating conditions. The combined sweet gas from the RGC Plant is fed to the LRP for separation into sales gas (which is predominantly methane), ethane, liquefied petroleum gas (LPG) and condensate.

Due to the high CO_2 content of the raw gas, the processing capacity of the CO_2 trains is normally limited by the CO_2 removal capacity of the hot potassium carbonate process. Table 2.1.1 gives an indication of the maximum capacities of each train for processing raw gas to produce sweet gas that meets the Santos specification of 2.5 mol% CO_2, and two sets of typical operating data from 2002 are presented in Table 2.1.2. The performance of the CO_2 trains is critical to the successful operation of the Moomba Processing Facility since the RGC Plant is one of the facility's bottlenecks. The gas flow through the RGC Plant sets the gas flow through the Moomba Processing Facility and therefore the sales gas, ethane and LPG production rates.

Table 2.1.1: Nameplate capacity of the CO_2 trains.

	CO_2 Removal Capacity (10^6 sm^3/d)	Raw Gas CO_2 Content (mol%)		
		16	18	20
		Maximum Raw Gas Capacity (10^6 sm^3/d)		
Train #1	0.30	2.17	1.89	1.67
Train #2	0.30	2.17	1.89	1.67
Train #3	0.50	3.61	3.15	2.79
Train #4	0.54	3.90	3.40	3.01
Train #5	0.58	4.19	3.65	3.23
Train #6	0.69	4.98	4.34	3.84
Train #7	0.96	6.93	6.04	5.35
Total	3.87	27.95	24.34	21.56

Note: sm^3/d refers to m^3/d at standard conditions, i.e. dry gas at 15°C and 1 atm.

Table 2.1.2: Typical operating data for the CO_2 trains from 2002.

	CO_2 Train Data Set #1							CO_2 Train Data Set #2						
	#1	#2	#3	#4	#5	#6	#7	#1	#2	#3	#4	#5	#6	#7
Raw Gas														
mol% CO_2 [a]	18.5	18.5	18.5	18.5	18.5	18.5	18.5	19.2	19.2	19.2	19.2	19.2	19.2	19.2
ppm H_2S	20	20	20	20	20	20	20	15	15	15	15	15	15	15
Flow (10^6 sm^3/d) [b]	1.95	1.65	2.93	3.35	3.35	4.08	5.55	1.80	1.55	2.79	3.18	3.26	3.99	4.56
Temperature (°C)	38	38	95	95	95	95	95	35	35	93	93	93	93	93
Sweet Gas														
mol% CO_2 [a]	2.5	2.5	2.5	2.5	2.5	2.5	2.5	2.8	2.8	2.9	2.9	3.1	2.5	1.2
ppm H_2S	< 4	< 4	< 4	< 4	< 4	< 4	< 4	< 4	< 4	< 4	< 4	< 4	< 4	< 4
Temperature (°C)	110	110	110	110	110	110	110	112	112	113	112	112	113	113
Acid Gas														
CO_2 (10^6 sm^3/d) [b]	0.32	0.27	0.48	0.55	0.55	0.67	0.91	0.30	0.26	0.47	0.53	0.54	0.68	0.83
Temperature (°C) [c]	103	103	80	103 [d]	95	94	94	102	103	75	103 [d]	95	94	94
Lean Solution														
CO_2 loading [e]	0.38	0.38	0.38	0.38	0.38	0.38	0.38	0.40	0.40	0.40	0.40	0.44	0.35	0.35
H_2S loading [e]	0.0	0.0	0.0	0.0	0.0	0.0	0.0	0.0	0.0	0.0	0.0	0.0	0.0	0.0
wt% K_2CO_3 [f]	27	27	30	30	30	30	30	28	28	30	29	30	31	30
Flow (m^3/h)	550	550	670	812	1000	1000	1068	481	475	638	758	923	940	946
Temperature (°C)	110	110	110	110	110	110	110	112	112	112	112	112	113	112
Rich Solution														
CO_2 loading [e]	0.82	0.75	0.86	0.84	0.75	0.83	0.96	0.85	0.80	0.89	0.89	0.84	0.82	0.94
H_2S loading [e]	$< 6\times10^{-5}$	$< 5\times10^{-5}$	$< 6\times10^{-5}$	$< 6\times10^{-5}$	$< 5\times10^{-5}$	$< 6\times10^{-5}$	$< 7\times10^{-5}$	$< 4\times10^{-5}$	$< 4\times10^{-5}$	$< 5\times10^{-5}$	$< 5\times10^{-5}$	$< 4\times10^{-5}$	$< 5\times10^{-5}$	$< 5\times10^{-5}$
Flow (m^3/h)	570	567	700	845	1034	1040	1122	499	490	667	789	955	980	995
Temperature (°C)	110	110	117	117	117	117	117	112	112	118	119	118	120	120
Sour Water														
ppm CO2	-	-	500	500	500	500	500	-	-	600	600	600	500	300
Flow (m^3/h)	-	-	1.3	1.5	1.5	1.8	2.6	-	-	1.2	1.4	1.4	1.8	2.1
Absorber														
Pressure (bar)	70	70	70	70	70	70	70	70	70	70	70	70	70	70
Pressure drop (bar)	< 0.2	< 0.2	< 0.2	< 0.2	< 0.2	< 0.2	< 0.2	< 0.2	< 0.2	< 0.2	< 0.2	< 0.2	< 0.2	< 0.2
Regenerator														
Pressure (bar)	1.3	1.3	1.3	1.3	1.3	1.3	1.3	1.3	1.3	1.3	1.3	1.3	1.3	1.3
Pressure drop (bar)	< 0.1	< 0.1	< 0.1	< 0.1	< 0.1	< 0.1	< 0.1	< 0.1	< 0.1	< 0.1	< 0.1	< 0.1	< 0.1	< 0.1
Cooling Water Circuit														
Water Flow (m^3/h)	456	456	818	1079	-	-	-	456	456	818	1079	-	-	-
Cooler Duty (MW)	6.89	6.89	14.24	17.80	-	-	-	6.89	6.89	14.24	17.80	-	-	-
Overhead Condenser														
Temperature (°C)	60	60	60	60	60	60	60	60	60	60	60	60	60	60
Pressure (bar)	1.08	1.08	1.08	1.08	1.08	1.08	1.08	1.08	1.08	1.08	1.08	1.08	1.08	1.08
Solution Reboiler														
Steam flow (t/h) [g]	29.0	24.4	34.8	42.3	44.3	49.3	64.9	23.6	21.6	35.0	36.0	37.1	49.6	54.3

[a] This refers to the CO_2 content in the dry gas. [b] sm^3/d refers to m^3/d at standard conditions (dry gas at 15°C and 1 atm). [c] This is the vapour temperature entering the regenerator wash sections in CO_2 trains #1 and #2 and leaving the wash sections in trains #3 to #7. [d] The value for train #4 is unexpectedly high compared to the typical value of 80°C (Santos Ltd, 1998). [e] The CO_2 and H_2S loading refer to the moles of CO_2 and H_2S per equivalent mole of K_2CO_3 in the solution. The equivalent moles of K_2CO_3 are defined as the total number of moles of K_2CO_3 in the solution if all the $KHCO_3$, KHS and K_2S in the solution are converted back into K_2CO_3. [f] This refers to the equivalent weight percent of K_2CO_3 in the solution. [g] The low pressure steam enters the reboilers at 140°C and 3.6 bar, while the steam condensate leaves at 138°C and 3.4 bar.

2.1.3 Process Chemistry

Figure 2.1.3 summarises the various absorption, desorption and equilibrium reactions that take place in the hot potassium carbonate process. These reactions are discussed in detail in the following sections.

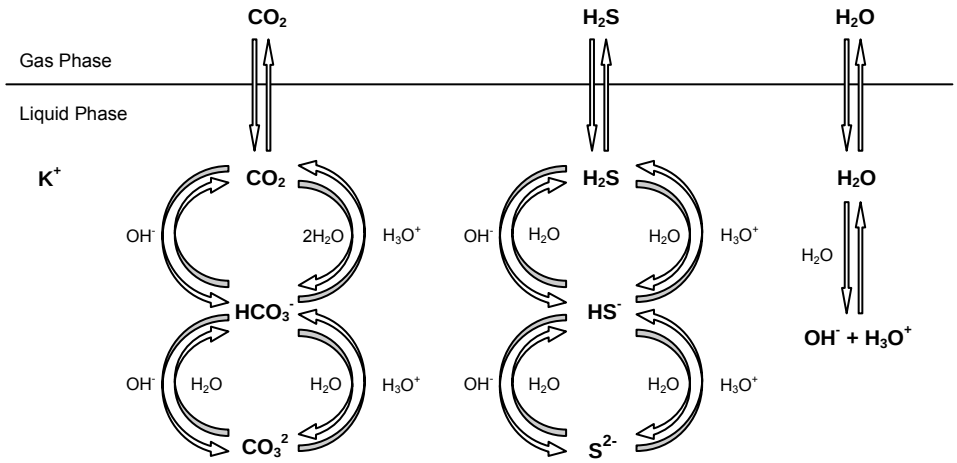

Figure 2.1.3: Reaction flow scheme for the hot potassium carbonate process.

2.1.3.1 Acid Gas Absorption

CO_2 and H_2S absorption takes place in the hot potassium carbonate process via a series of reactions, as summarised in Table 2.1.3.

Table 2.1.3: Acid gas absorption reactions in the hot potassium carbonate process.

1. Physical Absorption	
$CO_{2(g)} \longleftrightarrow CO_{2(aq)}$	(R2.1.1)
$H_2S_{(g)} \longleftrightarrow H_2S_{(aq)}$	(R2.1.2)
2. Chemical Absorption	
$CO_2 + CO_3^{2-} + H_2O \longleftrightarrow 2 \cdot HCO_3^-$	(R2.1.3)
$H_2S + CO_3^{2-} \longleftrightarrow HCO_3^- + HS^-$	(R2.1.4)
Mechanism 1:	
$CO_3^{2-} + H_2O \longleftrightarrow HCO_3^- + OH^-$	(R2.1.5)
$CO_2 + OH^- \longleftrightarrow HCO_3^-$	(R2.1.6)
$H_2S + OH^- \longleftrightarrow HS^- + H_2O$	(R2.1.7)
$HS^- + OH^- \longleftrightarrow S^{2-} + H_2O$	(R2.1.8)
Mechanism 2:	
$CO_2 + 2 \cdot H_2O \longleftrightarrow HCO_3^- + H_3O^+$	(R2.1.9)
$H_2S + H_2O \longleftrightarrow HS^- + H_3O^+$	(R2.1.10)
$HS^- + H_2O \longleftrightarrow S^{2-} + H_3O^+$	(R2.1.11)
$CO_3^{2-} + H_3O^+ \longleftrightarrow HCO_3^- + H_2O$	(R2.1.12)

The absorption process begins with the diffusion of the two acid gases to the gas-liquid interface followed by physical absorption into the solution (reactions (R2.1.1) and (R2.1.2)). The aqueous CO_2 and H_2S then react with K_2CO_3 to give potassium bicarbonate ($KHCO_3$) and potassium bisulfide (KHS). Since K_2CO_3, $KHCO_3$ and KHS are all strong electrolytes, they can be assumed to be fully dissociated in water, and can therefore be represented by carbonate (CO_3^{2-}), bicarbonate (HCO_3^-) and bisulfide (HS^-) ions (reactions (R2.1.3) and (R2.1.4)).

There are two possible mechanisms by which CO_2 and H_2S can react with the potassium carbonate solution (Astarita et al., 1981). The CO_3^{2-} ions can first react with water to generate hydroxide (OH^-) ions, which then react with CO_2 and H_2S to give HCO_3^- and HS^- ions (reactions (R2.1.5) to (R2.1.7)). The HS^- ions also react with the OH^- ions to give sulfide (S^{2-}) ions (reaction (R2.1.8)). Alternatively, CO_2 and H_2S react with water to produce HCO_3^-, HS^- and hydronium (H_3O^+) ions, which then react with the CO_3^{2-} ions to form more HCO_3^- ions in what is known as the "acidic mechanism" (reactions (R2.1.9), (R2.1.10) and (R2.1.12)). Further H_3O^+ ions and S^{2-} ions are formed from the reaction between the HS^- and water (reaction (R2.1.11)).

Of the eight chemical absorption reactions, only the two CO_2 reactions (R2.1.6) and (R2.1.9) are kinetically controlled. The remainder involve simple proton transfers and are considered to occur instantaneously. The instantaneous nature of the H_2S reactions leads to a considerably faster absorption rate for H_2S compared to CO_2, which enables the selective absorption of H_2S over CO_2 using the hot potassium carbonate process. However, the hot potassium carbonate process is not suitable for treating gases for which H_2S is the only acid gas impurity. Some CO_2 has to be present in the untreated gas in order to regenerate the potassium carbonate solution. Otherwise, all the K_2CO_3 in the solution will eventually be converted to KHS, which has been found to be essentially non-regenerable (Tosh et al., 1960). This is further discussed in the next section on solution regeneration.

Reactions (R2.1.6) and (R2.1.9) provide the rate-controlling steps for CO_2 absorption. At pH levels exceeding 8, reaction (R2.1.6) is fast whereas reaction (R2.1.9) is extremely slow (Astarita et al., 1981). Since hot potassium carbonate processes typically operate in the pH range of 9 to 11 (Kohl and Neilson, 1997), the absorption rate of CO_2 is predominantly governed by reaction (R2.1.6). Reaction (R2.1.9) has a comparably negligible effect and can be ignored. It should also be noted that within the pH range of interest, the equilibrium constants for reactions (R2.1.8) and (R2.1.11) are so low that it can be assumed that essentially no S^{2-} ions are formed and all the absorbed H_2S is present as either aqueous H_2S or HS^- ions (Astarita et al., 1983).

Neglecting reaction (R2.1.9), the overall reaction rate for the absorption of CO_2 into hot potassium carbonate solution can be expressed as (Danckwerts and Sharma, 1966):

$$R_{CO_2} = k' \cdot \left(C_{CO_2} - C_{CO_2}^{\ eq} \right) \tag{2.1.1}$$

where k' is the pseudo-first-order reaction constant, defined as:

$$k' = k_{OH^-} \cdot C_{OH^-} \tag{2.1.2}$$

k_{OH^-} is the forward rate constant for reaction (R2.1.6), C is the molar concentration, and $C_{CO_2}^{eq}$ is the concentration of CO_2 at chemical equilibrium. CO_2 can be considered to undergo a pseudo-first-order reaction due to the buffering nature of carbonate-bicarbonate systems which ensures the concentration of OH^- ions near the surface of the liquid is not significantly depleted by the absorbed CO_2 and remains relatively constant.

Astarita and co-workers (1983) have presented the following equation for k_{OH^-}:

$$\log k_{OH^-} = 13.635 - \frac{2895}{T} + 0.08 \cdot I_c \tag{2.1.3}$$

$$I_c = \frac{1}{2} \cdot \sum_j z_j^{\,2} \cdot C_j \tag{2.1.4}$$

where k_{OH^-} is in m^3/kmol·s, I_c is the solution ionic strength in kmol/m^3, T is the temperature in K, z is the ionic charge, and C is the molar concentration in kmol/m^3. Equation (2.1.3) has been validated for temperatures up to 110°C and for solution ionic strengths up to 8 kmol/m^3. Since these conditions correspond to the typical operating conditions of the hot potassium carbonate process, equation (2.1.4) can be applied to this process with confidence.

Similar expressions for k_{OH^-} have also been developed by other workers, such as:

Pohorecki and Moniuk (1988): $$\log k_{OH^-} = 11.916 - \frac{2382}{T} + \frac{1}{2} \cdot \sum_j b_j \cdot C_j \cdot z_j^{\,2} \tag{2.1.5}$$

Kucka and co-workers (2002): $$\ln k_{OH^-} = 31.121 - \frac{6612}{T} + \beta_{CO_2} \cdot I_c \tag{2.1.6}$$

The ion contribution factors b_j for species relevant to the hot potassium carbonate process are given in Table 2.1.4, and the temperature dependence of the contribution factor β_{CO_2} for CO_2 absorption into potassium hydroxide (KOH) solutions is:

$$\beta_{CO_2} = 0.00033968 \cdot T^2 - 0.021215 \cdot T + 33.506 \tag{2.1.7}$$

Equation (2.1.5) has only been validated at 20°C (although the first two infinite dilution terms have been validated for up to 41°C) and is applicable to solution ionic strengths greater than 0.5 kmol/m^3. Equation (2.1.6) has been validated for temperatures up to 50°C and for solution ionic strengths up to 3 kmol/m^3. These equations therefore may not be applicable to the hot potassium carbonate process, unlike equation (2.1.3).

Table 2.1.4: Ion contribution factors (Pohorecki and Moniuk, 1988).

Species	b (m^3/kmol)
K^+	0.220
OH^-	0.220
HCO_3^-	0 [a]
CO_3^{2-}	0.085
HS^-	0 [a]
S^{2-}	0 [a]

[a] Not available so set as 0.

2.1.3.2 Solution Regeneration

The regeneration of the rich potassium carbonate solution requires the desorption of the absorbed CO_2 and H_2S from the solution. Up to two-thirds of the absorbed acid gas is flashed off through the significant reduction in pressure between the absorber and regenerator (Astarita et al., 1981), and the remainder is desorbed through the reboil stripping of the partially regenerated solution. The CO_2 and H_2S desorption reactions are summarised in Table 2.1.5.

Table 2.1.5: Acid gas desorption reactions in the hot potassium carbonate process.

1. Chemical Desorption	
$2 \cdot HCO_3^- \longleftrightarrow CO_2 + CO_3^{2-} + H_2O$	(R2.1.13)
$HCO_3^- + HS^- \longleftrightarrow H_2S + CO_3^{2-}$	(R2.1.14)
Mechanism 1:	
$HCO_3^- \longleftrightarrow CO_2 + OH^-$	(R2.1.15)
$S^{2-} + H_2O \longleftrightarrow HS^- + OH^-$	(R2.1.16)
$HS^- + H_2O \longleftrightarrow H_2S + OH^-$	(R2.1.17)
$HCO_3^- + OH^- \longleftrightarrow CO_3^{2-} + H_2O$	(R2.1.18)
Mechanism 2:	
$HCO_3^- + H_3O^+ \longleftrightarrow CO_2 + 2 \cdot H_2O$	(R2.1.19)
$S^{2-} + H_3O^+ \longleftrightarrow HS^- + H_2O$	(R2.1.20)
$HS^- + H_3O^+ \longleftrightarrow H_2S + H_2O$	(R2.1.21)
$HCO_3^- + H_2O \longleftrightarrow CO_3^{2-} + H_3O^+$	(R2.1.22)
2. Physical Desorption	
$CO_{2(aq)} \longleftrightarrow CO_{2(g)}$	(R2.1.23)
$H_2S_{(aq)} \longleftrightarrow H_2S_{(g)}$	(R2.1.24)

The acid gas desorption process involves the reversal of reactions (R2.1.3) and (R2.1.4) to regenerate K_2CO_3 and the two acid gases (reactions (R2.1.13) and (R2.1.14)), followed by the diffusion of the evolved acid gases to the gas-liquid interface (reactions (R2.1.23) and (R2.1.24)). Reactions (R2.1.13) and (R2.1.14) take place in the following sequence of steps. First, reactions (R2.1.6) to (R2.1.8) and reactions (R2.1.9) to (R2.1.11) are reversed to generate CO_2 and H_2S from the HCO_3^-,

HS^- and S^{2-} ions (reactions (R2.1.15) to (R2.1.17) and reactions (R2.1.19) to (R2.1.21), respectively). Then reactions (R2.1.5) and (R2.1.12) are then reversed to regenerate the CO_3^{2-} ions from the HCO_3^- ions (reactions (R2.1.18) and (R2.1.22)).

Like their reverse reactions, reactions (R2.1.15) and (R2.1.19) are slow, rate-determining steps while the remaining reactions are instantaneous proton transfers. Reaction (R2.1.19) is extremely slow under the conditions of interest and its effect on the desorption rate of CO_2 can be neglected (Pohorecki and Kucharski, 1991).

It should be noted that reactions (R2.1.15) and (R2.1.19) will occur even if H_2S is the only acid gas impurity, as its absorption leads to the formation of both HCO_3^- and HS^- ions. Consequently, with each absorption-regeneration cycle, some HCO_3^- ions are lost from the system through the generation of CO_2. However, the absorption of H_2S does not produce enough HCO_3^- ions to compensate for this loss (Tosh et al., 1960). The regeneration of the potassium carbonate solution is dependent on the presence of HCO_3^- ions, which are necessary in order for reactions (R2.1.18) and (R2.1.22) to proceed. If no CO_2 is absorbed from the untreated gas, there will eventually be insufficient HCO_3^- ions in the system to regenerate the CO_3^{2-} ions.

As for the absorption of CO_2 into potassium carbonate solution, the desorption of CO_2 from potassium carbonate solutions can be treated as a pseudo-first-order reaction with the following overall reaction rate:

$$R_{-CO_2} = k' \cdot \left(C_{CO_2}^{\ eq} - C_{CO_2} \right) \tag{2.1.8}$$

where k' is the pseudo-first-order rate constant as defined in equation (2.1.2), C is the molar concentration, and the superscript eq denotes the condition of chemical equilibrium. Consequently, the desorption reaction kinetics can be described by the expression for k_{OH^-} (equation (2.1.3)) presented by Astarita and co-workers (1983).

An alternative approach has been proposed by Pohorecki and Kucharski (1991), who have developed the following expression for k':

$$k' = k'' \cdot \frac{C_{CO_3^{2-}}}{C_{HCO_3^-}} \tag{2.1.9}$$

$$\ln k'' = 27.821 - \frac{8514}{T} + 0.5456 \cdot I_c - 0.02760 \cdot I_c^{\ 2} \tag{2.1.10}$$

The rate constant k' and the kinetic coefficient k" are in 1/s, the molar concentrations $C_{CO_3^{2-}}$ and $C_{HCO_3^-}$ are in kmol/m^3, the temperature T is in K, and the molar ionic strength I_c is in kmol/m^3. Equations (2.1.9) and (2.1.10) are valid for temperatures between 60 and 100°C and solution ionic

strengths between 2 to 8 kmol/m^3, which correspond to the typical operating conditions for the hot potassium carbonate process.

2.1.3.3 CO_2-H_2S-K_2CO_3-$KHCO_3$-KHS-K_2S-H_2O System Equilibria

Aside from the above absorption and desorption reactions, the chemistry of the hot potassium carbonate process is also dependent on the equilibria governing the CO_2-H_2S-K_2CO_3-$KHCO_3$-KHS-K_2S-H_2O system, as summarised in Table 2.1.6.

Table 2.1.6: CO_2-H_2S-K_2CO_3-$KHCO_3$-KHS-K_2S-H_2O system equilibria.

Vapour-Liquid Equilibria	
$H_2O_{(g)} \longleftrightarrow H_2O_{(aq)}$	(R2.1.25)
$CO_{2(g)} \xleftrightarrow{H_{CO_2}} CO_{2(aq)}$	(R2.1.26)
$H_2S_{(g)} \xleftrightarrow{H_{H_2S}} H_2S_{(aq)}$	(R2.1.27)
Liquid Phase Chemical Equilibria	
$2 \cdot H_2O \xleftrightarrow{K_{H_2O}} OH^- + H_3O^+$	(R2.1.28)
$CO_2 + 2 \cdot H_2O \xleftrightarrow{K_{CO_2}} HCO_3^- + H_3O^+$	(R2.1.29)
$HCO_3^- + H_2O \xleftrightarrow{K_{HCO_3^-}} CO_3^{2-} + H_3O^+$	(R2.1.30)
$H_2S + H_2O \xleftrightarrow{K_{H_2S}} HS^- + H_3O^+$	(R2.1.31)
$HS^- + H_2O \xleftrightarrow{K_{HS^-}} S^{2-} + H_3O^+$	(R2.1.32)

The chemical dissociation equilibrium relations for five liquid equilibria (R2.1.28) to (R2.1.32) and the temperature dependence of the equilibrium constants are given in Table 2.1.7. Also included are the temperature dependence of the Henry's Law constants for CO_2 and H_2S. The equilibrium and Henry's Law constants are taken on a mole fraction basis at infinite dilution in pure water and are valid for temperatures between 0° and 150°C.

By taking CO_2, H_2S, H_2O and K_2CO_3 to be the unspeciated liquid phase species in the CO_2-H_2S-K_2CO_3-$KHCO_3$-KHS-K_2S-H_2O system, the liquid phase ionic speciation is described by the equilibrium relations in Table 2.1.7 and the liquid phase equations in Table 2.1.8. The corresponding vapour phase composition is represented by the vapour-liquid phase equilibrium expressions in Table 2.1.8. These equations can be extended to accommodate any inert molecular solute species, such as nitrogen, methane and other hydrocarbons which are present in the Moomba CO_2 trains.

Table 2.1.7: Temperature dependence of the equilibrium and Henry's Law constants.

Constant	A	B	C	D	Equilibrium Relation [d]	
	$\ln K = A + \frac{B}{T} + C \cdot \ln T + D \cdot T$ T in K					
K_{H_2O} [a]	132.899	-13445.9	-22.4773	0.0	$\frac{x_{H_3O^+} \cdot x_{OH^-}}{x_{H_2O}^2} \cdot \frac{\gamma^*_{H_3O^+} \cdot \gamma^*_{OH^-}}{\gamma_{H_2O}^2}$	(2.1.11)
K_{CO_2} [a]	231.465	-12092.1	-36.7816	0.0	$\frac{x_{H_3O^+} \cdot x_{HCO_3^-}}{x_{CO_2} \cdot x_{H_2O}^2} \cdot \frac{\gamma^*_{H_3O^+} \cdot \gamma^*_{HCO_3^-}}{\gamma^*_{CO_2} \cdot \gamma_{H_2O}^2}$	(2.1.12)
$K_{HCO_3^-}$ [a]	216.050	-12431.7	-35.4819	0.0	$\frac{x_{H_3O^+} \cdot x_{CO_3^{2-}}}{x_{HCO_3^-} \cdot x_{H_2O}} \cdot \frac{\gamma^*_{H_3O^+} \cdot \gamma^*_{CO_3^{2-}}}{\gamma^*_{HCO_3^-} \cdot \gamma_{H_2O}}$	(2.1.13)
K_{H_2S} [a]	214.582	-12995.4	-33.5471	0.0	$\frac{x_{H_3O^+} \cdot x_{HS^-}}{x_{H_2S} \cdot x_{H_2O}} \cdot \frac{\gamma^*_{H_3O^+} \cdot \gamma^*_{HS^-}}{\gamma^*_{H_2S} \cdot \gamma_{H_2O}}$	(2.1.14)
K_{HS^-} [b]	-9.74196	-8585.47	0.0	0.0	$\frac{x_{H_3O^+} \cdot x_{S^{2-}}}{x_{HS^-} \cdot x_{H_2O}} \cdot \frac{\gamma^*_{H_3O^+} \cdot \gamma^*_{S^{2-}}}{\gamma^*_{HS^-} \cdot \gamma_{H_2O}}$	(2.1.15)
	$\ln H = A + \frac{B}{T} + C \cdot \ln T + D \cdot T$ H in bar, T in K					
H_{CO_2} [c]	159.1997	-8477.711	-21.9574	0.00578075	-	
H_{H_2S} [a]	346.6251	-13236.800	-55.0551	0.05956500	-	

[a] Austgen and co-workers (1989) [b] Drummond (1981) [c] Chen (1980) [d] x is the liquid phase mole fraction, γ^* is the un-symmetric activity coefficient, and γ is the symmetric activity coefficient (Section A.1 in Appendix A contains a brief explanation of the different activity coefficient reference states).

Table 2.1.8: Liquid phase relations and vapour-liquid equilibria expressions.

	Liquid Phase Relations	
Electroneutrality	$x_{H_3O^+} + x_{K^+} = x_{OH^-} + x_{HCO_3^-} + 2 \cdot x_{CO_3^{2-}} + x_{HS^-} + 2 \cdot x_{S^{2-}}$	(2.1.16)
Overall Balance	$x_{H_2O} + x_{H_3O^+} + x_{OH^-} + x_{K^+} + x_{CO_2} + x_{HCO_3^-} + x_{CO_3^{2-}} + x_{H_2S} + x_{HS^-} + x_{S^{2-}} = 1$	(2.1.17)
K^+ Balance	$x_{K^+} = 2 \cdot n_{K_2CO_3} \cdot n_{total}$	(2.1.18)
CO_2 Balance	$x_{CO_2} + x_{HCO_3^-} + x_{CO_3^{2-}} = \left(n_{CO_2} + n_{K_2CO_3}\right) \cdot n_{total}$	(2.1.19)
H_2S Balance	$x_{H_2S} + x_{HS^-} + x_{S^{2-}} = n_{H_2S} \cdot n_{total}$	(2.1.20)
H_2O Balance	$x_{H_2O} + 2 \cdot x_{H_3O^+} - 2 \cdot x_{CO_2} - 2 \cdot x_{HCO_3^-} - 3 \cdot x_{CO_3^{2-}} + 2 \cdot x_{H_2S} + x_{HS^-} = \left(-2 \cdot n_{CO_2} - 3 \cdot n_{K_2CO_3} + 2 \cdot n_{H_2S} + n_{H_2O}\right) \cdot n_{total}$	(2.1.21)
	Vapour-Liquid Equilibria Expressions	
For (R2.1.25)	$y_{H_2O} \cdot \varphi_{H_2O} \cdot P = x_{H_2O} \cdot \gamma_{H_2O} \cdot \varphi^s_{H_2O} \cdot P^s_{H_2O} \cdot \exp\left(\frac{V^s_{L,H_2O} \cdot \left(P - P^s_{H_2O}\right)}{R \cdot T}\right)$	(2.1.22)
For (R2.1.26)	$y_{CO_2} \cdot \varphi_{CO_2} \cdot P = x_{CO_2} \cdot \gamma^*_{CO_2} \cdot H_{CO_2} \cdot \exp\left(\frac{\bar{v}^{\infty}_{CO_2} \cdot \left(P - P^s_{H_2O}\right)}{R \cdot T}\right)$	(2.1.23)
For (R2.1.27)	$y_{H_2S} \cdot \varphi_{H_2S} \cdot P = x_{H_2S} \cdot \gamma^*_{H_2S} \cdot H_{H_2S} \cdot \exp\left(\frac{\bar{v}^{\infty}_{H_2S} \cdot \left(P - P^s_{H_2O}\right)}{R \cdot T}\right)$	(2.1.24)

Notation: x is the liquid phase mole fraction in the speciated system; n is the number of moles in the unspeciated liquid phase; n_{total} is the total number of moles in the speciated liquid phase; y is the vapour phase mole fraction in equilibrium with the speciated liquid phase; H is the Henry's Law constant; V_L is the liquid molar volume; $\bar{v}^{\infty}$ is the partial molar volume at infinite dilution in water; P is the system pressure; T is the absolute system temperature; R is the gas constant; γ and γ^* are the symmetric and un-symmetric activity coefficients; and φ is the fugacity coefficient. The superscript s indicates the vapour pressure P^s.

Since the inert species do not participate in any liquid phase chemical equilibria, the resulting material balance and vapour-liquid equilibrium expression are:

$$x_j = n_j \cdot n_{total} \qquad \text{for j = inert molecular species} \qquad (2.1.25)$$

$$y_j \cdot \varphi_j \cdot P = x_j \cdot \gamma_j^* \cdot H_j \cdot \exp\left(\frac{\overline{v}_j^{\infty} \cdot \left(P - P_{H_2O}^s\right)}{R \cdot T}\right) \qquad \text{for j = inert molecular species} \qquad (2.1.26)$$

The left-hand side of the overall balance (2.1.17) must also be extended to include x_j for any inert molecular species.

In summary, the hot potassium carbonate process involves a multicomponent system with two-phase mass transfer coupled with chemical reactions. Its simulation therefore requires the consideration of multicomponent mass transport theory, chemical reaction theory, and the effects of various driving forces such as multicomponent diffusion and chemical interactions. This is best achieved via the non-equilibrium rate-based approach (Taylor and Krishna, 1993; Kenig et al., 2001, Brettschneider et al., 2004), which is discussed in the following section.

2.2 The Non-Equilibrium Rate-Based Approach

2.2.1 The MESH Equations

The non-equilibrium rate-based approach is based on a set of balance equations, commonly known as the MESH (Material balance, Equilibrium, Summation and entHalpy balance) equations (Taylor and Krishna, 1993). For comparison, the MESH equations for the simple equilibrium stage approach and the non-equilibrium rate-based approach are both provided in Table 2.2.1. Both approaches assume the division of the absorption or desorption column into artificial height segments, called stages. However, in the equilibrium stage approach, thermodynamic equilibrium is assumed to exist between the vapour and liquid streams leaving each stage (Seader and Henley, 1998). In contrast, the non-equilibrium rate-based approach assumes that equilibrium only exists at the vapour-liquid interface, hence the separate balances for each phase (Taylor and Krishna, 1993).

For tray columns, each equilibrium stage represents an ideal tray, while each non-equilibrium stage is equivalent to a real tray. As thermodynamic equilibrium is rarely achieved in practice, the equilibrium stage approach uses tray efficiencies to relate the ideal trays to real trays, such as the widely used Murphree vapour efficiency (Murphree, 1925):

$$E_{Murph,i} = \frac{y_{i,j} - y_{i+1,j}}{K_{i,j} \cdot x_{i,j} - y_{i+1,j}} \qquad \text{for } j = 1...NC \qquad (2.2.9)$$

which replaces equation (2.2.2) in the equilibrium stage MESH equations. In the case of packed columns, the packed bed is divided into a series of stages over which equations (2.2.1) to (2.2.8) can be applied. For the equilibrium stage approach, the number of equilibrium stages N_{eqm} is related to the real packed column height H_c via the "height of packing equivalent to a theoretical plate" or HETP:

$$H_c = HETP \cdot N_{eqm} \qquad (2.2.10)$$

While the MESH equations are sufficient for the equilibrium stage approach, the non-equilibrium rate-based approach requires an additional set of mass and energy transfer relations. These relations describe the rate of mass and energy transfer across the vapour-liquid interface and are used to determine the interphase molar and energy fluxes.

It should be noted that the inclusion of tray efficiencies can enable the satisfactory application of the equilibrium stage approach to chemical absorption and desorption processes, as will be demonstrated in the later chapters of this work. However, these tray efficiencies had to be first derived from a rigorous non-equilibrium model in order for the equilibrium stage approach to reasonably represent the effect of chemical absorption and desorption in the hot potassium carbonate process. The added complexity of the non-equilibrium rate-based approach facilitates a greater understanding of the mass and energy transfer processes that occur in such chemical absorption and desorption systems.

Table 2.2.1: The MESH equations for a stage I and j = 1…NC components.

	Equilibrium Stage Approach	Non-Equilibrium Rate-Based Approach	
Stage Diagram:	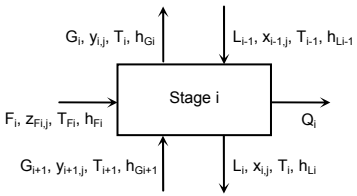	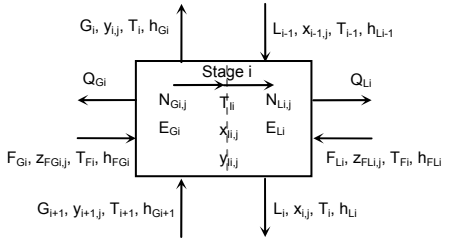	
Material Balance:	$\frac{\partial M_{i,j}}{\partial t} = F_i \cdot z_{Fi,j} + G_{i+1} \cdot y_{i+1,j} + L_{i-1} \cdot x_{i-1,j} - G_i \cdot y_{i,j} - L_i \cdot x_{i,j}$	$\frac{\partial M_{Gi,j}}{\partial t} = F_{Gi} \cdot z_{GFi,j} + G_{i+1} \cdot y_{i+1,j} - G_i \cdot y_{i,j} - N_{Gi,j} \cdot a_{Ii} \cdot V_i$ $\frac{\partial M_{Li,j}}{\partial t} = F_{Li} \cdot z_{FLi,j} + L_{i-1} \cdot x_{i-1,j} - L_i \cdot x_{i,j} + N_{Li,j} \cdot a_{Ii} \cdot V_i$ $N_{Gi,j} = N_{Li,j}$	(2.2.1)
Equilibrium Relation:	$y_{i,j} = K_{i,j} \cdot x_{i,j}$		(2.2.2)
Summation Equations:	$\sum_{j=1}^{NC} y_{i,j} = 1$ and $\sum_{j=1}^{NC} x_{i,j} = 1$		(2.2.3)
Enthalpy Balance:	$\frac{\partial U_i}{\partial t} = F_i \cdot h_{Fi} + G_{i+1} \cdot h_{Gi+1} + L_{i-1} \cdot h_{Li-1} - G_i \cdot h_{Gi} - L_i \cdot h_{Li} - Q_i$	$\frac{\partial U_{Gi}}{\partial t} = F_{Gi} \cdot h_{FGi} + G_{i+1} \cdot h_{Gi+1} - G_i \cdot h_{Gi} - Q_{Gi} - E_{Gi} \cdot a_{Ii} \cdot V_i$ $\frac{\partial U_{Li}}{\partial t} = F_{Li} \cdot h_{FLi} + L_{i-1} \cdot h_{Li-1} - L_i \cdot h_{Li} - Q_{Li} + E_{Li} \cdot a_{Ii} \cdot V_i$ $E_{Gi} = E_{Li}$	(2.2.4)
Material Holdup:	$M_{i,j} = \left(y_{i,j} \cdot C_{Gti} \cdot \phi_{Gi} + x_{i,j} \cdot C_{Lti} \cdot \phi_{Li}\right) \cdot V_i$	$M_{Gi,j} = y_{i,j} \cdot C_{Gti} \cdot \phi_{Gi} \cdot V_i$ $M_{Li,j} = x_{i,j} \cdot C_{Lti} \cdot \phi_{Li} \cdot V_i$	(2.2.5)
Energy Holdup:	$U_i = \left(h_{Gi} \cdot C_{Gti} \cdot \phi_{Gi} + h_{Li} \cdot C_{Lti} \cdot \phi_{Li} - P_i\right) \cdot V_i$	$U_{Gi} = \left(h_{Gi} \cdot C_{Gti} \cdot \phi_{Gi} - P_i\right) \cdot V_i$ $U_{Li} = h_{Li} \cdot C_{Lti} \cdot \phi_{Li} \cdot V_i$	(2.2.6)
Stage Volume:	$V_i = \frac{\pi \cdot D_i^{\,2} \cdot H_i}{4}$		(2.2.7)
Stage Pressure:	$P_i = P_{i+1} - \Delta P_i$		(2.2.8)

Notation: M is the component material holdup; F, G and L are the feed, vapour phase and liquid phase molar flow rates; N is the molar flux across the vapour-liquid interface; a_I is the effective interfacial area for mass transfer; x, y and z_F are the liquid phase, vapour phase and feed mole fractions; K is the equilibrium constant; NC is the number of components in the system; U is the energy holdup; h is the enthalpy; Q is the stage heat loss; E is the energy flux across the vapour-liquid interface; T is the temperature; C_t is the phase molar density; ϕ is the phase volumetric holdup; V is the stage volume; D is the stage diameter; H is the stage height; P is the stage pressure; and ΔP is the stage pressure drop. The subscripts F, G, L and I denote the feed, vapour phase, liquid phase and the vapour-liquid interface, while the subscripts i and j refer to stage i and component j.

2.2.2 The Mass Transfer Relations

The mass transfer at the vapour-liquid interface can be described by a variety of different theoretical concepts, including the two-film model (Lewis and Whitman, 1923), the Higbie (1935) penetration model, and the Danckwerts (1951) surface renewal model. The two-film model is most commonly employed due to its simplicity and the wide range of correlations available in literature for estimating its parameters.

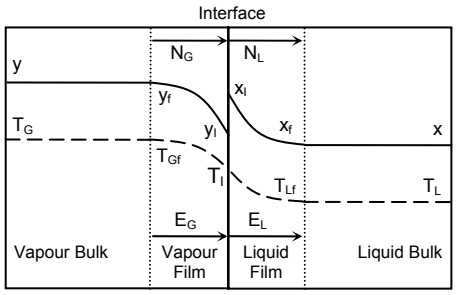

Figure 2.2.1: The two-film model for simultaneous mass and energy transfer.

In this model, two stationary films are postulated to exist adjacent to the vapour-liquid interface, as depicted in Figure 2.2.1. It is assumed that all resistance to mass transfer is concentrated in these two stagnant films, and that mass transfer within the films takes place only by steady-state molecular diffusion due to the insignificant thickness of the films (Taylor and Krishna, 1993). The concentration gradient is the driving force for diffusion across the films, and physical equilibrium is achieved at the interface. In the bulk phases beyond the films, it is assumed that there are such high levels of mixing that chemical equilibrium exists. These key assumptions result in one-dimensional mass transfer normal to the interface (Taylor and Krishna, 1993).

Pilot plant studies of a hot potassium carbonate process for the simultaneous absorption of CO_2 and H_2S have shown that for CO_2 absorption, the liquid film resistance to mass transfer predominates, i.e. CO_2 absorption is liquid-phase limited (Yih and Lai, 1987). However, H_2S absorption and desorption were shown to be primarily influenced by the vapour film resistance, making them vapour-phase limited processes. Neither film resistance were found to dominate during CO_2 desorption, hence both vapour-phase and liquid-phase resistances must be considered. The film resistances to mass transfer are described by mass transfer coefficients, which are further discussed in a later section.

The multicomponent diffusion in the vapour and liquid films can be described by a number of theoretical equations, which are summarised in Table 2.2.2. The most rigorous of these mass transfer relations are the Maxwell-Stefan equations, which relate the component diffusion fluxes to their chemical and electrical potential gradients. However, given their complexity, the Maxwell-Stefan equations are often simplified by assuming that the system is sufficiently dilute that the diffusional interactions between the components can be ignored. This gives rise to Fick's Law for the vapour

phase and to the Nernst-Planck equation for the liquid phase, both of which can be further simplified by neglecting the convective mass transfer due to the bulk flow. If the effect of the electrical potential gradient is ignored, the Nernst-Planck equation reduces to Fick's Law.

Table 2.2.2: Mass transfer relations (Taylor and Krishna, 1993).

Vapour Phase Mass Transfer Relations		
Maxwell-Stefan Equations	$\frac{y_{fj}}{\delta_G \cdot R \cdot T_G} \cdot \frac{d\mu_{Gj}}{d\eta_G} = \sum_{k=1}^{NC} \frac{y_{fj} \cdot J_{Gk} - y_{fk} \cdot J_{Gj}}{C_{Gt} \cdot Đ_{Gjk}}$ $N_{Gj} = J_{Gj} + y_{fj} \cdot \sum_{j=1}^{NC} N_{Gj}$	(2.2.11)
Fick's Law	$J_{Gj} = -C_{Gt} \cdot k_{Gj} \cdot \frac{dy_{fj}}{d\eta_G} = C_{Gt}^{av} \cdot k_{Gj} \cdot \left(y_j - y_{Ij}\right)$ $N_{Gj} = J_{Gj} + y_{fj} \cdot \sum_{j=1}^{NC} N_{Gj} = J_{Gj} + y_j^{av} \cdot \sum_{j=1}^{NC} N_{Gj}$ and $y_j^{av} = \frac{y_j + y_{Ij}}{2}$	(2.2.12)
Simplified Fick's Law	$N_{Gj} = -C_{Gt} \cdot k_{Gj} \cdot \frac{dy_{fj}}{d\eta_G} = C_{Gt} \cdot k_{Gj} \cdot \left(y_j - y_{Ij}\right)$	(2.2.13)
Liquid Phase Mass Transfer Relations		
Maxwell Stefan Equations	$\frac{x_{fj}}{\delta_L \cdot R \cdot T_L} \cdot \frac{d\mu_{Lj}}{d\eta_L} + \frac{x_{fj} \cdot z_j \cdot F}{\delta_L \cdot R \cdot T_L} \cdot \frac{d\varphi}{d\eta_L} = \sum_{k=1}^{NC} \frac{x_{fj} \cdot J_{Lk} - x_{fk} \cdot J_{Lj}}{C_{Lt} \cdot Đ_{Ljk}}$ $\frac{d\varphi}{d\eta_L} = -\frac{R \cdot T_L}{F} \cdot \frac{\sum_{j=1}^{NC} z_j \cdot D_{Lj} \cdot \frac{dx_{fj}}{d\eta_L}}{\sum_{j=1}^{NC} z_j^2 \cdot D_{Lj} \cdot x_{fj}}$ and $\sum_{j=1}^{NC} x_{fj} \cdot z_j$	(2.2.14)
Nernst-Planck Equation	$N_{Lj} = -\frac{C_{Lt} \cdot D_{Lj}}{\delta_L} \cdot \left(\frac{dx_{fj}}{d\eta_L} + \frac{x_{fj} \cdot z_j \cdot F}{R \cdot T_L} \cdot \frac{d\varphi}{d\eta_L} \right) + x_j \cdot N_{solvent}$	(2.2.15)
Simplified Nernst-Planck Equation	$N_{Lj} = -\frac{C_{Lt} \cdot D_{Lj}}{\delta_L} \cdot \left(\frac{dx_{fj}}{d\eta_L} + \frac{x_{fj} \cdot z_j \cdot F}{R \cdot T_L} \cdot \frac{d\varphi}{d\eta_L} \right)$	(2.2.16)
Fick's Law	$J_{Lj} = -C_{Lt} \cdot k_{Lj} \cdot \frac{dx_{fj}}{d\eta_L} = C_{Lt}^{av} \cdot k_{Lj} \cdot \left(x_{Ij} - x_j\right)$ $N_{Lj} = J_{Lj} + x_{fj} \cdot \sum_{j=1}^{NC} N_{Lj} = J_{Lj} + x_j^{av} \cdot \sum_{j=1}^{NC} N_{Lj}$ and $x_j^{av} = \frac{x_j + x_{Ij}}{2}$	(2.2.17)
Simplified Fick's Law	$N_{Lj} = -C_{Lt} \cdot k_{Lj} \cdot \frac{dx_{fj}}{d\eta_L} = C_{Lt} \cdot k_{Lj} \cdot \left(x_{Ij} - x_j\right)$	(2.2.18)
Mass Transfer Coefficients	$k_{Gj} = \frac{D_{Gj}}{\delta_G}$ and $k_{Lj} = \frac{D_{Lj}}{\delta_L}$	(2.2.19)

Notation: x and y are the liquid and vapour phase mole fractions; δ is the film thickness; R is the gas constant; T is the absolute temperature; μ is the chemical potential; η is the dimensionless film coordinate; J is the diffusion flux; N is the molar flux; C_t is the total mole concentration or molar density; $Đ_{jk}$ is the Maxwell-Stefan diffusivity for the binary component pair j-k; NC is the number of components in the system; k is the mass transfer coefficient; D is the effective diffusivity; z is the ionic charge; F is Faraday's constant; and φ is the electrical potential. The subscripts G and L denote the vapour and liquid phases; the subscripts f and I denote the film and the vapour-liquid interface; and the subscripts j and solvent denote the j^{th} component and the solvent. The superscript av denotes the average.

Both the simplified Nernst-Planck equation and the simplified Fick's Law have been successfully applied to the non-equilibrium rate-based modelling of the hot potassium carbonate process. Al-Ramdhan (2001) developed her sieve plate absorber model based on the former equation, while others (Joshi et al., 1981; Staton, 1985; Suenson et al., 1985; Marini et al., 1985; Sanyal et al., 1988; Rao, 1990, 1991; Todinca, 1995; Todinca et al., 1997; Rahimpour and Kashkooli, 2004) have used the latter equation to model packed absorber columns. A number of packed regenerator column models have also been developed based on the simplified Fick's Law (Staton, 1985; Suenson et al., 1985; Marini et al., 1985; Rao, 1991; Todinca, 1994, 1995). The successful application of both mass transfer equations indicates that the mass transfer in this electrolyte system can be reasonably represented without including the effect of the electrical potential gradient.

However, studies on other similar acid gas removal processes have shown that while the exclusion of the electrical potential gradient from the mass transfer relations does not adversely affect the predicted removal of CO_2, the removal of H_2S is significantly underestimated (Schneider and Górak, 2001; Thiele et al., 2005ab). Nevertheless, given that the hot potassium carbonate process of interest is focussed on the removal of CO_2 and involves negligible levels of H_2S, the omission of the electrical potential gradient is considered to be a valid model simplification for this work.

2.2.3 The Energy Transfer Relations

As for mass transfer, the two-film model is used to describe the energy transfer across the vapour-liquid interface. Consequently, all the resistance to energy transfer is assumed to be concentrated in thin, stagnant vapour and liquid films existing on either side of the interface. The energy transfer within these films is assumed to occur only by steady-state heat conduction, driven by the temperature gradient. As depicted in Figure 2.2.1, the temperatures are equal at the interface and are uniform in the bulk phases. These assumptions are analogous to those for the two-film model for mass transfer, and lead to the equivalent conclusion of one-dimensional energy transfer normal to the interface.

The energy fluxes across the vapour-liquid interface are represented by the following equations, which are analogous to Fick's Law (Taylor and Krishna, 1993; Kucka et al., 2003):

Vapour:
$$E_G = -\alpha_G \cdot \frac{dT_{Gf}}{d\eta_G} + \sum_{j=1}^{NC} N_{Gj} \cdot h_{Gj} = \alpha_G \cdot (T_G - T_I) + \sum_{j=1}^{NC} N_{Gj} \cdot h_{Gj} \qquad (2.2.20)$$

Liquid:
$$E_L = -\alpha_L \cdot \frac{dT_{Lf}}{d\eta_L} + \sum_{j=1}^{NC} N_{Lj} \cdot h_{Lj} = \alpha_L \cdot (T_I - T_L) + \sum_{j=1}^{NC} N_{Lj} \cdot h_{Lj} \qquad (2.2.21)$$

where α is the heat transfer coefficient, T is the temperature, and h is the partial molar enthalpy. The subscripts G, L and I indicate the vapour phase, the liquid phase and the vapour-liquid interface. The first terms in equations (2.2.20) and (2.2.21) are the conductive heat fluxes which are analogous to the diffusion fluxes J for mass transfer, while the second terms represent the convective contributions to the energy transfer.

For a non-reactive process, the inclusion of the above mass and energy transfer relations complete the set of non-equilibrium rate-based model equations, known as the MERQ (Material balance, Energy balance, Rate and eQuilibrium) equations (Taylor and Krishna, 1993). The following section discusses the modifications required to include the effect of the hot potassium carbonate process liquid phase chemical reactions.

2.2.4 The Effect of Chemical Reactions

The effect of chemical reactions can be incorporated into the MERQ equations in one of three ways: chemical equilibrium relations, reaction rate expressions or enhancement factors. It should be noted that no changes are required for the energy balances, provided the enthalpies are calculated using standard enthalpies of formation, as these directly account for the heats of reaction.

2.2.4.1 Chemical Equilibrium Relations

Consider a homogenous chemical reaction of the form:

$$\upsilon_{A_1} A_1 + ... + \upsilon_{A_{NA}} A_{NA} \xrightarrow{R} \upsilon_{P_1} P_1 + ... + \upsilon_{P_{NP}} P_{NP} \qquad \text{(R2.2.1)}$$

$$R = k_f \cdot \prod_{a}^{NA} \left(x_{A_a} \cdot \gamma_{A_a}\right)^{\upsilon_{A_a}} - k_r \cdot \prod_{p}^{NP} \left(x_{P_p} \cdot \gamma_{P_p}\right)^{\upsilon_{P_p}} = k_f^c \cdot \prod_{a}^{NA} C_{A_a}{}^{\upsilon_{A_a}} - k_r^c \cdot \prod_{p}^{NP} C_{P_p}{}^{\upsilon_{P_p}} \qquad (2.2.22)$$

where R is the molar reaction rate, k is the mole fraction rate constant, k^c is the molar concentration rate constant, υ is the stoichiometric coefficient, x is the mole fraction, γ is the activity coefficient, C is the molar concentration, and the subscripts f and r denote the forward and reverse reactions.

If reaction (R2.2.1) is very fast or instantaneous, its effect on the rate of mass transfer can be described by the chemical equilibrium relations:

$$K_{eq} = \frac{k_f}{k_r} = \frac{\prod_{p}^{NP} \left(x_{P_p} \cdot \gamma_{P_p}\right)^{\upsilon_{P_p}}}{\prod_{a}^{NA} \left(x_{A_a} \cdot \gamma_{A_a}\right)^{\upsilon_{A_a}}} \quad \text{and} \quad K_{eq}^c = \frac{k_f^c}{k_r^c} = \frac{\prod_{p}^{NP} C_{P_p}{}^{\upsilon_{P_p}}}{\prod_{a}^{NA} C_{A_a}{}^{\upsilon_{A_a}}} \qquad (2.2.23)$$

where K_{eq} is the mole-fraction equilibrium constant and K_{eq}^c is the molar-concentration equilibrium constant. In the case of slow or kinetically controlled reactions like the rate-controlling steps for the hot potassium carbonate process, reaction rate expressions or enhancement factors have to be employed. The chemical equilibrium relations alone are inadequate for the hot potassium carbonate process, as demonstrated by Park and Edgar (1984).

2.2.4.2 Reaction Rate Expressions

The reaction rate R for slow or kinetically controlled reactions can be applied over an entire phase or just within the film region. For the bulk liquid phase, the liquid phase component material balance in the non-equilibrium MESH equations is replaced by:

$$\frac{\partial M_{Li,j}}{\partial t} = F_{Li} \cdot z_{FLi,j} + L_{i-1} \cdot x_{i-1,j} - L_i \cdot x_{i,j} + \left(N_{Li,j} \cdot a_{li} + R_{i,j} \cdot \phi_{Li}\right) \cdot V_i \qquad \text{for } j = 1...NC \qquad (2.2.24)$$

In the liquid film, mass transfer and chemical reactions occur simultaneously so the effect of the reactions is included by performing a differential component balance over the film (Kucka et al., 2003):

$$\frac{1}{\delta_L} \cdot \frac{\partial N_{Li,j}}{\partial \eta_L} - R_{i,j} = 0 \qquad \text{for } j = 1...NC \qquad (2.2.25)$$

This differential balance accounts for the difference between the component molar fluxes at the vapour-liquid interface and at the film-bulk phase boundary due to the chemical reactions, and replaces the material flux balance in the non-equilibrium MESH equations. The assumption of a linear film concentration profile reduces equation (2.2.25) to:

$$N_{Li,j} = N_{Gi,j} + R^{av}_{i,j} \cdot \delta_L \qquad \text{for } j = 1...NC \qquad (2.2.26)$$

It may be valid to assume chemical equilibrium in the bulk liquid phase and a linear film concentration profile for the hot potassium carbonate process. Schneider and Górak (2001) found that these two assumptions did not significantly affect the predicted removal of CO_2 and H_2S for an amine gas sweetening process, unlike the assumption of chemical equilibrium in the film. The film reactions are therefore a key parameter that must be included when modelling chemical absorption processes.

Reaction rate expressions have been utilised with success in a number of non-equilibrium rate-based absorption models for various acid gas removal processes (Kenig et al., 1999; Kucka et al., 2003; Ebrahimi et al., 2003), but have not been implemented for the hot potassium carbonate process.

2.2.4.3 Enhancement Factors

Enhancement factors are the alternative method of incorporating the effect of slow or kinetically-controlled reactions into the MERQ equations. These are theoretically derived factors which describe the acceleration of the interfacial diffusion fluxes due to chemical reactions:

$$EF_j = \frac{J^{Chem}_{Lj}}{J^{Phys}_{Lj}} = \frac{-\frac{D_{Lj}}{\delta_L} \cdot \left.\frac{\partial C_j}{\partial \eta_L}\right|_{Interface}}{k_{Lj} \cdot C^{av}_{Lt} \cdot \left(x_{lj} - x_j\right)} \qquad \text{for } j = 1...NC \qquad (2.2.27)$$

where J is the diffusion flux, D is the diffusivity, δ is the film thickness, η is the dimensionless film coordinate, C is the molar concentration, k is the mass transfer coefficient, C^{av}_{Lt} is the average liquid

phase molar density, x is the liquid phase mole fraction, and NC is the number of components. The subscripts I and L indicate the vapour-liquid interface and the liquid phase, while the superscripts Chem and Phys indicate the presence and the absence of chemical reactions.

The application of such enhancement factors requires the liquid phase mass transfer relations in the MERQ equations to be replaced by:

$$N_{Lj} = EF_j \cdot C_{Lt}^{av} \cdot k_{Lj} \cdot \left(x_{Ij} - x_j\right) + x_j^{av} \cdot \sum_{j=1}^{NC} N_{Lj} \qquad \text{for } j = 1...NC \qquad (2.2.28)$$

Numerous enhancement factors have been proposed in literature (van Swaaij and Versteeg, 1992). One of the most widely used is the expression developed by Danckwerts and Kennedy (1954) from the surface renewal model:

$$EF_A = \frac{(K'+1) \cdot \sqrt{1 + Ha_A{}^2 \cdot \frac{K'+1}{K'}}}{K' + \sqrt{1 + Ha_A{}^2 \cdot \frac{K'+1}{K'}}} \qquad (2.2.29)$$

$$K' = \frac{C_P}{C_A} \qquad \text{and} \qquad Ha_A = \frac{\sqrt{D_A \cdot k}}{k_{LA}} \qquad (2.2.30)$$

where K' is the pseudo-equilibrium constant, k is the first-order or pseudo-first-order reaction rate constant, k_L is the liquid phase mass transfer coefficient, and Ha is the dimensionless Hatta number. This enhancement factor is applicable to reversible first-order and pseudo-first-order reactions, like the rate-controlling reactions in the hot potassium carbonate process. Danckwerts (1970) observed that the predictions made by this enhancement factor were in numerical agreement with those by the equivalent two-film theory enhancement factor. It is therefore applicable to the flux equation (2.2.28), which was derived using the two-film theory.

The Hatta number compares the maximum rate of reaction in the liquid film to the maximum rate of mass transfer through the liquid film, and can therefore be used to characterise the reaction kinetic regime (Danckwerts, 1970). According to Charpentier (1981), reactions with Ha<0.3 are slow with respect to the mass transfer and occur only in the bulk liquid phase, whereas reactions with Ha>3 are fast with respect to the mass transfer and are completed within the liquid film. Moderately fast reactions, characterised by 0.3≤ Ha≤ 3, take place in both the bulk liquid phase and the liquid film.

There is a view that enhancement factors may be inadequate for chemical reaction systems involving reversible reactions due to the use of inappropriate assumptions during their derivation (Schneider and Górak, 2001; Noeres et al., 2003). This has been refuted by de Leye and Froment (1986) and Mayer (2002), who compared the use of enhancement factors and reaction rate expressions for the simulation of amine gas sweetening processes. Both methods produced very similar results, despite the significantly greater computation time required by the more rigorous reaction rate expressions.

This may be the reason why the previous models developed for the hot potassium carbonate process (Joshi et al., 1981; Staton, 1985; Suenson et al., 1985; Marini et al., 1985; Sanyal et al., 1988; Rao, 1990, 1991; Todinca, 1994, 1995; Todinca et al., 1997; Al-Ramdhan, 2001; Rahimpour and Kashkooli, 2004) have used enhancement factors instead of reaction rate expressions to represent the effect of chemical reactions. For confirmation, the use of reaction rate expressions and enhancement factors will be compared in this work for the hot potassium carbonate process.

2.2.5 Mass and Energy Transfer Coefficients

The solution of the MERQ equations requires the mass and energy transfer coefficients, for which there exist a number of empirical and semi-theoretical correlations. Since the Moomba CO_2 trains consist only of randomly packed columns, correlations for tray columns and columns with structured packings are not considered here.

2.2.5.1 Mass Transfer Coefficients and the Interfacial Area

To effectively describe the mass transfer between the vapour and liquid phases in a randomly packed column, it is imperative to know the vapour and liquid film resistances to mass transfer and the area over which the two phases are in intimate contact such that mass transfer can occur. The film resistances are represented by the vapour and liquid component mass transfer coefficients, while the area of phase contact is known as the effective interfacial area. Numerous empirical and semi-theoretical correlations for estimating these parameters are available in literature, a comprehensive review of which has been presented by Wang and co-workers (2005).

After careful consideration of the available mass transfer coefficient and effective interfacial area correlations, the widely used correlations proposed by Onda and co-workers (1968ab) will be used in this work due to their general applicability and simplicity. These correlations are summarised in Table 2.2.3. The sole packing-specific constant required for these correlations is the critical surface tension parameter σ_c, which accounts for the wettability of different packing materials. For metal packings, such as those used in the Moomba CO_2 trains, σ_c is equal to 0.075 N/m.

Table 2.2.3: Mass transfer coefficient and effective interfacial area correlations (Onda et al., 1968ab).

Vapour Phase Mass Transfer Coefficient	$k_{Gj} = \begin{cases} 2.0 \cdot \frac{D_{Gj}}{a \cdot d_N} \cdot \left(\frac{\rho_G \cdot v_G}{a \cdot \mu_G} \right)^{0.7} \cdot \left(\frac{\mu_G}{\rho_G \cdot D_{Gj}} \right)^{1/3} & \text{if } d_N < 0.015\text{m} \\ 5.23 \cdot \frac{D_{Gj}}{a \cdot d_N} \cdot \left(\frac{\rho_G \cdot v_G}{a \cdot \mu_G} \right)^{0.7} \cdot \left(\frac{\mu_G}{\rho_G \cdot D_{Gj}} \right)^{1/3} & \text{if } d_N \geq 0.015\text{m} \end{cases}$	(2.2.31)
Liquid Phase Mass Transfer Coefficient	$k_{Lj} = 0.0051 \cdot (a \cdot d_N)^{0.4} \cdot \left(\frac{\mu_L \cdot g}{\rho_L} \right)^{1/3} \cdot \left(\frac{\rho_L \cdot v_L}{a_l \cdot \mu_L} \right)^{2/3} \cdot \left(\frac{\mu_L}{\rho_L \cdot D_{Lj}} \right)^{-0.5}$	(2.2.32)
Effective Interfacial Area	$\frac{a_l}{a} = 1 - e^{-1.45 \cdot \left(\frac{\sigma_c}{\sigma_L} \right)^{0.75} \cdot \left(\frac{\rho_L \cdot v_L}{a \cdot \mu_L} \right)^{0.1} \cdot \left(\frac{v_L^2 \cdot a}{g} \right)^{-0.05} \cdot \left(\frac{\rho_L \cdot v_L^2}{a \cdot \sigma_L} \right)^{0.2}}$	(2.2.33)
Phase Flow Velocities	$v_G = \frac{4 \cdot G}{\pi \cdot D_c^2 \cdot C_{Gt}}$ and $v_L = \frac{4 \cdot L}{\pi \cdot D_c^2 \cdot C_{Lt}}$	(2.2.34)

Note: All variables are in SI units. Notation: k is the mass transfer coefficient; D_j is the component diffusivity; ρ is the mass density; μ is the viscosity; a is the packing specific surface area; a_l is the effective interfacial area; v is the phase flow velocity; g is the gravitational constant; d_N is the nominal packing size; σ_L is the surface tension; σ_c is the critical surface tension parameter; D_c is the column diameter; G and L are the vapour and liquid phase molar flow rates; C_t is the molar density; and the subscripts G and L denote the vapour and liquid phases.

2.2.5.2 Energy Transfer Coefficients

In an analogous manner to mass transfer, the vapour and liquid film resistances to energy transfer are described by the vapour and liquid energy transfer coefficients. For simultaneous mass and energy transfer, as in the case of the hot potassium carbonate process, the component energy transfer coefficients α can be determined from the corresponding mass transfer coefficients k via the Chilton-Colburn analogy (Bird and co-workers, 1960):

Vapour: $$\frac{\alpha_{Gj}}{k_{Gj}} = \rho_G \cdot \hat{C}_{pG} \cdot Le_G^{2/3} = \rho_G \cdot \hat{C}_{pG} \cdot \left(\frac{\lambda_G}{\rho_G \cdot \hat{C}_{pG} \cdot D_{Gj}} \right)^{2/3} \quad (2.2.35)$$

Liquid: $$\frac{\alpha_{Lj}}{k_{Lj}} = \rho_L \cdot \hat{C}_{pL} \cdot Le_L^{2/3} = \rho_L \cdot \hat{C}_{pL} \cdot \left(\frac{\lambda_L}{\rho_L \cdot \hat{C}_{pL} \cdot D_{Lj}} \right)^{2/3} \quad (2.2.36)$$

where ρ is the mass density, $\hat{C}_p$ is the mass heat capacity, Le is the dimensionless Lewis number, λ is the thermal conductivity, and D is the diffusivity. The subscripts G and L refer to the vapour and liquid phases, while the subscript j denotes the component j.

The phase energy transfer coefficients can then be obtained from the mole-fraction-weighted averages of the component coefficients:

$$\alpha_G = \sum_{j=1}^{NC} y_j \cdot \alpha_{Gj} \quad \text{and} \quad \alpha_L = \sum_{j=1}^{NC} x_j \cdot \alpha_{Lj} \quad (2.2.37)$$

where x and y are the liquid and vapour phase mole fractions, and NC is the number of components in the system.

While the above mass and energy transfer correlations enable the calculation of the mass and energy transfer coefficients, the solution of the MERQ equations is incomplete without knowledge of two key hydrodynamic parameters. These are discussed in the following section.

2.2.6 Packed Column Hydrodynamics

The hydrodynamic behaviour of randomly packed columns, such as the absorber and regenerator columns in Moomba CO_2 trains, can be described by two key parameters: the liquid volumetric holdup and the column pressure drop. The former represents the quantity of liquid that accumulates within the packing during column operation, while the latter describes the resistance to vapour flow due to the packing and liquid volumetric holdup. A number of empirical and semi-theoretical correlations have been proposed for describing the hydrodynamic behaviour of randomly packed columns, a detailed review of which has been provided by Kister (1992).

The particle model hydrodynamic correlations presented by Stichlmair and co-workers (1989) will be utilised in this work due to their simplicity and greater theoretical consistency than the corresponding channel model hydrodynamic correlations (Stichlmair and Fair, 1998). As summarised in Table 2.2.4, the Stichlmair correlations include a separate expression for the liquid volumetric holdup in the pre-loading operating region, which was only validated for the air-water system. Although potassium carbonate solution has a higher surface tension and viscosity than water, this expression may be valid for the hot potassium carbonate process. Surface tension has a negligible effect on the liquid volumetric holdup for high surface tension (>0.027 N/m) liquids (Strigle, 1994), and the equation has been shown to be applicable for liquid viscosities up to 5 cP (Stichlmair et al., 1989).

Three packing-specific constants are required for the Stichlmair hydrodynamic correlations. These are easily derived from the packing characteristics and the dry pressure drop curves published by packing manufacturers. Table 2.2.5 gives the constants for a number of metal random packings, some of which are used in the Moomba CO_2 trains.

In summary, the non-equilibrium rate-based approach rigorously considers the effects of the chemical potential, electrical potential and temperature gradients and the column hydrodynamics on the transfer of mass and energy between the vapour and liquid phases. This makes it particularly suitable for modelling rate-controlled processes like the hot potassium carbonate process. Since the hot potassium carbonate process involves an aqueous electrolyte system, a key requirement for developing an accurate and detailed process model is an effective representation of the complex non-ideal electrolyte system thermodynamic behaviour. This is discussed in the next section.

Table 2.2.4: Hydrodynamic relations (Stichlmair et al., 1989).

Pre-loading Liquid Volumetric Holdup	$\phi_{Lo} = 0.555 \cdot \left(\frac{v_L{}^2 \cdot a}{g \cdot \phi^{4.65}} \right)^{1/3}$	(2.2.38)
Liquid Volumetric Holdup	$\phi_L = \phi_{Lo} \cdot \left(1 + 20 \cdot \left(\frac{\Delta P_{irr}}{H \cdot \rho_L \cdot g} \right)^2 \right)$	(2.2.39)
Vapour Volumetric Holdup	$\phi_G = \phi - \phi_L$	(2.2.40)
Dry Bed Pressure Drop	$\frac{\Delta P_{dry}}{H} = \frac{3 \cdot f_o}{4} \cdot \left(\frac{1-\phi}{\phi^{4.65}} \right) \cdot \frac{\rho_G \cdot v_G{}^2}{d_p}$ $f_o = \frac{C_1}{Re_G} + \frac{C_2}{\sqrt{Re_G}} + C_3$ $Re_G = \frac{\rho_G \cdot v_G \cdot d_p}{\mu_G}$ $d_P = \frac{6 \cdot (1-\phi)}{a}$	(2.2.41)
Irrigated Bed Pressure Drop	$\frac{\Delta P_{irr}}{\Delta P_{dry}} = \left(\frac{1-\phi+\phi_L}{1-\phi} \right)^{\frac{2+c}{3}} \cdot \left(1 - \frac{\phi_L}{\phi} \right)^{-4.65}$ $c = \frac{1}{f_o} \cdot \left(\frac{-C_1}{Re_G} - \frac{C_2}{2 \cdot \sqrt{Re_G}} \right)$	(2.2.42)
Vapour Head Contribution	$\Delta P_{vap} = \rho_G \cdot \phi_G \cdot g \cdot H$	(2.2.43)
Overall Pressure Drop	$\Delta P = \Delta P_{irr} + \Delta P_{vap}$	(2.2.44)

Note: All variables are in SI units. Notation: ϕ is the packing voidage; ϕ_L is the liquid volumetric holdup; ϕ_G is the vapour volumetric holdup; ϕ_{Lo} is the pre-loading liquid volumetric holdup; v is the flow velocity; a is the packing specific surface area; g is the gravitational constant; ΔP is the pressure drop over the packed bed; ΔP_{vap} is the pressure drop due to the static head of vapour in the packing; H is the height of packing; ρ is the mass density; d_p is the packing particle diameter; f_o is the particle friction factor; Re is the Reynolds number; μ is the viscosity; and C_1, C_2 and C_3 are packing-specific constants. The subscripts G and L refer to the vapour and liquid phases, while the subscripts irr and dry denote the irrigated packed bed and the dry packed bed.

Table 2.2.5: Packing characteristics and constants for metal random packings.

Packing Type	Number	d_N (m)	a (m^2/m^3)	ϕ (m^3/m^3)	C_1	C_2	C_3
Cascade Mini-Ring® [a]	2	0.044	164	0.950	63.90	-12.68	2.45
(CMR™)	3	0.063	105	0.960	38.05	-5.23	2.04
	4	0.090	79	0.960	38.25	-3.51	2.03
Flexiring® [a]	2	0.050	102	0.960	15.98	-1.56	2.54
	3.5	0.090	65	0.970	63.78	-8.78	2.82
Hy-Pak® [a]	2	0.060	88	0.971	47.31	-10.81	2.96
	3	0.090	60	0.973	32.90	1.98	2.61
Intalox® Metal Tower Packing [a]	40	0.040	169	0.973	6.90	-1.32	1.78
(IMTP®)	50	0.050	81	0.978	3.88	-0.50	2.43
	70	0.070	48	0.981	658.85	-78.21	4.36
Nutter Ring [b]	2	0.050	96	0.979	123.51	-28.46	4.35
	2.5	0.063	83	0.982	91.74	-19.36	4.09
	3	0.080	66	0.984	156.22	-21.33	3.98
Pall Ring® [c]	2	0.050	102	0.960	15.98	-1.56	2.54
	3.5	0.090	65	0.970	63.78	-8.78	2.82

[a] Packing constants were derived from the dry pressure drop capacity curves provided by Koch-Glitsch (2003ab). [b] Packing constants were derived from the dry pressure drop capacity curves provided by Sulzer Chemtech (2006). [c] Pall Rings® are equivalent to Flexirings® (Kister, 1992).

2.3 Electrolyte Thermodynamics

The non-ideal behaviour exhibited by electrolyte systems arises from the short-range molecular interactions between the non-ionic species and the strong long-range electrostatic interactions between the ionic species. The former type of interactions can be effectively described by traditional thermodynamic models, such as the Redlich-Kwong equation of state (Redlich and Kwong, 1949), the Non-Random Two-Liquid (NRTL) model (Renon and Prausnitz, 1968), and the Universal Quasi-Chemical (UNIQUAC) model (Abrams and Prausnitz, 1975). However, these models are unable to accommodate the additional complexity and non-idealities resulting from the electrostatic interactions.

Consequently, specialised electrolyte thermodynamic models were developed to enable a more accurate description of electrolyte systems, as described in the excellent reviews provided by Zemaitis and co-workers (1986), Renon (1996), Loehe and Donohue (1997) and Anderko and co-workers (2002). Most of these electrolyte thermodynamic models are extensions of traditional thermodynamic models, and can be divided into two broad categories: electrolyte activity coefficient models and electrolyte equations of state. Electrolyte activity coefficient models are applied only to the liquid phase, and require a traditional equation of state for the vapour phase. In contrast, electrolyte equations of state are applied to both phases. The majority of the published electrolyte thermodynamic models fall into the former category, including the highly popular Pitzer (Pitzer, 1973) and Electrolyte NRTL (Chen and Evans, 1986) models. There are relatively few electrolyte equations of state available; the most well-known of these is the Fürst-Renon equation of state (Fürst and Renon, 1993).

An evaluation of the available electrolyte thermodynamic models identified the Electrolyte NRTL, the Pitzer and the Extended UNIQUAC (Sander et al., 1986ab) models as the most suitable liquid phase thermodynamic models for the hot potassium carbonate process (Ooi et al., 2005). Key factors considered in this evaluation included: applicability to the hot potassium carbonate process, robustness and computational accuracy, model simplicity and ease of implementation, and availability in commercial process simulation software. The three models satisfied the above criteria, and have been applied to vapour-liquid equilibria calculations for the CO_2-K_2CO_3-$KHCO_3$-H_2O system with success (Chen, 1980; Thomsen and Rasmussen, 1999; Al-Ramdhan, 2001; Cullinane and Rochelle, 2004; Hilliard, 2005; Ooi et al., 2005).

The major disadvantage with such rigorous electrolyte thermodynamic models is that these models all involve a number of adjustable parameters. For example, the Electrolyte NRTL model includes two types of adjustable parameters (the interaction energy parameter τ and the non-randomness factor α), whereas the Pitzer Model requires up to six different types (ionic interaction parameters B, C, Φ and Ψ, and solute interaction parameters λ and μ). In order for these electrolyte thermodynamic models to accurately describe the dependency of the individual component activity coefficients on the liquid (and/or vapour) phase composition, these adjustable parameters have to be regressed from experimental data. If insufficient data are available, rigorous thermodynamic models may perform no

better than a simplified thermodynamic model that ignores the composition dependence of the activity coefficients.

One such simplified thermodynamic model was presented by Astarita and co-workers (1983) for gas treatment processes involving chemical absorption and desorption. It has been successfully adapted for the hot potassium carbonate process and has been used in a number of non-equilibrium rate-based models for this process (Joshi et al., 1981; Staton, 1985; Sanyal et al., 1988; Rao, 1990, 1991; Rahimpour and Kashkooli, 2004). A similarly simple thermodynamic approach, which assumes constant activity coefficients of unity, has also been applied to the non-equilibrium rate-based modelling of the hot potassium carbonate process (Suenson et al., 1985; Marini et al., 1985; Todinca, 1994, 1995; Todinca et al., 1997). Only the absorber column model presented by Al-Ramdhan (2001) for the hot potassium carbonate process includes rigorous electrolyte thermodynamics.

Despite the above reliance on simplified thermodynamic models, it is believed that there is sufficient data on the hot potassium carbonate process to justify the use of a rigorous electrolyte thermodynamic model. Consequently, in this work, the Electrolyte NRTL model will be used to perform the liquid phase thermodynamic calculations for the non-equilibrium rate-based process model, while the Soave-Redlich-Kwong (SRK) equation of state (Soave, 1972) will be applied to the vapour phase calculations. The model equations for these two thermodynamic models are included in Sections A.2 and A.3 in Appendix A.

Having reviewed the various aspects of the non-equilibrium rate-based approach and selected the electrolyte thermodynamic model, the final requirement to be considered in the development of an accurate and detailed process model of the hot potassium carbonate process is the process simulation platform. This is discussed in the following section.

2.4 Process Simulation Platform

The commercial process simulation package HYSYS® is presently the primary process simulator utilised by Santos due to its particular affinity for modelling oil and gas processing systems. It is therefore the desired simulation platform for the Moomba CO_2 train process models. However, there are two significant disadvantages with using HYSYS® in this current work: the standard HYSYS® component and property package libraries do not include electrolyte components or suitable electrolyte property models[1], and HYSYS® employs the equilibrium stage approach with stage component efficiencies for the calculation of column operations.

The absence of electrolyte components and appropriate electrolyte property models can be overcome through HYSYS®'s customisation features, which enable the creation of hypothetical components and custom property models. It is therefore theoretically possible to create electrolyte components and to incorporate electrolyte property models into HYSYS® to enable the simulation of the hot potassium carbonate process. However, such custom property models may not be sufficiently robust or reliable. Alternatively, a commercial electrolyte package, such as the one from OLI Systems, can be added to HYSYS®. However, these are limited to steady-state simulations and were therefore not considered for this work.

A more viable option is to import custom unit operations with integrated property calculations into HYSYS®. Such models can be developed in Aspen Custom Modeler®, an equation-based simulator, which will enable the column operations to be modelled with the non-equilibrium rate-based approach. Thermodynamic and physical property calculations can be incorporated into these models by interfacing Aspen Custom Modeler® with the Aspen Properties® property calculation software, which contains electrolytes and electrolyte models in its component and property model databanks. Aspen Custom Modeler®, paired with Aspen Properties®, is therefore suitable for developing individual process models of the unit operations in the hot potassium carbonate process for importation into HYSYS®. However, this approach was considered impractical for two reasons: the high degree of modelling rigor required to properly interface the imported models with HYSYS® to ensure sufficient robustness and reliability; and more importantly, the significant computation time associated with the Aspen Custom Modeler® models.

The absorber and regenerator columns are the key unit operations for the hot potassium carbonate process. The performance of the overall process is dependant on these two columns, which are heavily influenced by the non-ideal electrolyte system behaviour due to the process reactions. The other incidental unit operations are less affected by the presence of electrolytes and can be modelled using standard HYSYS® unit operations and hypothetical HYSYS® electrolyte components. Although

[1] HYSYS® does have a proprietary Amines Property Package which is based on the Kent-Eisenberg model (Kent and Eisenberg, 1976) for the CO_2-H_2S-Amine system. However, this model is specific to this particular electrolyte system and is therefore not applicable to the hot potassium carbonate process.

not theoretically correct, the thermodynamic and physical properties for these hypothetical components can be calculated with a standard HYSYS® property package by adjusting the model parameters to fit experimental data. This novel approach can be extended to the absorber and regenerator columns by customising the standard HYSYS® column operations through the use of stage efficiencies to represent the effects of the liquid phase reactions. These customised models can then be validated by comparison with the more rigorous Aspen Custom Modeler® column models and plant data.

Consequently, to satisfy the first three objectives of this work, rigorous non-equilibrium rate-based column models will be developed in Aspen Custom Modeler®, while complete process models of the Moomba CO_2 trains will be developed in HYSYS®. Due to the computational time constraints, the absorber and regenerator columns in the HYSYS® process models will be represented by customised standard HYSYS® column operations, which will be validated against the rigorous Aspen Custom Modeler® models and plant data.

It should be noted that there are available commercial software options which are suitable for modelling electrolyte systems, such as ChemCAD, Aspen Plus®, VMGSim and gPROMS. While these software packages apparently enable the simulation of the hot potassium carbonate process, either through inbuilt electrolyte property packages[1] or via commercial electrolyte packages[2], they were not used in this work as the selection of the final simulation platform was dictated by Santos. The other alternative considered was to write a completely custom simulation program in Fortran or a similar programming language. However, this approach was not pursued due to the availability of equation-oriented simulation platforms like Aspen Custom Modeler®, which allow a similar level of custom coding but provide access to inbuilt solver routines.

[1] ChemCAD's Electrolytes Package is based on the Electrolyte NRTL and Pitzer models, while Aspen Plus® has Aspen Properties® inbuilt. VMGSim's AMINES++ package was originally designed specifically for amine electrolyte systems, but has apparently been extended to enable the simulation of acid gas removal using amines with potassium carbonate solution. Unlike the other process simulators, the basis of the AMINES++ package is not available in accessible literature and it is therefore difficult to judge its suitability for the hot potassium carbonate process.

[2] gPROMS can be integrated with Aspen Properties® or the OLI Systems commercial electrolyte package for electrolyte thermodynamic and physical property calculations. It is similar to Aspen Custom Modeler® in that it is an equation-oriented simulation environment that can facilitate the development of process models from first principles.

2.5 Multivariable Process Control

The final objective of this work is to demonstrate a potential application of the HYSYS® process model by using it to analyse the controllability of the Moomba CO_2 trains. This is a multivariable control problem due to the multiple manipulated and controlled variables associated with the hot potassium carbonate process. While a number of sophisticated multivariable control strategies have been developed, the simple conventional diagonal (or decentralised) control structure remains the most widely used approach for multivariable control (Luyben and Luyben, 1997). Consequently, this work will focus on the development of diagonal control structures for the CO_2 trains.

The diagonal control structure treats a multivariable or MIMO (multiple-output multiple-input) system as a collection of multiple SISO (single-input single-output) control loops, in which one controlled variable is paired with one manipulated variable. The design of such a control structure requires some understanding of the dynamic characteristics of the process of interest. Luyben and Luyben (1997) provide a concise review of the available methods for identifying the process dynamics, the two most simple and popular of which are discussed in the following section.

2.5.1 Process Dynamic Behaviour

2.5.1.1 Step Response Models

The process dynamic behaviour can be determined from the process response to step inputs. Table 2.5.1 illustrates the most common types of dynamic process behaviour.

For the purpose of process control design and analysis, most chemical processes can be represented by the simple FOPDT (first-order plus dead time) process model (Luyben and Luyben, 1997). Integrating systems are a special case of a first-order system, and can be represented by a modified form of the FOPDT model, known as the IPDT (integrating plus dead time) model. Oscillatory processes ($0 < \zeta < 1$) are best described by the USOPDT (underdamped second-order plus dead time) model; however, the FODPT model can approximate an USOPDT process via the following parameters (Panda et al., 2004):

$$K_p = K_p \qquad \text{and} \qquad \tau_p = 2 \cdot \zeta \cdot \tau \qquad \text{and} \qquad \theta = \frac{\tau}{2 \cdot \zeta} + \theta_{USOPDT} \tag{2.5.1}$$

where θ_{USOPDT} is the dead time for the USOPDT process. These simplified process models can also be used to approximate systems with an inverse response, since an inverse response has a deteriorating effect on control similar to that of a dead time (Skogestad, 2003). For such systems, the $e^{-\theta \cdot s}$ term represents the effective time delay due to the dead time and the inverse response.

Table 2.5.1: Common dynamic process behaviour (Stephanopoulos, 1984; Wade, 2004).

Process Transfer Function	Step Response Curve	Step Response Function
First-Order Plus Dead Time (FOPDT) $G_p(s) = \frac{K_p \cdot e^{-\theta \cdot s}}{\tau_p \cdot s + 1}$	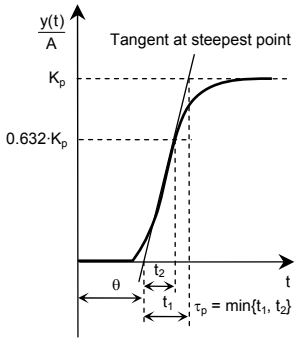	$\frac{y(t)}{A} = K_p \cdot \left(1 - e^{-\left(\frac{t-\theta}{\tau_p}\right)}\right)$
Integrating Plus Dead Time (IPDT) $G_p(s) = \frac{K_p \cdot e^{-\theta \cdot s}}{\tau_p \cdot s} = \frac{K'_p \cdot e^{-\theta \cdot s}}{s}$	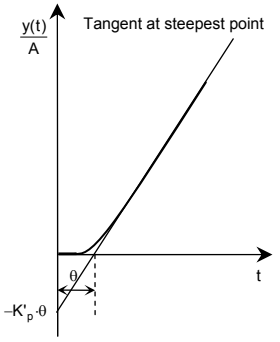	$\frac{y(t)}{A} = K'_p \cdot (t - \theta)$
Underdamped Second-Order Plus Dead Time (USOPDT) $G_p(s) = \frac{K_p \cdot e^{-\theta \cdot s}}{\tau^2 \cdot s^2 + 2 \cdot \tau \cdot \zeta \cdot s + 1}$ where $0 < \zeta < 1$	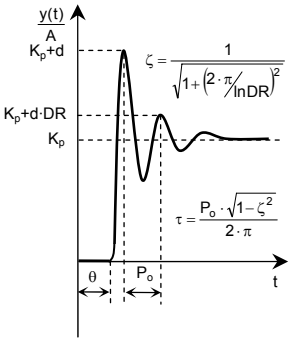	$\frac{y(t)}{A} = K_p \cdot \left(1 - \frac{e^{-\zeta \cdot \left(\frac{t-\theta}{\tau}\right)}}{\sqrt{1-\zeta^2}} \cdot \sin\left(\omega \cdot (t-\theta) + \phi\right)\right)$ $\omega = \frac{\sqrt{1-\zeta^2}}{\tau}$ $\phi = \tan^{-1}\left(\frac{\sqrt{1-\zeta^2}}{\zeta}\right)$

Notation: $G_p(s)$ is the process transfer function; $y(t)$ is the step response function; K_p is the steady-state process gain; τ_p is the process time constant; K'_p is the integrator gain; τ is the natural period of oscillation; ζ is the damping factor; θ is the dead time; A is the step size; DR is the decay ratio; P_o is the period of oscillation; and d is the height of the first overshoot.

2.5.1.2 Frequency Response Methods

Alternatively, the process dynamics can be identified from the process response to specific frequencies. The most famous frequency domain method is the one proposed by Ziegler and Nichols (1942), which is based on determining the point of marginal stability. This point can be found by placing the process under proportional control and increasing the controller gain until a constant-amplitude limit-cycle response is obtained. The controller gain at this point is the ultimate gain K_u and the period of oscillation is the ultimate period P_u. A major disadvantage of this method is that the system is driven towards instability, which may be dangerous in practice.

An improved frequency domain method was recently proposed by Åström and Hagglünd (1984). This auto-tune variation (ATV) method inserts a relay as the process feedback controller in order to induce

a small limit-cycle disturbance between the manipulated and controlled variables. The period of the resulting limit-cycle oscillation is the ultimate period P_u, while the ultimate gain K_u can be calculated from the oscillation amplitude A and the height of the relay h:

$$K_u = \frac{4 \cdot h}{A \cdot \pi} \tag{2.5.2}$$

Unlike the Ziegler-Nichols method, the ATV method can ensure the process is not unduly upset through the careful selection of the relay height. However, the ATV method is only suitable for processes with significant dead time (Svrcek et al., 2006).

Once the process dynamics have been identified by one of the above methods, they can be used to design SISO controller algorithms, which are discussed in the following section.

2.5.2 SISO Controller Algorithms

2.5.2.1 PID Controllers

PID controllers are the simplest and most widely used method of process control in the chemical processing industry (Svrcek et al., 2006). Detailed analyses of PID control theory are provided by Seborg and co-workers (1989) and Stephanopoulos (1984), while Svrcek and co-workers (2006) present a more concise overview for practical application purposes.

Numerous forms of PID controllers have been proposed (O'Dwyer, 2003), the simplest of which is the parallel structure:

$$G_c(s) = K_c \cdot \left(1 + \frac{1}{\tau_I \cdot s} + \tau_D \cdot s\right) \tag{2.5.3}$$

where $G_c(s)$ is the controller transfer function, K_c is the controller gain, τ_I is the integral time constant, and τ_D is the derivative time constant. Derivative action is not widely used in practice as it amplifies any process noise, which can lead to large and unnecessary control action (Luyben and Luyben, 1997, Svrcek et al., 2006).

PID controllers are usually tuned by trial-and-error or via formal tuning rules. The former approach is described in detail by Wade (2004), while O'Dwyer (2003) has compiled an extensive survey of the formal tuning rules available in literature. The most well-known are the simple classical rules developed by Ziegler and Nichols (1942, 1943), which can produce reasonable control performance, but tend to be too aggressive for most applications as they give large controller gains and short integral times (Svrcek et al., 2006). More conservative tuning rules have since been developed, the simplest of which are the rules proposed by Tyreus and Luyben (1992). These produce less underdamped control loops, and are therefore often preferred over the Ziegler-Nichols rules (Svrcek et

al., 2006). Table 2.5.2 summarises the Ziegler-Nichols and Tyreus-Luyben tuning rules, while Table 2.5.3 presents PID tuning rules that are specific to liquid level control loops.

Table 2.5.2: Ziegler-Nichols and Tyreus-Luyben controller tuning rules.

Controller	K_c	τ_I (min)	τ_D (min)	Comments
Ziegler-Nichols (Ziegler and Nichols, 1942, 1943)				
P	$\frac{\tau_p}{K_p \cdot \theta}$ or $\frac{K_u}{2}$	–	–	$\frac{\theta}{\tau_p} \leq 1.0$
PI	$\frac{0.9 \cdot \tau_p}{K_p \cdot \theta}$ or $\frac{K_u}{2.2}$	$3.33 \cdot \theta$ or $\frac{P_u}{1.2}$	–	$\frac{\theta}{\tau_p} \leq 1.0$
PID	$\frac{1.2 \cdot \tau_p}{K_p \cdot \theta}$ or $\frac{K_u}{1.7}$	$2 \cdot \theta$ or $\frac{P_u}{2}$	$0.5 \cdot \theta$ or $\frac{P_u}{8}$	$\frac{\theta}{\tau_p} \leq 1.0$
Tyreus-Luyben (Tyreus and Luyben, 1992; Luyben, 1996)				
PI	$\frac{0.49}{K_p \cdot \theta}$ or $\frac{K_u}{3.2}$	$8.75 \cdot \theta$ or $2.2 \cdot P_u$	–	
PID	$\frac{0.72}{K_p \cdot \theta}$ or $\frac{K_u}{2.2}$	$8.75 \cdot \theta$ or $2.2 \cdot P_u$	$0.64 \cdot \theta$ or $\frac{P_u}{6.3}$	

Table 2.5.3: Liquid level PID controller tuning rules (Wade, 2004).

Tuning Criterion	K_c	τ_I (min)	τ_D (min)
Critically damped	$\frac{0.74 \cdot \Delta F_{in}}{\Delta L_{max}}$	$\frac{4.0 \cdot V}{K_c \cdot F_{max}}$	–
QDR (DR = 0.25)	$\frac{0.50 \cdot \Delta F_{in}}{\Delta L_{max}}$	$\frac{0.74 \cdot V}{K_c \cdot F_{max}}$	–
Minimum IAE (DR = 0.05)	$\frac{0.32 \cdot \Delta F_{in}}{\Delta L_{max}}$	$\frac{0.19 \cdot V}{K_c \cdot F_{max}}$	–

Notation: QDR is the quarter decay ratio; IAE is the integral of the absolute error; DR is the decay ratio; ΔF_{in} is the maximum percentage step change in inflow that can be expected, ΔL_{max} is the maximum allowable percentage deviation from the controller setpoint, V is the holdup volume between the maximum and minimum level control points, and F_{out} is the maximum flow rate through the control valve.

2.5.2.2 Advanced Controller Algorithms

PID controllers do not always provide sufficient control action to produce the desired process response. In such situations, improved process control may be obtained by the introduction of more complex feedback control algorithms (e.g. cascade control or selective control) and/or feedforward control action. Such advanced classical control algorithms are discussed in depth in a number of texts, including those by Seborg and co-workers (1989), Stephanopoulos (1984) and Shinskey (1979).

For particularly difficult control problems, such as non-linear processes and non-stationary processes, enhanced process control may be provided by modern control algorithms. The most popular of these include adaptive, inferential, model predictive and intelligent control algorithms. Concise overviews of these modern control algorithms are provided by Åström and Hagglünd (1995) and Seborg and co-workers (1989), while more detailed discussions have been presented by Wittenmark (1997), Joseph

(1999), Garcia and co-workers (1989), Lee and Cooley (1997), Qin and Badgwell (2003) and Stephanopoulos and Han (1996).

For the purposes of this work, advanced controller algorithms will not be considered and only PID controllers will be utilised in the development of the diagonal control structures for the CO_2 trains.

2.5.3 Selection of Diagonal Control Structure

For a MIMO process like the hot potassium carbonate process, there exist a number of alternative sets of controlled (output) and manipulated (input) variables that can be used to develop a diagonal control structure. The selection of different sets of input and output variables for a given process will result in different control structure alternatives. Typically, the set of controlled variables is selected on the basis of engineering judgement (Luyben and Luyben, 1997), while the set of manipulated variables is chosen using the analysis methods described below.

2.5.3.1 The Condition Number and the Morari Resiliency Index

Singular value decomposition (Golub and Kahan, 1965) is a useful tool for analysing the control loop sensitivity of a MIMO process. Since process sensitivity affects the control system behaviour, singular value decomposition is often used to select the set of manipulated variables for control.

One useful index derived from the singular value decomposition of the process transfer matrix $\mathbf{G_p}(s)$ is the Morari resiliency index (MRI) (Yu and Luyben, 1986). This is the minimum singular value $\sigma_{min}(s)$ of $\mathbf{G_p}(s)$ and is a measure of the inherent ability of the process to handle uncertainties. The smaller the MRI, the more sensitive the process is to uncertainties. Consequently, the set of manipulated variables should be selected to give the largest MRI over the frequency range of interest. For feedback control, the frequency range of particular importance is from about 0.01 to 1 rad/min (Skogestad et al., 1990).

The singular value decomposition also gives the condition number (CN) (Grosdidier et al., 1985):

$$CN = \frac{\sigma_{max}(s)}{\sigma_{min}(s)} \tag{2.5.4}$$

where $\sigma_{max}(s)$ is the ratio of the maximum singular value of $\mathbf{G_p}(s)$. This index provides a quantitative indication of the system sensitivity. A process is said to be well-conditioned and relatively insensitive to uncertainties if CN is close to 1. Large condition numbers (CN>10) imply unbalanced sensitivity to process uncertainties and may indicate control problems (Skogestad and Postlethwaite, 1996). Consequently, the set of manipulated variables with the smallest CN should be selected.

It should be noted that CN and the MRI are scale-dependent and are therefore functions of the units of $\mathbf{G_p}(s)$. To circumvent this problem, $\mathbf{G_p}(s)$ should be scaled based on physical grounds, e.g. by dividing each variable by its allowed range (Skogestad and Postlethwaite, 1996).

2.5.3.2 The Disturbance Condition Number and the Disturbance Cost

The sensitivity of a MIMO process to disturbances also affects the control system behaviour, and should also be considered in the selection of the manipulated variables. Two useful indices are the disturbance condition number (DCN) (Skogestad and Morari, 1987) and the disturbance cost (DC) (Lewin, 1996):

$$\mathrm{DCN} = \frac{\left\| \mathbf{G_p}^{-1}(s) \cdot \mathbf{G_d}(s) \cdot \mathbf{d}(s) \right\|_2}{\left\| \mathbf{G_d}(s) \cdot \mathbf{d}(s) \right\|_2} \cdot \sigma_{max}(s) \tag{2.5.5}$$

$$\mathrm{DC} = \left\| \mathbf{G_p}^{-1}(s) \cdot \mathbf{G_d}(s) \cdot \mathbf{d}(s) \right\|_2 \tag{2.5.6}$$

where $\mathbf{G_d}(s)$ is the process disturbance transfer function matrix, and $\mathbf{d}(s)$ is the process disturbance vector. Both DCN and DC provide an indication of the extent of control action required to reject a disturbance. Small values for DCN (~1) and DC indicate the system is relatively insensitive to the disturbance and hence less control action is needed to eliminate its effect. Consequently, the set of manipulated variables should be selected to give the smallest DCN and DC. Like CN and the MRI, DCN and DC are scale-dependent, so it is important that $\mathbf{G_d}(s)$ and $\mathbf{d}(s)$ are well-scaled.

It should be noted that the above four indices are dependent on the choice of controlled and manipulated variables, but are unaffected by permutations in the control loop pairings. Therefore, these indices can only be used to discriminate between alternative diagonal control structures and are not applicable for selecting the configuration (variable pairings) for the diagonal control structure.

2.5.4 Selection of Diagonal Control Structure Configuration

Ideally, the diagonal control structure resulting from the selected controlled and manipulated variables should have minimal interaction between its SISO control loops (Svrcek et al., 2006). Since there are N! feasible control loops for an N×N MIMO system, the following analysis methods are used to identify suitable diagonal control structure configurations.

2.5.4.1 The Relative Gain Array

The most well-known and extensively applied variable pairing tool is the relative gain array (**RGA**), which was proposed by Bristol (1966) as a measure of the SISO control loop interactions in a diagonal control structure. For an N×N MIMO process, the **RGA** is a dimensionless matrix whose ij^{th} element λ_{ij} is the relative gain of a controlled variable y_i to a manipulated variable m_j:

$$\lambda_{ij} = \frac{\left(\partial y_i / \partial m_j \right)_m}{\left(\partial y_i / \partial m_j \right)_y} = \mathbf{G_{p,ij}}(s) \cdot \left(\mathbf{G_p}^{-1} \right)^T_{ij}(s) \qquad \text{for } i,j = 1, \ldots, N \tag{2.5.7}$$

The relative gains are unaffected by scaling and provide a quantitative comparison of how each manipulated variable affects each controlled variable. In general, variable pairings should be selected such that the relative gains are positive and as close to 1 as possible over the frequency range of interest (Skogestad and Postlethwaite, 1996). This minimises the interaction between the loops, thereby preventing stability problems caused by interaction.

2.5.4.2 The Niederlinski Index and the Morari Index of Integral Controllability

Once suitable SISO control loop pairings have been determined from the **RGA**, the rows and columns of $\mathbf{G_p}(s)$ can be reordered such that the paired elements are located along the diagonal to correspond with the diagonal control structure. The reordered process transfer matrix $\underline{\mathbf{G}}_\mathbf{p}(s)$ enables the application of the Niederlinski index (NI) (Niederlinski, 1971):

$$NI = \frac{\det\left(\underline{\mathbf{G}}_\mathbf{p}(0)\right)}{\prod_{i=1}^{N} \underline{\mathbf{G}}_{\mathbf{p},ii}(0)} \tag{2.5.8}$$

to analyse the stability of the selected control loop pairings at steady-state (s=0). If all the SISO controllers contain integral action and have positive loop gains, a negative NI proves that the specified diagonal control structure will definitely be closed-loop unstable (Grosdidier et al., 1985). Therefore, any variable pairings that give a negative NI should be eliminated. For a 2×2 system, a positive NI satisfies the necessary conditions for closed-loop stability. However, for higher order systems, a positive NI indicates the system may or may not be unstable, and its stability should therefore be tested by dynamic simulation.

An alternative measure of the stability of a diagonal control structure is the Morari index of integral controllability (MIC) (Grosdidier et al., 1985; Yu and Luyben, 1986):

$$MIC = \lambda_{\underline{\mathbf{G}}_\mathbf{p}^{+}(0)} \tag{2.5.9}$$

where $\lambda_{\underline{\mathbf{G}}_\mathbf{p}^{+}(0)}$ is the vector of the eigenvalues of the matrix $\underline{\mathbf{G}}_\mathbf{p}^{+}(0)$, which is obtained from $\underline{\mathbf{G}}_\mathbf{p}(0)$ by adjusting the signs so that all the diagonal elements are positive. If all the SISO controllers contain integral action and have positive loop gains, a negative eigenvalue for $\underline{\mathbf{G}}_\mathbf{p}^{+}(0)$ will produce an unstable diagonal control structure. Consequently, any variable pairings that result in a negative MIC element should be eliminated.

2.5.5 Analysis of Diagonal Control Structure Performance

After an appropriate diagonal control structure configuration has been identified from the above methods, its performance can be analysed through the use of the performance relative gain array (**PRGA**) and the closed-loop disturbance gain (**CLDG**) matrix (Skogestad and Postlethwaite, 1996):

$$\mathbf{PRGA} = \underline{\mathbf{G}}_{\mathbf{p,diag}}(s) \cdot \underline{\mathbf{G}}_\mathbf{p}^{-1}(s) \tag{2.5.10}$$

$$\mathbf{CLDG} = \underline{\mathbf{G}}_{\mathbf{p,diag}}(s) \cdot \underline{\mathbf{G}}_{\mathbf{p}}^{-1}(s) \cdot \mathbf{G}_{\mathbf{d}}(s) \tag{2.5.11}$$

where $\underline{\mathbf{G}}_{\mathbf{p,diag}}(s)$ is a diagonal matrix consisting of the diagonal elements of $\underline{\mathbf{G}}_{\mathbf{p}}(s)$.

For acceptable disturbance rejection and setpoint tracking performance, the following condition must be satisfied for each control loop i, disturbance k and setpoint j (Skogestad and Postlethwaite, 1996):

$$\left|1 + \mathbf{G}_{\mathbf{OL},i}(s)\right| > \max_{k,j}\left\{\left|\mathbf{CLDG}_{ik}\right|, \left|\mathbf{PRGA}_{ij}\right|\right\} \tag{2.5.12}$$

$$\mathbf{G}_{\mathbf{OL},i}(s) = \underline{\mathbf{G}}_{\mathbf{p},ii}(s) \cdot \mathbf{G}_{\mathbf{c},i}(s) \tag{2.5.13}$$

where $\mathbf{G}_{\mathbf{OL},i}(s)$ is the open-loop transfer function and $\mathbf{G}_{\mathbf{c,i}}(s)$ is the controller transfer function for loop i. Consequently, disturbances and setpoint changes corresponding to large **CLDG** and **PRGA** elements will be more difficult to control. It should be noted that $|1+\mathbf{G}_{\mathbf{OL},i}(s)|$ need only be larger than $|\mathbf{PRGA}_{ij}|$ at frequencies where the setpoints are tracked, which is usually limited to low frequencies (ω<1 rad/min) (Skogestad and Postlethwaite, 1996). Similarly, having $|1+\mathbf{G}_{\mathbf{OL},i}(s)|$ larger than $|\mathbf{CLDG}_{ikj}|$ is only required at frequencies at which control is needed for disturbance rejection, i.e. when $|\mathbf{CLDG}_{ikj}|$ is greater than 1 (Skogestad and Postlethwaite, 1996).

The validity of the above analyses should always be verified through dynamic simulation, which requires the individual SISO controllers to be tuned. The next section describes such a tuning method for diagonal control structures.

2.5.6 Tuning of Diagonal Control Structures

Since the early 1970s, a number of different controller tuning methods have been proposed for diagonal control structures (Huang et al., 2003). The most well-known of these is the biggest log-modulus tuning (BLT) method (Luyben, 1986), which will be applied in this work because of its simplicity.

The BLT method involves the following steps:

1. The PI Ziegler-Nichols settings for each SISO controller for the selected control loop pairings are calculated. For FOPDT process models, these settings are determined from the ultimate gain K_u and ultimate period P_u, as shown in Table 2.52. K_u and P_u can be obtained from the cross-over frequency ω_{co} as follows:

$$\phi_i = 180° = \tan^{-1}\left(-\tau_{p,i} \cdot \omega_{co,i}\right) + \left(-\theta_i \cdot \omega_{co,i}\right) \qquad \text{for i = 1,…,N} \tag{2.5.14}$$

$$K_{u,i} = \text{sign}\left(K_{p,i}\right) \cdot \sqrt{\left(\tau_{p,i} \cdot \omega_{co,i}\right)^2 + 1} \qquad \text{for i = 1,…,N} \tag{2.5.15}$$

$$P_{u,i} = \frac{2 \cdot \pi}{\omega_{co,i}} \qquad \text{for i = 1,…,N} \tag{2.5.16}$$

where ϕ is the phase lag, τ_p is the process time constant, θ is the process dead time and K_p is the process gain.

2. A detuning factor F is assumed (typically between 1.5 and 4) and is used to determine the settings for each SISO controller from the calculated Ziegler-Nichols settings:

$$K_{c,i} = \frac{K_{c,i}^{ZN}}{F} \qquad \text{for i = 1,…,N} \tag{2.5.17}$$

$$\tau_{I,i} = \tau_{I,i}^{ZN} \cdot F \qquad \text{for i = 1,…,N} \tag{2.5.18}$$

where $K_{c,j}$ are the controller gains, τ_{Ij} are the controller integral time constants, and N is the order of the MIMO system. The superscript ZN indicates the Ziegler-Nichols settings.

3. Based on the assumed value of F and the resulting controller settings, a multivariable Nyquist plot is created of the scalar function W:

$$W = -1 + \det\left(\mathbf{I} + \underline{\mathbf{G_p}}(s) \cdot \mathbf{G_c}(s)\right) \tag{2.5.19}$$

where **I** is the identity matrix. This plot is used to check if the system is closed-loop unstable by determining whether it encircles the critical (-1, 0) point. If the system is closed-loop stable (i.e. it doesn't encircle the critical point), then W is used to determine the closed-loop log modulus L_c:

$$L_c = 20 \cdot \log\left|\frac{W}{1+W}\right| \tag{2.5.20}$$

4. F is adjusted until the biggest log-modulus $L_{c,max}$ is equal to 2·N, where $L_{c,max}$ is the peak in the plot of L_c over the entire frequency range.

The above method has been found to yield a reasonable compromise between robustness and performance (Luyben and Luyben, 1997), and can be extended to include derivative action and/or individually weighted SISO loops (Monica et al., 1988).

2.5.7 Control of Acid Gas Removal Processes

A literature survey was performed to identify any previous applications of multivariable process control techniques for the hot potassium carbonate process. While there is some published research on the control of acid gas removal processes, it focuses on the removal of acid gases by amine solvents. No research has been published that is specific to the hot potassium carbonate process. However, for the interest of the reader, the available literature on the control of acid gas removal processes is summarised below.

A significant quantity of the available literature on the control of acid gas removal processes is based on work performed on the large-scale computer-controlled CO_2-MEA pilot plant at Imperial College in London. Much of this research concerned the development and application of modern control algorithms to obtain improved control for the pilot plant's pressure, level, flow and composition control loops. This included the multivariable controller based on the Nyquist array method (Rosenbrock, 1974) that was successfully designed and implemented by Albrecht and co-workers (1980) to control the lean and rich solvent compositions. This multivariable controller was found to perform considerably better than two independent SISO controllers. Due to the similarities between the CO_2-MEA process and the hot potassium carbonate process, this finding suggests that a multivariable controller may be required for the hot potassium carbonate process.

A number of workers also considered the implementation of adaptive control on the Imperial College pilot plant. These included Fortescue and co-workers (1981), who developed a self-tuning regulator with a forgetting factor. This control scheme was applied to the pilot plant's pressure loops, which demonstrated its viability as an alternative to conventional PI controllers that require periodic manual retuning due to process non-linearities. Based on this work, Ydstie and co-workers (1985) introduced an element of model predictive control, resulting in a more robust and flexible self-tuning regulator. The implementation of this control algorithm on the pilot plant's pressure, flow and level control loops showed that it could perform as well as a well-tuned PID controller over a wide range of operating conditions. The extended horizon self-tuning regulator was further extended by Kershenbaum and Pérez-Correa (1989) to include a feedforward component. The resulting feedforward/feedback self-tuning regulator was applied to the absorber level control loop, and was found to be more robust and effective than the simple feedback self-tuning regulator for the control of processes with large and variable time delays.

Some work was also performed on the application of linear and non-linear model predictive control algorithms on the Imperial College pilot plant, an overview of which was presented by Kershenbaum (2000). It was found that both the linear DMC (dynamic matrix control) and non-linear receding horizon model predictive control algorithms were very reliable in controlling the sweet gas composition of the plant for both setpoint tracking and disturbance rejection in the absence of pilot plant/model mismatches. However, poorer controller performance was observed when the pilot plant conditions differed from those used to develop the process model. The performance deterioration was more significant for the non-linear controller, and resulted in instability for sufficiently large mismatches between the pilot plant and the process model. The division of the operating region into several zones with different process models was found to partially compensate for this limitation.

More recently, the control of a smaller-scale CO_2-amine pilot plant was studied by van der Lee and co-workers (2001, 2003, 2004), with a particular focus on reducing the plant energy requirements. It was found that a combination of model predictive and PID control could provide good disturbance rejection and handling of setpoint changes, as well as lowering the energy consumption of the pilot plant. More

effective disturbance rejection was achieved through the implementation of an on-line monitoring system for the solvent CO_2 loading, which enabled the liquid composition to be introduced as a feedforward component in the control strategy.

It was noted that only a limited amount of work has been published in refereed journals on the control of industrial-scale acid gas removal plants[1]. However, it is expected that the control schemes developed for the above pilot plants would be relatively insensitive to scale-up. This was demonstrated by Alatiqi and co-workers (1993) who analysed the controllability of two industrial CO_2-MEA plants to identify a suitable diagonal control structure. A similar analysis was also performed on the process transfer function matrix obtained by Albrecht and co-workers (1980) for the Imperial College pilot plant, which resulted in the same loop pairings and closed-loop stability predictions as for the industrial plants.

[1] Some papers have been presented on the control of industrial scale acid gas removal plants at specialist conferences, like the Laurence Reid Natural Gas Conditioning Conferences. Notable contributors to this subject include William Poe and co-workers.

2.6 Summary

In summary, there is a significant body of work that has been performed on the non-equilibrium rate-based modelling of chemical absorption and desorption processes. However, the preceding literature review has identified the following two gaps in the literature regarding the non-equilibrium rate-based modelling of the hot potassium carbonate process:

- None of the previous models presented for the hot potassium carbonate process have used reaction rate expressions to represent the effect of chemical reactions.

- None of the previous models presented for the hot potassium carbonate process have considered rigorous electrolyte thermodynamics for both the absorber and regenerator columns.

A considerable amount of work has also been published regarding multivariable process control, and the control of acid gas removal processes has been studied in some detail. However, the above review of the available literature noted the following gap concerning the process control of the hot potassium carbonate process:

- No previous work has been published regarding the multivariable control of the hot potassium carbonate process.

Consequently, in fulfilling the project objectives stated in Section 1.1, the succeeding chapters of this thesis will attempt to address the above gaps in the literature, in accordance with the thesis structure outlined in Section 1.2.

From Figure 1.2.1, it can be observed that the main body of this thesis is divided into four key parts, the first being the above literature review. The second part, consisting of Chapters 3 to 5, focuses on the work performed in Aspen Custom Modeler® to develop and apply a new non-equilibrium rate-based model for the hot potassium carbonate process. Chapters 6 to 8 comprise the third part of this thesis, and concentrate on the work performed in HYSYS® to develop process models of the CO_2 trains using a novel approach. The fourth and final part of this thesis, Chapters 9 and 10, addresses the application of the HYSYS® process models for analysing the multivariable controllability of the CO_2 trains.

CHAPTER 3

THERMODYNAMIC AND PHYSICAL PROPERTIES OF THE HOT POTASSIUM CARBONATE SYSTEM

This chapter is the first of three chapters focussing on the simulation work performed in the Aspen Custom Modeler® simulation environment to develop a new non-equilibrium rate-based model for the hot potassium carbonate process.

As discussed in the preceding literature review, the hot potassium carbonate process involves a multicomponent electrolyte system, which requires specialised property models to accurately represent its complex non-ideal behaviour. In this chapter, a brief overview is provided of the various property models that were used in this work to calculate the thermodynamic and physical properties for the hot potassium carbonate system. Particular attention is paid to the regression of the adjustable parameters for the Electrolyte NRTL model, which was used to determine the key property of interest: the liquid phase activity coefficients.

3.1 Summary of Property Models

The thermodynamic and physical property calculations for modelling the hot potassium carbonate process in Aspen Custom Modeler® were primarily performed using the Aspen Properties® property calculation software. Where the property models provided in the Aspen Properties® databanks were not suitable, the property calculations were instead performed using either alternative models from literature or empirical correlations.

The property models used in this work are listed in Tables 3.1.1 and 3.1.2. Also included in these tables are the references from which the model equations and/or model parameter values were taken. Table 3.1.3 details the literature data used in the regression of some of the property model parameters.

Table 3.1.1: Vapour phase thermodynamic and physical property models.

Property	Model	References
Fugacity coefficients	SRK	Soave (1972) [a]
		Poling and co-workers (2001) [b]
Enthalpy	Ideal gas heat capacity	Poling and co-workers (2001) [b]
		Aspen Technology Inc (2003) [a]
	SRK	Soave (1972) [a]
Heat capacity	Via the vapour phase enthalpy	Poling and co-workers (2001) [b]
Molecular weight	Weighted average	Poling and co-workers (2001) [b]
Molar density	SRK	Soave (1972) [a]
Dynamic viscosity	Dean-Stiel	Dean and Stiel (1965) [a]
	DIPPR	Rowley and co-workers (1998) [a, b]
	Wilke	Wilke (1950) [a]
Thermal conductivity	DIPPR	Rowley and co-workers (1998) [a, b]
	Stiel-Thodos	Stiel and Thodos (1964) [a]
	Wassiljewa-Mason-Saxena	Poling and co-workers (2001) [b]
		Mason and Saxena (1958) [a]
Diffusivity	Blanc's Law	Reid and co-workers (1977) [a]
	Chapman-Enskog-Brokaw	Poling and co-workers (2001) [a]
	Dawson-Khoury-Kobayashi	Reid and co-workers (1977) [a]

[a] Reference for model. [b] Reference for model parameters.

Table 3.1.2: Liquid phase thermodynamic and physical property models.

Property	Model	References
Activity coefficients	Electrolyte NRTL	Chen and Evans (1986) [a]
Enthalpy	Electrolyte NRTL	Chen and Evans (1986) [a]
		Zemaitis and co-workers (1986) [b]
	Henry's Law	Chen (1980) [b]
		Austgen and co-workers (1989) [b]
		Fernández-Prini and co-workers (2003) [b]
		de Hemptinne and co-workers (2000) [b]
	Ideal gas heat capacity	Poling and co-workers (2001) [b]
		Aspen Technology Inc (2003) [a]
	Watson	Reid and co-workers (1977) [a]
Heat capacity	Aspen Properties® polynomial	Aspen Technology Inc (2003) [a, b]
Molecular weight	Weighted average	Poling and co-workers (2001) [b]
		Zemaitis and co-workers (1986) [b]
Vapour pressure	Extended Antoine	Rowley and co-workers (1998) [a, b]
Molar density	Amagat's Law	Aspen Technology Inc (2003) [a]
	Clarke Aqueous Electrolyte	Chen and co-workers (1983) [a]
	Rackett	Spencer and Danner (1972) [a]
Partial molar volume	Brelvi-O'Connell	Brelvi and O'Connell (1972) [a]
		Austgen and co-workers (1989) [b]
		Zemaitis and co-workers (1986) [b]
Dynamic viscosity	Andrade	Reid and co-workers (1977) [a]
	Breslau-Miller	Breslau and Miller (1972) [a]
		Breslau and co-workers (1974) [a]
	Jones-Dole	Jones and Dole (1929) [a]
Surface tension	Empirical correlation	-
Thermal conductivity	Empirical correlation	-
Diffusivity	Nernst	Horvath (1985) [a]
		Robinson and Stokes (1965)
		Onda and co-workers (1971)
	Ratcliff-Holdcroft	Ratcliff and Holdcroft (1963) [a]
	Stokes-Einstein	Poling and co-workers (2001) [a]
		Wang (1965) [b]
		Ferrell and Himmelblau (1967) [b]
		Witherspoon and Saraf (1965) [b]
		Hayduk and Laurie (1974) [b]
		Versteeg and van Swaaij (1988) [b]
		Tamimi and co-workers (1994) [b]

[a] Reference for model. [b] Reference for model parameters.

Table 3.1.3: Property data sources for the hot potassium carbonate system.

Property	References
Vapour-liquid equilibria	Tosh and co-workers (1959) Tosh and co-workers (1960)
Liquid heat capacity	Aseyev and Zaytsev (1996) UOP Gas Processing (1998)
Liquid Mass density	Armand Products Company (1998) Chernen'kaya and Revenko (1975) Bocard and Mayland (1962) UOP Gas Processing (1998)
Liquid dynamic viscosity	Chernen'kaya and Revenko (1975) Correia and co-workers (1980) Gonçalves and Kestin (1981) Bocard and Mayland (1962) UOP Gas Processing (1998)
Surface tension	Armand Products Company (1998) UOP Gas Processing (1998) Bedekar (1955)
Liquid thermal conductivity	Chernen'kaya and Revenko (1973) UOP Gas Processing (1998)

The hot potassium carbonate process is governed by the behaviour of the CO_2-H_2S-K_2CO_3-$KHCO_3$-KHS-K_2S-H_2O system, in particular, its liquid phase thermodynamics. Consequently, the key property of interest is the activity coefficients which, in this work, were calculated using the Electrolyte NRTL model. The regression of the adjustable model parameters for the Electrolyte NRTL model is discussed in the next section. For the purpose of brevity, detailed discussions of the other thermodynamic and physical property models have not been included in the main body of this thesis, but are instead located in Appendix B.

3.2 The Electrolyte NRTL Model

The Electrolyte NRTL model, as described in Section A.2 in Appendix A, was used to determine the activity coefficients for this work. This model includes two forms of adjustable binary parameters, τ and α, which must be determined from experimental data to ensure an accurate representation of the liquid phase thermodynamics. There are three types of these binary parameters: molecule-molecule, molecule-electrolyte and electrolyte-electrolyte (with a common cation or anion). A complete list is given in Table 3.2.1.

Table 3.2.1: Adjustable binary parameters for the Electrolyte NRTL model.

Binary Interaction Pair	Energy Parameter τ		Non-randomness Factor α	
Molecule-Molecule	$\tau_{mm'}$	$\tau_{m'm}$	$\alpha_{mm'}$	$\alpha_{m'm}$
Molecule-Electrolyte	$\tau_{m,ca}$	$\tau_{ca,m}$	$\alpha_{m,ca}$	$\alpha_{ca,m}$
Electrolyte-Electrolyte	$\tau_{ca,c'a}$	$\tau_{c'a,ca}$	$\alpha_{ca,c'a}$	$\alpha_{c'a,ca}$
	$\tau_{ac,a'c}$	$\tau_{a'c,ac}$	$\alpha_{ac,a'c}$	$\alpha_{a'c,ac}$

It should be noted that not all the adjustable binary parameters are independent, as indicated by the following relations:

$$\tau_{ca,c'a} = -\tau_{c'a,ca} \quad \text{and} \quad \tau_{ac,a'c} = -\tau_{a'c,ac} \tag{3.2.1}$$

$$\alpha_{mm'} = \alpha_{m'm} \quad \text{and} \quad \alpha_{m,ca} = \alpha_{ca,m} \tag{3.2.2}$$

$$\alpha_{ca,c'a} = \alpha_{c'a,ca} \quad \text{and} \quad \alpha_{ac,a'c} = \alpha_{a'c,ac} \tag{3.2.3}$$

As suggested by Chen and Evans (1986), a default value of 0.2 was set for the non-randomness factors, and the energy parameters were assumed to have the following dependence on temperature:

$$\tau = A + \frac{B}{T} + C \cdot \left(\frac{T^{ref} - T}{T} + \ln\left(\frac{T}{T^{ref}} \right) \right) \tag{3.2.4}$$

where T is the absolute temperature and T^{ref} is equal to 298.15 K. While values for the adjustable parameters A, B and C can be determined from the regression of data, it is not always possible to obtain statistically significant results for the adjustable parameters for all the binary interaction pairs (Chen and Evans, 1986). It is therefore important to identify the key binary interaction pairs when determining parameters for a system of interest.

For the hot potassium carbonate process, the system of interest is the CO_2-H_2S-K_2CO_3-$KHCO_3$-KHS-K_2S-H_2O system, which comprises of ten species: two cations (K^+ and H_3O^+), five anions (HCO_3^-, CO_3^{2-}, HS^-, S^{2-} and OH^-) and three molecular species (H_2O, CO_2 and H_2S). Compared with the concentrations of the other ions, the concentrations of H_3O^+ and OH^- ions are negligible. Similarly, the CO_2 and H_2S concentrations are insignificant when compared with that of H_2O. Therefore, the four key molecule-electrolyte binary interaction pairs are H_2O-(K^+,HCO_3^-), H_2O-(K^+,CO_3^{2-}), H_2O-(K^+,HS^-) and H_2O-(K^+,S^{2-}). The interactions between H_2O and the two acid gases are also important, so the

parameters for the molecule-molecule binary interaction pairs of H_2O-CO_2 and H_2O-H_2S are also of significance.

It should be noted that six possible salts can be formed from the cations and anions present in this system: K_2CO_3, $KHCO_3$, KHS, K_2S, KOH and H_2CO_3. Electrolyte-electrolyte parameters can be important when dealing with salt precipitation; however, the salt concentrations considered in this work did not necessitate the inclusion of the respective salt precipitation equilibrium reactions. For this reason, the electrolyte-electrolyte interactions were ignored and the corresponding parameters were assumed to be zero.

The Aspen Properties® databanks include values for the adjustable parameters for the CO_2-H_2S-K_2CO_3-$KHCO_3$-KHS-K_2S-H_2O system. However, these values were found to give a poor fit to the literature data. Consequently, the adjustable parameter values for the four key molecule-electrolyte binary interaction pairs were re-regressed from literature data using the Aspen Properties® Data Regression System (DRS). Adjustable parameter values for the other binary interaction pairs were taken from the Aspen Properties® databanks. The full set of adjustable parameters used in this work is provided in Tables C.1.1 and C.1.2 in Appendix C.

The re-regressed adjustable parameter values were determined via two sets of DRS regression runs, which are described in the following sections. The data utilised in these regression runs consisted of temperature T, pressure P, liquid phase mole fraction x and vapour phase mole fraction y values. The maximum likelihood method of Britt and Luecke (1973) was used to minimise the objective function Q:

$$Q = \sum_i W_i \cdot \sum_j \left[\left(\frac{\left(T_j^{est} - T_j^{expt}\right)^2}{\sigma_{T_j}^{\ 2}} \right) + \left(\frac{\left(P_j^{est} - P_j^{expt}\right)^2}{\sigma_{P_j}^{\ 2}} \right) + \sum_{k=1}^{NC-1} \left(\frac{\left(x_{j,k}^{est} - x_{j,k}^{expt}\right)^2}{\sigma_{x_{j,k}}^{\ 2}} \right) + \sum_{k=1}^{NC-1} \left(\frac{\left(y_{j,k}^{est} - y_{j,k}^{expt}\right)^2}{\sigma_{y_{j,k}}^{\ 2}} \right) \right] \tag{3.2.5}$$

where W_i is the weight of data group i, σ is the standard error associated with a data point, NC is the number of components, the subscripts est and expt signify the estimated and experimental values for each variable, the subscript j signifies the data point j, and the subscript k signifies the component k.

The objective function was minimised through the manipulation of the estimated values of the variables and the model parameters. This minimisation process was subject to the vapour-liquid equilibrium constraints, the chemical equilibrium constraints for all the reactions included in the system, and the parameter bounds.

3.2.1 The CO_2-K_2CO_3-$KHCO_3$-H_2O System

The first set of DRS regression runs was performed using Tosh and co-workers' (1959) vapour-liquid equilibrium data for the CO_2-K_2CO_3-$KHCO_3$-H_2O system to obtain adjustable parameter values for the H_2O-(K^+,HCO_3^-) and H_2O-(K^+,CO_3^{2-}) binary interaction pairs.

Tosh and co-workers (1959) measured the partial pressure of CO_2 over aqueous potassium carbonate-potassium bicarbonate solutions as a function of the CO_2 loading (or the fractional conversion of K_2CO_3 to $KHCO_3$), the solution K_2CO_3 equivalent weight percent[1] and temperature. 20, 30 and 40 wt% equivalent K_2CO_3 solutions were studied over a temperature range of 70° to 130°C and a CO_2 loading range of 0.10 to 0.83. These conditions correspond to the typical operating conditions for the Moomba CO_2 trains.

The liquid phase composition was determined using the apparent component approach. This method ignores the solution chemistry and only considers the resulting molecular components present in the liquid phase. For the CO_2-K_2CO_3-$KHCO_3$-H_2O system, the apparent liquid phase components were taken to be CO_2, K_2CO_3 and H_2O. The apparent liquid phase composition was determined from the vapour-liquid equilibrium data using the following equations:

$$n_{K_2CO_3} = \frac{wf_{K_2CO_3}}{MW_{K_2CO_3}} \tag{3.2.6}$$

$$n_{H_2O} = \frac{1 - wf_{K_2CO_3}}{MW_{H_2O}} \tag{3.2.7}$$

$$n_{CO_2} = n_{K_2CO_3} \cdot F_{CO_2} \tag{3.2.8}$$

$$x_j = \frac{n_j}{\sum_j n_j} \qquad \text{for } j = CO_2, K_2CO_3 \text{ and } H_2O \tag{3.2.9}$$

where n is the number of moles, $wf_{K_2CO_3}$ is the equivalent weight fraction of K_2CO_3 of the solution, MW is the molecular weight, F_{CO_2} is the CO_2 loading, and x is the liquid phase mole fraction.

The vapour phase constraint for the DRS regression runs was that only CO_2 was present (Al-Ramdhan, 2001; Hilliard, 2005), and the system pressure was taken to be the partial pressure of CO_2. The standard errors associated with the temperature, pressure and liquid component mole fractions were set as 0.1°C, 5% and 0.1%, respectively. Since the vapour phase was assumed to be pure CO_2, the standard errors for the vapour component mole fractions were set as 0%.

[1] The equivalent weight percent of K_2CO_3 is defined as the total concentration of K_2CO_3 in the solution if all the $KHCO_3$ in the solution is converted back into K_2CO_3.

A series of regression runs were performed, and the resulting optimal set of adjustable parameter values is presented in Table 3.2.2. The procedure which was used to obtain the optimal parameter set is outlined in Appendix C. Figures 3.1.1 and 3.1.2 compare the predicted CO_2 partial pressure values against the literature data. The average absolute deviation between the predicted and literature values was 12.4%. This is considered to be acceptable since the relative uncertainty for measurements of partial pressure is normally between 5 to 10%, but can be as high as 15% (Thomsen and Rasmussen, 1999). In comparison, the average absolute deviation between the predicted and literature values was 39.2% when the Aspen Properties® databank parameter values were used.

Table 3.2.2: Electrolyte NRTL parameters for the CO_2-K_2CO_3-$KHCO_3$-H_2O system.

Parameter	Component j	Component k	Parameter Value [a]	Standard Deviation
A	H_2O	(K^+,CO_3^{2-})	-5.020	1.096
A	(K^+,CO_3^{2-})	H_2O	-0.176	0.105
A	H_2O	(K^+,HCO_3^-)	6.250	1.215
A	(K^+,HCO_3^-)	H_2O	-3.728	0.966
B	H_2O	(K^+,CO_3^{2-})	-250.640	76.407
B	(K^+,CO_3^{2-})	H_2O	-864.400	532.813
B	H_2O	(K^+,HCO_3^-)	0 [b]	0 [c]
B	(K^+,HCO_3^-)	H_2O	0 [b]	0 [c]
C	H_2O	(K^+,CO_3^{2-})	0 [b]	0 [c]
C	(K^+,CO_3^{2-})	H_2O	0 [b]	0 [c]
C	H_2O	(K^+,HCO_3^-)	0 [b]	0 [c]
C	(K^+,HCO_3^-)	H_2O	0 [b]	0 [c]

[a] The parameter values are in SI units. [b] Parameter value was fixed at zero. [c] Parameter value was fixed so no standard deviation was determined.

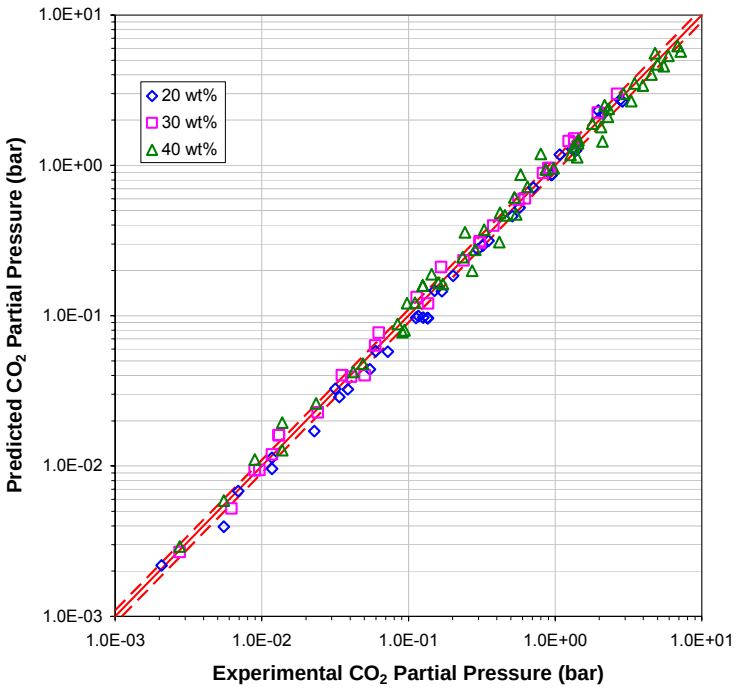

Figure 3.2.1: Comparison between the Electrolyte NRTL predictions and the experimental data. The points represent the CO_2 partial pressures over 20, 30 and 40 wt% equivalent K_2CO_3 solutions. The dashed lines (---) represent the ± 10% lines.

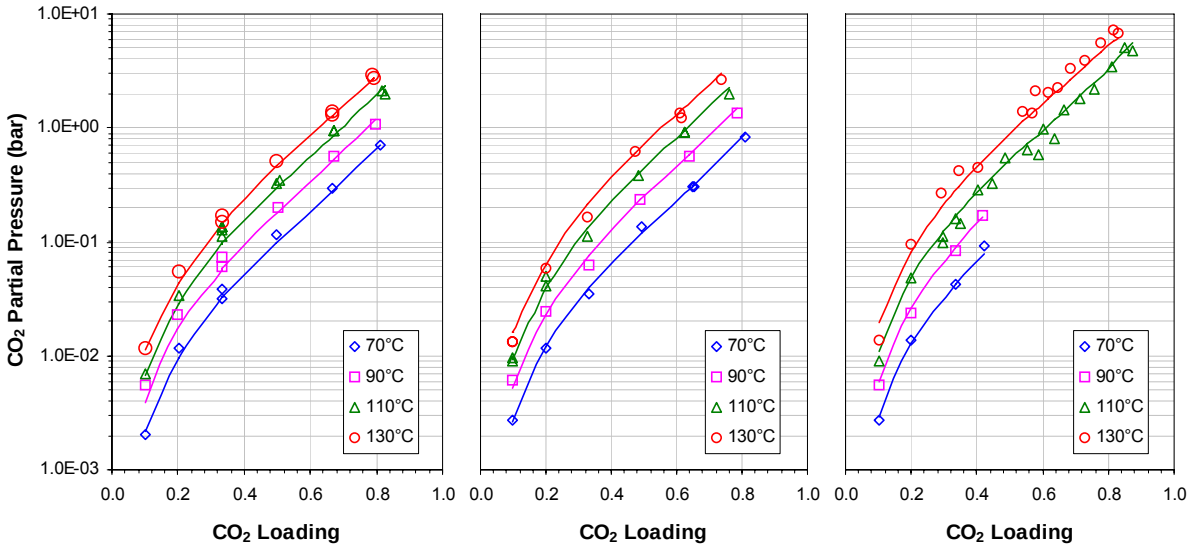

Figure 3.2.2: CO_2 partial pressure over K_2CO_3 solution as a function of CO_2 loading. The points represent the data from Tosh and co-workers (1959) for (a) a 20 wt% equivalent K_2CO_3 solution, (b) a 30 wt% equivalent K_2CO_3 solution and (c) a 40 wt% equivalent K_2CO_3 solution. The lines indicate the corresponding Electrolyte NRTL predicted values. Note: The CO_2 loading is not strictly dimensionless; its units are actually $(\text{mol } CO_2)\cdot(\text{mol } K_2CO_3)^{-1}$.

3.2.2 The CO_2-H_2S-K_2CO_3-$KHCO_3$-KHS-K_2S-H_2O System

In the second set of DRS regression runs, adjustable parameter values for the H_2O-(K^+,HS^-) and H_2O-(K^+,S^{2-}) binary interaction pairs were obtained using Tosh and co-workers' (1960) vapour-liquid equilibrium data for the CO_2-H_2S-K_2CO_3-$KHCO_3$-KHS-K_2S-H_2O system and the parameter values given in Table 3.2.2.

Tosh and co-workers (1960) measured the partial pressures of H_2S and CO_2 over aqueous potassium carbonate-potassium bicarbonate solutions as a function of the equivalent H_2S content[1], the fractional conversion of K_2CO_3 to $KHCO_3$ and KHS, the solution K_2CO_3 equivalent weight percent[2] and temperature. 20, 30 and 40 wt% equivalent K_2CO_3 solutions were studied over a temperature range of 70° to 130°C, an equivalent H_2S content range of 10 to 1500 mol/m^3 and fractional conversions between 0.073 and 0.68. It should be noted that the equivalent H_2S content for the Moomba CO_2 trains is typically between 0.5 and 2 mol/m^3; however, no literature data are available for such low concentrations of H_2S in potassium carbonate-potassium bicarbonate solutions.

As for the previous set of partial pressure data, the apparent component approach was used to determine the liquid phase composition. The apparent liquid phase components for the CO_2-H_2S-K_2CO_3-$KHCO_3$-KHS-K_2S-H_2O system were taken to be H_2S, CO_2, K_2CO_3 and H_2O. The following equations were used to determine the apparent liquid phase composition:

$$n_{K_2CO_3} = \frac{wf_{K_2CO_3}}{MW_{K_2CO_3}} \tag{3.1.6}$$

$$n_{H_2O} = \frac{1 - wf_{K_2CO_3}}{MW_{H_2O}} \tag{3.1.7}$$

$$n_{H_2S} = \frac{\hat{C}_{H_2S}}{\rho_{solution} \cdot 1000} \tag{3.1.10}$$

$$n_{CO_2} = n_{K_2CO_3} \cdot F_C - n_{H_2S} \tag{3.1.11}$$

$$x_j = \frac{n_j}{\sum_j n_j} \qquad \text{for j = } H_2S,\ CO_2,\ K_2CO_3 \text{ and } H_2O \tag{3.1.12}$$

where n is the number of moles, $wf_{K_2CO_3}$ is the equivalent weight fraction of K_2CO_3 of the solution, MW is the molecular weight, $\hat{C}_{H_2S}$ is the equivalent H_2S content, ρ is the density, F_c is the fractional conversion of K_2CO_3 to $KHCO_3$ and KHS, and x is the liquid phase mole fraction.

[1] The equivalent H_2S content is defined as the number of moles of H_2S reacting with 1 m^3 of solution to form $KHCO_3$ and KHS.

[2] The equivalent weight percent of K_2CO_3 is defined here as the total concentration of K_2CO_3 in the solution if all the $KHCO_3$ and KHS in the solution are converted back into K_2CO_3.

Following advice from Aspen Technology (Popolizio, 2005) and the results of several preliminary regressions, the vapour phase constraint was taken to be that only H_2S was present. Correspondingly, the system pressure was taken to be the partial pressure of H_2S. The standard errors associated with the temperature, pressure and liquid component mole fractions were set as 0.1°C, 5% and 0.1%, respectively. Since the vapour phase was assumed to be pure H_2S, the standard errors for the vapour component mole fractions were set as 0%.

A series of regression runs were performed, and the resulting optimal set of adjustable parameter values is presented in Table 3.2.3. Appendix C outlines the method used to determine the optimal parameter set. Figures 3.2.3 and 3.2.4 compare the predicted H_2S partial pressure values against the literature data. The average absolute deviation between the predicted and literature values was 16.5% with the regressed parameter values, compared to 81.9% when the Aspen Properties® databank parameter values were used.

Table 3.2.3: Electrolyte NRTL parameters for the CO_2-H_2S-K_2CO_3-$KHCO_3$-KHS-K_2S-H_2O system.

Parameter	Component j	Component k	Parameter Value [a]	Standard Deviation
A	H_2O	(K^+,HS^-)	3.076	1.028
A	(K^+,HS^-)	H_2O	-3.253	0.337
A	H_2O	(K^+,S^{2-})	3.438	3.079
A	(K^+, S^{2-})	H_2O	-6.305	1.311
B	H_2O	(K^+, HS^-)	0 [b]	0 [c]
B	(K^+, HS^-)	H_2O	-226.148	91.333
B	H_2O	(K^+, S^{2-})	4206.772	1127.216
B	(K^+, S^{2-})	H_2O	-267.739	180.213
C	H_2O	(K^+, HS^-)	0 [b]	0 [c]
C	(K^+, HS^-)	H_2O	0 [b]	0 [c]
C	H_2O	(K^+, S^{2-})	0 [b]	0 [c]
C	(K^+, S^{2-})	H_2O	0 [b]	0 [c]

[a] The parameter values are in SI units. [b] Parameter value was fixed at zero. [c] Parameter value was fixed so no standard deviation was determined.

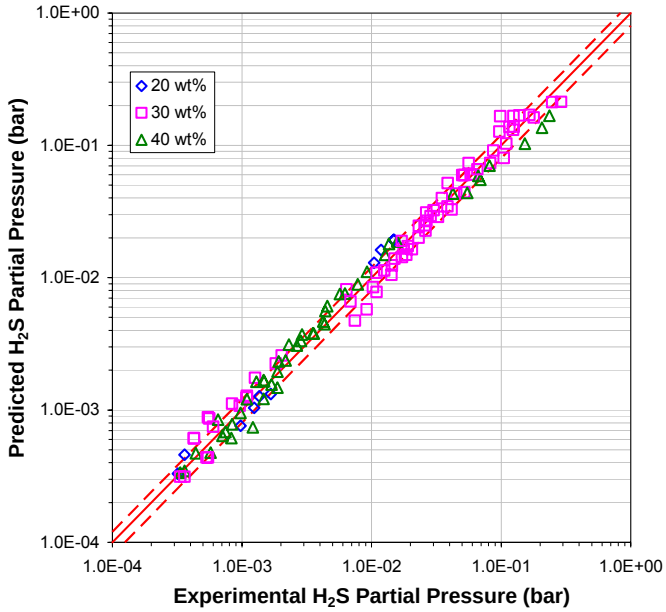

Figure 3.2.3: Comparison between the Electrolyte NRTL predictions and the experimental data. The points represent the H_2S partial pressures over 20, 30 and 40 wt% equivalent K_2CO_3 solutions. The dashed lines (---) represent the ± 20% lines.

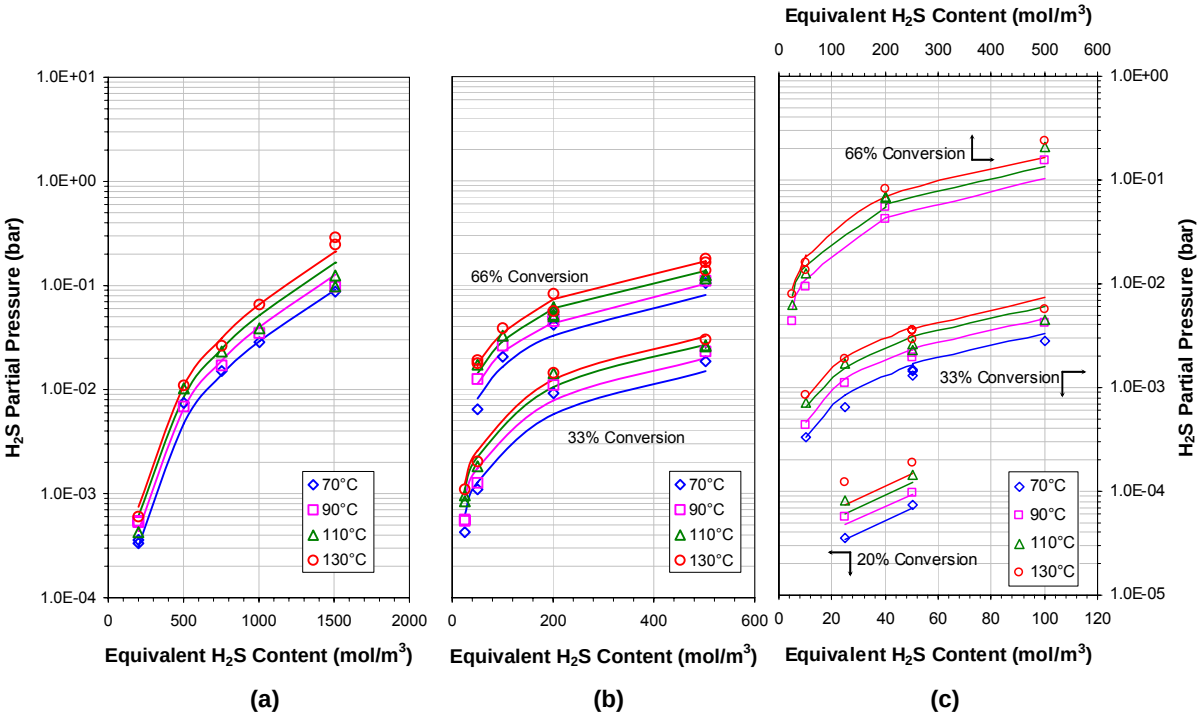

Figure 3.2.4: H_2S partial pressure over K_2CO_3 solution as a function of equivalent H_2S content. The points represent the data from Tosh and co-workers (1960) for (a) a 30 wt% equivalent K_2CO_3 solution converted only by H_2S, (b) a 30 wt% equivalent K_2CO_3 solution converted by H_2S and CO_2 and (c) a 40 wt% equivalent K_2CO_3 solution converted by H_2S and CO_2. The lines indicate the corresponding Electrolyte NRTL predicted values.

3.3 Summary

In summary, this chapter provided a brief description of the physical and thermodynamic property models that were applied in this work to model the properties of the hot potassium carbonate system. Particular attention was given to the Electrolyte NRTL model, while more detailed discussions of the other property models were provided in Appendix B.

To ensure an accurate representation of the liquid phase thermodynamics for the hot potassium carbonate system, the adjustable parameters for the Electrolyte NRTL model were regressed from literature data. Comparison between the regressed parameter values and the default values provided in the Aspen Properties® databanks showed that a significant improvement in model predictions was achieved with the regressed values. Similar improvements in the model predictions for some of the other physical and thermodynamic properties were obtained by replacing the Aspen Properties® default model parameter values with values regressed from literature data or by developing empirical correlations from the literature data.

The property models described in this chapter were used to perform the physical and thermodynamic calculations for the non-equilibrium rate-based model that was developed for the hot potassium carbonate process in Aspen Custom Modeler®. The following chapter discusses the development and validation of this process model.

CHAPTER 4

ASPEN CUSTOM MODELER® PROCESS MODEL DEVELOPMENT

Having described the relevant physical and thermodynamic property models for the hot potassium carbonate system in the previous chapter, this chapter continues the development of a new non-equilibrium rate-based model for the hot potassium carbonate process by considering the model equations and their implementation in Aspen Custom Modeler® for the Santos Moomba CO_2 trains.

Three alternative stage models of varying complexity are presented in this chapter for the absorber and regenerator columns for the hot potassium carbonate process, along with equations for several simple ancillary unit models. The three stage models are evaluated via a series of preliminary Aspen Custom Modeler® simulations to identify the optimal model in terms of model detail and complexity, solution accuracy and computation time.

This chapter discusses the development of two model adjustments to correct the column models for deviations between the model predictions and plant data from the Santos Moomba Processing Facility. Also included is a sensitivity analysis to determine the effects of various model parameters on the CO_2 and H_2S mass transfer rates predicted by the model.

Using the corrected column models and the ancillary unit models, CO_2 train process models are developed in Aspen Custom Modeler®, based on simplified configurations for the Moomba CO_2 trains. These process models are compared with the plant data used in the model development process, and are also validated against an independent set of plant data.

4.1 Process Model Equations

4.1.1 The Column Model Equations

Mathematical equations for modelling packed bed absorber and regenerator columns can be derived from either the equilibrium or the non-equilibrium rate-based stage approaches described in Section 2.2. In this work, three different sets of model equations were developed to identify the appropriate model complexity and to facilitate simulation convergence:

1. An equilibrium stage model with chemical equilibrium (Model 1),
2. A non-equilibrium rate-based stage model with enhancement factors (Model 2), and
3. A non-equilibrium rate-based stage model with reaction rate expressions (Model 3).

The three models were developed based on the following key assumptions:

1. Adiabatic column operation
2. Vapour and liquid phase plug flow
3. Apparent composition basis for the material balances
4. Reactions in the liquid film and chemical equilibrium in the bulk liquid phase (Models 2 and 3)

The assumption of adiabatic operation was considered to be valid due to the use of insulation in the Moomba CO_2 trains to prevent heat losses, whereas the plug flow conditions were assumed to simplify the modelling process. In reality, the vapour and liquid phase flows deviate from plug flow, with significantly more mal-distribution occurring in the liquid phase (Stichlmair and Fair, 1998). In the CO_2 trains, liquid re-distributors have been installed to reduce the degree of liquid mal-distribution; however, it is expected that some mal-distribution still occurs. While it was possible to include the effects of this mal-distribution in the column model equations, large-scale pilot plant studies would have been required to investigate the mal-distribution in the CO_2 trains, and these were beyond the scope of this work.

Following the approach used by Mayer (2001), Brettschneider and co-workers (2004) and Thiele (2007) to successfully develop chemical absorption and desorption models for various aqueous electrolyte systems, the model material balances were based on the apparent liquid and vapour phase compositions. For the liquid phase, the apparent composition ignores the solution chemistry, unlike the true composition, and only consists of molecular or undissociated electrolyte species. The apparent vapour phase composition, however, is identical to the true vapour phase composition due to the absence of electrolyte and ionic species in the vapour phase.

For the CO_2 trains, the apparent liquid phase composition consists of the acid gases (CO_2 and H_2S), the solvent (H_2O and K_2CO_3) and the inert vapour phase components (N_2, CH_4, C_2H_6, C_3H_8, C_4H_{10}, C_5H_{12}, C_6H_{14} and C_7H_{16}). In contrast, the true composition for this system is comprised of the vapour phase components (CO_2, H_2S, H_2O, N_2, CH_4, C_2H_6, C_3H_8, C_4H_{10}, C_5H_{12}, C_6H_{14} and C_7H_{16}) and the ionic species (H_3O^+, OH^-, K^+, CO_3^{2-}, HCO_3^-, HS^- and S^{-2}) which participate in the chemical equilibria

(R2.1.28) to (R2.1.32). As depicted in Figures 4.1.1 to 4.1.3, the true and apparent compositions are related by speciation relations, thereby enabling the computation of the true composition for the phase equilibria calculations.

The fourth model assumption was established after an investigation into the Hatta numbers for the rate-determining reactions (R2.1.6) and (R2.1.15) for the hot potassium carbonate process. It was found that the Hatta numbers for the two reactions were greater than 3 under the typical operating conditions for the CO_2 trains. Consequently, the reactions were considered to be sufficiently fast that they were completed within the liquid film and that the bulk liquid phase was at chemical equilibrium (Charpentier, 1981). However, the two reactions could not be considered as instantaneous, unlike proton transfer reactions, necessitating the inclusion of the liquid film kinetics in the two non-equilibrium stage column models.

The model equations for the three column models are summarised on the following pages. It should be noted that these equations only apply to the packed sections within the columns.

4.1.1.1 Model 1: Equilibrium Stage Model

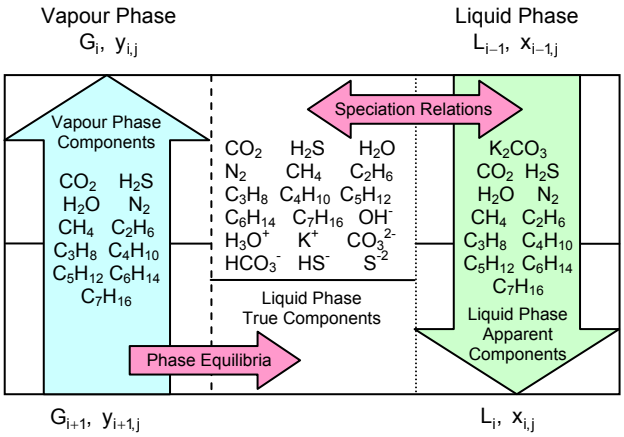

Figure 4.1.1: Equilibrium stage for Model 1 (adapted from Thiele (2007)).

The model equations for Model 1, the equilibrium stage model with chemical equilibrium, are:

Material balances:	Equilibrium stage MESH equation (2.2.1)
Equilibrium relations:	Equilibrium stage MESH equation (2.2.2)
Summation equations:	Equilibrium stage MESH equation (2.2.3)
Enthalpy balances:	Equilibrium stage MESH equation (2.2.4)
	Adiabatic condition $Q_i = 0$
Mass transfer relations:	None required
Energy transfer relations:	None required
Reaction kinetics:	None required
Phase equilibria relations:	Vapour-liquid equilibrium expressions (2.1.22) to (2.1.24) and (2.1.26)
Speciation relations:	Chemical equilibrium relations (2.1.11) to (2.1.15)
	Liquid phase relations (2.1.16) to (2.1.21) and (2.1.25)
Pressure drop relations:	Pressure drop equations (2.2.8) and (2.2.44)
	Hydrodynamic equations (2.2.38) to (2.2.42)
	Static vapour head equation (2.2.43)

4.1.1.2 Model 2: Non-Equilibrium Stage Model with Enhancement Factors

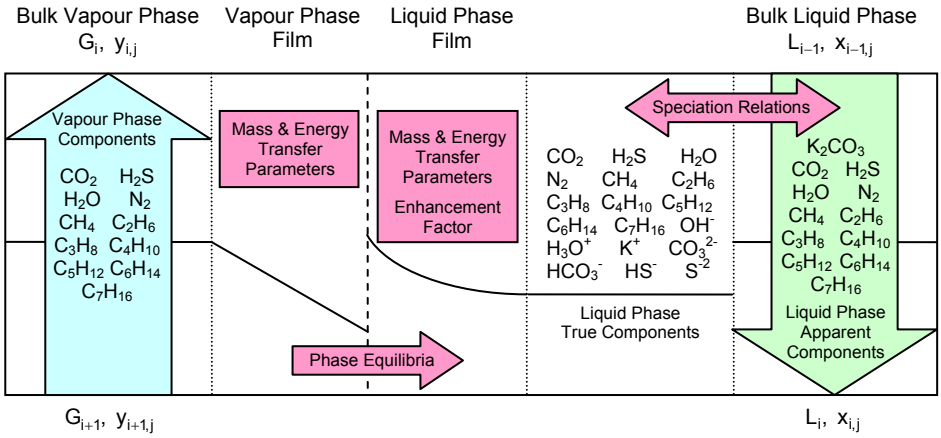

Figure 4.1.2: Non-equilibrium stage for Model 2 (adapted from Thiele (2007)).

The model equations for Model 2, the non-equilibrium rate-based stage model with enhancement factors, are:

Material balances:	Non-equilibrium stage MERQ equation (2.2.1)
Equilibrium relations:	Non-equilibrium stage MERQ equation (2.2.2)
Summation equations:	Non-equilibrium stage MERQ equation (2.2.3)
Enthalpy balances:	Non-equilibrium stage MERQ equation (2.2.4)
	Adiabatic condition $Q_{Gi} = Q_{Li} = 0$
Mass transfer relations:	Non-equilibrium stage MERQ equations (2.2.12) and (2.2.28)
	Mass transfer correlations (2.2.31) to (2.2.33)
Energy transfer relations:	Non-equilibrium stage MERQ equations (2.2.20) and (2.2.21)
	Energy transfer correlations (2.2.35) to (2.2.37)
Reaction kinetics:	Enhancement factor expression (2.2.29)
	Reaction rate constant expression (2.1.3)
Phase equilibria relations:	Vapour-liquid equilibrium expressions (2.1.22) to (2.1.24) and (2.1.26)
Speciation relations:	Chemical equilibrium relations (2.1.11) to (2.1.15)
	Liquid phase relations (2.1.16) to (2.1.21) and (2.1.25)
Pressure drop relations:	Pressure drop equations (2.2.8) and (2.2.44)
	Hydrodynamic equations (2.2.38) to (2.2.42)
	Static vapour head equation (2.2.43)

4.1.1.3 Model 3: Non-Equilibrium Stage Model with Reaction Rate Expressions

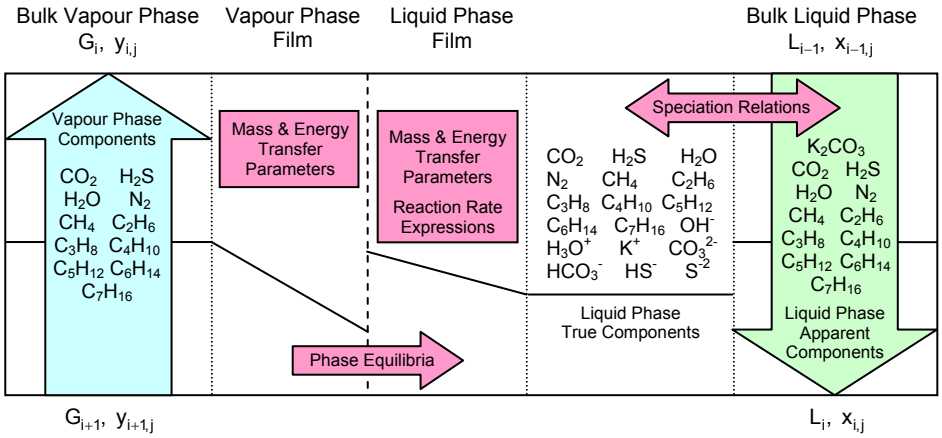

Figure 4.1.3: Non-equilibrium stage for Model 3 (adapted from Thiele (2007)).

The model equations for Model 3, the non-equilibrium rateb-based stage model with reaction rate expressions, are:

Material balances:	Non-equilibrium stage MERQ equations (2.2.1) and (2.2.26)
Equilibrium relations:	Non-equilibrium stage MERQ equation (2.2.2)
Summation equations:	Non-equilibrium stage MERQ equation (2.2.3)
Enthalpy balances:	Non-equilibrium stage MERQ equation (2.2.4)
	Adiabatic condition $Q_{Gi} = Q_{Li} = 0$
Mass transfer relations:	Non-equilibrium stage MERQ equations (2.2.12) and (2.2.17)
	Mass transfer correlations (2.2.31) to (2.2.33)
Energy transfer relations:	Non-equilibrium stage MERQ equations (2.2.20) and (2.2.21)
	Energy transfer correlations (2.2.35) to (2.2.37)
Reaction kinetics:	Reaction rate equation (2.2.22)
	Chemical equilibrium constant expression (2.2.23)
	Reaction rate constant expression (2.1.3)
Phase equilibria relations:	Vapour-liquid equilibrium expressions (2.1.22) to (2.1.24) and (2.1.26)
Speciation relations:	Chemical equilibrium relations (2.1.11) to (2.1.15)
	Liquid phase relations (2.1.16) to (2.1.21) and (2.1.25)
Pressure drop relations:	Pressure drop equations (2.2.8) and (2.2.44)
	Hydrodynamic equations (2.2.38) to (2.2.42)
	Static vapour head equation (2.2.43)

As suggested by Schneider and Górak (2001), the liquid film reactions were represented in Model 3 by assuming a linear liquid film concentration profile and applying the averaged reaction kinetics. This simplification eliminated the need to discretise the liquid film, thereby reducing the number of model equations and hence, the required computation time.

4.1.2 The Regenerator Wash Section Model Equations

Besides the packed beds that are represented by the above model equations, the regenerator columns also contain wash sections, as illustrated in Figure 2.1.2. In CO_2 trains #5 to #7, the wash sections are comprised of two valve trays. In contrast, the wash sections in CO_2 trains #1 to #4 consist of a cooling water circuit in which the vapour entering the packed bed in the wash section is cooled and partially condensed by a constant recirculating flow of water.

To simplify the Aspen Custom Modeler® simulations, the valve tray wash sections were modelled as single equilibrium stages with a pressure drop of 1.0 kPa[1], while the more complex cooling water circuits were treated as full reflux condensers with a pressure drop of 1.38 kPa[2] and water as the duty fluid. Following the example of Krishnamurthy and Taylor (1985), these units were also represented by single equilibrium stages. Consequently, the general wash section model equations are similar to those for Model 1:

Material balances:	Equilibrium stage MESH equation (2.2.1)
Equilibrium relations:	Equilibrium stage MESH equation (2.2.2)
Summation equations:	Equilibrium stage MESH equation (2.2.3)
Enthalpy balances:	Equilibrium stage MESH equation (2.2.4)
Mass transfer relations:	None required
Energy transfer relations:	None required
Reaction kinetics:	None required
Phase equilibria relations:	Vapour-liquid equilibrium expressions (2.1.22) to (2.1.24) and (2.1.26)
Speciation relations:	Chemical equilibrium relations (2.1.11) to (2.1.15)
	Liquid phase relations (2.1.16) to (2.1.21) and (2.1.25)
Pressure drop relations:	Pressure drop equation (2.2.8)

For the valve tray-type wash sections, there is no energy input so the adiabatic condition $Q_i = 0$ was applied. In the case of the cooling water circuits, the cooler duties Q_{Cooler} were related to the water flow rate F_{water} and the water enthalpies $h_{water,in}$ and $h_{water,out}$ at the inlet and outlet conditions:

$$Q_{Cooler} = F_{water} \cdot \left(h_{water,out} - h_{water,in}\right) \qquad (4.1.1)$$

and the outlet water temperature was set equal to the temperature of the liquid stream leaving the wash section.

[1] This equates to a pressure drop of 4 inches of H_2O per valve tray, as recommended by Kister (1992).

[2] This equates to a pressure drop of 0.5 – 0.6 inches of H_2O per foot of wash section packing, as recommended by Kister (1992).

4.1.3 The Reboiler and Condenser Model Equations

The remaining major components of the regenerator columns are the solution reboilers, the overhead condensers and the overhead catchpots. Like the regenerator wash sections, the solution reboilers for the regenerator columns were treated as equilibrium stages, as recommended by Krishnamurthy and Taylor (1985). Similarly, the overhead condenser and overhead catchpot for each regenerator column were modelled as a combined equilibrium stage. As a result, the reboiler and condenser model equations are similar to those for the regenerator wash sections:

Material balances:	Equilibrium stage MESH equation (2.2.1)
Equilibrium relations:	Equilibrium stage MESH equation (2.2.2)
Summation equations:	Equilibrium stage MESH equation (2.2.3)
Enthalpy balances:	Equilibrium stage MESH equation (2.2.4)
Mass transfer relations:	None required
Energy transfer relations:	None required
Reaction kinetics:	None required
Phase equilibria relations:	Vapour-liquid equilibrium expressions (2.1.22) to (2.1.24) and (2.1.26)
Speciation relations:	Chemical equilibrium relations (2.1.11) to (2.1.15)
	Liquid phase relations (2.1.16) to (2.1.21) and (2.1.25)
Pressure drop relations:	Pressure drop equation (2.2.8)

The duty fluid for the solution reboilers is low pressure steam, which completely condenses in the reboilers. Given the conservation of energy and mass, the reboiler duties Q_{Reb} were therefore calculated from:

$$Q_{Reb} = F_{steam} \cdot \left(h_{condensate} - h_{steam}\right) = -F_{steam} \cdot \Delta h_{H_2O}^{vap} \tag{4.1.2}$$

where F_{steam} is the steam flow rate, $h_{condensate}$ and h_{steam} are the condensate and steam enthalpies, and $\Delta h_{H_2O}^{vap}$ is the enthalpy of vaporisation of water. For the condensers, the duty fluid is air and the condenser duties Q_{Cond} were related to the air flow rate F_{air} and the enthalpies of air $h_{air,in}$ and $h_{air,out}$ at the inlet and outlet conditions, respectively:

$$Q_{Cond} = F_{air} \cdot \left(h_{air,out} - h_{air,in}\right) \tag{4.1.3}$$

The pressure drops ΔP across the reboilers were set equal to the pressure drops due to the static liquid head ΔP_{liq} in the reboilers:

$$\Delta P = \Delta P_{liq} = \rho_L \cdot g \cdot H_{liq} \tag{4.1.4}$$

where H_{liq} is the liquid height; while the pressure drops ΔP across the combined condenser and catchpot stages were determined from the condenser pressure drops ΔP_{Cond} (which were set at 13.8 kPa[1]) and the pressure drops due to the static liquid head ΔP_{liq} in the overhead catchpots:

$$\Delta P = \Delta P_{Cond} + \Delta P_{liq} = \Delta P_{Cond} + \rho_L \cdot g \cdot H_{liq} \quad (4.1.5)$$

The effect of the static vapour head was neglected (Strigle, 1994) due to the low operating pressures for the reboilers and condensers.

4.1.4 Other Ancillary Unit Model Equations

To simplify the Aspen Custom Modeler® simulations, the pressure drop between the absorber and regenerator columns was represented by a valve model while a pump model was used to represent the pressure increase between the two columns. These two ancillary units were treated as equilibrium stages with the following general model equations:

Material balances:	Equilibrium stage MESH equation (2.2.1)
Equilibrium relations:	Equilibrium stage MESH equation (2.2.2)
Summation equations:	Equilibrium stage MESH equation (2.2.3)
Enthalpy balances:	Equilibrium stage MESH equation (2.2.4)
Mass transfer relations:	None required
Energy transfer relations:	None required
Reaction kinetics:	None required
Phase equilibria relations:	Vapour-liquid equilibrium expressions (2.1.22) to (2.1.24) and (2.1.26)
Speciation relations:	Chemical equilibrium relations (2.1.11) to (2.1.15)
	Liquid phase relations (2.1.16) to (2.1.21) and (2.1.25)
Pressure drop relations:	Pressure drop equation (2.2.8)

For the valve model, the pressure drop was assumed to occur adiabatically and the valve duty Q_{Valve} was set as zero. Since some of the dissolved CO_2 and H_2S are flashed off from the depressurisation, the full set of equations given above was implemented in the valve model.

In contrast, no phase change takes place in the pump model, so the phase equilibria and speciation relations were not required and the vapour phase terms in the remaining relations were eliminated. The pressure rise across the pump was assumed to occur isothermally so the pump outlet temperature T_{out} was set equal to the inlet temperature T_{in}:

$$T_{out} = T_{in} \quad (4.1.6)$$

[1] This equates to a pressure drop of 2 psi which is typical of air cooler-type condensers (Hudson Products Corporation, 2002).

4.1.5 Numerical Solution

In order to solve the mathematical absorber and regenerator column models developed for the CO_2 trains, the above model equations were implemented in Aspen Custom Modeler® using its object-oriented modelling language. The resulting set of differential and algebraic equations were reduced to a set of non-linear algebraic equations by the elimination of the time derivatives under steady-state conditions.

Group decomposition was then applied to divide this large set of equations into a series of smaller equation sub-sets, which were solved more efficiently than if the entire equation set was solved simultaneously. These equation sub-sets were solved using the slow but very robust non-linear Newton method, which calculates a new Jacobian matrix at each iteration. On average, the computation time required to solve the individual steady-state column models varied between 1 to 3 minutes, depending on the model complexity, the column size and the initial values for the model variables.

The convergence criterion was based on the equation residuals with an absolute equation tolerance of 1×10^{-5}. Convergence was achieved when the residual for each equation was reduced to below the set tolerance. To facilitate convergence, the model equations were implemented such that Model 1, being the simplest, was used to generate initial values for Model 2. Likewise, Model 2 was used to initialise the variables for the more complex Model 3.

4.2 Preliminary CO_2 Train Simulations

Based on the first set of typical operating data provided in Table 2.1.2, a series of preliminary simulations were conducted to investigate the performance of the individual Aspen Custom Modeler® absorber and regenerator column models. The corresponding column model configurations are shown in Figure 4.2.1. The only notable difference between the absorber column models that is not depicted in the diagram below is the number of packed beds in each column. This varied between one and three, depending on the CO_2 train.

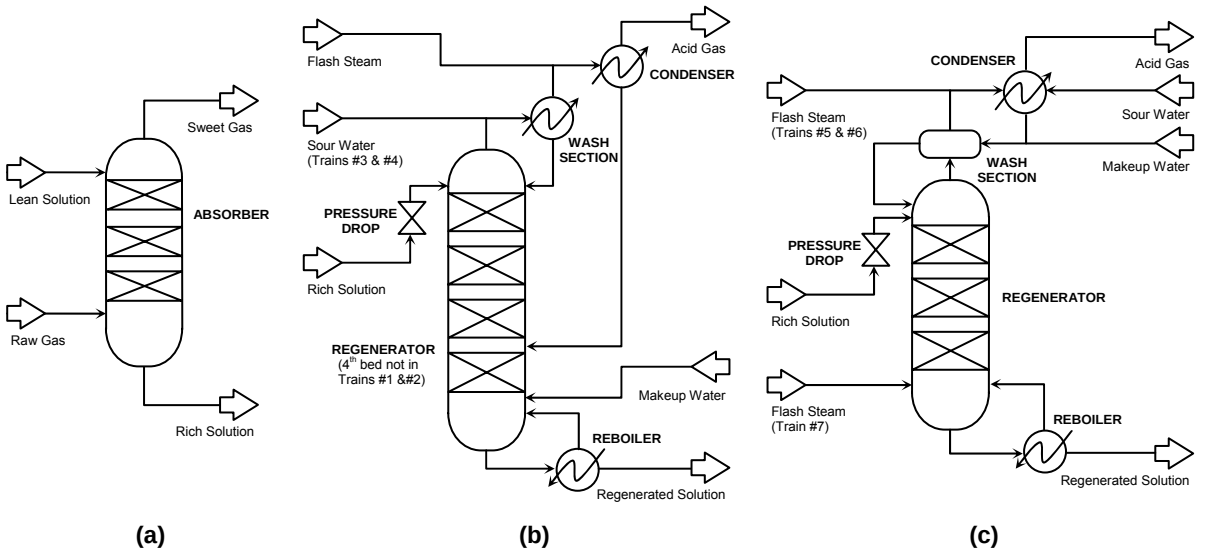

Figure 4.2.1: Preliminary Aspen Custom Modeler® simulation column configurations. (a) The absorber model for Trains #1 to #7. (b) The regenerator model for Trains #1 to #4. (c) The regenerator model for Trains #5 to #7.

4.2.1 Number of Model Stages

In order to apply the model equations to the CO_2 trains, the packed heights of the absorber and regenerator columns had to be first discretised into a number of stages. To minimise the number of model equations, and therefore the computation time, a series of simulation runs using Models 2 and 3 were performed on the absorber and regenerator in CO_2 train #1 (the absorber and regenerator with the shortest packed heights) to evaluate the discretisation of these two columns into different numbers of stages.

The predicted sweet gas CO_2 and H_2S content and the overall predicted CO_2 and H_2S absorption rates for the absorber are shown in Figure 4.2.2. Figure 4.2.3 compares the predicted regenerated solution CO_2 and H_2S loading and the overall predicted CO_2 and H_2S desorption rates for the regenerator.

For the absorber, negligible differences were observed between the values corresponding to 15 stages and the final asymptotic values. Similarly, there were negligible differences between the

values corresponding to 20 stages and the final asymptotic values for the regenerator. The optimal number of stages was therefore taken to be 15 for the absorber and 20 for the regenerator, which correspond to absorber and regenerator stage heights of approximately 0.49 and 0.96 m, respectively. These optimal stage heights were then used to discretise the packed heights of the taller absorber and regenerator columns in the CO_2 trains.

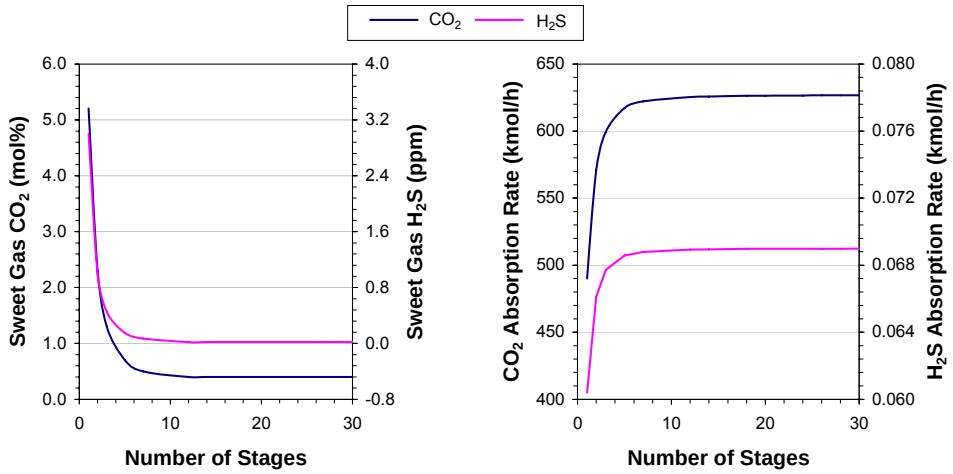

Figure 4.2.2: Results of the absorber discretisation simulation runs for CO_2 train #1. (a) Sweet gas composition and (b) total absorption rates as a function of the number of stages.

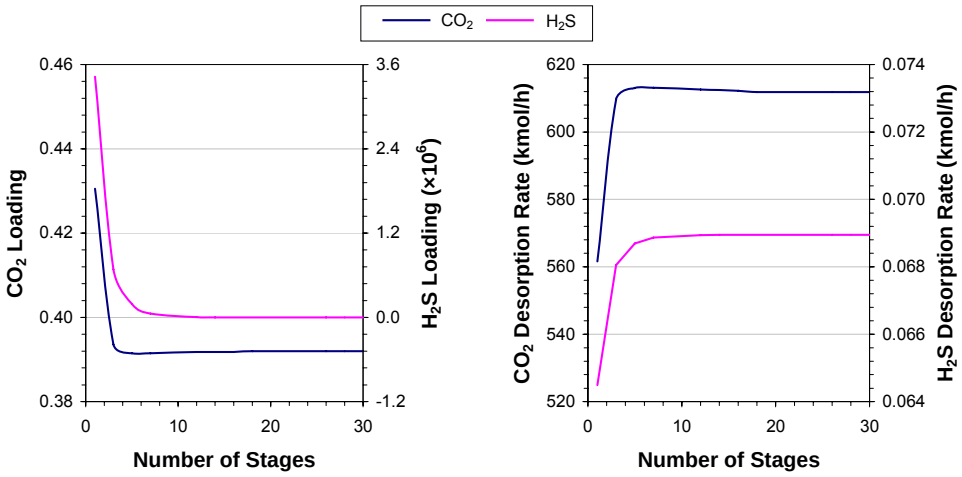

Figure 4.2.3: Results of the regenerator discretisation simulation runs for CO_2 train #1. (a) CO_2 and H_2S loading in the regenerated solution and (b) total desorption rates as a function of the number of stages. Note: The CO_2 and H_2S loadings are not strictly dimensionless; their units are actually (mol CO_2)·(mol K_2CO_3)$^{-1}$ and (mol H_2S)·(mol K_2CO_3)$^{-1}$.

4.2.2 The Different Modelling Approaches

Once the optimal stage heights were established, a series of simulations were run to compare the performances of Models 1, 2 and 3 for each absorber and regenerator, in order to determine the appropriate model complexity.

The CO_2 and H_2S vapour phase profiles predicted by the three different mathematical models for the absorbers in CO_2 trains #1 and #7 are compared in Figure 4.2.4, which also compares the liquid phase CO_2 and H_2S loading profiles predicted for the corresponding regenerators. The absorber and regenerator profiles for the other five CO_2 trains were very similar in shape to those for CO_2 train #1, and are included in Figures D.1.1 and D.1.2 in Appendix D.

The general shapes of the absorber and regenerator profiles were as anticipated. The vapour phase CO_2 and H_2S concentrations decreased up the absorber columns, while the liquid phase CO_2 and H_2S loading decreased down the regenerator columns. A slight initial increase in the liquid phase CO_2 loading was observed at the top of the regenerator columns. This phenomenon was caused by contact between the flashed-off CO_2 entering the columns and the condensed steam leaving the wash sections. A portion of the CO_2 was absorbed by the condensed steam, resulting in the observed increase in CO_2 loading at the top of the regenerator columns.

As expected, the absorber CO_2 and H_2S vapour phase profiles obtained from the equilibrium stage model (Model 1) differed considerably from those produced by the two non-equilibrium stage models (Models 2 and 3), which agreed closely. Similarly, much closer agreement was observed between the regenerator loading profiles predicted by Models 2 and 3 than with those predicted by Model 1. However, all three models did predict very similar compositions for the sweet gas leaving the top of the absorbers, as well as very similar acid gas loadings for the solution exiting the bottom of the regenerators. Despite this agreement with the more complex models, Model 1 was considered to be only suitable for initialisation runs due to the significant deviations observed for the absorber profiles.

As the simplest mathematical model, it was not surprising that Model 1 had the shortest computation times. The computation times associated with Model 2 were typically between 50 to 150% greater than that for Model 1, and similar increments in computation time were observed for Model 3 compared to Model 2. Despite the increased computation time and model complexity, the close agreement (within ±2%) between the profiles produced by Models 2 and 3 indicated that no significant improvement in the simulation results was achieved by using rigorous rate expressions instead of enhancement factors. This confirmed the earlier findings of de Leye and Froment (1986a) and Mayer (2001). It was therefore decided to employ Model 2 for subsequent simulations.

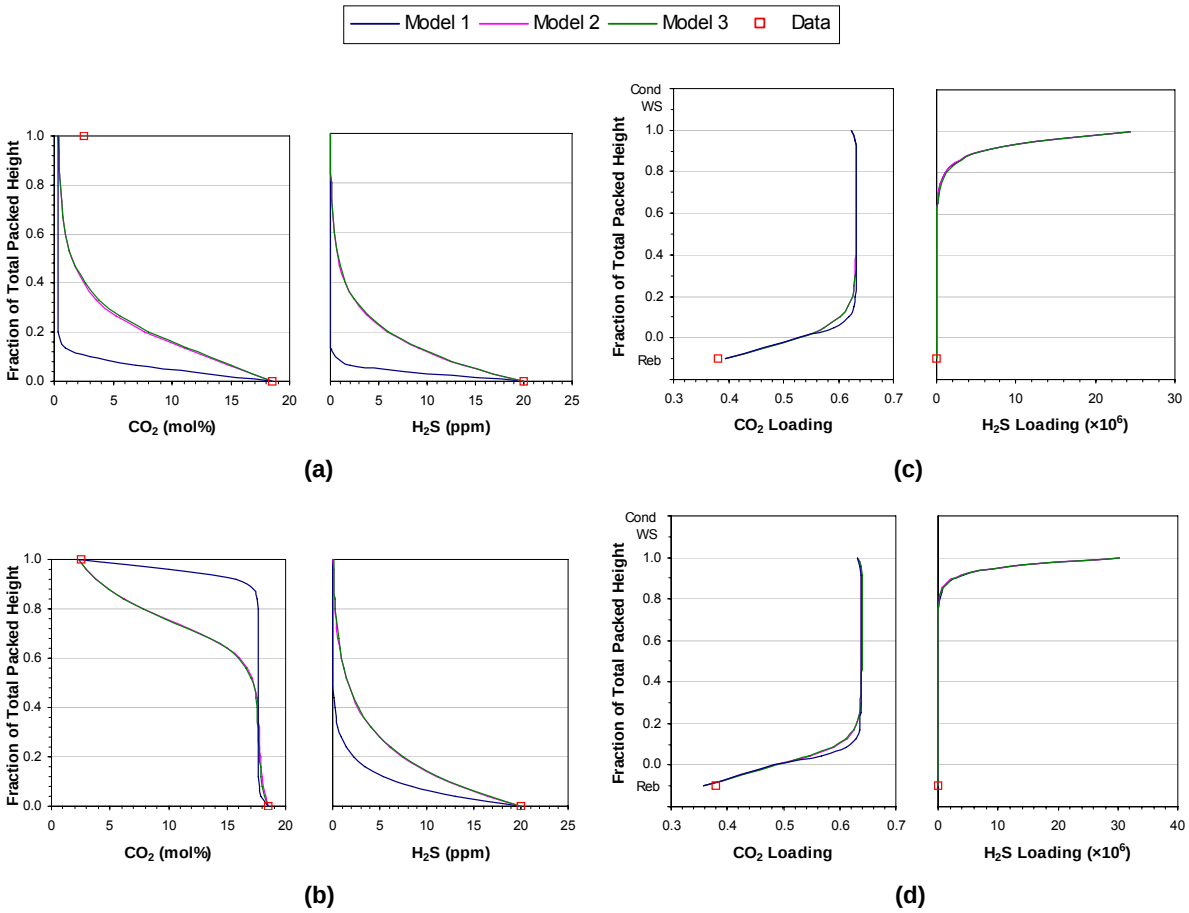

Figure 4.2.4: Results of the different modelling approaches for CO_2 trains #1 and #7. Absorber CO_2 and H_2S vapour phase profiles for (a) CO_2 train #1 and (b) CO_2 train #7. Regenerator liquid phase CO_2 and H_2S loading profiles for (c) CO_2 train #1 and (d) CO_2 train #7. (Cond = condenser, WS = wash section, Reb = reboiler)

4.3 Column Model Adjustments

It was observed in the previous section that the sweet gas CO_2 content predicted by the three mathematical models for the absorbers in CO_2 trains #1 to #6 deviated significantly from the data values. In contrast, a much smaller difference was observed for the absorber in CO_2 train #7. Small deviations from the data values were also observed for the predicted CO_2 loading at the bottom of the seven regenerators. The following sections investigate the reasons for these deviations and discuss the model adjustments required to correct them.

4.3.1 Liquid Phase Enthalpy Correction

Given that the chemical absorption and desorption are temperature-dependent processes, the temperature profiles along the absorber and regenerator columns were examined to determine if the calculated temperatures had contributed to the above-mentioned deviations. For comparison, the temperature profiles predicted by Model 2 for CO_2 trains #1 and #7 are provided in Figure 4.3.1. The corresponding temperature profiles for CO_2 trains #2 to #6 are given in Figures D.2.1 and D.2.2 in Appendix D.

Distinctive temperature bulges were observed in the absorber temperature profiles. These were caused by an initial rise in the solution temperature as it flowed down the columns (due to the exothermic nature of CO_2 absorption), followed by a temperature drop near the bottom of absorbers when the solution came into contact with the cooler raw gas. While the shapes of the absorber temperature profiles were as expected, the predicted absorber bottom temperatures were approximately 8°C higher than the data values. The overly high temperatures in the lower part of the absorbers were thought to have led to the predicted over-absorption of CO_2. However, they were not considered to be the sole contributory factor since the absorber in CO_2 train #7 had the highest predicted temperature profile but the smallest deviation for the sweet gas CO_2 content.

For the regenerators, the liquid phase temperatures were observed to remain relatively constant in the top two-thirds of the columns and to increase in the lower third of the columns, reaching a maximum at the reboilers. This correlated well with the corresponding CO_2 loading profiles in Figure 4.2.4. The solution CO_2 loading also remained relatively constant in the top two-thirds of the columns before decreasing to a minimum at the reboilers. These observed phenomena resulted from the rich solution coming into contact with the hot stripping steam generated from the solution reboilers. The rich solution experienced a temperature rise while the steam stripped CO_2 from the solution.

Close agreement was observed between the vapour and liquid phase temperature profiles within the regenerator columns while above the regenerator columns, the vapour phase temperatures decreased to a minimum at the condensers. In contrast to the absorbers, there was closer agreement between the temperatures predicted for the regenerators and the data values (within ±3°C). This suggested the regenerator temperatures were not the reason for the deviation between the predicted CO_2 loading for the regenerated solution and the data values.

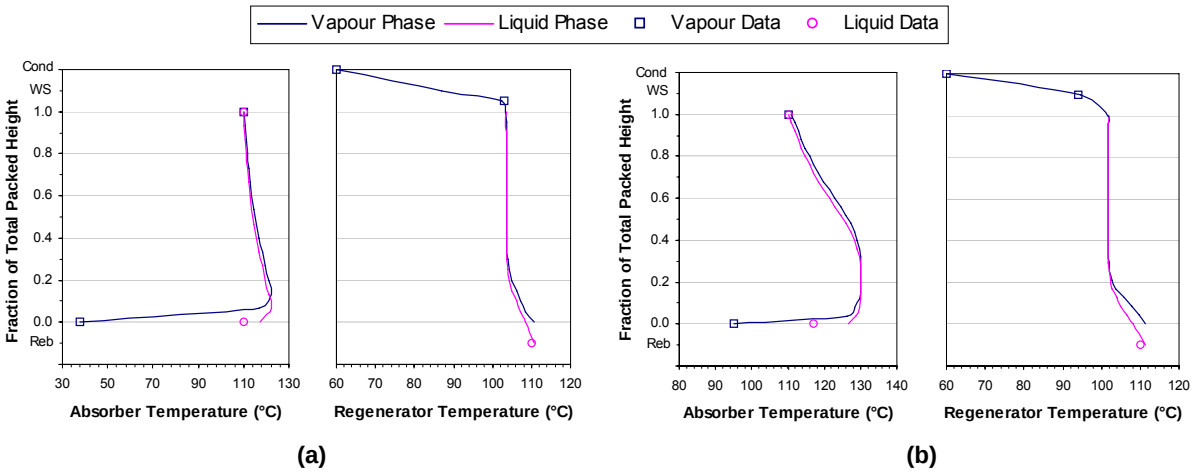

Figure 4.3.1: Temperature profiles for CO_2 trains #1 and #7. Temperature profiles predicted by Model 2 for (a) CO_2 train #1 and (b) CO_2 train #7. (Cond = condenser, WS = wash section, Reb = reboiler)

The column temperatures were determined from the enthalpy balances, making the temperatures dependent on the enthalpy values calculated from the thermodynamic property models. The vapour phase enthalpies were calculated from the SRK equation of state, which has been shown to give very good predictions for vapour phase enthalpies for mixtures of hydrocarbons and light gases (Poling et al., 2001).

The liquid phase enthalpies were calculated using the Electrolyte NRTL model and were based on an approximation (equation (B.1.7)) which neglects the effect of pressure on the liquid phase partial molar enthalpy. The close agreement between the predicted temperatures and the data values for the regenerator confirmed the validity of this approximation for atmospheric pressures. However, the disparity observed for the absorber temperatures indicated that this approximation was not valid at the much higher absorber operating pressures. Consequently, the effect of adjustments to the liquid phase enthalpy on the vapour and liquid phase temperatures and the CO_2 absorption rate in the seven absorbers was investigated.

A series of absorber simulation runs were performed, in which the liquid phase enthalpy h_L was corrected via the following linear expression:

$$h_L = a \cdot h_L^{ENRTL} + b \qquad (4.3.1)$$

where a and b are adjustable constants, and h_L^{ENRTL} is the liquid phase enthalpy calculated from the Electrolyte NRTL model. It was observed that as the liquid phase enthalpy became more negative, the absorber temperatures decreased, along with the CO_2 and H_2S absorption rates, albeit insignificantly.

The values for the constants a and b were adjusted iteratively to achieve the best agreement with the design temperatures for the seven absorbers. The resulting values of 0.7201 and -0.0933 for a and b,

respectively, were found to give an absolute average deviation of 0.5% and a maximum absolute deviation of 0.9%. The corrected and uncorrected absorber temperature profiles for CO_2 trains #1 and #7 are compared in Figure 4.3.2. The corresponding temperature profiles for the remaining five CO_2 trains are given in Figures D.2.1 and D.2.2 in Appendix D. The considerable improvement observed for the corrected absorber temperature profiles indicated that the simple linear form for equation (4.3.1) was sufficient and the use of a more complex expression was unnecessary.

Unlike the absorber temperatures, the CO_2 absorption rate was not significantly affected by the liquid phase enthalpy correction since the resulting CO_2 vapour phase profiles closely resembled those obtained with the uncorrected liquid phase enthalpies, as seen in Figure 4.3.2. The H_2S absorption rate and vapour phase profiles were similarly unaffected by the liquid phase enthalpy correction. Consequently, as observed for the regenerators, the calculated temperatures did not contribute to the deviations in the CO_2 vapour phase profiles observed in the absorbers. This suggested that a model parameter sensitive to CO_2 mass transfer was instead the cause for the observed deviations in the absorber CO_2 vapour phase profiles and the regenerator CO_2 loading profiles. The sensitivity of the absorber and regenerator column models to the key mass transfer parameters is investigated in the next section.

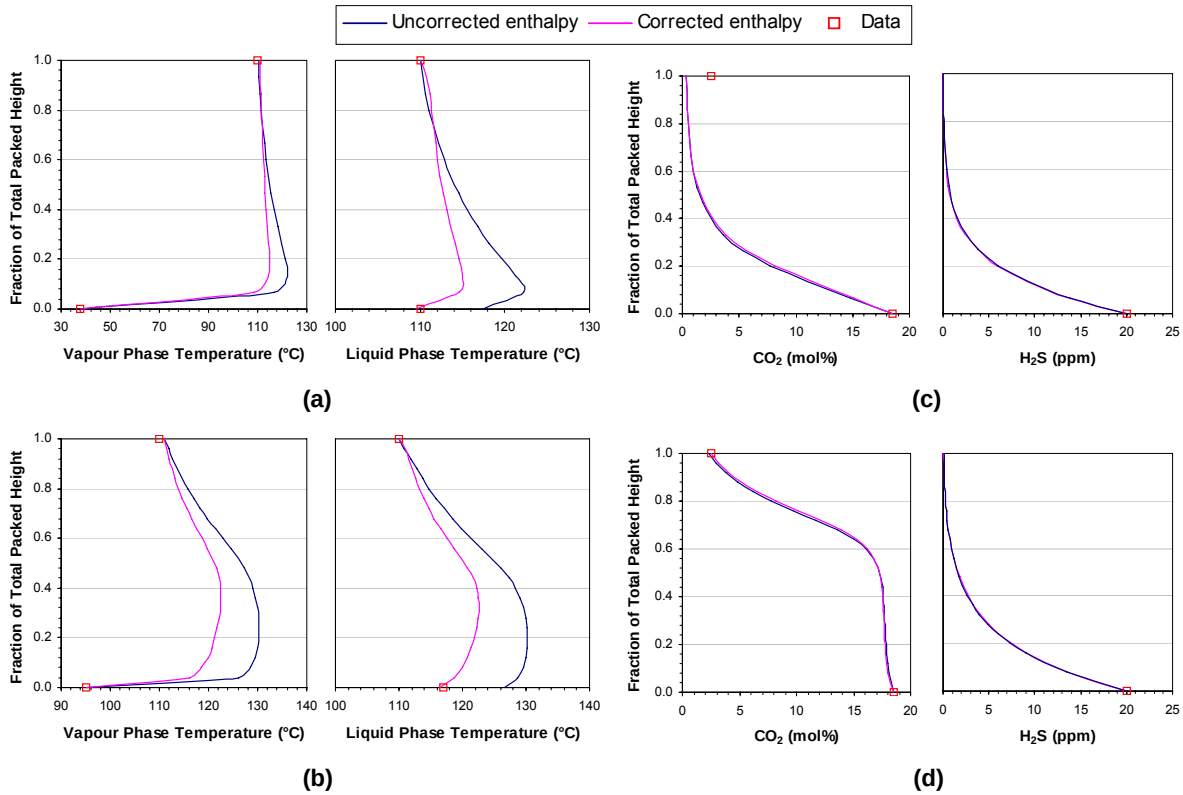

Figure 4.3.2: Effect of the liquid phase enthalpy correction on the absorber profiles. Temperature profiles for (a) CO_2 train #1 and (b) CO_2 train #7. CO_2 and H_2S vapour phase profiles for (c) CO_2 train #1 and (d) CO_2 train #7.

4.3.2 Sensitivity to Model Parameters

The four key model parameters that are sensitive to CO_2 mass transfer are the effective interfacial area a_I, the vapour phase mass transfer coefficient k_G, the liquid phase mass transfer coefficient k_L, and the reaction rate constant k_{OH^-}. These were calculated using the correlations presented by Onda and co-workers (1968ab) (equations (2.2.31) to (2.2.33)) and Astarita and co-workers (1983) (equation (2.1.3)).

To determine the variation associated with the parameter values, the above correlations were compared against the alternative mass transfer and reaction rate constant correlations given in Section 2.1.3 and Table D.2.1 in Appendix D, using the average CO_2 train phase properties. The resulting parameter values and corresponding percentage deviations are given in Table 4.3.1.

Given the wide variations in the model parameter values observed in Table 4.3.1, it was considered highly likely that the observed deviations in the column composition profiles were caused by the errors associated with calculated parameter values. To investigate the sensitivity of the two column models to the variations in these four model parameters, a series of simulation runs were performed for the absorbers and regenerators in CO_2 trains #1 and #7, in which the model parameters were changed by ±50%. The absorbers in CO_2 trains #2 to #6 were not included in the sensitivity studies since they were observed to behave quite similarly to the absorber in CO_2 train #1 from their temperature and composition profiles. The regenerators in these five trains were likewise excluded due to their similar behaviour to the regenerators in CO_2 trains #1 and #7.

To assess the sensitivity of the absorber column model to the four model parameters, the relative changes in the total CO_2 and H_2S absorption rates and the sweet gas CO_2 and H_2S content were compared, as depicted in Figure 4.3.3. From these plots, it was evident that the absorber column model was most sensitive to the effective interfacial area. The changes in the acid gas absorption rates and sweet gas content associated with the effective interfacial area were significantly greater than the corresponding changes for the reaction rate constant and the vapour and liquid phase mass transfer coefficients. These findings agree with the results presented by Schneider and Górak (2001), who performed a similar sensitivity analysis on their non-equilibrium rate-based absorber model for an amine gas treatment process.

The magnitude and direction of the changes in the sweet gas CO_2 content indicated that the predicted over-absorption of CO_2 observed in Figure 4.2.4 could be corrected by the introduction of an adjustment factor to reduce the effective interfacial area. Given the different order of magnitude for these changes for the absorbers in CO_2 trains #1 and #7, it was expected that this factor would not be constant for the seven CO_2 trains, but would instead have to be fitted for each absorber. The inclusion of the effective interfacial area adjustment factor was the second model adjustment applied to the absorber column model (the first being the liquid phase enthalpy correction term), and is discussed in the next section.

Table 4.3.1: The average variation associated with the model parameter values for the CO_2 train absorbers and regenerators. The bracketed values are the percentage deviations from the correlations used in this work.

	CO_2 Train Absorbers							CO_2 Train Regenerators						
	#1	#2	#3	#4	#5	#6	#7	#1	#2	#3	#4	#5	#6	#7
a_l (m^2/m^3)														
Onda and co-workers (1968ab) [a]	97	83	99	100	59	59	58	89	84	135	138	79	79	135
Puranik and Vogelpohl (1974)	113 (16%)	98 (18%)	121 (22%)	129 (29%)	87 (47%)	76 (47%)	79 (35%)	93 (4%)	89 (5%)	137 (2%)	144 (5%)	87 (9%)	86 (9%)	139 (3%)
Kolev (1976)	52 (-47%)	44 (-47%)	57 (-43%)	61 (-39%)	50 (-15%)	50 (-15%)	44 (-24%)	42 (-53%)	31 (-63%)	51 (-62%)	54 (-61%)	38 (-52%)	38 (-52%)	52 (-62%)
Billet and Schultes (1999)	159 (63%)	161 (94%)	174 (77%)	190 (90%)	209 (255%)	207 (252%)	178 (206%)	132 (49%)	134 (58%)	132 (-2%)	140 (2%)	142 (79%)	142 (80%)	134 (-1%)
k_{G,CO_2} (cm^2/s)														
Onda and co-workers (1968ab) [a]	0.08	0.11	0.12	0.13	0.16	0.19	0.20	2.41	2.61	1.40	1.58	2.36	2.43	1.59
Van Krevelen and Hoftijzer (1948)	0.05 (-46%)	0.05 (-57%)	0.07 (-43%)	0.07 (-42%)	0.08 (-50%)	0.10 (-49%)	0.10 (-49%)	0.86 (-64%)	0.87 (-67%)	0.67 (-52%)	0.77 (-51%)	0.89 (-62%)	0.92 (-62%)	0.78 (-51%)
Shulman and co-workers (1955)	0.28 (232%)	0.23 (112%)	0.38 (223%)	0.42 (220%)	0.34 (107%)	0.39 (104%)	0.40 (103%)	5.24 (118%)	5.03 (93%)	6.25 (348%)	7.03 (343%)	5.43 (130%)	5.56 (129%)	7.04 (342%)
k_{L,CO_2} (cm^2/s)														
Onda and co-workers (1968ab) [a]	0.20	0.20	0.23	0.26	0.39	0.40	0.36	0.10	0.11	0.09	0.10	0.13	0.13	0.09
Van Krevelen and Hoftijzer (1948)	0.14 (-28%)	0.16 (-22%)	0.17 (-28%)	0.19 (-28%)	0.30 (-23%)	0.31 (-22%)	0.29 (-21%)	0.07 (-26%)	0.08 (-24%)	0.06 (-35%)	0.07 (-35%)	0.10 (-26%)	0.10 (-27%)	0.06 (-36%)
Shulman and co-workers (1955)	0.57 (188%)	0.62 (206%)	0.64 (174%)	0.70 (165%)	0.70 (78%)	0.70 (76%)	0.64 (78%)	0.40 (290%)	0.55 (420%)	0.46 (400%)	0.49 (389%)	0.48 (260%)	0.47 (265%)	0.46 (405%)
k_{OH^-} ($\times 10^6$ $m^3/kmol \cdot s$)														
Astarita and co-workers (1983) [a]	3.4	3.4	3.8	3.9	3.8	3.8	3.5	3.4	3.4	3.7	3.7	3.8	3.8	3.7
Pohorecki and Moniuk (1988)	2.4 (-29%)	2.4 (-28%)	2.8 (-25%)	2.9 (-26%)	3.0 (-21%)	2.9 (-24%)	2.4 (-30%)	380 (-99%)	390 (-99%)	43 (-88%)	43 (-88%)	45 (-88%)	44 (-88%)	44 (-88%)

[a] These are the mass transfer and reaction rate constant correlations used in the Aspen Custom Modeler® column models.

To evaluate the sensitivity of the regenerator column model to the model parameters, the relative changes in the total CO_2 and H_2S desorption rates and the regenerated solution CO_2 and H_2S loading were compared in Figure 4.3.4. It should be noted that the similarity between the sensitivity analysis results for the regenerators in CO_2 trains #1 and #7 was not surprising since the two regenerators were expected to behave very similarly, given their temperature and CO_2 loading profiles. As for the absorber column model, the effective interfacial area was found to be the most significant model parameter for the regenerator column model.

However, in contrast to the absorber column model, the relative changes for all four model parameters were observed to be insignificant, especially those associated with the H_2S desorption rate, which had order of magnitudes around 10^{-5} to 10^{-7} and are not clearly depicted in Figure 4.3.4. Although the relative changes in the regenerated solution H_2S loading were large, the actual H_2S loading was extremely low (around the order of 10^{-13}), and therefore changes of a few orders of magnitude to the H_2S loading were still relatively inconsequential.

These insignificant relative changes indicated that an effective interfacial area adjustment factor for the regenerator column model would be inadequate for correcting the deviations observed in Figure 4.2.4 for the regenerated solution CO_2 loading. Adjustment of the steam flow to the solution reboilers was considered more appropriate, given the regenerator column model's significant sensitivity to this key operating parameter. This is illustrated in Figure 4.3.5, which compares the relative changes in the CO_2 desorption rate and regenerated solution loading for changes of ±15% to the reboiler steam flow. Consequently, unlike the absorber column model, no adjustment factors or correction terms were applied to the regenerator column model.

It should be noted from Figure 4.3.3 that the changes in the liquid phase mass transfer coefficient had a stronger effect on the CO_2 absorption rate and the sweet gas CO_2 content than the corresponding changes in the vapour phase mass transfer coefficient. In contrast, Figure 4.3.4 shows the vapour and liquid phase mass transfer coefficients having similar levels of influence on the CO_2 desorption rate and the regenerated solution CO_2 loading. This indicated that the main resistance to CO_2 mass transfer lay in the liquid phase for the CO_2 train absorbers, whereas in the regenerators, neither phase resistance dominated.

Figures 4.3.3 and 4.3.4 also indicate that H_2S mass transfer was vapour-phase limited in both the absorbers and regenerators. The vapour phase mass transfer coefficient was observed to have a stronger effect on the H_2S absorption rate and the sweet gas content compared to the liquid phase mass transfer coefficient. A similar trend for the H_2S desorption rate and the solution loading was observed for the regenerators. These results regarding the CO_2 and H_2S mass transfer limitations are in agreement with the empirical findings of Yih and Lai (1987), thereby validating the mass transfer relations utilised in this work.

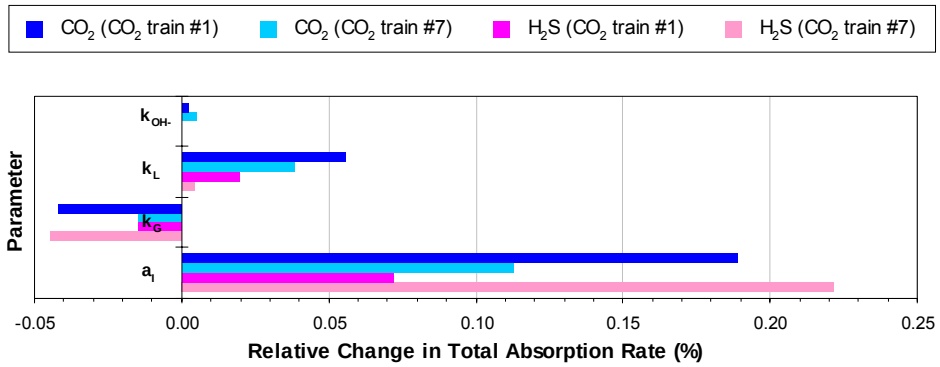

(a)

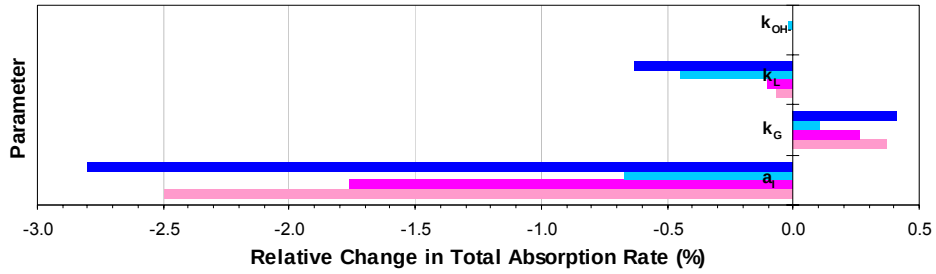

(b)

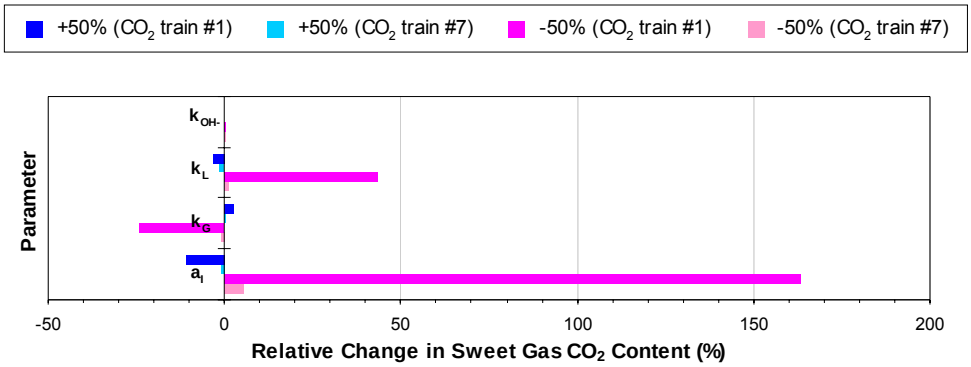

(c)

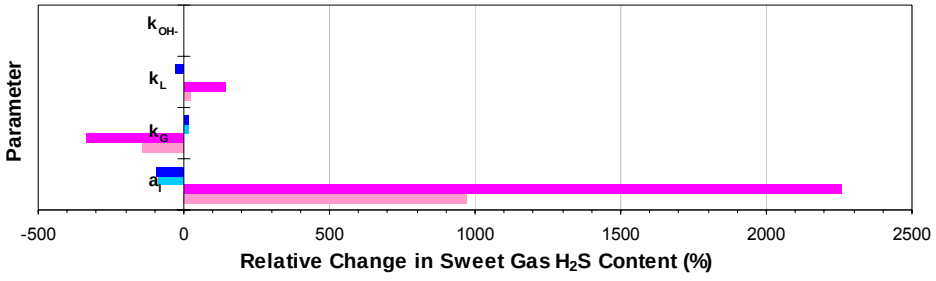

(d)

Figure 4.3.3: Sensitivity analysis results for the absorber column model (Model 2). Relative changes in the total CO_2 and H_2S absorption rates for the CO_2 trains #1 and #7 after (a) a 50% increase and (b) a 50% decrease in the model parameters, and the corresponding changes in (c) the sweet gas CO_2 content and (d) the sweet gas H_2S content.

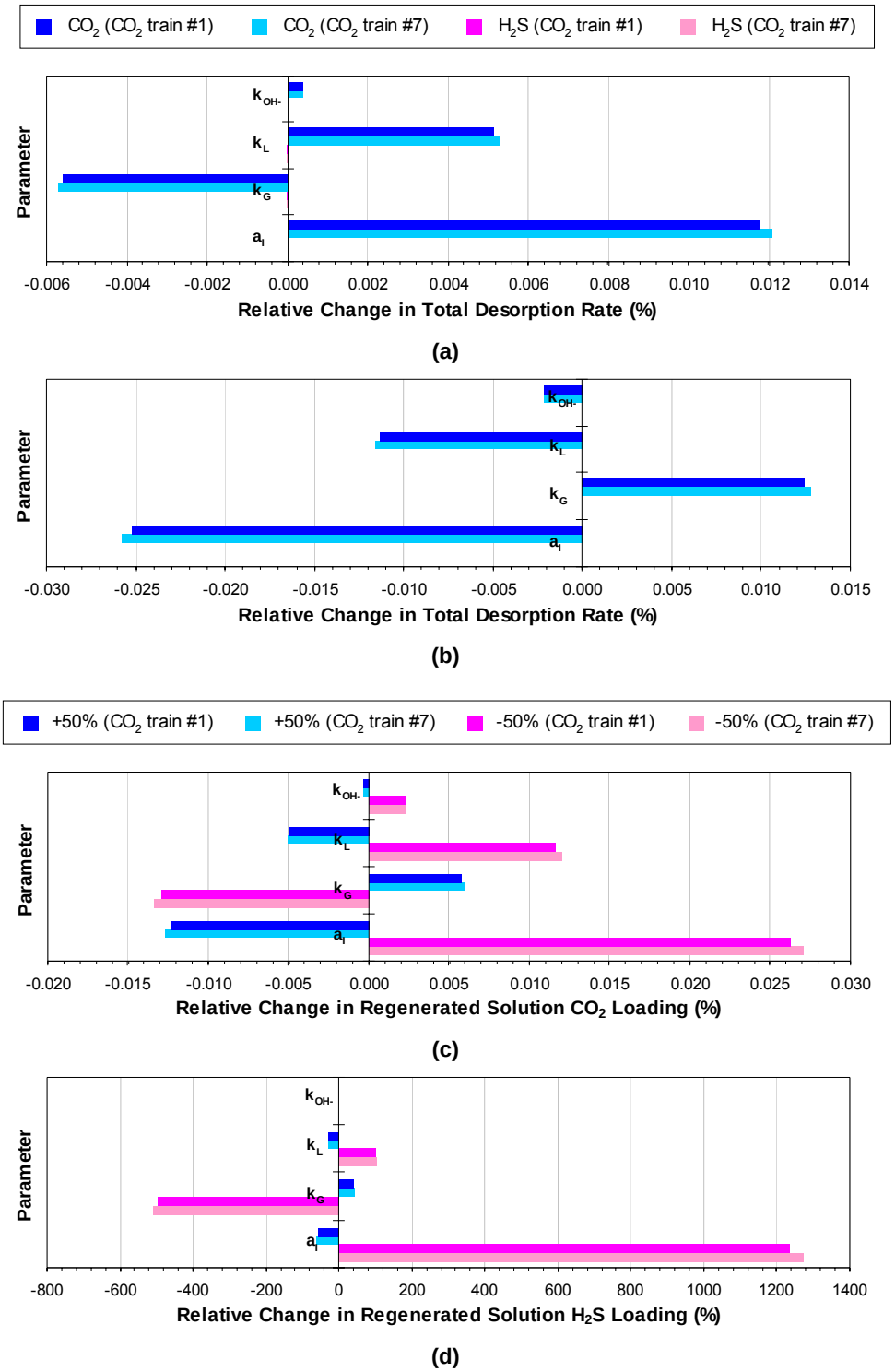

Figure 4.3.4: Sensitivity analysis results for the regenerator column model (Model 2). Relative changes in the total CO_2 and H_2S desorption rates for the CO_2 trains #1 and #7 after (a) a 50% increase and (b) a 50% decrease in the model parameters, and the corresponding changes in (c) the regenerated solution CO_2 loading and (d) the regenerated solution H_2S loading.

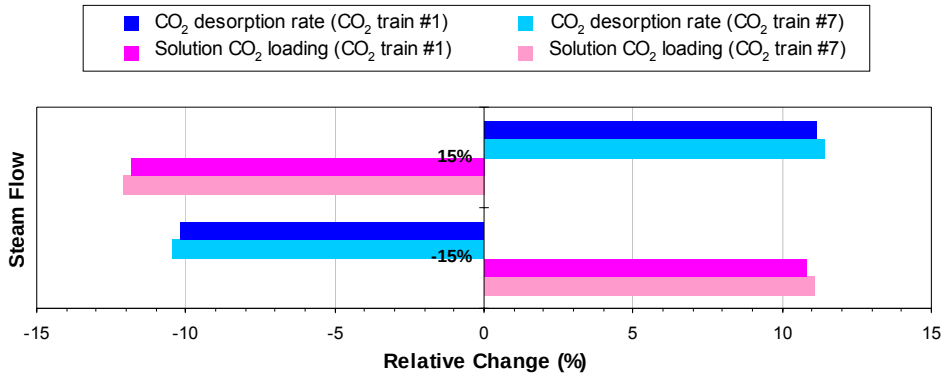

Figure 4.3.5: Effect of the solution reboiler steam flow on the regenerator column model (Model 2). Relative changes in the total CO_2 desorption rate and the regenerated solution CO_2 loading for changes of ±15% to the steam flow.

4.3.3 Effective Interfacial Area Adjustment Factor

In the preceding sections, it was determined that a model parameter sensitive to CO_2 mass transfer was the most likely cause for the sweet gas CO_2 content deviations observed in Figure 4.2.4. Of these model parameters, the effective interfacial area was identified as having the most significant effect on the rate of CO_2 mass transfer for the absorber column model.

Consequently, it was decided to apply an adjustment factor to the effective interfacial area in order to fit the absorber column model to the first set of CO_2 train data in Table 2.1.2. This follows a similar approach taken by Mayer (2002) to correct his non-equilibrium rate-based absorber model for an amine gas treatment process. Like Mayer (2002), who selected his effective interfacial area adjustment factor such that his model more closely agreed with his experimental results, the adjustment factors were adjusted iteratively in this work until optimal agreement was achieved between the predicted sweet gas CO_2 content and the data values.

Table 4.3.2 lists the individual adjustment factors obtained for each absorber, and compares the deviations between the predicted and data values for the sweet gas CO_2 content for the adjusted and unadjusted absorber column models. The effect of the adjustment factor on the CO_2 and H_2S vapour phase profiles for the absorbers in CO_2 trains #1 and #7 is shown in Figure 4.3.6. The corresponding vapour profiles for the other five CO_2 trains are included in Appendix D as Figure D.2.3.

A marked improvement in the absorber column model performance was evident for the first six CO_2 trains through the inclusion of the adjustment factors. A less obvious improvement in the predicted sweet gas CO_2 content was observed for CO_2 train #7 due to the smaller deviation between the unadjusted model's results and the data. However, notable changes in the shape of CO_2 and H_2S vapour phase profiles were observed after the inclusion of the adjustment factor.

Table 4.3.2: Effective interfacial area adjustment factor values and their effect on the CO_2 train absorbers.

Absorber	Effective Interfacial Area Adjustment Factor	Sweet Gas CO_2 Content Deviation (%)	
		Unadjusted Model	Adjusted Model
#1	0.300	84.95	0.21
#2	0.218	86.47	0.31
#3	0.312	83.34	0.14
#4	0.257	85.00	-0.05
#5	0.394	80.33	0.04
#6	0.295	84.74	-0.31
#7	0.525	4.27	-0.08

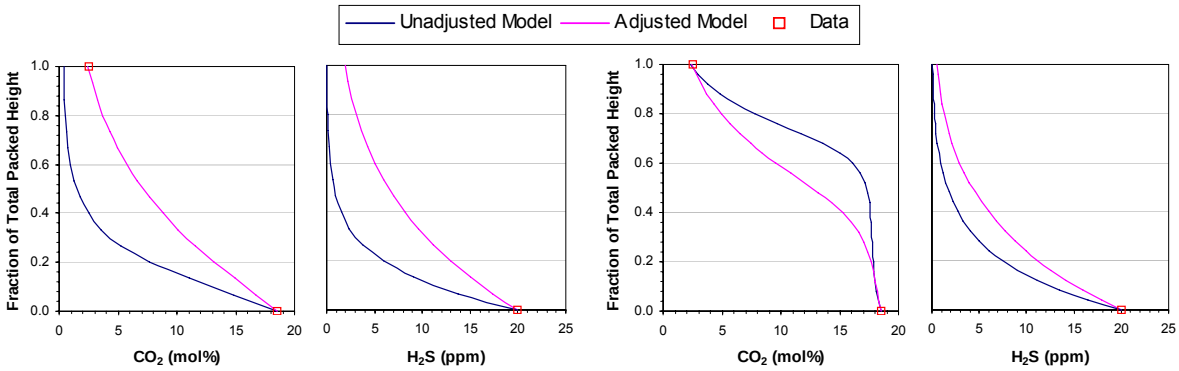

Figure 4.3.6: Effect of the effective interfacial area adjustment factor on the absorber CO_2 and H_2S vapour phase profiles. (a) CO_2 train #1. (b) CO_2 train #7.

4.4 CO_2 Train Model Validation

Using the model adjustments discussed in the previous sections, simplified models of the Santos Moomba CO_2 trains were constructed in Aspen Custom Modeler®, and their performances were compared against the two sets of typical operating data in Table 2.1.2. It should be noted that the first data set was used in the development of the absorber and regenerator column models, while the second set of data was used solely for model validation purposes.

Each CO_2 train model was configured according to the flow sheets given in Figure 4.4.1, which are simplified versions of the detailed process flow diagrams in Figure 2.1.2. The only notable difference between the models that is not shown in the diagram below is the number of packed beds in the absorber columns, which varied between one and three, depending on the CO_2 train.

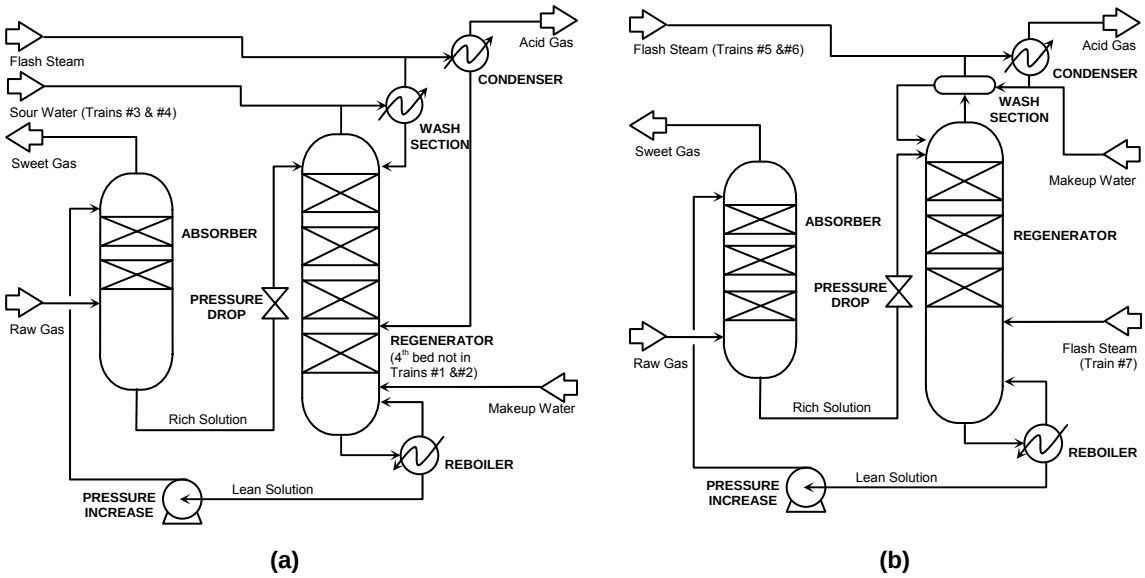

Figure 4.4.1: Simplified CO_2 train configurations for the Aspen Custom Modeler® simulations. (a) CO_2 trains #1 to #4. (b) CO_2 trains #5 to #7.

The resulting vapour and liquid phase composition profiles for the absorber and regenerator columns in CO_2 trains #1 and #7 are given in Figures 4.4.2 and 4.4.3, and the column temperature profiles are shown in Figure 4.4.4. The corresponding profiles for the other five CO_2 trains are very similar to those for CO_2 train #1, and are included as Figures D.3.1 to D.3.6 in Appendix D. Values for the operating parameters calculated by the CO_2 train models are provided in Tables 4.4.1 and 4.4.2, along with their percentage deviation from the data values listed in Table 2.1.2.

The absorber composition profiles in Figures 4.4.2 and 4.4.3 showed the CO_2 and H_2S vapour phase concentrations decreasing with the vapour flow up the columns while the acid gas loading in the liquid phase increased down the columns. For CO_2 trains #1 to #6, the CO_2 and H_2S vapour phase profiles indicated a gradual reduction in the vapour phase acid gas content along the absorbers, with the acid

gas content decreasing slightly more rapidly towards the bottom of the columns. This corresponded well with the liquid phase loading profiles, which showed the acid gas loading increasing at a marginally faster rate near the bottom of the absorbers.

For CO_2 train #7, the absorber H_2S vapour and liquid phase profiles resembled those for the other six CO_2 trains. In contrast, the absorber CO_2 profiles differed quite markedly. In the top and central regions of the column, the CO_2 profiles followed a similar trend to the profiles for the other six CO_2 trains. However, in the bottom section, there was a sharp decline in the rates at which the vapour phase CO_2 content decreased and the liquid phase CO_2 loading increased, giving rise to sigmoid curve-like profiles. This phenomenon was caused by the very high CO_2 loading in the lower part of the absorber (compared to the other six absorbers), which significantly reduced the capacity of the solution to further absorb CO_2 from the vapour phase in this region. The rich solution CO_2 loading was much higher for CO_2 train #7 than for the other six CO_2 trains due to its much larger CO_2 removal capacity per unit volume of solution, as indicated by the greater raw gas to lean solution flow ratio to the absorber.

In contrast to the absorbers, the CO_2 and H_2S vapour phase concentrations in the regenerators increased with the vapour flow up the columns while the acid gas loading in the liquid phase decreased down the columns. At the top of the regenerator columns, the condensed steam leaving the wash sections absorbed some of the flashed-off CO_2 entering the regenerators, resulting in a slight increase in the liquid phase CO_2 loading and a corresponding decrease in the vapour phase CO_2 concentration.

From a comparison of the liquid phase CO_2 and H_2S loading profiles in Figures 4.4.2 and 4.4.3, it was evident that a substantial portion of the acid gases absorbed in the rich solution leaving the absorbers was flashed off during the depressurisation between the absorber and regenerator columns. For all seven CO_2 trains, the remaining H_2S in the liquid phase was rapidly removed near the top of the regenerators, as indicated by the sharp increase in vapour phase H_2S content and the corresponding decrease in liquid phase H_2S loading in this region. The opposite behaviour was observed for the removal of CO_2, in that the vapour phase CO_2 content rapidly increased near the bottom of the regenerators while the liquid phase CO_2 loading decreased in this region. This indicated that the removal of the residual CO_2 in the solution was greatly facilitated by contact with the hot stripping steam generated from the solution reboilers.

The absorber temperature profiles provided in Figure 4.4.4 showed distinctive bulges due to the solution temperature rise from the exothermic absorption reactions and the temperature drop upon contact between the hot solution and the cooler raw gas near the bottom of the columns. A comparison of the liquid phase temperatures at the bottom of the absorbers and at the top of the regenerators indicated that the depressurisation between the two columns was accompanied by a temperature drop between 7 to 15°C, depending on the rich solution temperature.

In the regenerators, the solution temperature rapidly increased towards the bottom of the columns due to contact between the solution and the hot stripping steam from the solution reboilers. Within the regenerator columns, the vapour phase temperature profiles were observed to closely agree with the liquid phase profiles. Above the regenerator columns, the vapour temperatures decreased up through the wash sections, reaching a minimum at the condensers.

Good agreement was observed between the model results and both sets of plant data for all seven CO_2 trains. The calculated and data values for most of the operating parameters were within ±5%. Larger deviations of up to ±13.5% were observed for the reboiler steam flows, which had to be adjusted to give the desired regenerated solution CO_2 loading.

In the case of parameters for which only a maximum value was specified in Table 2.1.2 (i.e. the sweet gas H_2S content, the rich solution H_2S loading and the column pressure drops), the model calculated values were found to be within the given range. Percentage deviations were not determined for the lean solution H_2S loading since the data values were zero. However, the calculated values were of the order of 10^{-12} to 10^{-19} and were therefore viewed to be effectively zero.

The most significant deviations between the model results and the plant data were associated with the acid gas temperature for CO_2 train #4. For the two sets of plant data, the predicted temperatures were approximately 30% lower than the data values. However, these deviations were considered to be acceptable since the data values were unexpectedly high. According to the CO_2 train technical manual (Santos Ltd, 1998), the temperature of the acid gas leaving the regenerator wash section in CO_2 train #4 is typically around 80°C, which corresponds well with the model results.

The agreement between the model results and both sets of plant data was regarded as sufficiently close that no further model tuning was required to improve the model performances. The CO_2 train models developed in Aspen Custom Modeler® were therefore considered suitable for developing corresponding CO_2 train models in HYSYS® according to the novel approach described in Section 2.4. To obtain the data required to develop the HYSYS® models, a series of simulations were performed to investigate the effect of various operating parameters on the performance of the Aspen Custom Modeler® process models. These parametric studies are discussed in the next chapter.

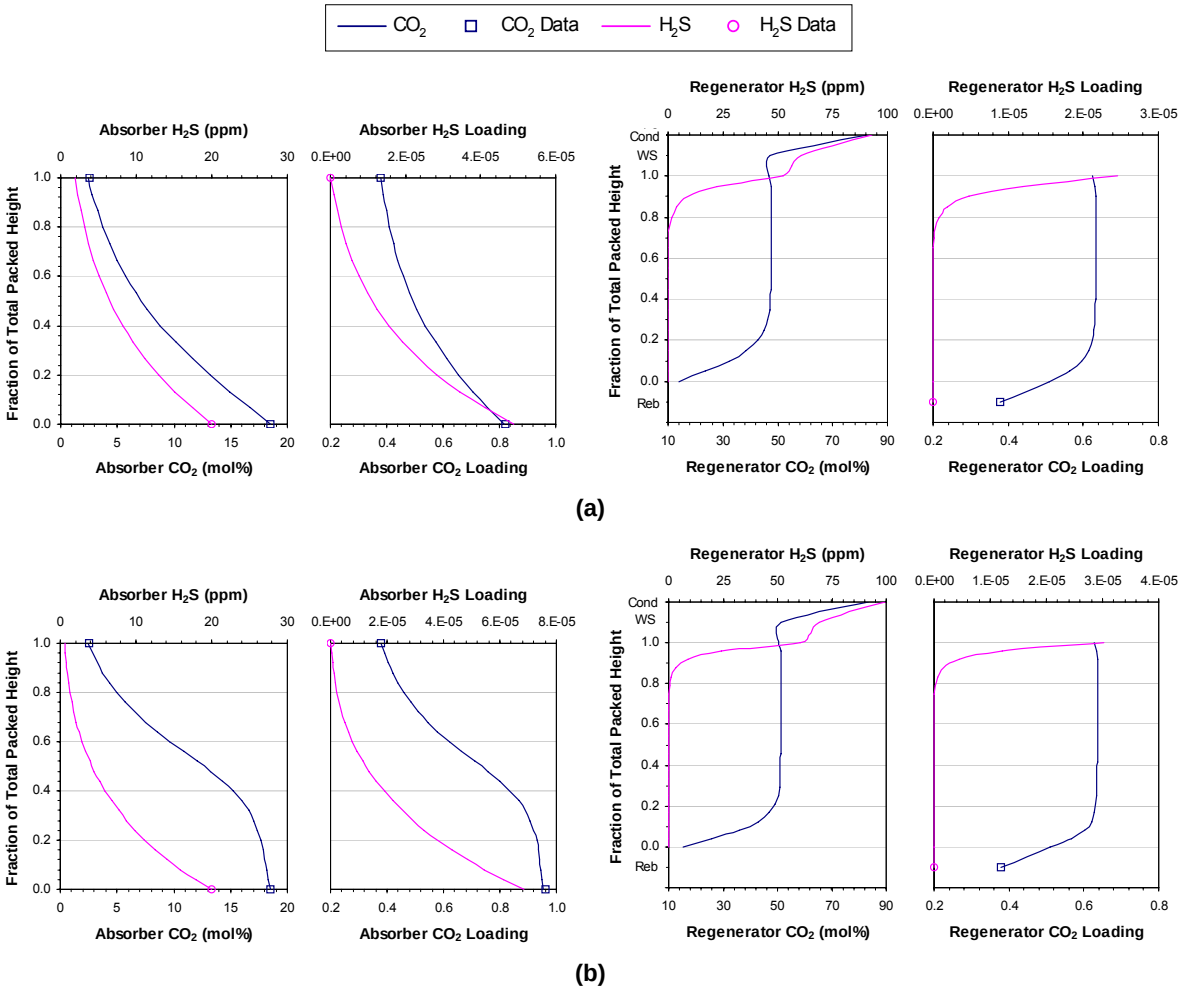

Figure 4.4.2: CO_2 and H_2S vapour and liquid phase profiles for the first set of plant data. (a) CO_2 train #1. (b) CO_2 train #7. (Cond = condenser, WS = wash section, Reb = reboiler)

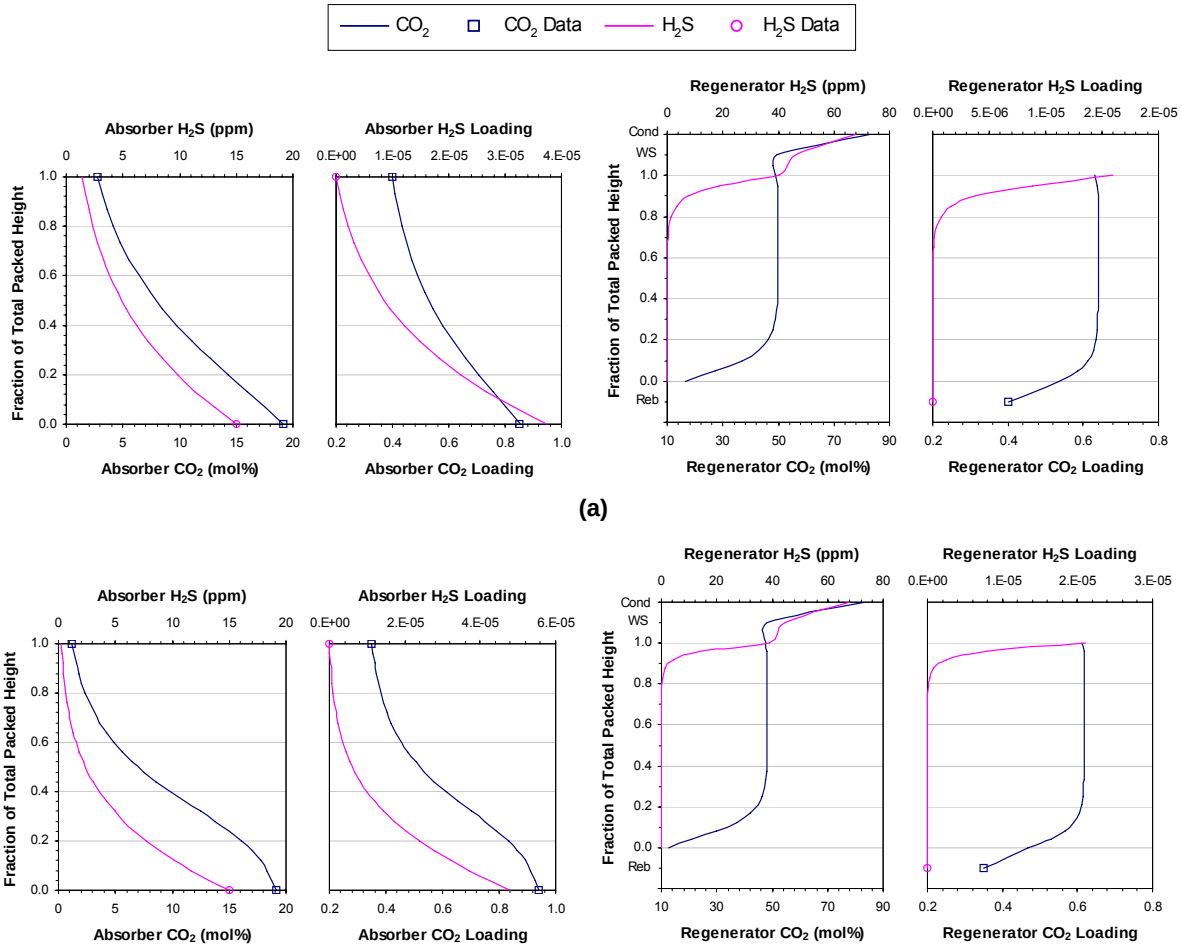

Figure 4.4.3: CO_2 and H_2S vapour and liquid phase profiles for the second set of plant data. (a) CO_2 train #1. (b) CO_2 train #7. (Cond = condenser, WS = wash section, Reb = reboiler)

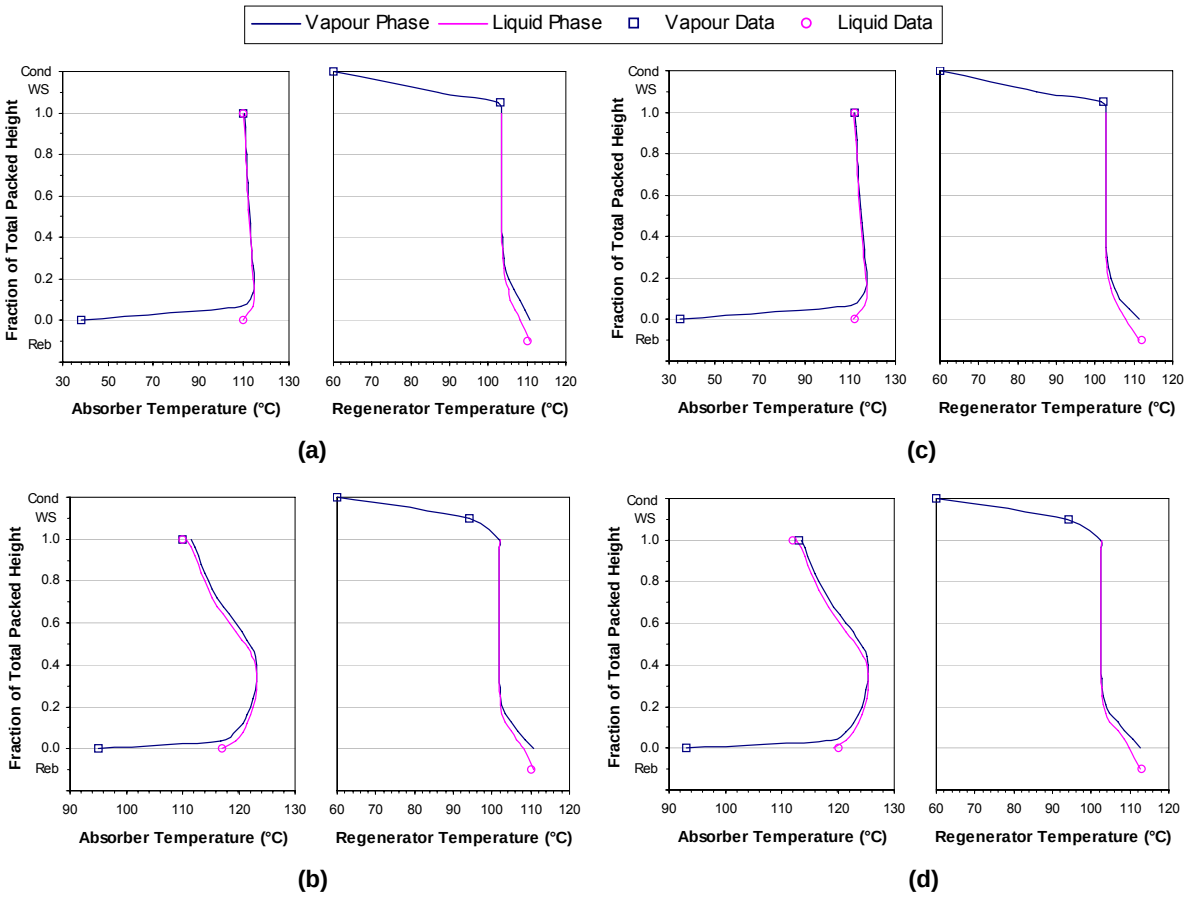

Figure 4.4.4: Vapour and liquid phase temperature profiles for the two sets of plant data. (a) CO_2 train #1 and (b) CO_2 train #7 profiles for the first set of data. (c) CO_2 train #1 and (d) CO_2 train #7 profiles for the second set of data. (Cond = condenser, WS = wash section, Reb = reboiler)

Table 4.4.1: CO_2 train simulation results for the first set of plant data in Table 2.1.2. The bracketed values are the percentage deviations from the data.

CO_2 Train	#1	#2	#3	#4	#5	#6	#7
Sweet Gas							
mol% CO_2 [a]	2.49 (-0.4%)	2.49 (-0.4%)	2.51 (0.4%)	2.51 (0.4%)	2.51 (0.4%)	2.50 (0.0%)	2.53 (1.2%)
ppm H_2S	1.91 (- [f])	2.03 (- [f])	1.70 (- [f])	1.82 (- [f])	2.00 (- [f])	1.83 (- [f])	0.58 (- [f])
Temperature (°C)	110.8 (0.7%)	110.7 (0.6%)	110.9 (0.8%)	110.9 (0.8%)	110.7 (0.6%)	110.9 (0.8%)	110.9 (0.8%)
Acid Gas							
CO_2 (10^6 sm^3/d) [b]	0.319 (-0.3%)	0.269 (-0.4%)	0.478 (-0.4%)	0.548 (-0.4%)	0.548 (-0.4%)	0.667 (-0.4%)	0.906 (-0.4%)
Temperature (°C) [c]	102.3 (-0.7%)	103.6 (0.6%)	79.1 (-1.1%)	76.3 (-25.9%)	94.5 (-0.5%)	94.4 (0.4%)	93.9 (-0.1%)
Lean Solution							
CO_2 loading [d]	0.380 (0.0%)	0.380 (0.0%)	0.380 (0.0%)	0.380 (0.0%)	0.380 (0.0%)	0.380 (0.0%)	0.380 (0.0%)
H_2S loading ($\times 10^{-16}$) [d]	278.5 (- [g])	30.1 (- [g])	2.2 (- [g])	2.2 (- [g])	3.1 (- [g])	0.9 (- [g])	0.9 (- [g])
wt% K_2CO_3 [e]	27.0 (0.0%)	27.0 (0.0%)	30.0 (0.0%)	30.0 (0.0%)	30.0 (0.0%)	30.0 (0.0%)	30.0 (0.0%)
Flow (m^3/h)	550.0 (0.0%)	550.0 (0.0%)	670.0 (0.0%)	812.0 (0.0%)	1000.0 (0.0%)	1000.0 (0.0%)	1068.0 (0.0%)
Temperature (°C)	110.6 (0.5%)	110.5 (0.5%)	110.7 (0.6%)	110.7 (0.6%)	110.7 (0.6%)	110.7 (0.6%)	110.7 (0.6%)
Rich Solution							
CO_2 loading [d]	0.815 (-0.6%)	0.748 (-0.3%)	0.864 (0.5%)	0.837 (-0.4%)	0.751 (0.1%)	0.832 (0.2%)	0.955 (-0.5%)
H_2S loading ($\times 10^{-5}$) [d]	4.9 (- [f])	4.1 (- [f])	5.5 (- [f])	5.2 (- [f])	4.2 (- [f])	5.1 (- [f])	6.8 (- [f])
Flow (m^3/h)	569.5 (-0.1%)	566.7 (-0.1%)	699.0 (-0.1%)	845.3 (0.0%)	1033.6 (0.0%)	1040.7 (0.1%)	1122.4 (0.0%)
Temperature (°C)	109.7 (-0.5%)	109.9 (-0.1%)	118.4 (1.2%)	118.1 (0.9%)	117.0 (0.0%)	118.1 (0.9%)	117.1 (0.1%)
Makeup Water [h]							
Flow (m^3/h)	1.27 (- [f])	0.96 (- [f])	2.39 (- [f])	2.66 (- [f])	2.39 (- [f])	3.22 (- [f])	5.25 (- [f])
Absorber							
Pressure drop (bar)	0.04 (- [f])	0.04 (- [f])	0.05 (- [f])	0.06 (- [f])	0.05 (- [f])	0.15 (- [f])	0.14 (- [f])
Regenerator							
Pressure drop (bar)	0.01 (- [f])	0.01 (- [f])	0.02 (- [f])	0.03 (- [f])	0.01 (- [f])	0.02 (- [f])	0.02 (- [f])
Solution Reboiler							
Steam flow (t/h)	30.6 (5.5%)	27.7 (13.5%)	36.5 (4.9%)	42.9 (1.4%)	47.3 (6.8%)	52.5 (6.5%)	60.3 (-7.1%)

[a] This refers to the CO_2 content in the dry gas. [b] sm^3/d refers to m^3/d at standard conditions (dry gas at 15°C and 1 atm). [c] This is the vapour temperature entering the regenerator wash sections in CO_2 trains #1 and #2 and leaving the wash sections in trains #3 to #7. [d] The CO_2 and H_2S loading refer to the moles of CO_2 and H_2S per equivalent mole of K_2CO_3 in the solution. The equivalent moles of K_2CO_3 are defined as the total number of moles of K_2CO_3 in the solution if all the $KHCO_3$, KHS and K_2S in the solution are converted back into K_2CO_3. [e] This refers to the equivalent weight percent of K_2CO_3 in the solution. [f] No percentage deviation was calculated as the corresponding data value was not given. [g] No percentage deviation was calculated as the data value was zero. [h] Includes the sour water recovered from the saturated sweet gas.

Table 4.4.2: CO_2 train simulation results for the second set of plant data in Table 2.1.2. The bracketed values are the percentage deviations from the data.

CO_2 Train	#1	#2	#3	#4	#5	#6	#7
Sweet Gas							
mol% CO_2 [a]	2.79 (-0.4%)	2.76 (-1.4%)	2.93 (1.0%)	2.95 (1.7%)	3.14 (1.3%)	2.49 (-0.4%)	1.22 (1.7%)
ppm H_2S	1.45 (- [f])	1.54 (- [f])	1.27 (- [f])	1.36 (- [f])	1.52 (- [f])	1.34 (- [f])	0.27 (- [f])
Temperature (°C)	112.2 (0.2%)	112.1 (0.1%)	112.5 (-0.4%)	112.4 (0.4%)	113.1 (1.0%)	113.5 (0.4%)	113.6 (0.5%)
Acid Gas							
CO_2 (10^6 sm^3/d) [b]	0.303 (1.0%)	0.261 (0.4%)	0.466 (-0.9%)	0.531 (0.2%)	0.539 (-0.2%)	0.681 (0.1%)	0.827 (-0.4%)
Temperature (°C) [c]	101.6 (-0.4%)	103.1 (-0.1%)	74.6 (-0.5%)	73.3 (-28.8%)	94.6 (-0.4%)	94.1 (0.1%)	94.3 (0.3%)
Lean Solution							
CO_2 loading [d]	0.400 (0.0%)	0.400 (0.0%)	0.400 (0.0%)	0.400 (0.0%)	0.440 (0.0%)	0.350 (0.0%)	0.350 (0.0%)
H_2S loading ($\times 10^{-16}$) [d]	1013.3 (- [g])	177.0 (- [g])	27.7 (- [g])	47.9 (- [g])	26759.0 (- [g])	0.005 (- [g])	0.021 (- [g])
wt% K_2CO_3 [e]	28.0 (0.0%)	28.0 (0.0%)	30.0 (0.0%)	29.0 (0.0%)	30.0 (0.0%)	31.0 (0.0%)	30.0 (0.0%)
Flow (m^3/h)	481.0 (0.0%)	475.0 (0.0%)	638.0 (0.0%)	758.0 (0.0%)	923.0 (0.0%)	940.0 (0.0%)	946.0 (0.0%)
Temperature (°C)	111.4 (-0.5%)	111.3 (0.6%)	111.8 (-0.3%)	111.7 (-0.3%)	112.5 (0.4%)	112.9 (-0.1%)	112.6 (0.5%)
Rich Solution							
CO_2 loading [d]	0.857 (0.8%)	0.799 (-0.1%)	0.896 (0.7%)	0.891 (0.1%)	0.838 (-0.2%)	0.825 (0.6%)	0.941 (0.1%)
H_2S loading ($\times 10^{-5}$) [d]	3.7 (- [f])	3.2 (- [f])	4.1 (- [f])	4.1 (- [f])	3.3 (- [f])	3.9 (- [f])	4.8 (- [f])
Flow (m^3/h)	499.4 (0.1%)	491.0 (0.2%)	666.1 (-0.1%)	790.0 (0.1%)	955.8 (0.1%)	981.4 (0.1%)	995.9 (0.1%)
Temperature (°C)	111.2 (-0.7%)	111.9 (-0.1%)	119.6 (1.4%)	119.2 (0.2%)	118.9 (0.8%)	120.5 (0.4%)	119.1 (-0.8%)
Makeup Water [h]							
Flow (m^3/h)	1.35 (- [f])	1.10 (- [f])	2.66 (- [f])	3.05 (- [f])	3.15 (- [f])	3.37 (- [f])	4.58 (- [f])
Absorber							
Pressure drop (bar)	0.04 (- [f])	0.04 (- [f])	0.05 (- [f])	0.06 (- [f])	0.05 (- [f])	0.15 (- [f])	0.13 (- [f])
Regenerator							
Pressure drop (bar)	0.01 (- [f])	0.01 (- [f])	0.01 (- [f])	0.02 (- [f])	0.01 (- [f])	0.02 (- [f])	0.02 (- [f])
Solution Reboiler							
Steam flow (t/h)	26.2 (11.0%)	23.9 (10.6%)	32.1 (-8.3%)	37.0 (2.8%)	35.1 (-5.4%)	53.6 (8.1%)	55.2 (1.7%)

[a] This refers to the CO_2 content in the dry gas. [b] sm^3/d refers to m^3/d at standard conditions (dry gas at 15°C and 1 atm). [c] This is the vapour temperature entering the regenerator wash sections in CO_2 trains #1 and #2 and leaving the wash sections in trains #3 to #7. [d] The CO_2 and H_2S loading refer to the moles of CO_2 and H_2S per equivalent mole of K_2CO_3 in the solution. The equivalent moles of K_2CO_3 are defined as the total number of moles of K_2CO_3 in the solution if all the $KHCO_3$, KHS and K_2S in the solution are converted back into K_2CO_3. [e] This refers to the equivalent weight percent of K_2CO_3 in the solution. [f] No percentage deviation was calculated as the corresponding data value was not given. [g] No percentage deviation was calculated as the data value was zero. [h] Includes the sour water recovered from the saturated sweet gas.

4.5 Summary

In summary, the development of a new non-equilibrium rate-based model for the hot potassium carbonate process was continued in this chapter. The relevant model equations were presented and their implementation in Aspen Custom Modeler® and application to the Moomba CO_2 trains were discussed.

Three alternative stage models were developed for the absorber and regenerator columns: an equilibrium model with chemical equilibrium (Model 1), a non-equilibrium rate-based model with enhancement factors (Model 2), and a non-equilibrium rate-based model with reaction rate expressions (Model 3). Following a series of preliminary Aspen Custom Modeler® simulations, Model 2 was identified as the optimal stage model for this work. The results produced by Model 2 were in close agreement with those for the more complex and computationally demanding Model 3. This indicated that the inclusion of the rigorous reaction rate expressions provided minimal improvement compared to the enhancement factor approach.

Significant deviations were observed between some of the absorber column model predictions and plant data from the Santos Moomba Processing Facility. An enthalpy correction term was developed to correct the absorber temperature profile, while the rate of CO_2 absorption was corrected via an adjustment factor for the absorber effective interfacial area. This parameter was identified as having the most significant effect on the CO_2 mass transfer rate by a sensitivity analysis of the various model parameters. In contrast, no model adjustments were required for the regenerator column model.

Using the above column models, along with simple models of the various ancillary units, process models of the CO_2 trains were developed in Aspen Custom Modeler®, based on simplified configurations for the CO_2 trains. The results from these models were found to agree well with the plant data used in the model development process, as expected. Good agreement was also observed with an independent set of data, thereby validating the Aspen Custom Modeler® process models.

The following chapter examines the effect of various operating parameters on the performance of the Aspen Custom Modeler® process models, in order to develop corresponding CO_2 train models in the HYSYS® simulation environment.

CHAPTER 5

ASPEN CUSTOM MODELER® CO_2 REMOVAL TRAIN PARAMETRIC STUDIES

The performance of the Santos Moomba CO_2 trains is influenced by many key factors. While some are constraints set by the design of the CO_2 trains, others are operating parameters that can vary or be manipulated to some degree. An investigation into the effects of the main operating parameters on the performance of the CO_2 trains was therefore considered vital to the development of reliable process models of the CO_2 trains in HYSYS®.

Following their successful development and validation in the previous chapter, the Aspen Custom Modeler® CO_2 train process models are studied in this chapter to determine the response of the CO_2 trains to changes in several key operating parameters. The results of a series of simulations, in which a specific operating parameter was adjusted while all other parameters were held constant, are presented and discussed. Particular attention is given to the effects of the operating parameters on the absorption and desorption of CO_2 in the CO_2 trains.

The parametric studies described in this chapter represent the final part of the Aspen Custom Modeler® simulation work performed for this work.

5.1 Solution Operating Parameters

Unsurprisingly, the effectiveness of the Moomba CO_2 trains is affected by the properties of the potassium carbonate solution as it is integral to the function of the CO_2 trains. This section investigates the influence of three key operating parameters associated with the potassium carbonate solution: flow rate, strength and acid gas loading.

5.1.1 Solution Flow Rate

The solution flow rate establishes the contact time between the vapour and liquid phases in the column packing, as well as determining the quantity of solution available for CO_2 and H_2S absorption in the absorbers and the quantity of rich solution exposed to the stripping steam in the regenerators.

The effect of the solution flow rate on the performance of the CO_2 trains is illustrated in Figure 5.1.1. The first two plots show the sweet gas CO_2 and H_2S content decreasing with increasing lean solution flow to the absorbers. This enhancement of the acid gas absorption processes resulted from the greater volumes of solution available per unit volume of acid gas. Although the increased flow rate also reduced the length of contact between the two phases, this did not have a noticeable detrimental effect on the gas absorption due to the rapid nature of acid gas mass transfer processes.

The differences observed in Chapter 4 between the performance of the absorbers in CO_2 trains #1 to #6 and the absorber in CO_2 train #7 were highlighted in Figure 5.1.1. The lean solution flow rate had a significantly greater effect on the sweet gas CO_2 content for CO_2 train #7, which also had a considerably lower sweet gas H_2S content than the other CO_2 trains. These trends in the sweet gas composition for CO_2 train #7 were also observed for the other operating parameters studied in this chapter. The two phenomena were attributed to the larger acid gas removal capacity of CO_2 train #7, which had its absorber operating far closer to the solution capacity limit, as indicated by the extremely high CO_2 loading in the rich solution. As a result, the performance of the CO_2 train #7 absorber was more sensitive to changes in the operating parameters.

The last plot of Figure 5.1.1 depicts the relationship between the rich solution flow rate and the CO_2 loading of the regenerated solution. Increasing the rich solution flow rate was found to increase the level of CO_2 remaining in the regenerated solution. This reduction in the extent of solution regeneration resulted from the lower volumes of stripping steam produced per unit volume of solution for the given reboiler duty. As for the absorbers, increasing the rich solution flow rate also shortened the phase contact time. However, this was expected to have a relatively insignificant effect due to the rapid nature of acid gas desorption.

A similar trend was observed between the regenerated solution H_2S loading and the rich solution flow rate. However, this was considered inconsequential due to the H_2S loading being of a very low order

of magnitude (between 10^{-10} and 10^{-22}). The H_2S loading therefore remained effectively zero despite spanning several orders of magnitude over the examined range of rich solution flow rates.

Although a wide range of solution flow rates have been included in Figure 5.1.1, it should be noted that during normal operation, the solution flow rates to the absorbers are usually maintained at a minimum of 90% of the first set of flow rates given in Table 2.1.2 (Santos Ltd, 1998). This operating constraint ensures optimal wetting of the absorber packing, which maximises the effective interfacial area between the vapour and liquid phases and hence, the mass transfer between the two phases. Keeping the solution flow rates above this minimum level also prevents corrosion of the absorber walls by ensuring they are adequately wetted.

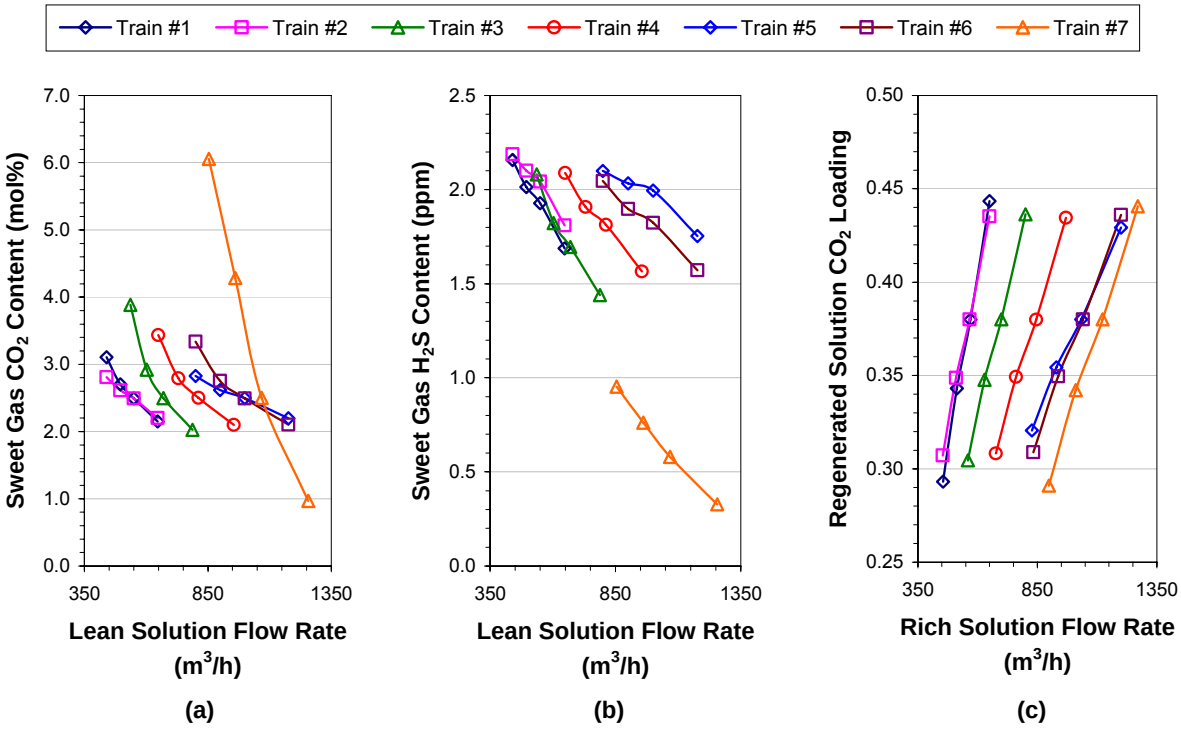

Figure 5.1.1: Effect of the solution flow rate on the performance of the CO_2 trains. The influence of the lean solution on (a) the sweet gas CO_2 content and (b) the sweet gas H_2S content; and the influence of the rich solution flow rate on (c) the regenerated solution CO_2 loading.

5.1.2 Solution Strength

As alluded to in the previous section, the performance of the CO_2 trains is limited by the capacity of the potassium carbonate solution to absorb acid gas. This capacity is dictated by two properties, one of which is the solution strength. The solution strength represents the total K_2CO_3 content of the solution and is usually expressed as the equivalent weight percent of K_2CO_3. This quantity is calculated by converting all the $KHCO_3$, KHS and K_2S present in the solution back into K_2CO_3.

The sensitivity of the performance of the CO_2 trains to the solution strength is presented in Figure 5.1.2. The first two plots show the concentrations of CO_2 and H_2S in the sweet gas decreasing with

increasing lean solution strength. This enhancement of the acid gas absorption was due to the greater solution absorption capacity arising from the higher total K_2CO_3 content of the solution and therefore, larger quantities of K_2CO_3 for reaction with CO_2 and H_2S. However, the ensuing higher levels of acid gas in the rich solution reduced the extent of solution regeneration for the given reboiler duty, and thereby increased the acid gas loading in the regenerated solution, as illustrated in the third plot of Figure 5.1.2. A similar relationship between the rich solution strength and the H_2S loading of the regenerated solution was also observed, but was regarded as insignificant since the H_2S loading remained essentially zero over the examined range of solution strengths.

It should be noted that the likelihood of solution crystallisation increases with solution strength. For this reason, the solution strength for the CO_2 trains is usually maintained between 25 and 30 wt% K_2CO_3 (Santos Ltd, 1998).

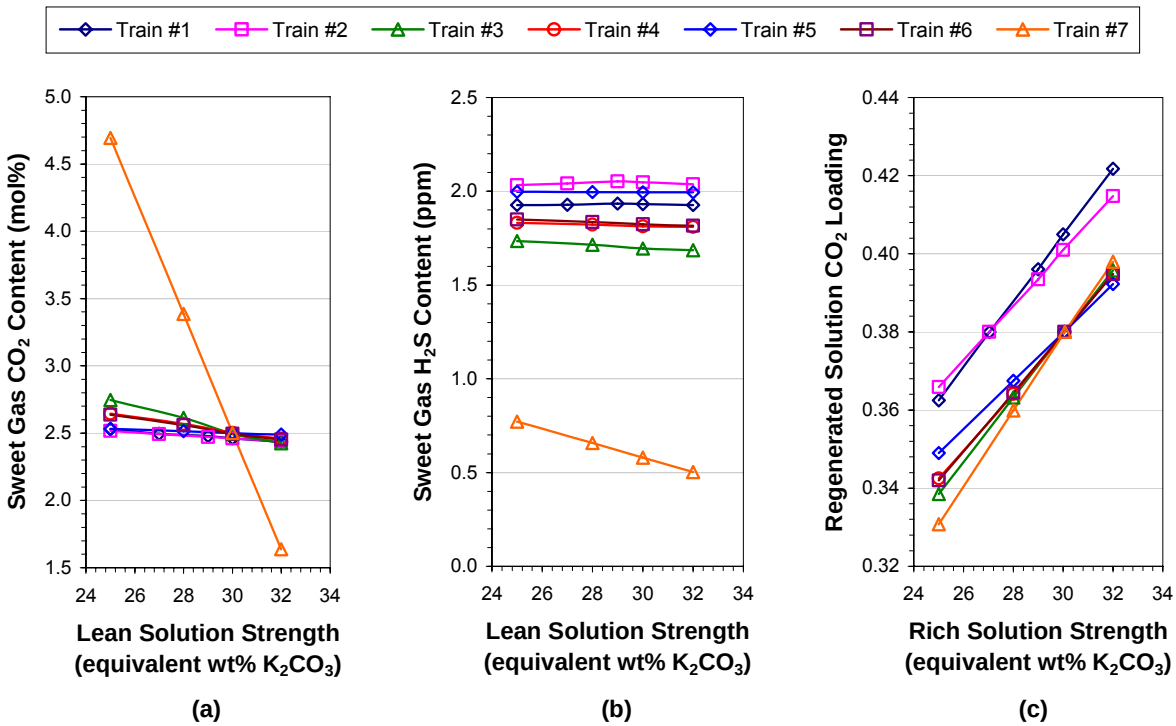

Figure 5.1.2: Effect of the solution strength on the performance of the CO_2 trains. The influence of the lean solution strength on (a) the sweet gas CO_2 content and (b) the sweet gas H_2S content; and the influence of the rich solution strength on (c) the regenerated solution CO_2 loading.

5.1.3 Solution Acid Gas Loading

The other property affecting the acid gas absorption capacity of the potassium carbonate solution is the solution acid gas loading. This property represents the amount of K_2CO_3 that has been converted to $KHCO_3$, KHS and K_2S through the absorption of acid gas. It is therefore is a measure of the actual amount of K_2CO_3 available for reaction with CO_2 and H_2S, and can be considered to be the combined CO_2 and H_2S loading in the solution. However, as the solution H_2S loading for the CO_2 trains is

negligible in comparison to the CO_2 loading, only the effect of the solution CO_2 loading on the performance of the CO_2 trains was considered here.

The effect of the solution CO_2 loading on the performance of the CO_2 trains is depicted in Figure 5.1.3. The first two plots illustrate the relationship between the acid gas content of the sweet gas and the lean solution CO_2 loading. Raising the lean solution CO_2 loading was observed to increase the level of acid gas in the sweet gas. This reduction in the extent of acid gas absorption was attributed to the lower solution absorption capacity due to the smaller quantity of K_2CO_3 available for reaction with CO_2 and H_2S.

In regenerators, the CO_2 loading of the regenerated solution was found to increase with the rich solution CO_2 loading, as shown in the last plot of Figure 5.1.3. This reduction in the extent of solution regeneration resulted from the larger quantities of CO_2 present in the rich solution, which reduced the volume of stripping steam available per unit volume of CO_2 for the given reboiler duty. A similar trend was observed for the H_2S loading of the regenerated solution, but was disregarded since the H_2S loading remained effectively zero due to its very low order of magnitude.

To ensure optimal removal of acid gas in the absorbers, the CO_2 trains are normally operated to maintain a lean solution CO_2 loading of less than 0.45 (Santos Ltd, 1998). This typically corresponds to a maximum CO_2 loading between 0.90 and 0.95 for the rich solution leaving the absorbers.

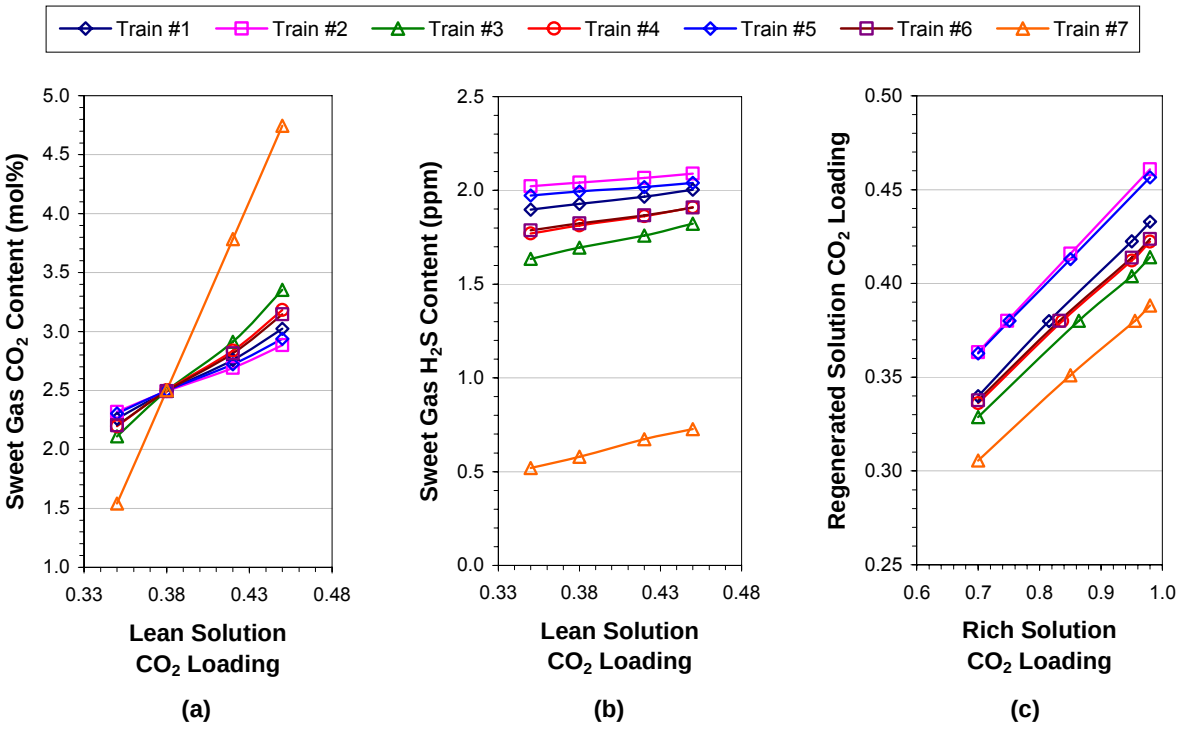

Figure 5.1.3: Effect of the solution CO_2 loading on the performance of the CO_2 trains. The influence of the lean solution CO_2 loading on (a) the sweet gas CO_2 content and (b) the sweet gas H_2S content; and the influence of the rich solution CO_2 loading on (c) the regenerated solution CO_2 loading.

5.2 Raw Gas Operating Parameters

Like the potassium carbonate solution, the raw gas plays an essential role in the function of the Moomba CO_2 trains. In this section, two key operating parameters associated with the raw gas, i.e. flow rate and acid gas content, are examined to determine their effect on the performance of the CO_2 trains.

5.2.1 Raw Gas Flow Rate

The flow rate of the raw gas to the CO_2 trains establishes the quantity of raw gas entering the absorbers and, therefore, the flow rate of the sweet gas. Furthermore, like the lean solution flow rate, the raw gas flow rate also determines the contact time between the vapour and liquid phases in the absorber packing.

The effect of the raw gas flow rate on the performance of the CO_2 trains is depicted in Figure 5.2.1. In the first two plots, the acid gas content of the sweet gas was observed to increase with the raw gas flow rate. This was primarily attributed to the larger volumes of raw gas to be treated per unit volume of solution, which decreased the volume of solution available per unit volume of acid gas and thereby constricted the acid gas absorption process. As for the solution flow rate, the reduced phase contact times arising from the higher gas flow rates were expected to have a relatively minor effect.

The higher raw gas flow rates also pushed the CO_2 train absorbers closer to the limits of the solution capacity, which led to higher levels of acid gas in the rich solution, the effect of which has been studied in the previous section. The relationship between the raw gas flow rate and the rich solution CO_2 loading is illustrated in the last plot in Figure 5.2.1. A similar trend was observed for the rich solution H_2S loading, but is not included here as the H_2S loading was negligible in comparison with the CO_2 loading.

During the normal operation of the CO_2 trains, the raw gas flow rate to the absorbers is dictated by the demand for sales gas. To maintain the desired sweet gas composition, changes in the raw gas flow rate are typically compensated for by corresponding changes in the solution flow rate (Santos Ltd, 1998).

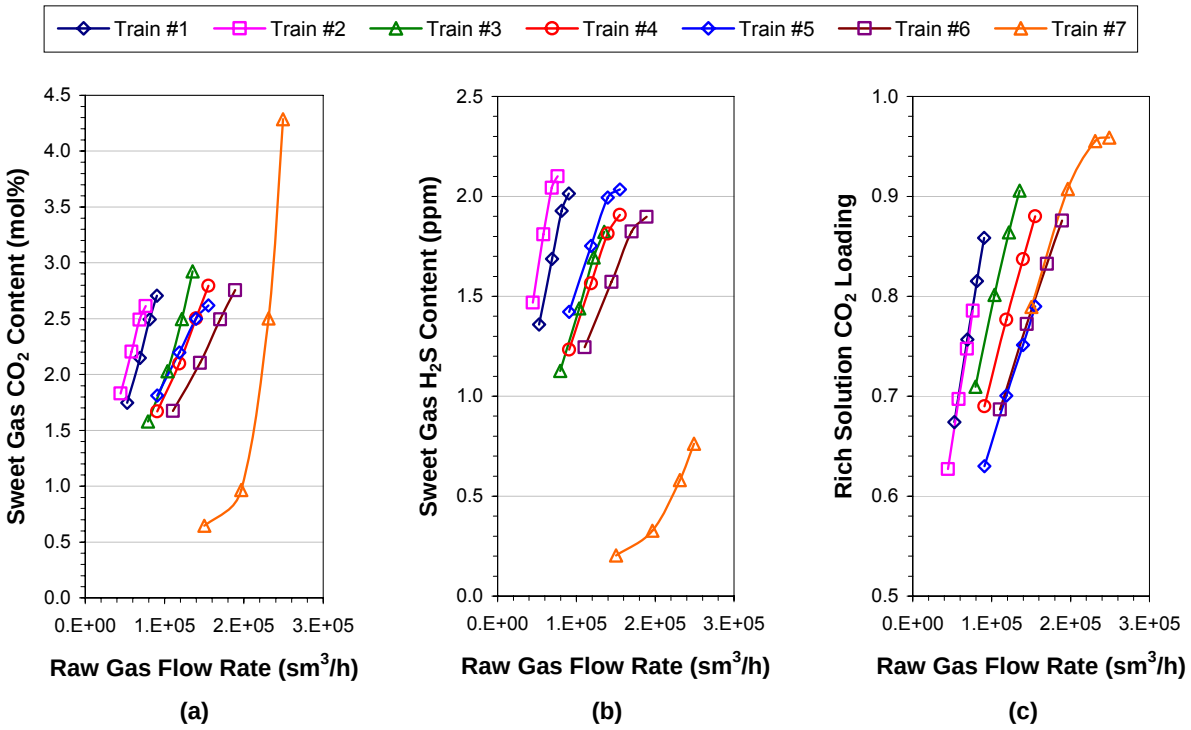

Figure 5.2.1: Effect of the raw gas flow rate on the performance of the CO_2 trains. Its influence on (a) the sweet gas CO_2 content, (b) the sweet gas H_2S content and (c) the rich solution CO_2 loading.

5.2.2 Raw Gas Acid Gas Content

Like the raw gas flow rate, the acid gas content of the raw gas also determines the quantity of acid gas entering the absorbers. The acid gas content of the raw gas is the combined CO_2 and H_2S content of the raw gas, the latter of which is negligible in comparison to the former. Consequently, only the effect of the raw gas CO_2 content on the performance of the CO_2 trains was considered here.

The sensitivity of the performance of the CO_2 trains to the CO_2 content of the raw gas is illustrated in Figure 5.2.2. The first two plots show the relationship between the acid gas content of the sweet gas and the CO_2 content of the raw gas. Raising the raw gas CO_2 content was observed to increase the acid gas content in the sweet gas. This was attributed to the greater volumes of CO_2 entering the absorbers per unit volume of available solution, which therefore constricted the acid gas absorption process.

As for the raw gas flow rate, increasing the raw gas CO_2 content also pushed the CO_2 train absorbers closer to the limits of the solution capacity, which led to higher levels of acid gas in the rich solution. The last plot in Figure 5.2.2 shows the effect of the raw gas CO_2 content on the rich solution CO_2 loading. The effect on the rich solution H_2S loading was negligible in comparison, and has therefore not been presented.

The acid gas content of the raw gas is dependent on the acid gas content of the raw gas supplied from the various gas fields. As for the raw gas flow rate, changes in the raw gas acid gas content are balanced by corresponding changes in the solution flow rate in order to maintain the desired sweet gas composition (Santos Ltd, 1998).

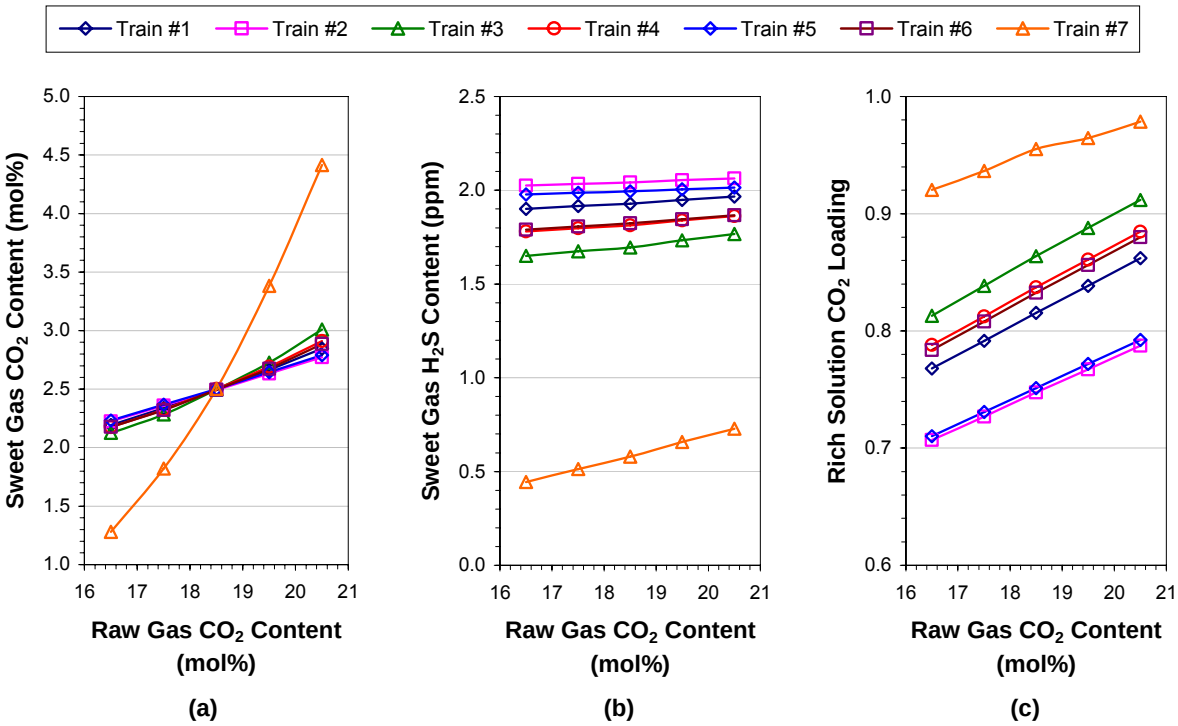

Figure 5.2.2: Effect of the raw gas CO_2 content on the performance of the CO_2 trains. Its influence on (a) the sweet gas CO_2 content, (b) the sweet gas H_2S content and (c) the rich solution CO_2 loading.

5.3 Column Operating Parameters

Apart from the solution and gas properties examined in the previous sections, the performance of the CO_2 trains is also dependent on a number of operating parameters associated with the operation of the absorber and regenerator columns. Four key column operating parameters are studied in this section: column temperature, column pressure, steam flow rate to the regenerator solution reboilers and makeup water flow rate to the regenerator overhead catchpots.

5.3.1 Column Temperatures

Due to the temperature dependency of the reaction rates and the equilibrium constants for the hot potassium carbonate system, the temperatures of the absorber and regenerator columns influence the rate at which the acid gas absorption and desorption processes take place.

In the absorbers, the column temperature profiles were observed to be primarily dependent on the temperature of the lean solution entering the columns. In comparison, the raw gas temperature had a relatively minor effect, as illustrated in the left and centre plots of Figure 5.3.1. As expected, the temperatures of the rich solution and sweet gas increased with the temperatures of the lean solution and raw gas.

Higher temperatures for the lean solution and raw gas also led to greater concentrations of CO_2 in the sweet gas, as shown in the right plots in Figure 5.3.1. This was the result of the higher temperatures in the absorber, which reduced the solubility of CO_2 in the potassium carbonate solution and retarded the slightly exothermic CO_2 absorption process. The influence of the raw gas and lean solution temperatures on the sweet gas H_2S content was negligible in comparison, and has therefore not been presented.

In the regenerators, the temperature of the rich solution was found to establish the column temperature profile, whereas the temperature of regenerator overhead condensers had little to no effect. These trends are presented in the left and centre plots of Figure 5.3.2. As expected, the temperatures of the regenerated solution and regenerator overheads increased with the rich solution temperature.

In contrast to the absorbers, increases in the column temperatures enhanced the performance of the regenerators due to the reduced acid gas in the solution. This enabled a greater fraction of acid gas to flash off during the pressure reduction between the absorber and regenerator columns, along with facilitating the steam stripping of the acid gas in the regenerators. Consequently, the CO_2 loading of the regenerated solution decreased as the regenerator temperature was increased, as shown by the two plots on the right in Figure 5.3.2. Similar trends were observed for the regenerated solution H_2S loading, but were considered inconsequential since the H_2S loading remained effectively zero due to its very low order of magnitude.

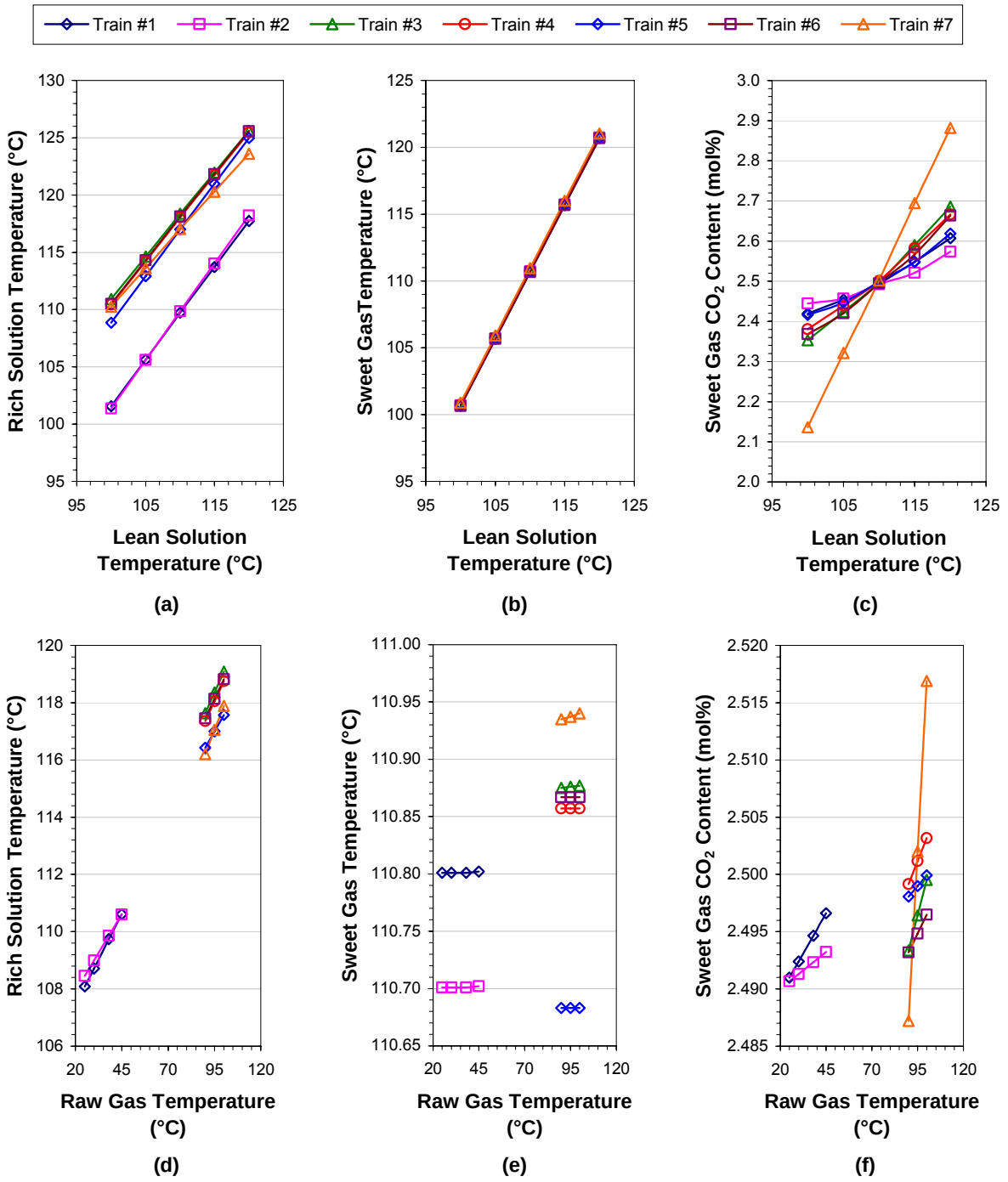

Figure 5.3.1: Effect of the absorber temperature on the performance of the CO_2 trains. The influence of the lean solution temperature on (a) the rich solution temperature, (b) the sweet gas temperature and (c) the sweet gas CO_2 content; and the influence of the raw gas temperature on (d) the rich solution temperature, (e) the sweet gas temperature and (f) the sweet gas CO_2 content.

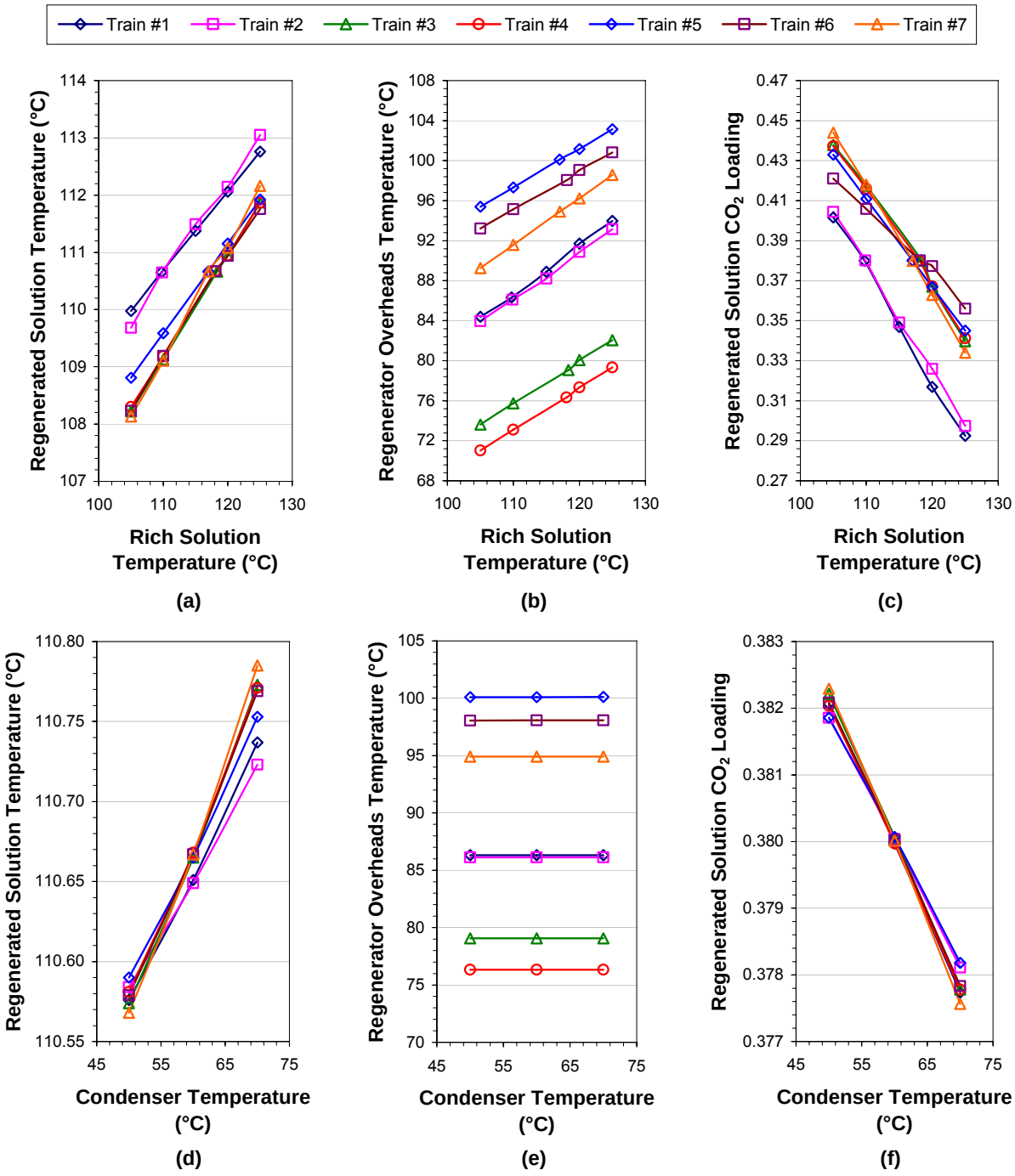

Figure 5.3.2: Effect of the regenerator temperature on the performance of the CO_2 trains. The influence of the rich solution temperature on (a) the regenerated solution temperature, (b) the regenerator overheads temperature and (c) the regenerated solution CO_2 loading; and the influence of the overhead condenser temperature on (d) the regenerated solution temperature, (e) the regenerator overheads temperature and (f) the regenerated solution CO_2 loading. (The regenerator overheads temperature is the temperature of the vapour leaving the regenerator wash sections.)

The temperatures of the lean (or regenerated) solution and rich solution are interdependent, as observed from Figures 5.3.1 and 5.3.2, and are usually between 100 and 120°C (Santos Ltd, 1998). For CO_2 trains #3 to #7, the raw gas to the absorbers is preheated to between 90 and 100°C by the sweet gas. In contrast, in CO_2 trains #1 and #2, the raw gas temperature is set by the temperature of the raw gas supplied from the gas fields and varies between 25 and 45°C, depending on the ambient conditions (Santos Ltd, 1998).

The overhead condenser temperatures are typically maintained between 60 and 70°C, which prevents the condensation of any hydrocarbons present in the regenerator overheads (Santos Ltd, 1998). This enables the hydrocarbons to be removed with the vented acid gas, instead of being returned to the regenerator where they may cause foaming.

5.3.2 Column Pressures

Like the column temperatures, the absorber and regenerator pressures affect the rate at which acid gas absorption and desorption take place. The column pressures determine the partial pressures of CO_2 and H_2S over the potassium carbonate solution and, therefore, the driving force for the mass transfer of acid gas between the vapour and liquid phases. The higher the pressure, the greater the acid gas partial pressures and hence, the larger the driving force for acid gas mass transfer into the liquid phase. Conversely, the lower the pressure, the smaller the acid gas partial pressures and therefore, the larger the driving force for acid gas mass transfer into the vapour phase.

As a result, the absorbers in the Moomba CO_2 trains are kept under high pressure to ensure sufficiently high partial pressures for acid gas absorption to take place. The relationships between the absorber pressure and the sweet gas CO_2 and H_2S concentrations are shown in the first two plots in Figure 5.3.3. As expected, it was observed that the rate of acid gas absorption increased with the absorber pressure.

In contrast, the regenerators are kept at low pressure to facilitate acid gas desorption. The last plot in Figure 5.3.3 presents the effect of the regenerator pressure on the CO_2 loading of the regenerated solution. Unsurprisingly, the extent of solution regeneration increased with decreasing regenerator pressure. A similar trend was observed for the regenerated solution H_2S loading; however, this was deemed insignificant since the H_2S loading remained essentially zero due to its very low order of magnitude.

The absorber pressure is set by the pressure of the raw gas, which is in turn dependent on the pressure of the raw gas supplied from the various gas fields (Santos Ltd, 1998). Typically, the absorber pressure is between 68 and 72 bar. The regenerator pressure is set by the head losses between the absorber and regenerator columns, and is normally between 1.2 and 1.4 bar.

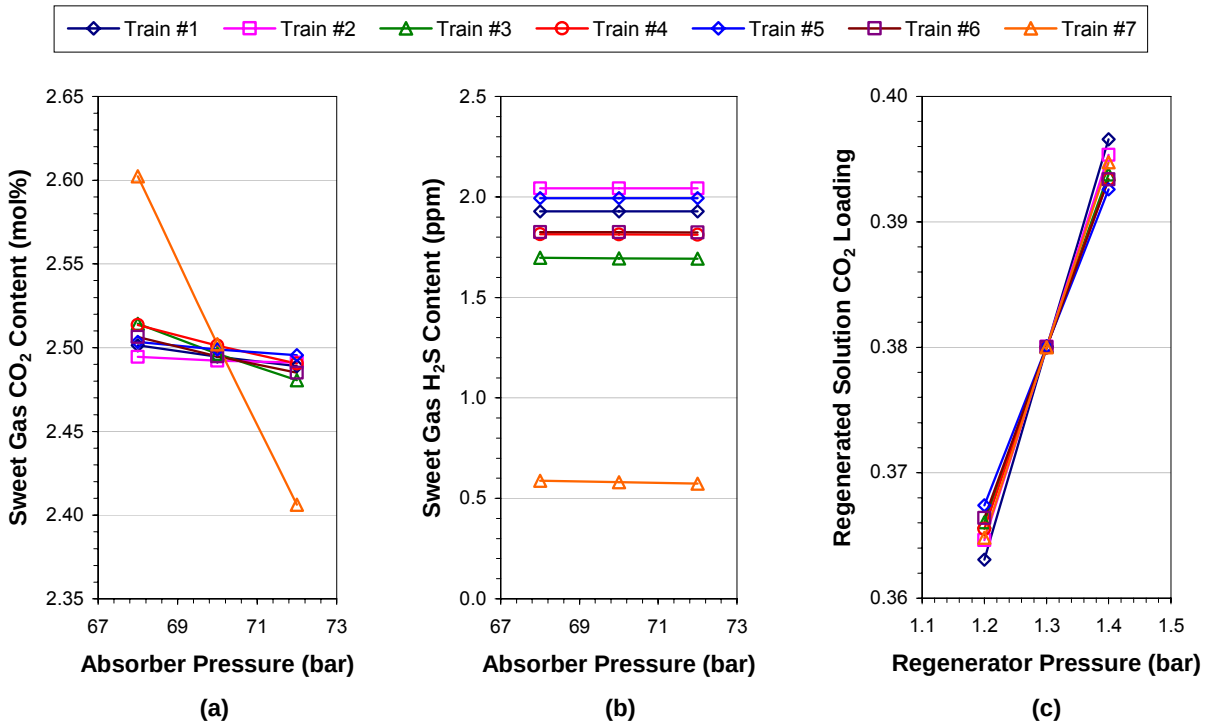

Figure 5.3.3: Effect of pressure on the performance of the CO_2 trains. The influence of the absorber pressure on (a) the sweet gas CO_2 content, (b) the sweet gas H_2S content; and the influence of the regenerator pressure on (c) the regenerated solution CO_2 loading.

5.3.3 Regenerator Solution Reboiler Steam Flow Rate

As discussed previously, the performance of the CO_2 trains is affected by the acid gas loading of the lean solution entering the absorbers. This, in turn, is dependent on the ability of the regenerators to strip the acid gas from the rich solution.

To facilitate the removal of acid gas from the rich solution, the regenerator solution reboilers boil the solution to generate stripping steam, which travels up the regenerator columns to strip CO_2 and H_2S from the downward flowing rich solution, and to further remove the CO_2 and H_2S remaining in the solution. The volume of stripping steam produced and the fraction of acid gas removed in the solution reboilers depend on the reboiler duties. Since the solution reboilers are heated by low pressure steam, the reboiler duties are set by the reboiler steam flow rates: the higher steam flow rates, the greater the reboiler duties.

The relationship between the steam flow rate and the CO_2 loading of the regenerated solution is shown in the first plot of Figure 5.3.4. Increasing the steam flow rate was found to enhance the extent of solution regeneration. This was attributed to the greater volumes of stripping steam generated per unit volume of rich solution and the larger fractions of acid gas boiled off in the reboilers. A similar trend was observed for the regenerated solution H_2S loading, but was regarded as inconsequential since the H_2S loading remained effectively zero due to its very low order of magnitude.

It was noted that the steam flow rates to the solution reboilers also affected the temperature of the regenerated solution. From the second plot in Figure 5.3.4, it was observed that the regenerated solution temperature increased with the steam flow, the effect of which was studied in the previous section concerning the column temperature.

Given the observed effect of the steam flow rate, it is not surprising that during normal operation of the CO_2 trains, the steam flow rates to the regenerator solution reboilers are adjusted to ensure sufficient solution regeneration to maintain the desired sweet gas composition (Santos Ltd, 1998).

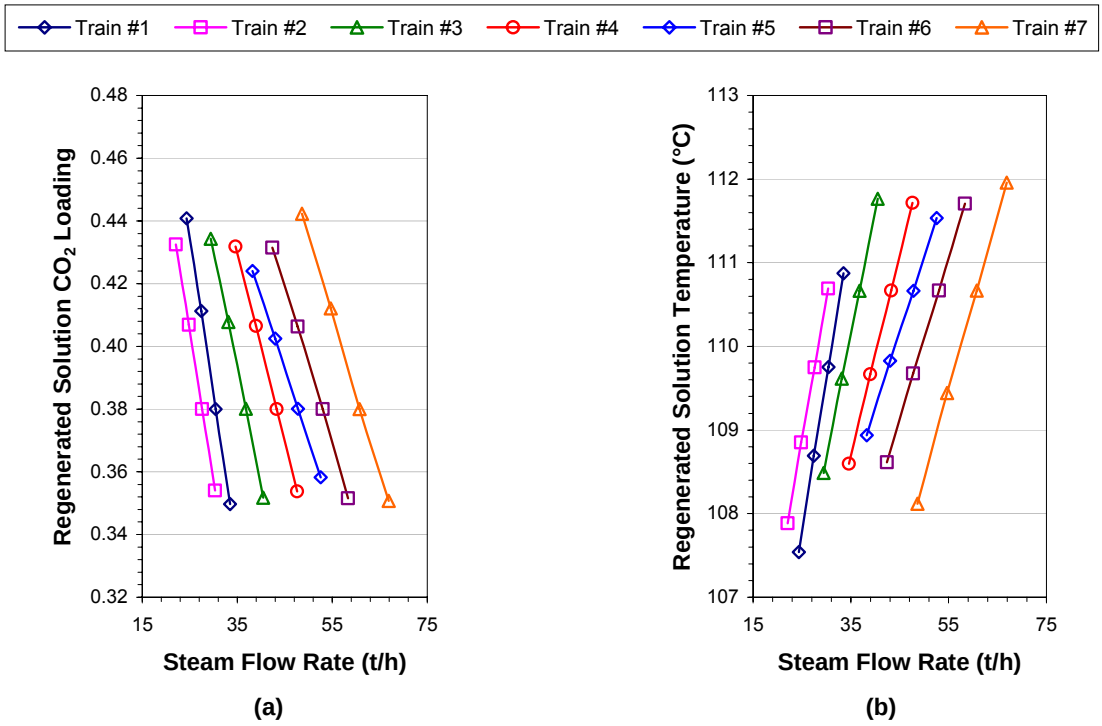

Figure 5.3.4: Effect of the steam flow rate to the regenerator solution reboilers on the performance of the CO_2 trains. Its influence on (a) the CO_2 loading of the regenerated solution and (b) the regenerated solution temperature.

5.3.4 Regenerator Makeup Water Flow Rate

The final column operating parameter of interest is the flow rate of makeup water to the regenerator overhead catchpots. This makeup water compensates for the loss of water from the potassium carbonate solution to the saturated sweet and acid gases leaving the absorbers and regenerator columns, respectively.

The effect of the makeup water flow rate on the performance of the CO_2 trains is presented in Figure 5.3.5. The first plot shows the CO_2 loading of the regenerated solution increasing with the makeup water flow rate. This was due to the increased solution flow rate, which decreased the volume of stripping steam generated per unit volume of solution and thereby reduced the extent of solution regeneration, as discussed in Section 5.1.1. A similar trend was observed for the H_2S loading, but

was considered insignificant since the H_2S loading remained effectively zero due to its very low order of magnitude.

The second plot in Figure 5.3.5 depicts the relationship between the makeup water flow rate and the solution strength of the regenerated solution. Increasing the makeup water flow rates was found to dilute the potassium carbonate solution and thereby reduce the solution strength, the effect of which was described in Section 5.1.2.

During normal operation, the makeup water flow rates are adjusted to maintain the solution flow rates and the solution strength for the CO_2 trains (Santos Ltd, 1998).

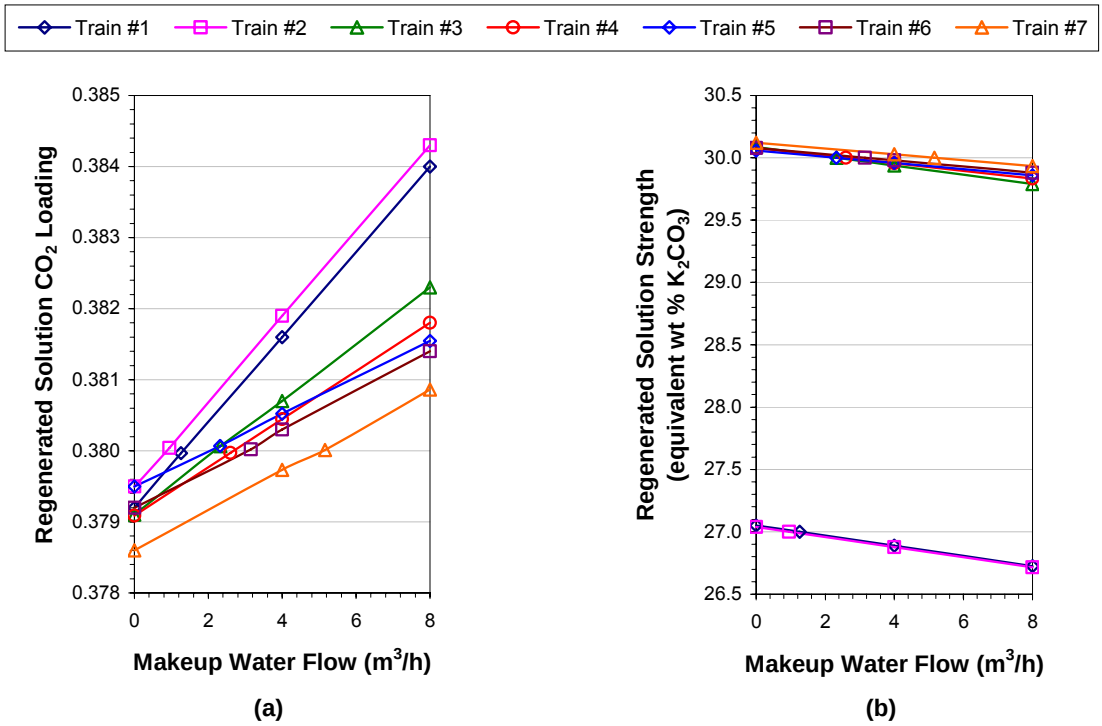

Figure 5.3.5: Effect of the makeup water flow rate to the regenerator overhead catchpots on the performance of the CO_2 trains. Its influence on (a) the CO_2 loading of the regenerated solution and (b) the regenerated solution strength.

5.4 Summary

In summary, this chapter presented and discussed the results of a series of simulations that were performed using the CO_2 train process models developed in Aspen Custom Modeler® in the previous two chapters. These simulations investigated the influence of several key operating parameters on the performance of the Moomba CO_2 trains in order to obtain sufficient information for the development of the HYSYS® CO_2 train process models in the following chapters. The results of these parametric studies will form the foundation of the novel modelling approach used in Chapters 6 and 7 to compensate for the limitations of HYSYS® regarding the simulation of electrolyte processes like the hot potassium carbonate process.

The seven CO_2 trains were found to behave quite similarly, with regard to the relationships observed between the operating parameters and the performance of the absorber and regenerator columns, as indicated by the acid gas content of the sweet gas and the regenerated solution. However, the parametric studies did highlight differences between the performance of the absorber in CO_2 train #7 and that of the other six absorbers. These dissimilarities were unsurprising given the column profiles presented in Chapter 4, and were attributed to the larger acid gas removal capacity of CO_2 train #7. Accordingly, the absorber in CO_2 train #7 operated far closer to the solution capacity limit, making it more sensitive to the operating parameters, compared to the absorbers in the other six CO_2 trains.

CHAPTER 6

MODELLING THE HOT POTASSIUM CARBONATE SYSTEM IN HYSYS®

As discussed in Chapter 2, HYSYS® is the primary process simulation package used by Santos, and is therefore the desired simulation platform for modelling the Moomba CO_2 trains. However, the HYSYS® has restricted capabilities with regard to the simulation of electrolyte systems like the hot potassium carbonate process. This chapter outlines a novel modelling approach which overcomes these limitations of HYSYS® to enable the development of reliable process models for the CO_2 trains.

The first part of this chapter focuses on the definition of hypothetical components to compensate for the lack of electrolyte components in the standard HYSYS® component library. It also discusses the selection of an appropriate property package and the application of column stage efficiencies in order to accurately represent the behaviour of the hot potassium carbonate process in HYSYS®.

The second part of this chapter briefly describes the property models used in HYSYS® for the thermodynamic and physical calculations for the hot potassium carbonate system. Particular attention is given to the regression of model parameters for the Peng-Robinson equation of state, which was used for the thermodynamic calculations.

This chapter begins the development of CO_2 train process models in HYSYS®, which is continued in the following three chapters.

6.1 The Modelling Approach

In this work, a novel approach was undertaken to model the hot potassium carbonate process in the HYSYS® simulation environment. This approach was designed to overcome the limitations of HYSYS® concerning such electrolyte systems, such that reliable process models for the CO_2 trains could be developed in HYSYS®. The following sections outline the three main aspects of this modelling approach: the definition of hypothetical components, the selection and modification of an appropriate property package and the application of column stage efficiencies.

6.1.1 Definition of Hypothetical Components

The first step in the development of any HYSYS® model is the definition of the components in the system of interest. In this work, the system of interest is the CO_2-H_2S-K_2CO_3-$KHCO_3$-KHS-K_2S-H_2O system, which forms the basis of the hot potassium carbonate process.

Unfortunately, none of the electrolyte species (i.e. K_2CO_3, $KHCO_3$, KHS, K_2S, K^+, H_3O^+, HCO_3^-, CO_3^{2-}, HS^-, S^{2-} and OH^-) associated with the above system are available as standard HYSYS® library components. However, such species can be introduced into a HYSYS® simulation as hypothetical HYSYS® components, which are denoted by asterisks: K_2CO_3*, $KHCO_3$*, KHS*, K_2S*, K^+*, H_3O^+*, HCO_3^-*, CO_3^{2-}*, HS^-*, S^{2-}* and OH^-*. This approach was followed for this work.

In HYSYS®, both hypothetical and library components are divided into a number of classes, such as Hydrocarbon, Organic, Inorganic and Miscellaneous, and two types of components are available within each class: liquid or solid. Given that components of the latter type do not participate in the vapour-liquid equilibrium calculations and can only be used in steady-state simulations, the eleven electrolyte species of interest were defined as liquid hypothetical components. Since the H_2O library component is a Miscellaneous-class component, the hypothetical electrolyte components were likewise created as components of the Miscellaneous class.

A number of property estimation methods are included in HYSYS® to estimate the critical, physical and thermodynamic properties of a hypothetical component. The default estimation methods for the Miscellaneous class of components are listed in Table 6.1.1. In this work, the following properties were specified for the hypothetical electrolyte components from literature data: molecular weight, normal boiling point, ideal liquid density, vapour pressure, ideal gas enthalpy, ideal gas Gibbs energy and heat of formation. The remaining properties were estimated via the HYSYS® default methods, which are discussed in further detail in Appendix E.

Table 6.1.1: Property estimation methods for the Miscellaneous class of hypothetical components.

Property	Default Estimation Methods	References
Critical temperature	Lee-Kesler	Kesler and Lee (1976)
	Bergman	Bergman (1976)
	Cavett	Cavett (1964)
Critical pressure	Lee-Kesler	Kesler and Lee (1976)
	Bergman	Bergman (1976)
	Cavett	Cavett (1964)
Critical volume	Pitzer	Pitzer et al. (1955)
Acentricity	Pitzer	Pitzer et al. (1955)
Molecular weight	Bergman	Bergman et al. (1975)
	Lee-Kesler	Kesler and Lee (1976)
Normal boiling point	Proprietary method	Hyprotech Ltd (2001a)
Vapour pressure	Riedel	Riedel (1954)
Ideal liquid density	Yen-Woods	Yen and Woods (1966)
Ideal gas enthalpy	Cavett	Cavett (1964)
Heat of formation	Joback	Joback (1984)
	Ratio with respect to octane	Hyprotech Ltd (2001a)
Ideal gas Gibbs energy	Proprietary method	Hyprotech Ltd (2001a)
Dipole moment	Set equal to zero	Hyprotech Ltd (2001a)
Radius of gyration	Proprietary method	Hyprotech Ltd (2001a)

Preliminary simulations with the full component set of H_2O, N_2, the hydrocarbons CH_4 to C_7H_{16} and the eleven hypothetical electrolyte components were performed to investigate the behaviour of the hypothetical components. It should be noted that a property package had to be selected in order to run these simulations, and this is discussed in the next section. It was found that the default values for the property package's adjustable parameters were inadequate for describing the interaction between the hypothetical components and H_2O. The hypothetical components tended to form a separate liquid phase (with the hydrocarbon components) from the aqueous phase containing H_2O, indicating that values for these parameters had to be regressed from literature data to ensure more correct liquid phase behaviour.

It was also discovered that the interaction parameters for the CO_2-H_2O and H_2S-H_2O component pairs are functions of temperature and therefore could not be altered, unlike the other component pair parameters with constant values. Since these two component pairs are critical to the behaviour of the hot potassium carbonate system, it was decided to clone the H_2O library component to create the hypothetical H_2O* component to enable the regression of these two significant component pair parameters. The H_2O* component was identical to H_2O, except that its interaction parameters could be specified and it no longer formed an aqueous phase. This resolved the issue with the formation of two separate liquid phases, although regression of the interaction parameters was still required to accurately represent the vapour-liquid equilibrium behaviour. The regression of the property package interaction parameters is discussed later in this chapter.

The preliminary simulations also compared the true and apparent component approaches for the liquid phase composition. The former method considers the liquid phase speciation reactions and resulted in a more complex system due to the involvement of all eleven hypothetical electrolyte components. A further complication was that the speciation reactions given in Table 2.1.6 and the kinetic reactions (R2.1.6) and (R2.1.15) had to be incorporated into the simulations to describe the vapour-liquid phase behaviour. The equilibrium reactions were easily specified in HYSYS®; however, the ionic strength dependency of the reaction constants for the two kinetic reactions had to be excluded since HYSYS® only considers these constants as functions of temperature, as defined by an extended form of the Arrhenius equation.

Besides this issue with the kinetic reaction constants, another problem with using the speciation and kinetic reactions in HYSYS® was that HYSYS® limits reactions to column, separator and reactor operations. Consequently, modelling difficulties were encountered for other types of equipment, namely valves, the power recovery turbines and the solution reboilers, in which CO_2 and H_2S are flashed off due to a pressure drop or the application of heat. It was not possible to properly simulate the desorption of CO_2 and H_2S in these operations without the use of chemical reactions as attempts to do so resulted in either mass balance inconsistencies (observed for the valves and power recovery turbines) or the absence of acid gas desorption (observed for the solution reboilers). Attempts to model these pieces of equipment using separator operations with reactions were just as unsuccessful as the separator operations could not converge to a solution.

Convergence difficulties were also experienced for the column operations, especially for the regenerators. Both the absorber and regenerator columns converged rapidly (within a couple of seconds) in the absence of reactions; however, problems were encountered with the inclusion of the speciation and kinetic reactions. The absorbers were found to converge fairly quickly if the simulation initial values were taken from a solved non-reactive absorption run; otherwise, convergence was not achieved. The regenerators, on the other hand, either had not reached a solution after a lengthy period of time (in excess of 10 minutes) or failed to converge, even when the solution to a non-reactive regeneration run was used as the initial values. This critical lack of convergence for the regenerator columns, along with the other above-mentioned modelling difficulties, rendered the true component approach infeasible for this work.

Fortunately, the simulation difficulties associated with the true component approach were avoided by the apparent component approach as this method ignores the solution chemistry. Consequently, only the K_2CO_3* hypothetical electrolyte component was required and the liquid phase reactions were excluded from the simulations. The effect of the solution chemistry on the performance of the absorber and regenerator columns was instead taken into account through the use of column stage efficiencies, which are discussed further on in this chapter. The physical and thermodynamic properties of the K_2CO_3* hypothetical component are given in Appendix E.

6.1.2 Selection of Property Package

The next step in the development of a HYSYS® model is the selection of an appropriate property package for the thermodynamic and physical property calculations associated with the HYSYS® model. Since suitable electrolyte property packages are not included in HSYSY®, one of the standard HYSYS® non-electrolyte property packages had to be used instead for this work.

In HYSYS®, the recommended default property package for oil, gas and petrochemical systems is the Peng-Robinson (PR) property package, which is based on a proprietary enhanced version of the PR equation of state (Peng and Robinson, 1976). The enhanced PR equation of state is also the basis for the Sour PR property package, which is a modification of the PR property package to suit sour water systems. The Sour PR property package combines the enhanced PR equation of state with the Wilson API-Sour method (Wilson, 1980) to account for the ionisation of CO_2 and H_2S in the aqueous phase. In the absence of an aqueous phase, the Sour PR property package reduces to the PR property package.

As shown in Section A.3.2 in Appendix A, the PR equation of state is relatively simple and requires only a single adjustable binary interaction parameter for every component pair in the system of interest. It is also applicable to both vapour and liquid phases. In contrast, the activity coefficient models available in HYSYS®, such as the NRTL model, are more complex. They involve a larger number of adjustable parameters and require the use of a separate vapour phase thermodynamic model. However, while activity coefficient models are more suitable for non-ideal systems, they should be limited to pressures less than 5 atm whereas the enhanced PR equation of state is applicable to pressures up to 1000 bar (Hyprotech Ltd, 2001a). Since the hot potassium carbonate process involves pressures around 70 bar, the enhanced PR equation of state was considered more appropriate for this work than the activity coefficient models available in HYSYS®.

An alternative to the enhanced PR equation of state, the Peng-Robinson Stryjek-Vera (PRSV) equation of state (Stryjek and Vera, 1986ab) was also considered. This model is an extension of the original PR equation of state and it forms the basis for the PRSV property package in HYSYS®. Stryjek and Vera (1986ab) introduced two new adjustable parameters (a pure component vapour pressure parameter and an additional component pair binary interaction parameter) to extend the applicability of the original PR equation of state to moderately non-ideal (non-electrolyte) systems.

However, despite these modifications, the PRSV equation of state still has the same inherent limitations as the enhanced PR equation of state with regard to the representation of electrolyte systems. Like all traditional thermodynamic models, neither equation of state can accurately describe the non-ideal behaviour associated with the electrostatic interactions observed in electrolyte systems. Since the modelling approach for this work involved the use of column stage efficiencies to compensate for the short-comings of the thermodynamic model, it was decided that the

thermodynamic model should be as simple as possible. Consequently, the enhanced PR equation of state was selected as the thermodynamic model for the HYSYS® simulations performed for this work.

A modified form of the standard PR property package was selected as the primary property package for the HYSYS® simulations. The modifications concerned the use of tabular physical property models instead of the default HYSYS® models to accommodate the hypothetical H_2O^* and $K_2CO_3^*$ components and to better represent the properties of the hot potassium carbonate system. However, these changes rendered the modified PR property package unsuitable for sour water systems, in which potassium carbonate was absent. As a result, a secondary property package, the standard Sour PR property package, was required for the sour water sections of the HYSYS® models, and a second component set was defined for these sections to exclude $K_2CO_3^*$ and to replace H_2O^* with the HYSYS® library component H_2O. The standard Sour PR property package was selected instead of the standard PR property package due to its greater accuracy in handling sour water systems.

The thermodynamic and physical property models associated with the two selected property packages are further discussed in Section 6.2 and in Appendix F.

6.1.3 Column Stage Efficiencies

As discussed in the preceding sections, a modified PR property package, based on an apparent component liquid phase composition, was used to characterise the physical and thermodynamic behaviour of the HYSYS® models developed in this work. This approach, however, did not facilitate the direct inclusion of the solution chemistry associated with the hot potassium carbonate process. Consequently, the effects of the speciation reactions and the kinetic reactions were instead indirectly accounted for through the use of column stage efficiencies.

In HYSYS®, column operations consist of equilibrium stages, which require stage efficiencies to relate the performance of these ideal stages to that of real stages in which thermodynamic equilibrium is not achieved. For steady-state simulations, these stage efficiencies are represented by a modified version of the Murphree stage efficiency, as defined in the first figure of Figure 6.1.1. This can be specified for each stage in one of two ways: as a single overall value (i.e. the same value is applied to all components on the stage) or as individual values for each component.

In contrast, in dynamic simulations, the stage efficiency is treated as a vapour bypass which diverts part of the vapour stream entering a stage so that it mixes with the vapour leaving the stage instead of mixing with the liquid entering the stage. This is illustrated in the second figure of Figure 6.1.1. Consequently, only a single overall efficiency value can be specified for each stage in dynamic mode. While the dynamic and steady-state stage efficiencies are not directly related mathematically, they share the same general effect on the column performance: the lower the stage efficiency, the poorer the column performance.

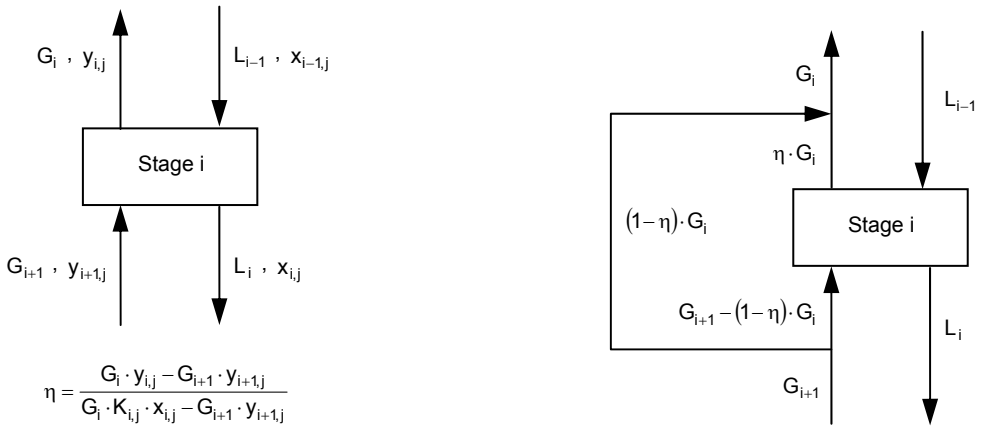

(a) **(b)**

Figure 6.1.1: The different definitions of the column stage efficiency η in HYSYS®. (a) Steady-state column. (b) Dynamic column (adapted from Hyprotech Ltd (2001b)).

In this work, the column stage efficiencies were not only used to represent the non-equilibrium behaviour of the absorber and regenerator columns in the Moomba CO_2 trains, but were also used to describe the effect of the liquid phase reactions on the column performance. To achieve this, stage efficiency correlations were developed for each HYSYS® CO_2 train model. These were based on the parametric studies for the Aspen Custom Modeler® CO_2 train models from Chapter 5, and defined the overall column efficiencies as functions of temperature, pressure, composition and flow. A similar approach is taken by the commercial add-in Amines property package for alkanolamine gas sweetening processes, in which CO_2 and H_2S component stage efficiencies are calculated as functions of the operating conditions, tray specifications and kinetic and mass transfer parameters (Hyprotech Ltd, 2001a).

Chapter 7 discusses the development and implementation of the stage efficiency correlations in greater detail.

6.2 Thermodynamic and Physical Property Models

6.2.1 Summary of Property Models

Two different property packages were used in the HYSYS® models to facilitate the more reliable simulation of the CO_2 trains: the PR and the Sour PR property packages. The standard HYSYS® property models presented in Table 6.2.1 were used to perform the general thermodynamic and physical property calculations for these two property packages. Table 6.2.1 also includes the references from which the relevant model equations and/or model parameters were taken.

Where the standard models were unsuitable, tabular property models were used instead for the property calculations. The model parameters for these tabular models, and for the enhanced PR equation of state, were derived from the literature data listed in Table 3.1.3.

Table 6.2.1: Thermodynamic and physical property models.

Property	PR Package	Sour PR Package	References
Fugacity coefficients	Enhanced PR	Enhanced PR	Peng and Robinson (1976)
Enthalpy	Enhanced PR	Enhanced PR	Peng and Robinson (1976)
Heat capacity	From C_v value	From C_v value	Hyprotech Ltd (2001a)
Molecular weight	Weighted average	Weighted average	Hyprotech Ltd (2001a)
Density	Enhanced PR (V) Tabular model (L)	Enhanced PR (V) COSTALD (L)	Peng and Robinson (1976), Hyprotech Ltd (2001a), Hankinson and Thomson (1979)
Dynamic viscosity	Modified Ely-Hanley (V) Tabular model (L)	Modified Ely-Hanley Twu (L) Modified Letsou-Stiel (L)	Ely and Hanley (1981), Hyprotech Ltd (2001a), Twu (1985), Letsou and Stiel (1973)
Surface tension	Tabular model (L)	Modified Brock-Bird (L) Proprietary polynomial (L)	Brock and Bird (1955), Hyprotech Ltd (2001a)
Thermal conductivity	Modified Ely-Hanley (V) Misic-Thodos (V) Chung (V) Tabular model (L)	Modified Ely-Hanley Misic-Thodos (V) Chung (V) Proprietary polynomial (L) Modified Missenard-Riedel (L) Latini (L) Sato-Riedel (L)	Ely and Hanley (1983), Hyprotech Ltd (2001a), Misic and Thodos (1961, 1963), Chung and co-workers (1988), Reid and co-workers (1977), Baroncini and co-workers (1980)

Note: (V) refers to the vapour phase and (L) refers to the liquid phase. If no phase is indicated, the model applies to both vapour and liquid phases.

The reliable simulation of the hot potassium carbonate process in HYSYS® requires an accurate representation of the thermodynamic behaviour of the CO_2-H_2S-K_2CO_3-$KHCO_3$-KHS-K_2S-H_2O system. Consequently, the key properties of interest are the fugacity coefficients, which were calculated using the enhanced PR equation of state. The next section discusses the regression of the adjustable model parameters for this thermodynamic model. For the purpose of brevity, detailed descriptions of the property models have not been included in the main body of this thesis. Instead, the equations for

the original PR equation of state are presented in Section A.3.2 in Appendix A, while the other thermodynamic and physical property models are discussed in greater detail in Appendix F.

6.2.2 The Enhanced Peng-Robinson Equation of State

As discussed previously, the enhanced PR equation of state, a HYSYS® proprietary version of the original PR equation of state, was used to determine the fugacity coefficients for this work. This equation of state requires a binary interaction parameter k_{jk} (where $k_{jk} = k_{kj}$ and $k_{jj} = 0$) for each component pair j-k in the system of interest. To ensure the best representation of the system thermodynamic behaviour, these interaction parameters should be determined from experimental data.

Binary interaction parameter values for the full set of non-hypothetical component pairs of interest are included in the HYSYS® property package library, and these default values were used in the Sour PR property package. For the PR property package, the presence of the hypothetical water H_2O^* and potassium carbonate $K_2CO_3^*$ components required the regression of vapour-liquid equilibrium data to obtain the parameter values. It should be noted that the default value is 0 for component pairs that are not included in the HYSYS® property package library.

For the hot potassium carbonate process, the system of interest is the CO_2-H_2S-K_2CO_3-$KHCO_3$-KHS-K_2S-H_2O system, which reduces to the CO_2-H_2S-K_2CO_3-H_2O system based on the apparent component approach. The five key component pairs in the PR property package were therefore H_2O^*-$K_2CO_3^*$, CO_2-H_2O^*, CO_2-$K_2CO_3^*$, H_2S-H_2O^* and H_2S-$K_2CO_3^*$. The binary interaction parameter values for these five pairs were determined from two sets of regressions, which are described in the following sections. The parameters for the remaining component pairs involving H_2O^* (i.e. N_2-H_2O^*, CH_4-H_2O^*, etc.) were set equal to the default HYSYS® values for the corresponding component pairs with H_2O.

Default HYSYS® parameter values were also used for the non-hypothetical component pairs. The CO_2-H_2S component pair parameter was kept at the HYSYS® default value and was not re-regressed (unlike the other component pairs in the CO_2-H_2S-K_2CO_3-H_2O system) because preliminary simulations showed that the parameter value sets that included the re-regressed CO_2-H_2S component pair parameter value resulted in negligible H_2S desorption in the regenerator.

It was expected that the enhanced PR equation of state would have inherent limitations in describing accurately the thermodynamic behaviour of the CO_2-H_2S-K_2CO_3-H_2O system. Consequently, the model could not be assumed to be capable of representing the vapour-liquid equilibrium data without any systematic deviation. Since this is one of the key assumptions in the maximum likelihood method, the simpler and statistically less rigorous implicit least squares method was instead applied to the parameter regressions.

The regressions were performed in a Microsoft® Excel spreadsheet, and the Gauss-Newton method (with the bisection rule) was used to minimise the following objective function Q:

$$Q = \sum_{i=1}^{ND} \sum_{j=1}^{NC} \left(\ln f_{L,i,j} - \ln f_{G,i,j} \right)^2 \qquad (6.2.1)$$

where ND is the number of data points, NC is the number of components, and f is the fugacity. The subscripts G and L refer to the vapour and liquid phases, respectively, and the subscripts i and j denote the data point i and the component j, respectively. The above objective function was minimised via the manipulation of the model parameters, subject to the vapour-liquid equilibrium constraints.

6.2.2.1 Parameters for the CO_2-K_2CO_3-H_2O system

The first set of regressions was performed to determine the binary interaction parameters for the H_2O*-K_2CO_3*, CO_2-H_2O* and CO_2-K_2CO_3* component pairs from the vapour-liquid equilibrium data presented by Tosh and co-workers (1959). Details of this data set were given in Section 3.2.1. The liquid phase composition was determined as for the Aspen Properties® DRS regression runs, i.e. from equations (3.2.6) to (3.2.9), and only CO_2 and H_2O* were assumed to be present in the vapour phase.

A series of regressions were performed and the resulting optimal set of parameter values is presented in Table 6.2.2, while Figure 6.2.1 compares the predicted CO_2 and H_2O* partial pressures against the literature data. The procedure used to obtain the optimal parameter set is described in Appendix G. The absolute average deviations between the predicted and literature values were 135.9% and 15.8% for CO_2 and H_2O*, respectively. In comparison, the average absolute deviations were substantially larger (24500.7% and 126.7%, respectively) when the default HYSYS® parameter values were used.

The large and systematic deviation between the experimental and literature values for the CO_2 partial pressures illustrated the inherent limitations for the enhanced PR equation of state in representing the CO_2-K_2CO_3-H_2O system, and confirmed the unsuitability of the maximum likelihood method for the regression of the parameter values. The inadequacy of the enhanced PR equation of state required the use of column stage efficiencies to more accurately represent the reactions occurring in the absorber and regenerator units in the HYSYS® CO_2 train models. This will be discussed further in the next chapter.

Table 6.2.2: Enhanced PR parameter values for the CO_2-K_2CO_3-H_2O system.

Component Pair	Parameter Value	Standard Deviation
H_2O*-K_2CO_3*	-1.1152	0.0748
CO_2-H_2O*	-0.5891	0.1019
CO_2-K_2CO_3*	-0.3836	0.2783

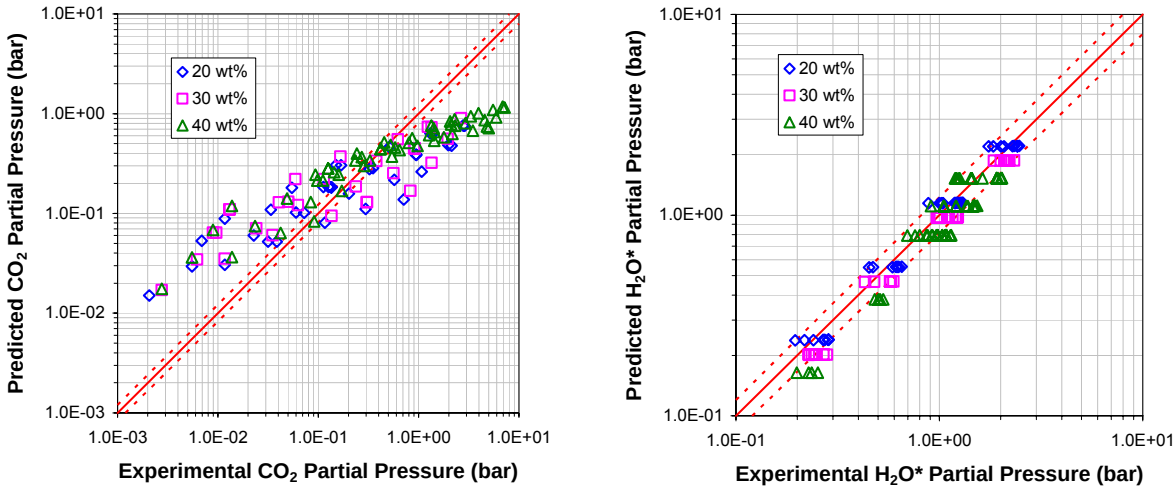

Figure 6.2.1: Comparison between the enhanced PR predictions and the experimental data. Partial pressure plots for (a) CO_2 and (b) H_2O*. The points represent the partial pressures over 20, 30 and 40 wt% equivalent K_2CO_3 solutions. The dashed lines (---) represent the ± 20% lines.

6.2.2.2 Parameters for the CO_2-H_2S-K_2CO_3-H_2O system

The second set of regressions was performed to determine the binary interaction parameters for the H_2S-H_2O* and H_2S-K_2CO_3* component pairs using the parameter values in Table 6.2.2 and the vapour-liquid equilibrium data presented by Tosh and co-workers (1960). Details of this data set were given in Section 3.2.2. The liquid phase composition was determined as for the Aspen Properties® DRS regression runs, i.e. from equations (3.2.6), (3.2.7) and (3.2.10) to (3.2.12). Only H_2S, CO_2 and H_2O* were assumed to be present in the vapour phase.

A series of regressions were performed and the resulting optimal set of parameter values is presented in Table 4.2.3, while Figure 4.2.2 compares the predicted CO_2, H_2S and H_2O* partial pressures against the literature data. The procedure used to obtain the optimal parameter set is described in detail in Appendix G. The absolute average deviations between the predicted and literature values were 63.7%, 19.9% and 274.5% for CO_2, H_2S and H_2O*, respectively. In comparison, the average absolute deviations were significantly larger (11576.1%, 144.7% and 24137.7%, respectively) when the default HYSYS® parameter values were used.

Most of the points on the plots in Figure 6.2.2 were found to be relatively evenly scattered about the y = x diagonal. However, a distinct outlying cluster of 30 wt% points was observed in the lower right-hand corner of the first plot in Figure 6.2.2. These points corresponded to the CO_2 partial pressures over a 30 wt% equivalent K_2CO_3 solution converted only by H_2S, and their substantial underestimation demonstrated the inherent limitations of the enhanced PR equation of state in representing the CO_2-H_2S-K_2CO_3-H_2O system. The enhanced PR equation of state could not adequately describe the system equilibria in Table 2.1.6, and consequently was unable to accommodate the CO_2-H_2S-K_2CO_3-H_2O system in which only H_2S is absorbed into the K_2CO_3 solution. However, this particular

inadequacy was not of concern for this work as the hot potassium carbonate process of interest focuses primarily on the removal of CO_2.

Table 6.2.3: Enhanced PR parameter values for the CO_2-H_2S-K_2CO_3-H_2O system.

Component Pair	Parameter Value	Standard Deviation
H_2S-H_2O*	-1.2366	0.5274
H_2S-K_2CO_3*	0.0951	2.3660

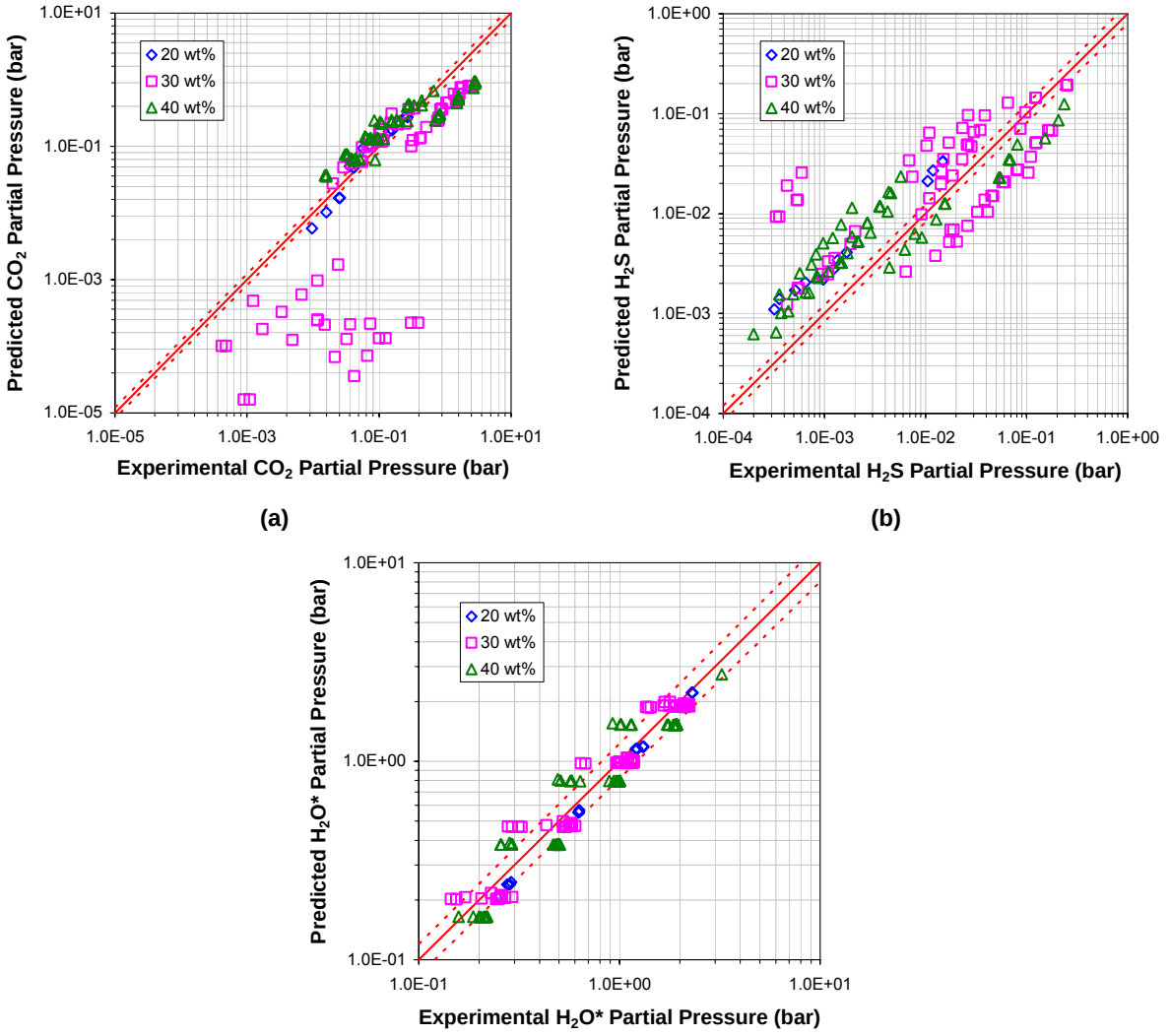

Figure 6.2.2: Comparison between the enhanced PR predictions and the experimental data. Partial pressure plots for (a) CO_2, (b) H_2S and (c) H_2O*. The points represent the partial pressures over 20, 30 and 40 wt% equivalent K_2CO_3 solutions. The dashed lines (---) represent the ± 20% lines.

6.3 Summary

In summary, this chapter outlined the novel modelling approach used in this work to overcome the limitations associated with modelling the hot potassium carbonate process in HYSYS®. The three main features of this approach were: the introduction of hypothetical electrolyte components, the selection of a suitable HYSYS® property package, and the application of column stage efficiencies.

The hypothetical electrolyte components were created to compensate for the absence of electrolyte components in the HYSYS® component library, which would have otherwise prevented the hot potassium carbonate system from being modelled in this simulation environment. The behaviour of the hypothetical components was investigated in a series of preliminary simulations, which determined that the liquid phase composition was most feasibly represented by the apparent component approach. However, by adopting the apparent component approach, the solution chemistry had to be represented implicitly through the property package model parameters and the use of column stage efficiencies.

Due to the lack of electrolyte property packages in HYSYS®, the PR property package was selected for its simplicity and was modified to provide a more accurate representation of the hot potassium carbonate system. Particular attention was given to the regression of the model parameters for the enhanced PR equation of state, while the modifications to the other property models in the PR property package were discussed in Appendix F. Significant improvements in the model predictions were achieved with the modifications to the PR property package; however, large systematic deviations were still observed for the vapour-liquid equilibria. These highlighted the inherent limitations of the enhanced PR equation of state in describing the chemistry associated with the hot potassium carbonate system.

To compensate for the above inadequacies, column stage efficiencies were applied to the absorber and regenerator columns to better represent the effects of the solution chemistry. These efficiencies are normally used to relate the ideal HYSYS® column stages to real non-equilibrium stages, and consequently also facilitated a more accurate depiction of the non-equilibrium behaviour of these columns. To enable a reasonable representation of the non-equilibrium column behaviour and the effects of the solution chemistry, the stage efficiencies were correlated against the column operating parameters based on the results of the Aspen Custom Modeler® parametric studies in Chapter 5. The development of these stage efficiency correlations and their implementation in the absorber and regenerator column models are further discussed in the following chapter.

CHAPTER 7

THE ABSORBER AND REGENERATOR COLUMN MODELS

This chapter continues the discussion on the simulation work performed in HYSYS® to model the hot potassium carbonate process in the form of the Moomba CO_2 trains. In this chapter, the focus shifts to the development of the absorber and regenerator column models, in particular, the correlation and implementation of column stage efficiencies.

It was determined in the previous chapter that, despite the modifications to the PR property package, the inherent limitations of the enhanced PR equation of state prevented the accurate representation of the solution chemistry for the hot potassium carbonate process. To compensate for this inadequacy, the application of column stage efficiencies was proposed to improve the performance of the absorber and regenerator column models.

This chapter investigates the feasibility of the above suggested modelling approach. Detailed absorber and regenerator column models for the CO_2 trains are developed using the standard HYSYS® operations. A series of preliminary simulations are performed to examine the performance of these column models and their sensitivity to variations in the column stage efficiencies. Finally, the Aspen Custom Modeler® parametric study results from Chapter 5 are used to correlate the column stage efficiencies with respect to the column operating parameters, and the implementation of these correlations in HYSYS® is discussed.

7.1 Absorber Column Models

In HYSYS®, column operations are treated as a series of equilibrium stages which comprise the column tray sections as well as any attached reboiler and condenser operations. In this work, the HYSYS® absorber operation, consisting solely of a tray section, was used to model the absorber columns in the Moomba CO_2 trains.

This approach necessitated the discretisation of the packed heights of the CO_2 train absorbers into a number of stages, just as required for the Aspen Custom Modeler® absorber models in Chapter 4. Consequently, the number of stages for each absorber operation was set equal to that for the corresponding Aspen Custom Modeler® absorber model. This ensured that the HYSYS® and Aspen Custom Modeler® absorber models were directly comparable. Other sizing information was obtained from the operator and vendor manuals and the technical data sheets and drawings stored in the Santos TIMS (The Information Management System) controlled documentation database.

An idiosyncrasy of the HYSYS® absorber operations is that they end with a tray and not a sump, unlike real absorber columns. In steady-state simulations, the absence of a column sump had no effect on the simulation results. However, in dynamic simulations, column sumps are essential to ensure proper pressure driven flow, and they enable the modelling of level control at the bottom of the column. Consequently, for this work, appropriately sized separator operations were used to represent the absorber sumps in HYSYS®, resulting in the general absorber model layout in Figure 7.1.1. For consistency with the real absorber columns, the vapour streams leaving the top of the modelled sumps were recycled back to the bottom of the absorber tray sections so that the absorber models only had two feed streams (RawGas and LeanSoln) and two product streams (SweetGas and RichSoln).

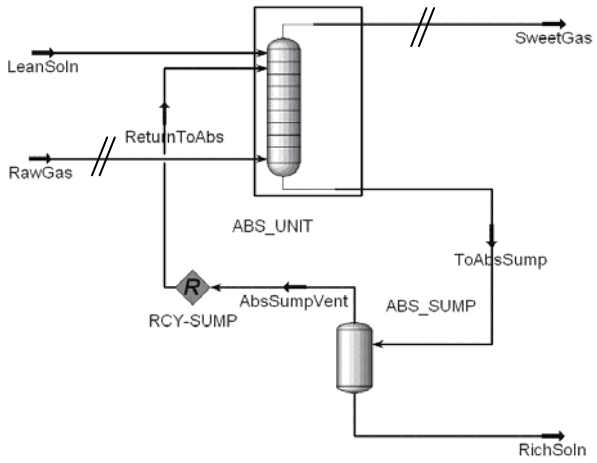

Figure 7.1.1: Process flow diagram of an absorber column model in HYSYS®. The // denote a change in property package.

It should be noted that in steady-state simulations, HYSYS® can only solve material recycle loops if they contain a recycle operation. For this reason, a recycle operation RCY-SUMP was included in the vapour return circuit at the bottom of the absorber models, as shown in Figure 7.1.1. The HYSYS® recycle operation acts as a theoretical tear in a material stream, in which the inlet stream properties are calculated based on assumed values for the outlet stream. The outlet stream conditions are modified iteratively until the two streams agree within a specified tolerance. In this work, the default variable tolerances were used in the recycle operations, except for the flow and composition tolerances. These were tightened by a factor of 10 to accommodate the extremely low concentration of H_2S in the system.

The physical and thermodynamic property calculations for the absorber models were performed using both the PR and the Sour PR property packages described in Chapter 6. The PR property package was the primary property package and was applied to the entire absorber model, except for the vapour feed and product streams. The property calculations for these two streams were instead performed by the Sour PR property package due to the absence of the hypothetical K_2CO_3* component.

To accommodate this change in property package between the two vapour streams and the rest of the absorber model, a transfer basis had to be specified. The T-P (Temperature-Pressure) flash transfer basis was selected, since it can be used between different property packages, unlike the default P-H (Pressure-Enthalpy) flash transfer basis (Aspen Technology Inc., 2006). For a material stream undergoing a change in property package, the T-P flash transfer basis transfers the composition, flow, temperature and pressure between the two property packages and recalculates the enthalpy and vapour fraction. In contrast, the P-H flash transfer basis transfers the composition, flow, pressure and enthalpy and recalculates the temperature and vapour fraction.

7.2 Regenerator Column Models

In contrast to the relatively simple absorber models described above, the regenerator column models were considerably more complex and involved different configurations for the seven CO_2 trains. This increased model complexity can be observed in Figure 7.2.1, which depicts the general layout of the two most dissimilar regenerator models: the regenerator models for CO_2 trains #1 and #7. For clarity, parallel items such as the solution reboilers have been represented by single units in Figure 7.2.1.

Besides the presence of the cooling water circuit in the model for CO_2 train #1, the other significant difference between the two models in Figure 7.2.1 concerned the solution reboilers. Kettle reboilers are used in CO_2 train #1 (and in CO_2 trains #2 to #4), whereas the solution reboilers in CO_2 train #7 (and in CO_2 trains #5 and #6) are semi-thermosyphon-type reboilers. These two types of reboilers operate in quite different ways. In kettle reboilers, the generated steam is fed back into the bottom of the regenerator while the heated solution leaves as the regenerator bottoms product. In contrast, the steam and solution from the semi-thermosyphon reboilers flow back together into the bottom of the regenerator. The two different reboiler operations are reflected in the dissimilar reboiler and sump arrangements shown in Figure 7.2.1.

Like the absorber column models, the regenerator column models for the CO_2 trains were developed around the HYSYS® absorber operation. The regenerator main packed sections were modelled by absorber operations with the same number of stages as for the corresponding Aspen Custom Modeler® regenerator models. Likewise, the regenerator wash sections were represented by absorber operations. For the valve tray-type wash sections, the number of stages was taken as the number of trays. For the packed wash sections, the HETP of the corresponding main packed section was used to determine the number of stages.

As for the absorber models, separator operations were used to model the regenerator sumps. These operations were also used to represent the overhead catchpots and the steam condensate receivers. The solution reboilers were modelled by heat exchanger operations, while the overhead condensers and water coolers were modelled as cooler operations. Pump operations were used to model the solution, cooling water, steam condensate and overhead condensate pumps, while valve operations were used to represent the pressure drops across the solution filters. The actual function of the filters was not considered in the HYSYS® simulations due to the exclusion of solid components from the simulation system. All these various components of the regenerator models were sized according to information obtained from the Santos TIMS database.

Up to five material recycle loops were associated with each regenerator model: the reboiler circuit, the solution filter circuit, the wash section circuit, the overhead condensate circuit and the cooling water circuit (only for CO_2 trains #1 to #4). The location of the recycle operations was carefully considered to maximise the model stability and to minimise the number required, so as to reduce the simulation computation time. Special consideration was given to ensure the assigned recycle operations could

also accommodate the solution recycle and sour water circuits between the absorber and regenerator models, thereby minimising the number of recycle operations required for the completed CO_2 train process models. Due to the configuration of the regenerator recycle loops, a minimum of three recycle operations were necessary for each regenerator model, as shown in Figure 7.2.1. The recycle operation configurations were identical for the regenerator models for CO_2 trains #1 to #4 and for the regenerator models for CO_2 trains #5 to #7.

Like the absorber column models, the PR and the Sour PR property packages from Chapter 6 were used to perform the physical and thermodynamic property calculations for the regenerator models. The PR property package was applied to the sections of the models in which the hypothetical K_2CO_3* component was present, namely the main packed sections, the solution reboilers and the regenerator sumps. Where K_2CO_3* was assumed to be absent (such as in the wash sections, the overhead condenser system, the cooling water circuits and the reboiler steam circuit), the property calculations were performed using the Sour PR property package. As for the absorber models, the T-P flash transfer basis was applied to all changes between the two property packages.

It should be noted that although the above assumption regarding the absence of K_2CO_3* in the regenerator wash sections and overhead condenser system is theoretically valid, it is not always true in practice (Willcocks, 2008). The regenerator condensate streams have been found to contain very small quantities of potassium carbonate due to some entrainment of the potassium carbonate solution at the top of the regenerator columns. Likewise, it is possible that, in practice, some potassium carbonate solution is also entrained at the top of the absorber columns, leading to the presence of potassium carbonate solution in the saturated sweet gas streams, and therefore the sour water streams.

Entrainment can be accounted for in the HYSYS® column operations by reducing the column stage efficiencies such that non-ideal separation of the various components occurs. However, this approach was unsuccessful for the hypothetical K_2CO_3* component as negligible carryover of K_2CO_3* was obtained for the absorber and regenerator column models. This lack of entrainment was attributed to the high boiling point[1] for K_2CO_3* as the use of lower values for the boiling point was found to increase the concentration of K_2CO_3* in the vapour phase. However, changes to the boiling point had undesirable effects on the other physical and thermodynamic properties for K_2CO_3* and on the phase equilibrium calculations for the potassium carbonate system. Consequently, given the relatively low levels of potassium carbonate reported in the sour water and condensate streams, it was considered reasonable to neglect the entrainment of potassium carbonate solution in this work.

[1] In actuality, the melting point of K_2CO_3 was used as the boiling point of K_2CO_3* since K_2CO_3 decomposes at temperatures near the melting point.

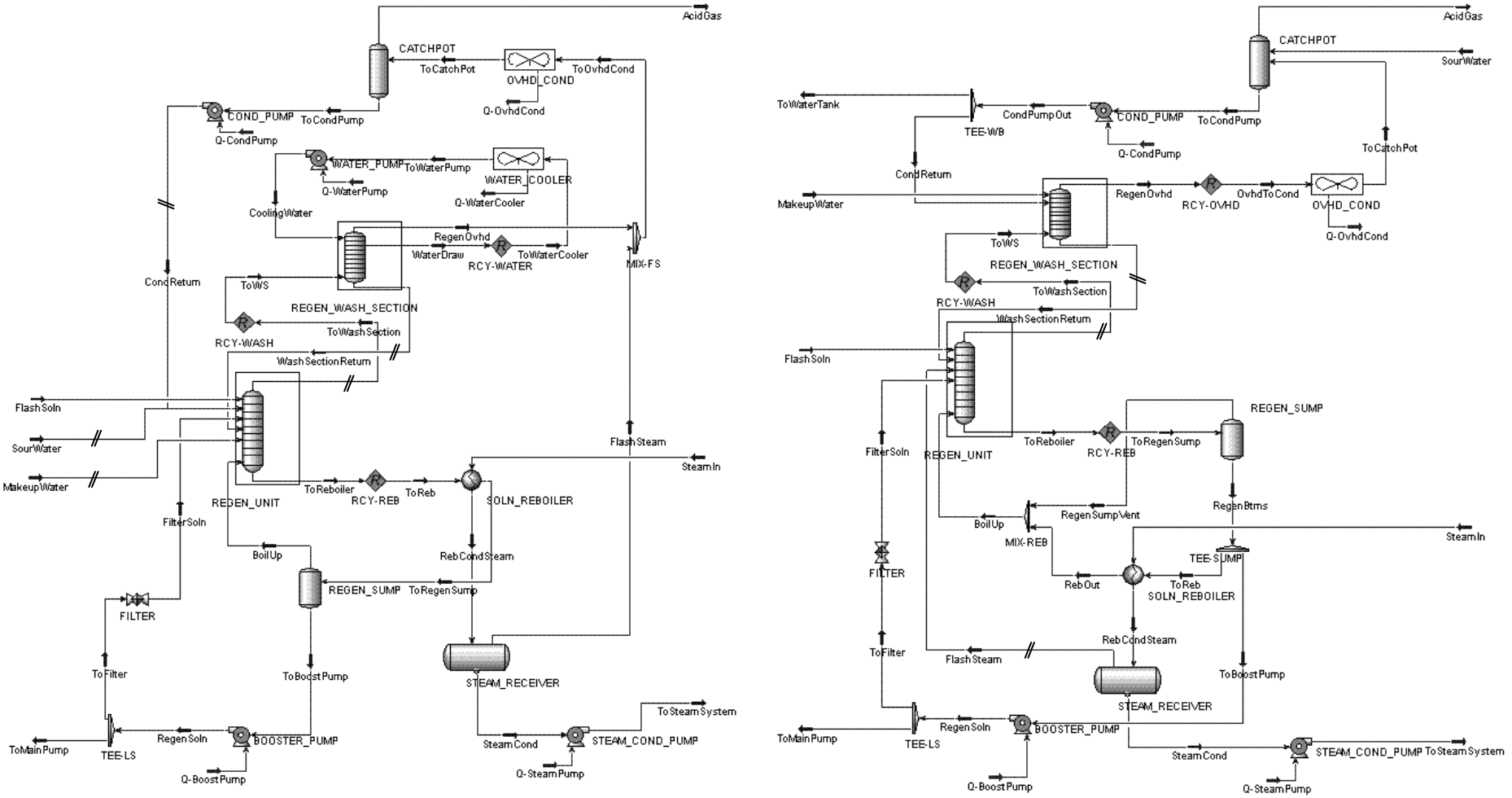

(a) **(b)**

Figure 7.2.1: Process flow diagrams of the two most dissimilar regenerator column models in HYSYS®. (a) The regenerator model for CO_2 train #1. (b) The regenerator model for CO_2 train #7. The // denote a change in property package.

7.3 Preliminary Column Model Simulations

A series of preliminary simulations were undertaken to investigate the performance of the individual HYSYS® absorber and regenerator column models. The results obtained from these column model simulations are discussed below.

7.3.1 Equilibrium Stage Model Performance

Using the first set of plant operating data provided in Table 2.1.2 and the default column stage efficiencies of 100% (i.e. equilibrium stages, $\eta = 1$), steady-state simulations of the absorber and regenerator columns in the Moomba CO_2 trains were performed. Figure 7.3.1 shows the acid gas composition (in the vapour phase for the absorbers and in the liquid phase for the regenerators) and temperature profiles predicted for the columns in CO_2 trains #1 and #7. The corresponding profiles for the remaining CO_2 trains were very similar to these, and are provided in Figures H.1.1 and H.1.2 in Appendix H.

Excessively high levels of acid gas absorption were predicted in all seven absorbers, with an average deviation of -82.0% between the predicted sweet gas CO_2 content and the plant data. The vapour phase composition profiles indicated extremely rapid removal of CO_2 and H_2S near the bottom of the absorbers, considerably more so than observed for the corresponding Aspen Custom Modeler simulations® in Chapter 4. This was reflected in the column temperature profiles, which featured sharper temperature bulges than observed for the Aspen Custom Modeler simulations®.

In contrast, much better agreement was observed between the plant data and the predicted profiles for the equilibrium stage HYSYS® regenerator models. The predicted CO_2 loading values for the regenerated solution were found to be within ±7% of the corresponding data values. The liquid phase composition profiles and the phase temperature profiles were also found to agree well with those from the corresponding Aspen Custom Modeler simulations® in Chapter 4.

The results of these equilibrium stage simulations indicated that the equilibrium stage approach was suitable for the CO_2 train regenerators. However, the equilibrium stage approach was inadequate for modelling the absorber columns since it greatly over-predicted the level of acid gas absorption. This suggested that decreasing the absorber stage efficiencies to below 100% (i.e. non-equilibrium stages, $\eta < 1$) would reduce the predicted acid gas absorption and therefore more accurately reflect the actual performance of the CO_2 train absorbers.

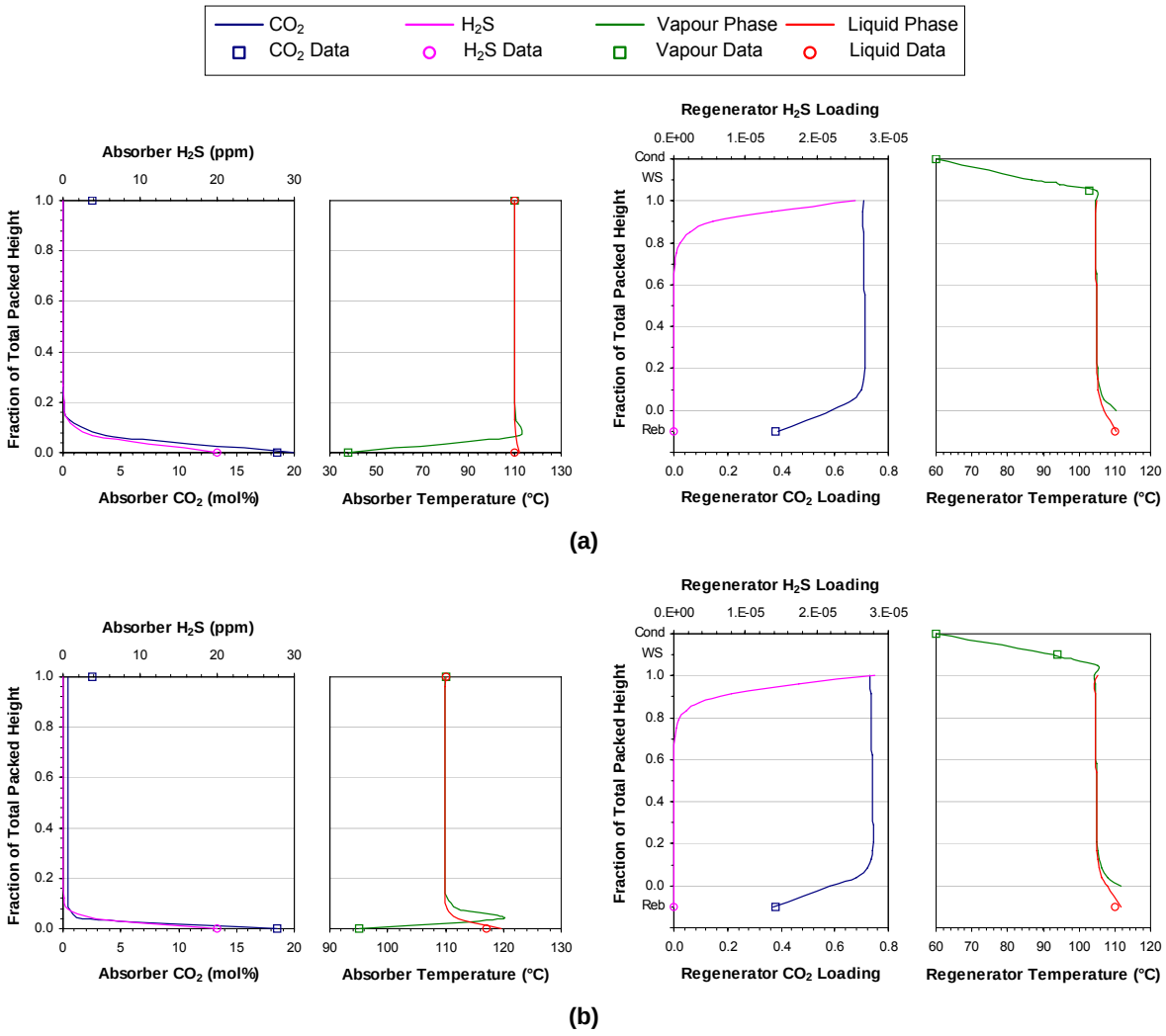

Figure 7.3.1: Equilibrium stage simulation results for the absorber and regenerator columns. (a) CO_2 train #1. (b) CO_2 train #7. (Cond = condenser, WS = wash section, Reb = reboiler) Note: The CO_2 and H_2S loadings are not strictly dimensionless; their units are actually (mol CO_2)·(mol K_2CO_3)$^{-1}$ and (mol H_2S)·(mol K_2CO_3)$^{-1}$.

7.3.2 Sensitivity to Column Stage Efficiencies

To test the above hypothesis, a series of simulation runs were performed for the absorber columns in CO_2 trains #1 and #7 in which the column stage efficiencies were decreased by 25, 50, 75 and 95%. Similar simulation runs were also undertaken for the corresponding regenerator columns to determine if their performance could be further improved through the adjustment of the stage efficiencies. The results of these sensitivity analyses are shown in Figures 7.3.2 to 7.3.5. CO_2 trains #2 to #6 were not included in this study as their absorber and regenerator columns were observed to behave very similarly to those in the two tested trains.

From Figure 7.3.2, it was evident that the rate of acid gas absorption decreased with decreasing absorber stage efficiencies. Correspondingly, the acid gas content of the sweet gas increased with the decreasing stage efficiencies. However, the CO_2 absorption rate and the sweet gas CO_2 content

were only observed to be significantly affected by stage efficiencies below 25%. In contrast, any reduction in the stage efficiencies resulted in the sweet gas H_2S content increasing by several orders of magnitude. Nevertheless, the effect of the stage efficiencies on the sweet gas H_2S content was still relatively inconsequential since the sweet gas H_2S content was extremely low (≤ 15 ppm).

Figure 7.3.3 compares the absorber column profiles for stage efficiencies of 5, 25 and 100% (η = 0.05, 0.25 and 1). It was observed that reducing the stage efficiencies from 100 to 25% resulted in composition and temperature profiles that more closely resembled those obtained from the Aspen Custom Modeler® simulations in Chapter 4. However, decreasing the stage efficiencies to 5% led to the significant under-absorption of CO_2. This indicated the performance of the HYSYS® absorber models could be made to more accurately reflect that of the actual CO_2 train absorbers if column stage efficiencies between 5 and 25% were used.

Like the absorber models, it was found that the smaller the column stage efficiencies, the more significant their effect on the regenerator models. However, the relative changes observed for the acid gas desorption rate and on the regenerated solution CO_2 loading were still relatively minor, being no more than ±12%, as shown in Figure 7.3.4. The relative changes in the regenerated solution H_2S loading were of a few orders of magnitude, but were still relatively inconsequential since the H_2S loading was extremely low (around the order of 10^{-9}).

Figure 7.3.5 shows how the regenerator column profiles became increasingly distorted as the stage efficiencies decreased from 100 to 5%, resulting in poorer agreement with the profiles obtained for the Aspen Custom Modeler® simulations in Chapter 4. This suggested that unlike the absorber models, the performance of the regenerator models could not be improved through the use of the column stage efficiencies.

As for the regenerator models developed in Aspen Custom Modeler®, adjustment of the steam flow to the solution reboilers was considered a more appropriate method of improving the performance of the HYSYS® regenerator models. Figure 7.3.6 illustrates the effect of ±15% changes on the performance of the equilibrium stage HYSYS® regenerator models. The regenerator models were found to be highly sensitive to changes in the reboiler steam flow; however, these changes did not cause any distortion of the column profiles, unlike the changes to the column stage efficiencies. These findings confirmed the suitability of using equilibrium stages for the regenerator column models. They also reflected the ineffectiveness of the model adjustments on the Aspen Custom Modeler® regenerator models, compared to the corresponding absorber models.

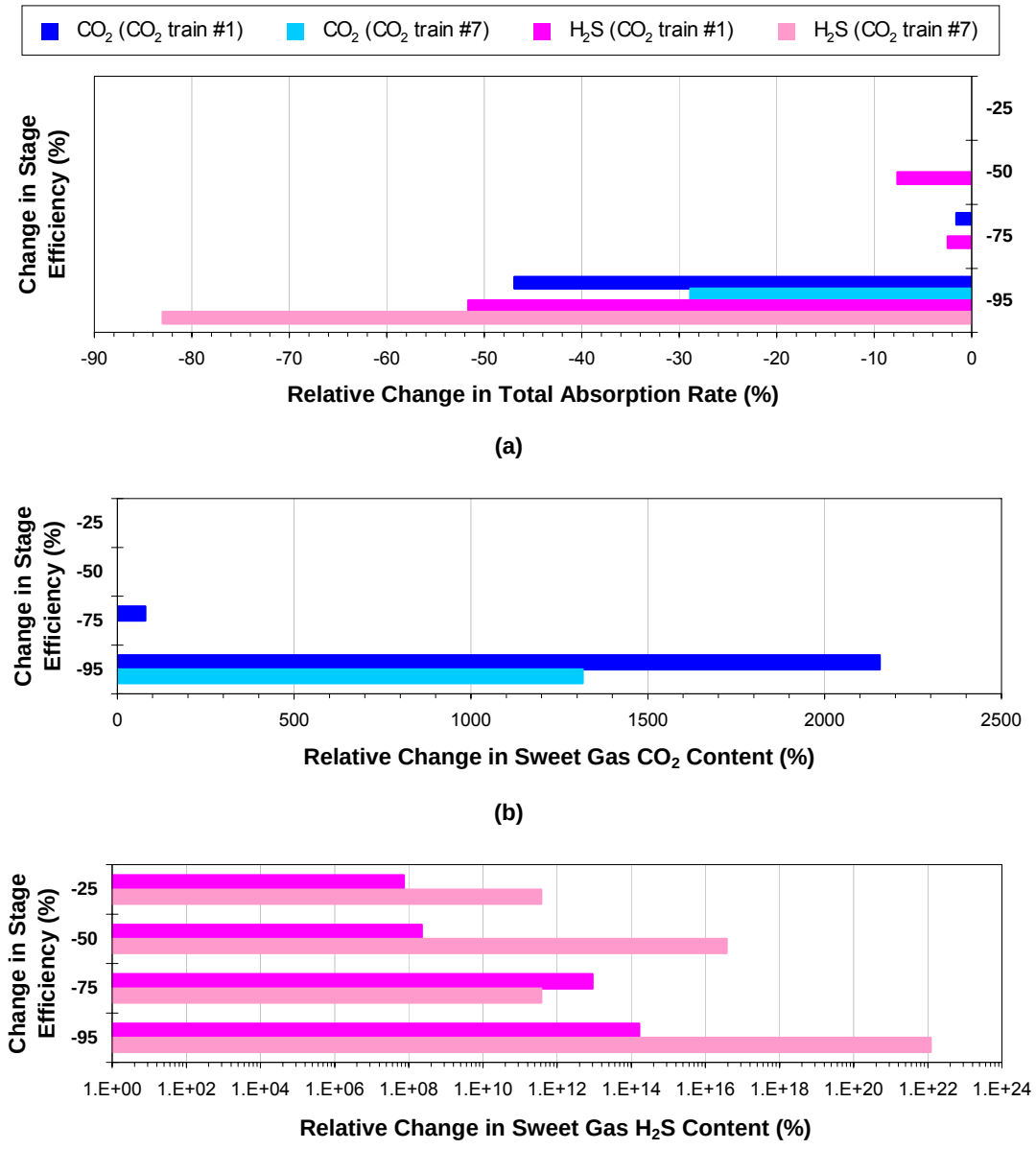

Figure 7.3.2: Sensitivity analysis results for the absorber models. Relative changes in (a) the total absorption rates, (b) the sweet gas CO_2 content and (c) the sweet gas H_2S content.

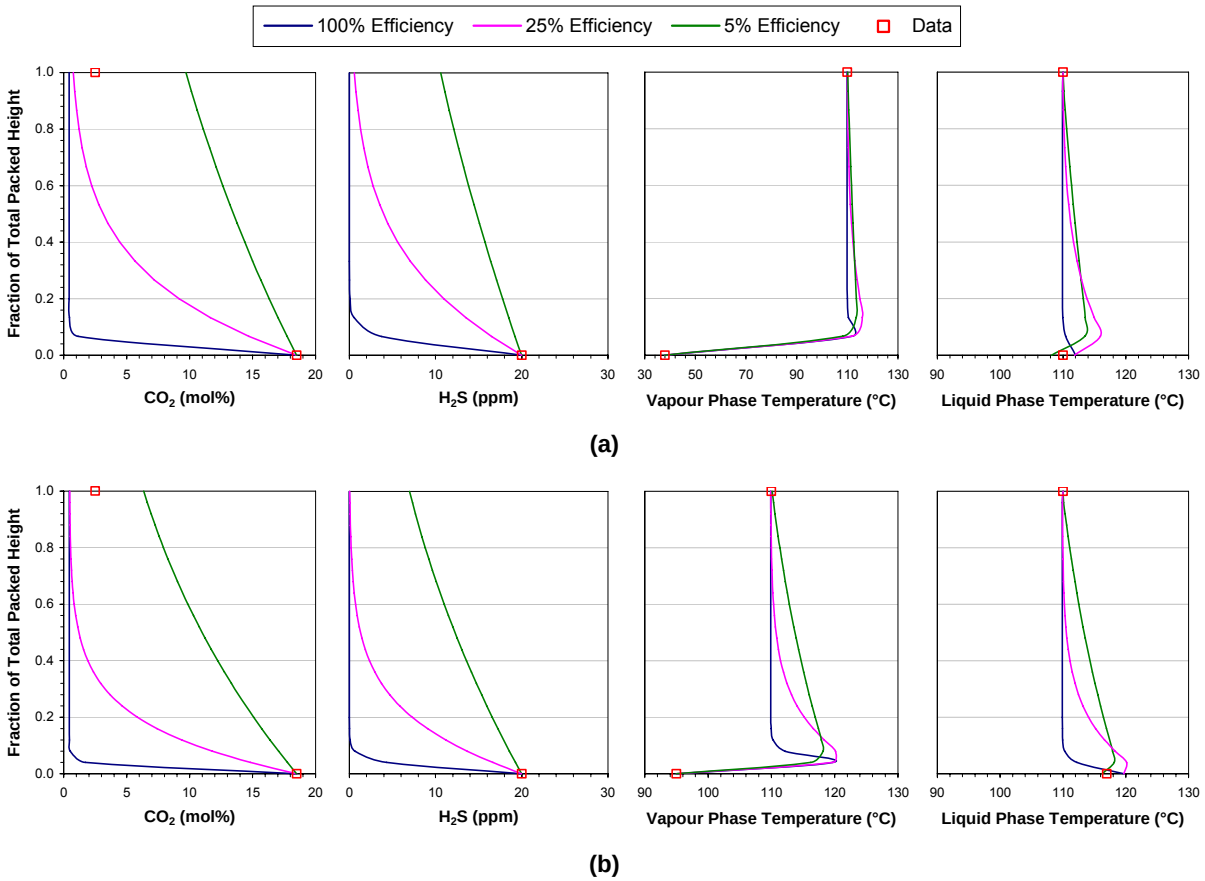

Figure 7.3.3: Effect of the column stage efficiencies on the absorber composition and temperature profiles. (a) CO_2 train #1. (b) CO_2 train #7.

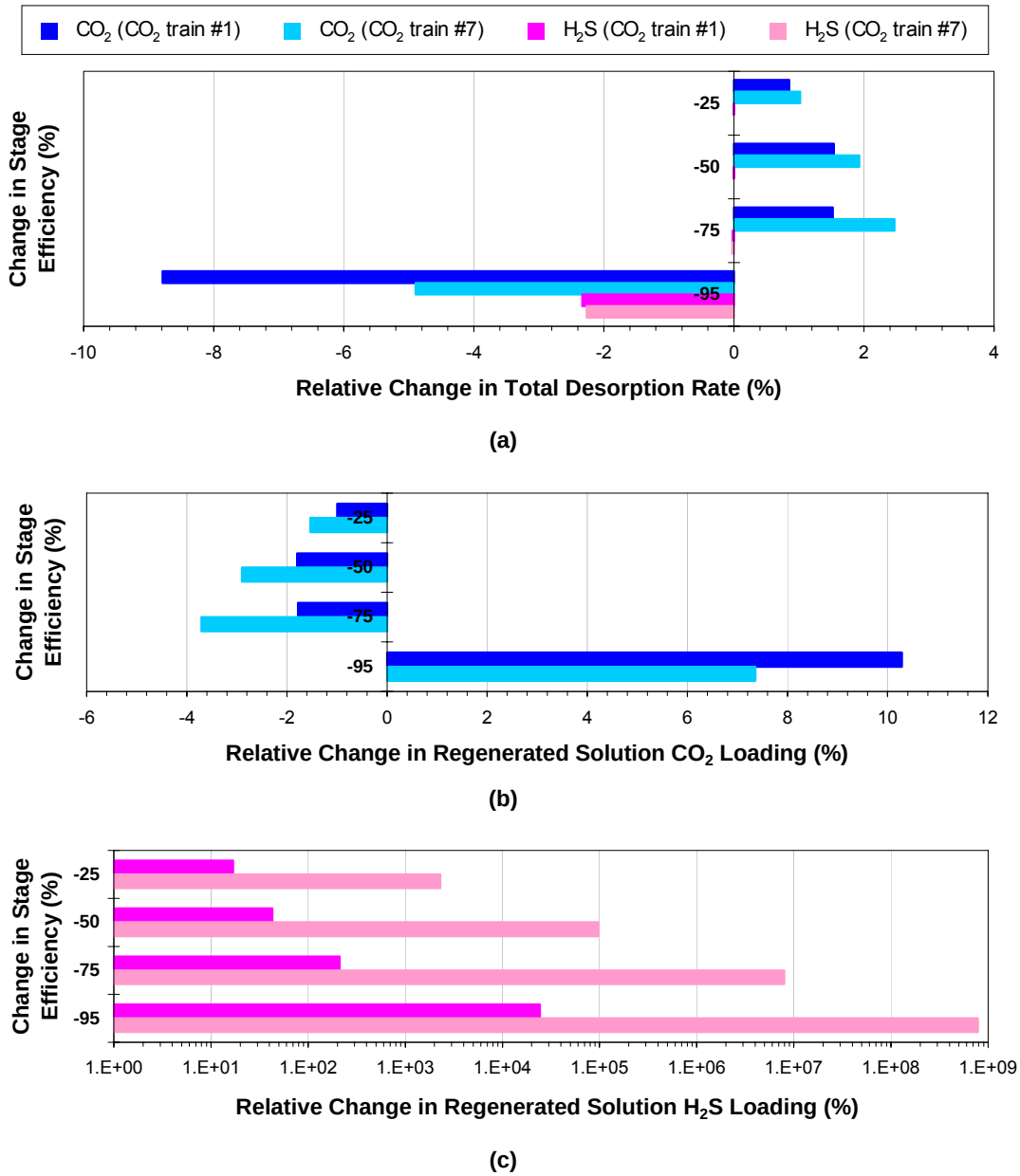

Figure 7.3.4: Sensitivity analysis results for the regenerator models. Relative changes in (a) the total desorption rates, (b) the regenerated solution CO_2 loading and (c) the regenerated solution H_2S loading.

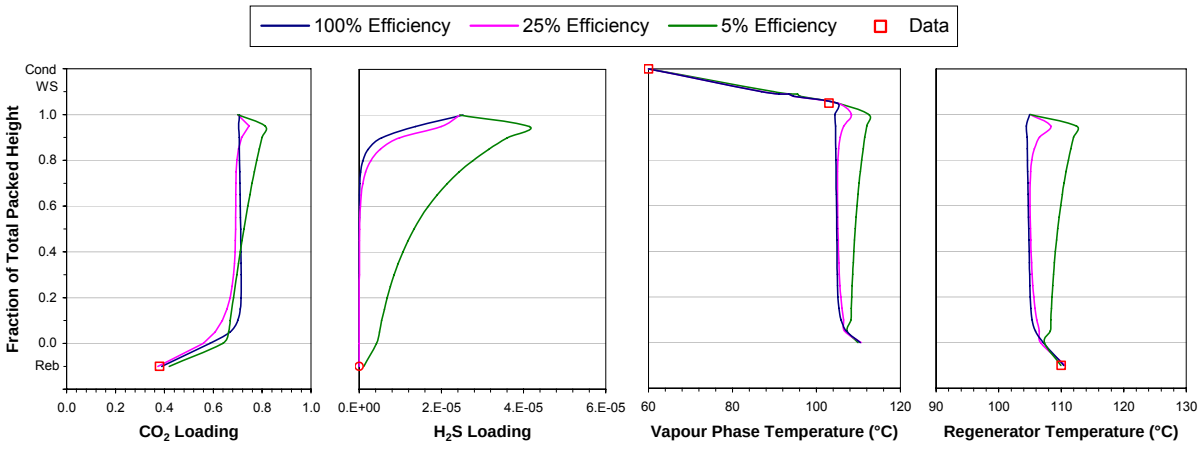

(a)

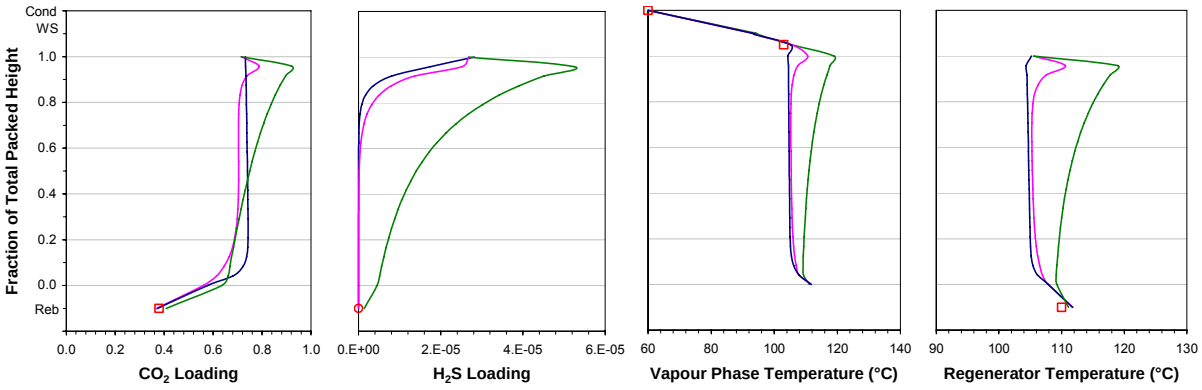

(b)

Figure 7.3.5: Effect of the column stage efficiencies on the regenerator composition and temperature profiles. (a) CO_2 train #1. (b) CO_2 train #7. (Cond = condenser, WS = wash section, Reb = reboiler)

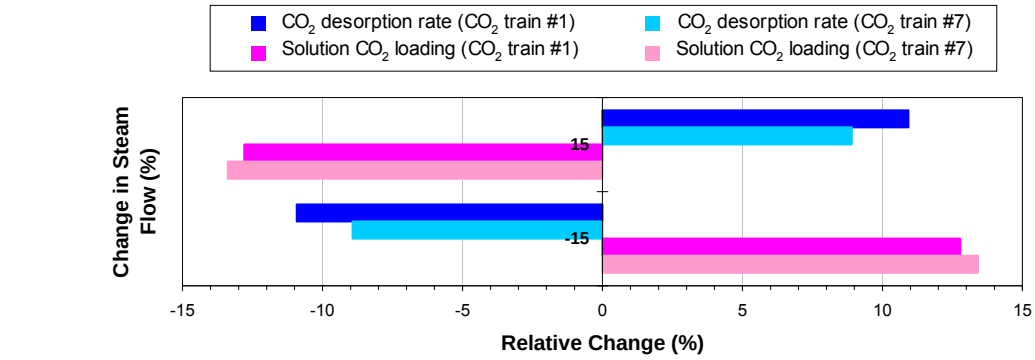

(a)

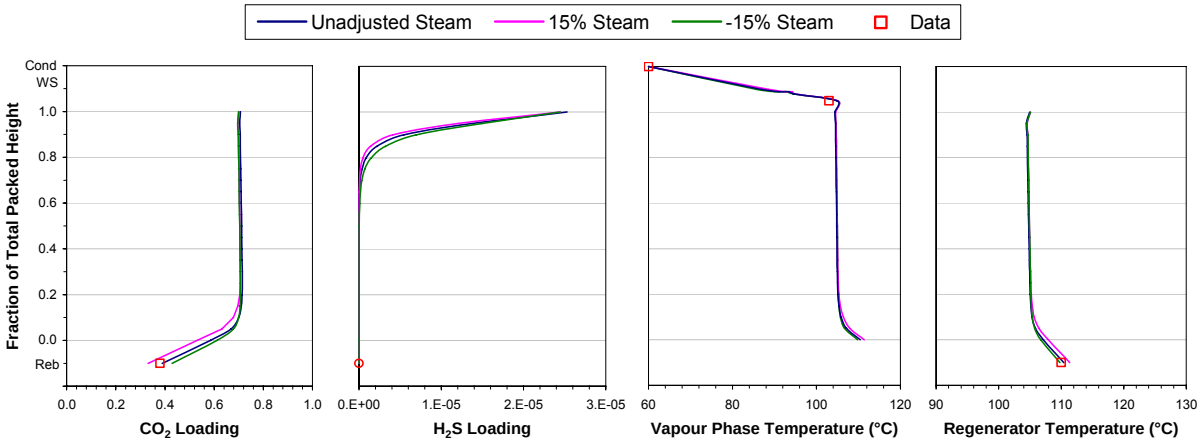

(b)

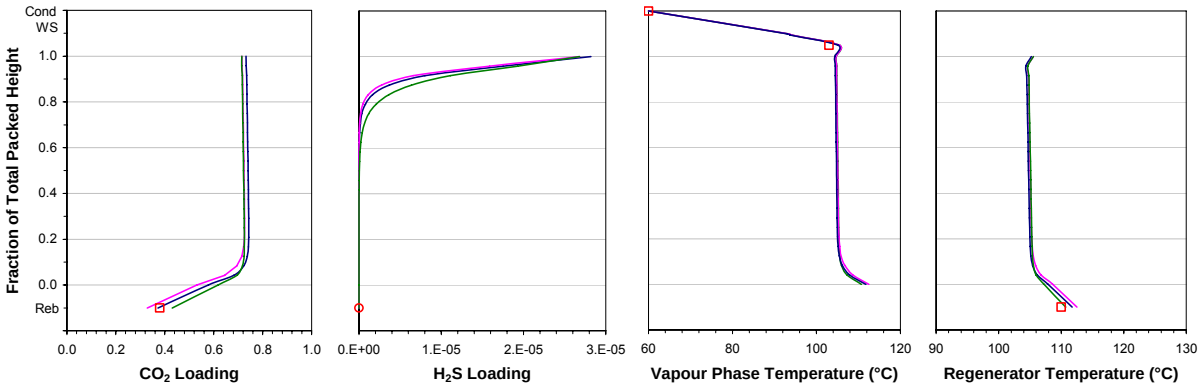

(c)

Figure 7.3.6: Effect of the reboiler steam flow on the regenerator column performance. The effect on (a) the total CO_2 desorption rate and the regenerated solution CO_2 loading, and the effect on the regenerator composition and temperature profiles for (b) CO_2 train #1 and (c) CO_2 train #7. (Cond = condenser, WS = wash section, Reb = reboiler)

7.4 Column Stage Efficiency Correlations

Based on the findings of the above sensitivity study, it was decided that adjustment of the column stage efficiencies was only required for the absorber column models. The results of the Aspen Custom Modeler® parametric studies in Chapter 5 were used to develop stage efficiency correlations of the form:

$$\begin{aligned} E_{stage} = {} & C_0 + C_1 \cdot T_{RG} + C_2 \cdot T_{RG}^{\,2} + C_3 \cdot \hat{G}_{RG} + C_4 \cdot \hat{G}_{RG}^{\,2} + C_5 \cdot 100 \cdot y_{RG,CO_2} \\ & + C_6 \cdot 100 \cdot y_{RG,CO_2}^{\,2} + C_7 \cdot T_{LS} + C_8 \cdot T_{LS}^{\,2} + C_9 \cdot \hat{L}_{LS} + C_{10} \cdot \hat{L}_{LS}^{\,2} \\ & + C_{11} \cdot 100 \cdot wf_{LS,K_2CO_3} + C_{12} \cdot 100 \cdot wf_{LS,K_2CO_3}^{\,2} + C_{13} \cdot F_{LS,CO_2} \\ & + C_{14} \cdot F_{LS,CO_2}^{\,2} + C_{15} \cdot P_{Abs} + C_{16} \cdot P_{Abs}^{\,2} \end{aligned} \qquad (7.4.1)$$

where E_{stage} is the overall stage efficiency (between 0 and 1), T is the temperature in °C, $\hat{G}$ is the volumetric vapour phase flow in sm^3/h, $\hat{L}$ is the volumetric liquid phase flow in m^3/h, y_{CO_2} is the dry gas CO_2 mole fraction, $wf_{K_2CO_3}$ is the equivalent weight fraction of K_2CO_3, F_{CO_2} is the solution CO_2 loading, and P_{Abs} is the average absorber column pressure in bar. The subscripts RG and LS denote respectively the raw gas and lean solution entering the absorber.

The overall stage efficiency approach was used instead of individual component stage efficiencies for two reasons. Firstly, the component stage efficiencies are restricted to steady-state simulations, whereas overall stage efficiencies are applicable to both steady-state and dynamic simulations. Secondly and more importantly, unlike the component stage efficiencies, the overall stage efficiencies can be specified via HYSYS® macros written in the WinWrap™ Basic programming language (which is very similar to and is compatible with Visual Basic for Applications™). Since the stage efficiencies were expected to change during the course of a simulation due to changes in the column conditions as part of the convergence process, this feature was essential for the column stage efficiencies to be automatically updated upon the calculation of new efficiency values.

To simplify the calculation and specification of the column stage efficiencies, the stages in each absorber model were assumed to be of the same efficiency, instead of being assigned individual overall stage efficiency values. This approach required only one correlation for each absorber model, as opposed to one correlation per model stage, thereby simplifying the regression of the coefficient values. Very good results were obtained with this assumption, as indicated in Tables 7.4.1 and 7.4.2 and Figures 7.4.1 and 7.4.1. For all seven absorbers, the sweet gas CO_2 content predicted using the correlated stage efficiencies were found to be within ±10% of the corresponding Aspen Custom Modeler® values, with average absolute deviations between 0.01 and 1.60%. Consequently, the additional complexity associated with the specification of individual overall stage efficiencies could not be justified.

Table 7.4.1: Coefficients for the steady-state column stage efficiency correlations.

Absorber	#1	#2	#3	#4	#5	#6	#7
$C_0 \times 10^1$	2.456	2.154	-0.019	1.895	1.997	0.700	16.467
$C_1 \times 10^6$	-7.943	-2.514	-14.000	-5.608	-3.300	-5.100	-55.800
C_2	0.000	0.000	0.000	0.000	0.000	0.000	0.000
$C_3 \times 10^6$	-1.572	-1.355	-0.529	-0.929	-0.953	-0.591	1.261
C_4	0.000	0.000	0.000	0.000	0.000	0.000	0.000
$C_5 \times 10^3$	-4.783	-1.670	7.851	-5.762	-0.103	2.968	-46.452
$C_6 \times 10^4$	1.080	0.450	-2.675	1.265	0.000	-0.996	9.118
$C_7 \times 10^4$	1.322	6.150	-0.367	0.139	6.014	3.653	-4.162
$C_8 \times 10^6$	0.000	-1.871	0.000	0.000	-2.255	-1.650	0.000
$C_9 \times 10^4$	3.579	0.422	7.788	3.472	0.376	2.021	-1.670
$C_{10} \times 10^7$	-2.197	0.321	-4.742	-1.655	0.000	-0.765	1.891
$C_{11} \times 10^4$	5.539	7.625	12.871	7.044	3.054	5.775	-291.884
$C_{12} \times 10^6$	0.000	-4.773	0.000	0.000	0.000	0.000	639.126
$C_{13} \times 10^1$	-3.704	-2.150	-7.416	-4.382	-2.111	-3.331	-31.130
$C_{14} \times 10^1$	2.446	1.158	6.074	3.305	1.140	2.458	32.500
$C_{15} \times 10^5$	-8.875	-15.650	3.175	-2.900	-11.925	-3.100	79.825
C_{16}	0.000	0.000	0.000	0.000	0.000	0.000	0.000
MAD (%)	0.24	0.10	1.57	0.70	0.57	0.58	9.63
AAD (%)	0.06	0.01	0.18	0.11	0.12	0.08	1.60

Note: MAD = Maximum absolute deviation for the predicted sweet gas CO_2 content. AAD = Average absolute deviation for the predicted sweet gas CO_2 content.

Table 7.4.2: Coefficients for the dynamic column stage efficiency correlations.

Absorber	#1	#2	#3	#4	#5	#6	#7
$C_0 \times 10^2$	7.187	5.040	-5.054	7.433	7.736	0.706	103.800
$C_1 \times 10^5$	9.928	9.542	4.300	3.972	4.600	3.150	0.240
$C_2 \times 10^7$	-3.958	-3.601	0.000	0.000	0.000	0.000	0.000
$C_3 \times 10^7$	6.042	8.061	6.635	1.494	1.516	0.971	15.472
$C_4 \times 10^{12}$	-3.080	-4.369	-3.383	-0.662	-0.345	-0.382	-5.304
$C_5 \times 10^3$	-2.527	-0.848	4.315	-3.735	-0.311	1.820	-32.629
$C_6 \times 10^5$	4.942	1.444	-15.626	7.713	0.000	-6.625	65.487
$C_7 \times 10^5$	14.744	34.338	9.425	5.662	47.186	32.353	-23.168
$C_8 \times 10^7$	0.000	-7.754	-2.645	0.000	-15.794	-12.969	0.000
$C_9 \times 10^5$	17.042	1.998	45.608	21.244	2.438	13.110	-13.524
$C_{10} \times 10^7$	-1.020	0.143	-2.758	-1.004	0.000	-0.494	1.355
$C_{11} \times 10^4$	2.346	3.473	7.607	4.138	1.713	3.608	-193.693
$C_{12} \times 10^6$	0.000	-2.829	-0.278	0.000	0.000	0.000	421.163
$C_{13} \times 10^1$	-1.848	-0.940	-4.544	-2.744	-1.327	-2.164	-20.549
$C_{14} \times 10^1$	1.251	0.503	3.769	2.083	0.711	1.592	21.558
$C_{15} \times 10^4$	-6.230	-6.185	-4.469	-4.114	-5.276	-3.276	1.903
C_{16}	0.000	0.000	0.000	0.000	0.000	0.000	0.000
MAD (%)	0.27	0.22	1.57	0.75	0.58	0.61	9.95
AAD (%)	0.07	0.03	0.18	0.11	0.10	0.07	1.64

Note: MAD = Maximum absolute deviation for the predicted sweet gas CO_2 content. AAD = Average absolute deviation for the predicted sweet gas CO_2 content.

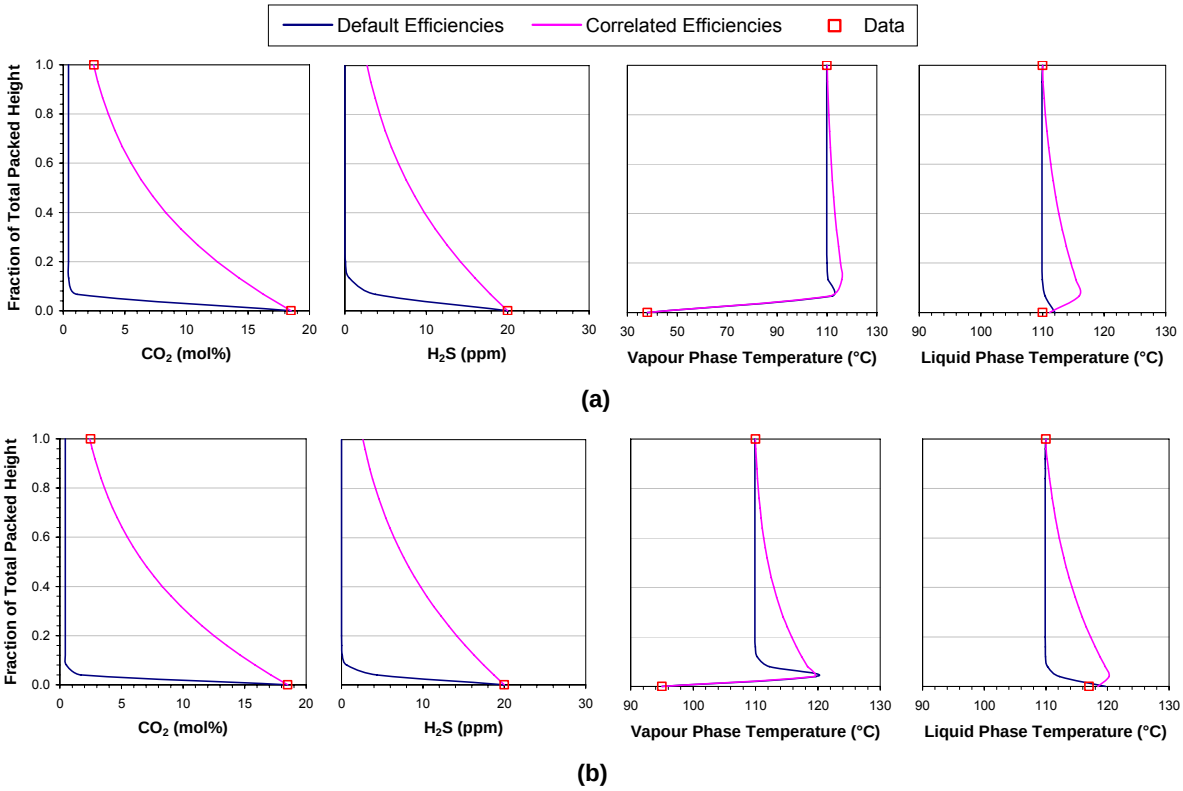

Figure 7.4.1: Effect of the correlated overall stage efficiencies on the steady-state absorber columns. (a) CO_2 train #1. (b) CO_2 train #7.

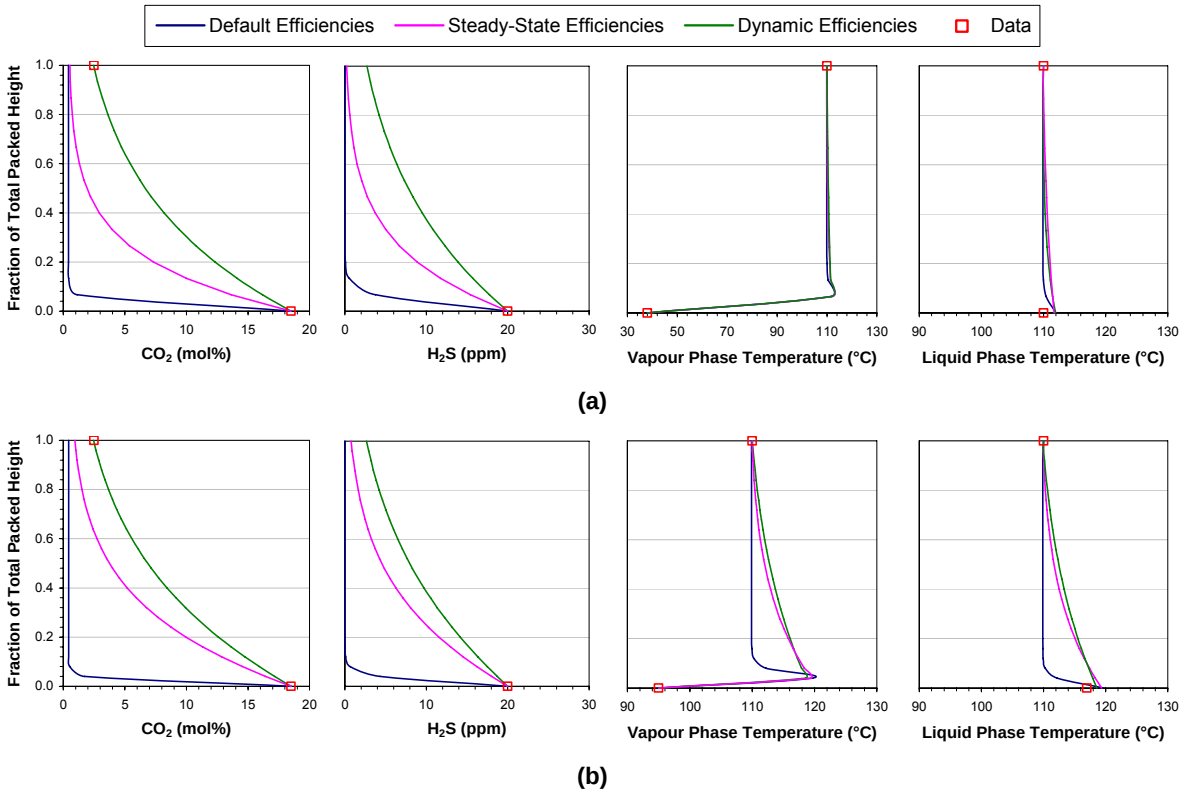

Figure 7.4.2: Effect of the correlated overall stage efficiencies on the steady-state behaviour of the dynamic absorber columns. (a) CO_2 train #1. (b) CO_2 train #7.

Values for the coefficients C_0 to C_{16} for the steady-state absorber models are given in Table 7.4.1, while Table 7.4.2 lists the coefficient values for the dynamic absorber models. The two different sets of coefficients were required due to the different manner in which the overall stage efficiencies are treated in the two simulation modes, as explained in Section 6.1.3.

Both sets of coefficient values were derived via the same procedure. First, a set of overall stage efficiencies corresponding to the results of the Aspen Custom Modeler® parametric studies were determined by iterative adjustment of the efficiencies until the steady-state CO_2 content of the sweet gas produced by the HYSYS® absorber models matched the Aspen Custom Modeler® results to within ±0.001%. The coefficients for equation (7.4.1) were then regressed from the resulting set of efficiencies using the Microsoft® Excel Regression Tool.

It should be noted that while this method of correlating the overall stage efficiencies produced excellent results for the sweet gas CO_2 content, it resulted in the significant over-prediction of the H_2S content. On average, the sweet gas H_2S concentrations calculated by the HYSYS® absorber models were 94.8% greater than the corresponding Aspen Custom Modeler® values. This limitation was however deemed acceptable for this work since the primary focus of the CO_2 trains is to remove CO_2.

The overall stage efficiency correlations were implemented in HYSYS® spreadsheets, like the one shown in Figure 7.4.3, which were linked to the HYSYS® absorber models. This enabled the automatic re-calculation of the stage efficiencies upon any changes to the relevant model process conditions. Macros, like the one provided in Table 7.4.3, were attached to the absorber models (in the form of HYSYS® user variables) to automatically update the absorber stage efficiencies with the newly calculated values. Separate macros (and therefore user variables) were set up for the steady-state and dynamic simulations since the two simulation modes involved different subroutines.

The absorber composition and temperature profiles predicted with the correlated column overall stage efficiencies for CO_2 trains #1 and #7 are given in Figures 7.4.1 and 7.4.2. The corresponding column profiles for the other five trains are included as Figures H.1.3 to H.1.6 in Appendix H. The need for separate steady-state and dynamic stage efficiency correlations was evident in Figure 7.4.2, which shows the under-prediction of the sweet gas CO_2 content at steady-state when the steady-state efficiencies were used for the dynamic absorber models.

It should also be noted that the steady-state temperature profiles for the dynamic absorbers differed in shape from those for the steady-state absorbers, most noticeably for the liquid phase temperature profiles. While the steady-state temperatures of the rich solution and sweet gas leaving the dynamic absorbers closely agreed with the temperatures predicted by the steady-state absorber models (within ±1°C), the distinctive temperature bulges in the lower part of the columns were absent. The absence of these characteristic bulges did not appear to adversely affect the dynamic simulation results, and was most likely due to the different definition of the overall stage efficiencies in dynamic simulations.

In dynamic simulations, the overall stage efficiency determines how much of the vapour entering a stage actually participates in the flash calculation for that stage, whereas in steady-state simulations, it represents the deviation of the vapour phase leaving a stage from the vapour that is in equilibrium with the liquid phase leaving that stage. As these two definitions are not directly equivalent, and given the low stage efficiencies of the absorber models (<0.25), it was not unexpected that there should be some dissimilarity between the results produced by the steady-state and dynamic simulations.

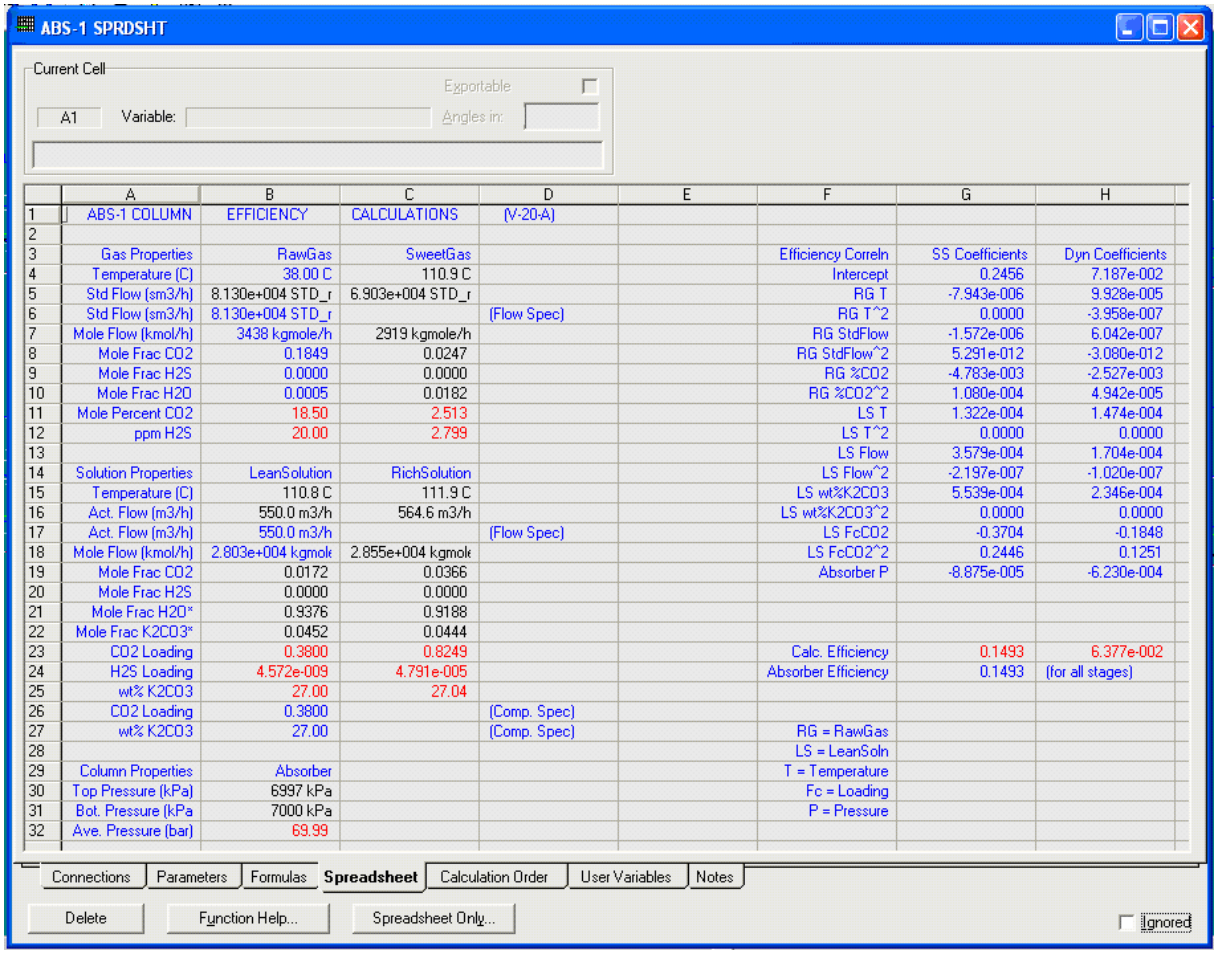

	A	B	C	D	E	F	G	H
1	ABS-1 COLUMN	EFFICIENCY	CALCULATIONS	(V-20-A)				
2								
3	Gas Properties	RawGas	SweetGas			Efficiency Correln	SS Coefficients	Dyn Coefficients
4	Temperature (C)	38.00 C	110.9 C			Intercept	0.2456	7.187e-002
5	Std Flow (sm3/h)	8.130e+004 STD_r	6.903e+004 STD_r			RG T	-7.943e-006	9.928e-005
6	Std Flow (sm3/h)	8.130e+004 STD_r		(Flow Spec)		RG T^2	0.0000	-3.958e-007
7	Mole Flow (kmol/h)	3438 kgmole/h	2919 kgmole/h			RG StdFlow	-1.572e-006	6.042e-007
8	Mole Frac CO2	0.1849	0.0247			RG StdFlow^2	5.291e-012	-3.080e-012
9	Mole Frac H2S	0.0000	0.0000			RG %CO2	-4.783e-003	-2.527e-003
10	Mole Frac H2O	0.0005	0.0182			RG %CO2^2	1.080e-004	4.942e-005
11	Mole Percent CO2	18.50	2.513			LS T	1.322e-004	1.474e-004
12	ppm H2S	20.00	2.799			LS T^2	0.0000	0.0000
13						LS Flow	3.579e-004	1.704e-004
14	Solution Properties	LeanSolution	RichSolution			LS Flow^2	-2.197e-007	-1.020e-007
15	Temperature (C)	110.8 C	111.9 C			LS wt%K2CO3	5.539e-004	2.346e-004
16	Act. Flow (m3/h)	550.0 m3/h	564.6 m3/h			LS wt%K2CO3^2	0.0000	0.0000
17	Act. Flow (m3/h)	550.0 m3/h		(Flow Spec)		LS FcCO2	-0.3704	-0.1848
18	Mole Flow (kmol/h)	2.803e+004 kgmole	2.855e+004 kgmole			LS FcCO2^2	0.2446	0.1251
19	Mole Frac CO2	0.0172	0.0366			Absorber P	-8.875e-005	-6.230e-004
20	Mole Frac H2S	0.0000	0.0000					
21	Mole Frac H2O*	0.9376	0.9188					
22	Mole Frac K2CO3*	0.0452	0.0444					
23	CO2 Loading	0.3800	0.8249			Calc. Efficiency	0.1493	6.377e-002
24	H2S Loading	4.572e-009	4.791e-005			Absorber Efficiency	0.1493	(for all stages)
25	wt% K2CO3	27.00	27.04					
26	CO2 Loading	0.3800		(Comp. Spec)				
27	wt% K2CO3	27.00		(Comp. Spec)		RG = RawGas		
28						LS = LeanSoln		
29	Column Properties	Absorber				T = Temperature		
30	Top Pressure (kPa)	6997 kPa				Fc = Loading		
31	Bot. Pressure (kPa	7000 kPa				P = Pressure		
32	Ave. Pressure (bar)	69.99						

Figure 7.4.3: An example HYSYS® spreadsheet for calculating the absorber overall stage efficiencies.

Table 7.4.3: An example HYSYS® macro for updating the absorber overall stage efficiencies.

```
'Updates the column stage efficiency for ABS-1

Option Explicit

Sub PostSolve() 'Sub DynCompositionPreStep() for dynamic simulations

  On Error Resume Next

  Dim hyCase As HYSYS.SimulationCase
  Dim hySprdsht As HYSYS.SpreadsheetOp
  Dim hyCol As HYSYS.ColumnOp
  Dim hyColStage As HYSYS.ColumnStage

  Dim dblOldEff As Double
  Dim dblNewEff As Double
  Dim tol As Double
  Dim intCount As Integer
  Dim intStages As Integer

  Set hyCase = ActiveCase
  Set hySprdsht = hyCase.Flowsheet.Operations.Item("ABS-1 SPRDSHT")
  Set hyCol = hyCase.Flowsheet.Operations.Item("V-20-A")

  intStages = hyCol.ColumnFlowsheet.ColumnStages.Count
  dblNewEff = hySprdsht.Cell("G23").CellValue
  dblOldEff = hySprdsht.Cell("G24").CellValue
  tol = 1e-5

  'Compare old and new values of calculated stage efficiency.  If less than tol, don't update.
  If Abs((dblNewEff-dblOldEff)/dblOldEff) <= tol Then
    Exit Sub
  Else
    'Don't update if calculated stage efficiency is outside the the range (0,1)
    If dblNewEff <= 0 Or dblNewEff > 1 Then
      Exit Sub
    End If
    'Update stage efficiency
    For intCount = 0 To (intStages-1)
      Set hyColStage = hyCol.ColumnFlowsheet.ColumnStages(intCount)
      hyColStage.SeparationStage.OverallEfficiencyValue = dblNewEff
    Next
    'Send update alert to Trace Window
    hyCase.Application.Trace "ABS-1 Stage Efficiency modified from " & dblOldEff & " to " & dblNewEff, False
  End If

  'Clear objects
  Set hyCase = Nothing
  Set hySprdsht = Nothing
  Set hyCol = Nothing
  Set hyColStage = Nothing

End Sub
```

7.5 Summary

In summary, this chapter focussed on the development of the absorber and regenerator column models for the HYSYS® CO_2 train process models. Particular attention was given to the correlation and implementation of column stage efficiencies to better represent the effects of the solution chemistry.

Detailed column models were constructed for the absorbers and regenerators in the CO_2 trains. The standard HYSYS® absorber operation formed the basis of both types of column models by representing the packed and/or tray sections of these columns. In addition, a variety of other standard HYSYS® operations, such as separator, pump and heat exchanger operations, were used to model various auxiliary parts, including the column sumps, circulation pumps and solution reboilers. The two property packages selected in Chapter 6, i.e. the PR and Sour PR property packages, were applied to different sections of the column models. The former was used in sections where the hypothetical K_2CO_3* component was present, while the latter was applied to sections in which it was absent.

Preliminary simulations were performed to investigate the performance of the column models using the default equilibrium stages, and to determine the effect of varying the column stage efficiencies. It was observed that the equilibrium stage approach was suitable for the regenerator column models, but not for the absorber column models. Significant improvements in the performance of the absorber column models were obtained by reducing the stage efficiencies. In contrast, the reboiler steam flow was found to have a greater effect on the performance of the regenerator column models. This was analogous to the Aspen Custom Modeler® column models, in that the model adjustments were only useful for the absorber models.

Consequently, the column stage efficiency correlations were only applied to the HYSYS® absorber column models. These correlations were developed from the results of the Aspen Custom Modeler® parametric studies in Chapter 5, thereby linking the HYSYS® absorber models to the rigorous rate-based non-equilibrium models from Chapter 4. Two sets of correlations were required, i.e. one for steady-state simulations and another for dynamic simulations, due to the differing definitions for the column stage efficiencies for the two simulation modes. These correlations were implemented via spreadsheet operations, which were linked to the absorber column models through HYSYS® user variables. This enabled the automatic updating of the stage efficiencies during the calculation process. Very good results were obtained with the correlated stage efficiencies.

The above absorber and regenerator column models form the basis of the CO_2 train process models in HYSYS®. The next chapter considers the development of steady-state HYSYS® process models for the Moomba CO_2 trains.

CHAPTER 8

HYSYS® CO_2 REMOVAL TRAIN PROCESS MODEL DEVELOPMENT

This chapter concerns the development of steady-state HYSYS® process models of the Moomba CO_2 trains. Particular attention is paid to the extension of the absorber and regenerator column models that were developed in the previous chapter.

The configurations of the Moomba CO_2 trains can be divided into two key sections: the absorption circuits and the regeneration circuits. In this chapter, the absorber and regenerator column models from Chapter 7 are expanded in order to develop HYSYS® models of these absorption and regeneration circuits. Particular focus is given to the inclusion of the various ancillary operations, such as the solution pumpset, and the representation of the relevant piping and head losses.

Complete steady-state HYSYS® CO_2 train process models are then created by linking the above absorption and regeneration circuit models. As in the case of the Aspen Custom Modeler® CO_2 train models, these HYSYS® process models are compared with the plant data used in the development of the Aspen Custom Modeler® models, and are also validated against an independent set of plant data.

8.1 Ancillary Operation Models

While the absorber and regenerator column models developed in the previous chapter formed the basis of the HYSYS® CO_2 train process models, a number of ancillary operations were also required to complete the process models. The following sections describe the development of such ancillary operation models.

8.1.1 Absorption Circuit Ancillary Models

The absorption circuits encompassing the absorber columns constitute a key part of the Moomba CO_2 trains. In order to model these absorption circuits in HYSYS®, the absorber column models from Chapter 7 were expanded to include a sweet gas separator and a gas-gas heat exchanger (only in trains #3 to #7), as shown in Figure 8.1.1.

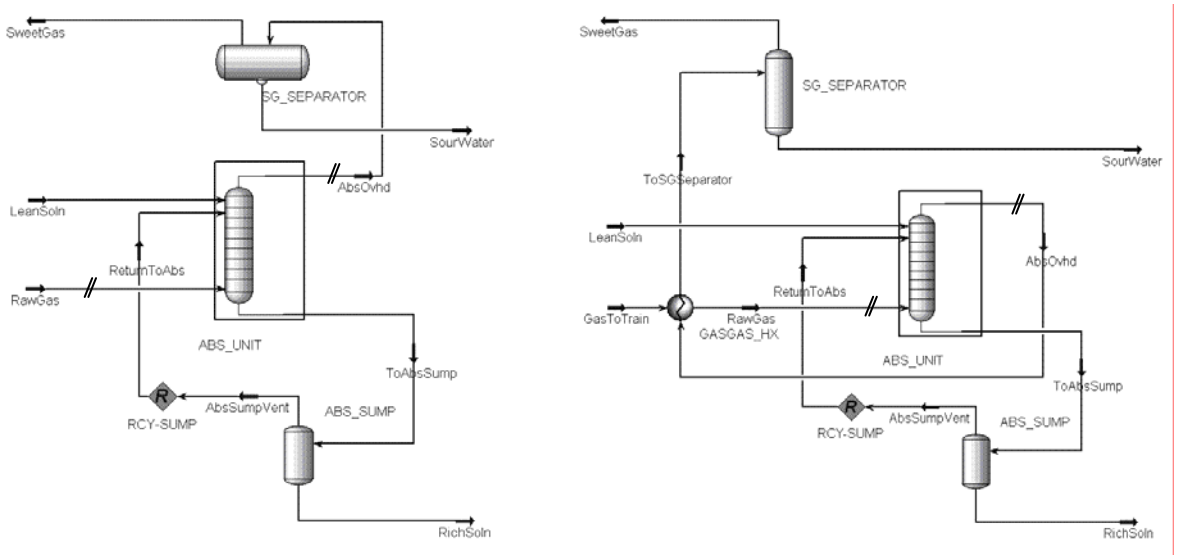

Figure 8.1.1: HYSYS® process flow diagram of the CO_2 train absorption circuits. (a) CO_2 trains #1 and #2. (b) CO_2 trains #3 to #7. The // denote a change in property package.

HYSYS® separator operations were used to model the sweet gas separators, while heat exchanger operations were used to represent the gas-gas heat exchangers. The relevant information required to size the separator and heat exchanger operations was determined from the available equipment datasheets and manuals in the Santos TIMS controlled documentation database.

Given that the gas-gas heat exchanger models did not involve the potassium carbonate solution, their thermodynamic and physical property calculations were performed using the Sour PR property package. This property package was also applied to the sweet gas separator models since it was assumed that there was no entrainment of K_2CO_3* at the top of the absorber columns, as previously discussed in Section 7.2.

8.1.2 Regeneration Circuit Ancillary Models

Another key section of the CO_2 trains are the regeneration circuits encircling the regenerator columns. In order to model these regeneration circuits in HYSYS®, the regenerator column models from Chapter 7 were expanded to include a solution pumpset model, which consisted of a main solution pump linked to a steam turbine and to a power recovery turbine (a hydraulic turbine) with a bypass valve, as illustrated in Figure 8.1.2.

A HYSYS® pump operation was used to model the main solution pump, while the steam turbine was represented by an expander operation. The pump and expander operations were both considered for the power recovery turbine since hydraulic turbines are not a default unit operation in HYSYS®. The pump and expander operations were found to give fairly similar results for the power recovery turbine, with the expander operation predicting a higher power recovery (by ≤ 10%) and a lower output temperature (by ≤ -1%) than the pump operation. Warning messages were generated about the presence of liquid in the inlet stream for the expander operation and the negative head for the pump operation, but these were non-fatal and could be safely ignored (Stone, 2005).

In the end, it was considered more appropriate to use the pump operation to represent the power recovery turbine for two reasons. First, hydraulic turbines behave like pumps in reverse and second, the expander operation is specific to gas expansion which is an isentropic process, unlike liquid expansion.

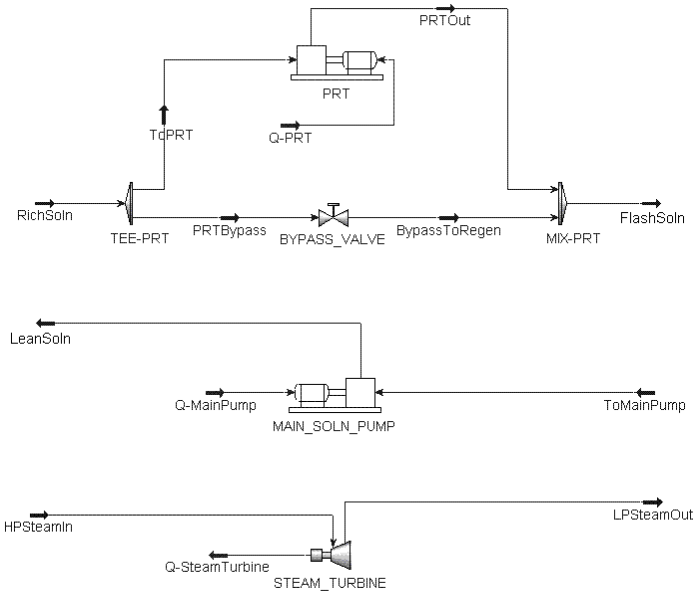

Figure 8.1.2: HYSYS® process flow diagram of the solution pumpset model.

The components of the solution pumpset model were sized according to the technical datasheets and equipment manuals available in the Santos TIMS database. The performance curves for the steam

turbine were not in the form required for the expander operation calculations, so the power output and steam input for the steam turbine were instead calculated via the HYSYS® spreadsheet shown in Figure 8.1.3.

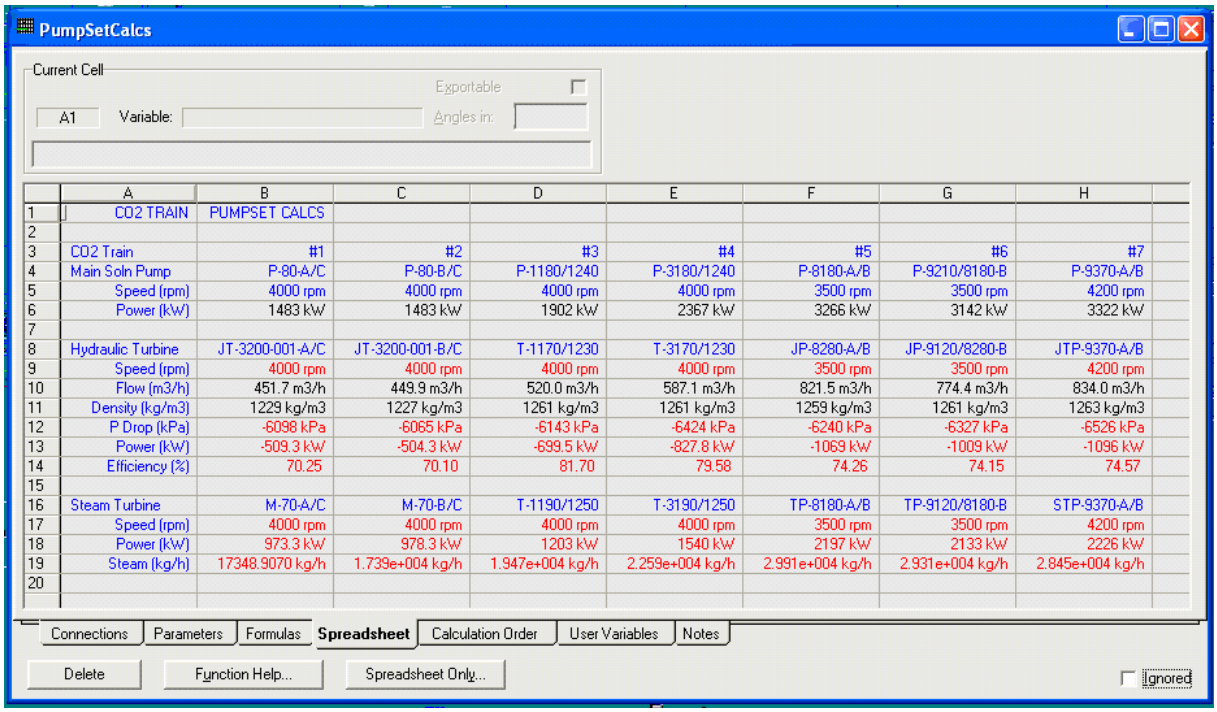

	A	B	C	D	E	F	G	H
1	CO2 TRAIN	PUMPSET CALCS						
2								
3	CO2 Train	#1	#2	#3	#4	#5	#6	#7
4	Main Soln Pump	P-80-A/C	P-80-B/C	P-1180/1240	P-3180/1240	P-8180-A/B	P-9210/8180-B	P-9370-A/B
5	Speed (rpm)	4000 rpm	4000 rpm	4000 rpm	4000 rpm	3500 rpm	3500 rpm	4200 rpm
6	Power (kW)	1483 kW	1483 kW	1902 kW	2367 kW	3266 kW	3142 kW	3322 kW
7								
8	Hydraulic Turbine	JT-3200-001-A/C	JT-3200-001-B/C	T-1170/1230	T-3170/1230	JP-8280-A/B	JP-9120/8280-B	JTP-9370-A/B
9	Speed (rpm)	4000 rpm	4000 rpm	4000 rpm	4000 rpm	3500 rpm	3500 rpm	4200 rpm
10	Flow (m3/h)	451.7 m3/h	449.9 m3/h	520.0 m3/h	587.1 m3/h	821.5 m3/h	774.4 m3/h	834.0 m3/h
11	Density (kg/m3)	1229 kg/m3	1227 kg/m3	1261 kg/m3	1261 kg/m3	1259 kg/m3	1261 kg/m3	1263 kg/m3
12	P Drop (kPa)	-6098 kPa	-6065 kPa	-6143 kPa	-6424 kPa	-6240 kPa	-6327 kPa	-6526 kPa
13	Power (kW)	-509.3 kW	-504.3 kW	-699.5 kW	-827.8 kW	-1069 kW	-1009 kW	-1096 kW
14	Efficiency (%)	70.25	70.10	81.70	79.58	74.26	74.15	74.57
15								
16	Steam Turbine	M-70-A/C	M-70-B/C	T-1190/1250	T-3190/1250	TP-8180-A/B	TP-9120/8180-B	STP-9370-A/B
17	Speed (rpm)	4000 rpm	4000 rpm	4000 rpm	4000 rpm	3500 rpm	3500 rpm	4200 rpm
18	Power (kW)	973.3 kW	978.3 kW	1203 kW	1540 kW	2197 kW	2133 kW	2226 kW
19	Steam (kg/h)	17348.9070 kg/h	1.739e+004 kg/h	1.947e+004 kg/h	2.259e+004 kg/h	2.991e+004 kg/h	2.931e+004 kg/h	2.845e+004 kg/h
20								

Figure 8.1.3: HYSYS® spreadsheet for the pumpset calculations.

This spreadsheet was also used for the power recovery turbine calculations in the steady-state simulation mode. Unlike in the dynamic simulation mode, there is no option in the steady-state mode to enable the pump operation to act as a hydraulic turbine. Consequently, the pump operation could not calculate the appropriate pressure drops from the positive head values for the power recovery turbine characteristic curves. Attempts to treat the turbine characteristic curves as having negative head values failed since these negative values could not be handled by the pump operation calculations. As a result, the "Use Curves" option was deactivated for the power recovery turbine models in the steady-state simulation mode, and the relevant characteristic curves were instead implemented in the spreadsheet.

In contrast, the spreadsheet calculations were not necessary for the power recovery turbine models in the dynamic simulation mode. Instead, the option "Pump is acting as turbine" was activated, which enabled the pump operation to calculate the pressure drop and recovered power from the characteristic curves. For this approach to work, the turbine head values had to be entered as positive values.

The physical and thermodynamic property calculations for the main solution pump and the power recovery turbine were performed with the modified PR property package. The Sour PR property

package was used for the steam turbine calculations since the steam turbine did not involve the potassium carbonate solution.

8.1.3 Control Valves and Piping Losses

A number of control valves were required for the HYSYS® CO_2 train process models. These were modelled using HYSYS® valve operations and included flow control valves for the raw gas and reboiler steam, as well as level control valves for the various vessels in the absorption and regeneration circuits. The relevant sizing information for these valves was obtained from the Santos TIMS database.

Valve operations were also used to represent the piping pressure losses in various parts of the CO_2 train process models, such as in the cooling water and overhead condensate circuits. Also included were the head losses due to the distance the potassium carbonate solution had to travel to reach the top of the absorber and regenerator columns. The sizing information required for these valve operations was determined from the available plant specifications in the Santos TIMS database. It should be noted that the piping losses could have instead been modelled by HYSYS® pipe segment operations, but were not since the additional complexity associated with the pipe segment operations was not considered necessary for this work.

8.2 Steady-State CO_2 Train Models

Detailed steady-state models of the Moomba CO_2 trains were developed in HYSYS® by linking the previously described absorption and regeneration circuit process models with the various valve operations. The resulting model configurations for CO_2 trains #1 and #7 are shown in Figures 8.2.1 and 8.2.2, while the corresponding process flow sheets for the other five trains are included as Figures H.2.1 to H.2.5 in Appendix H.

In HYSYS®, the only flow measurements that may be user-specified for a material stream are the molar flow, mass flow, standard ideal liquid volume flow and liquid volume flow at standard conditions, of which only one may be specified for each material stream to avoid specification conflicts. Other flow measurements, such as the standard gas flow and the actual volume flow, can only be calculated from the stream properties and the specified flow. However, the flow data for the CO_2 trains were in terms of the standard gas flow for the gas streams and the actual volume flow for the liquid streams. Consequently, adjust logical operations were attached to the unheated raw gas streams entering the absorber columns to manipulate the user-specified molar flows to obtain the desired standard gas flows.

Adjust operations were similarly set up for the lean solution streams entering the absorbers so as to achieve the required actual volume flows. To accommodate these adjust operations, a tee operation was used in each CO_2 train process model to split the solution stream leaving the main solution pump into an absorber feed stream and a material balance stream. This enabled the molar flow of the lean solution streams to be user-specified, instead of being calculated by the main solution pumps. Manual adjustment of the makeup water flow to the regenerators was required to ensure negligible calculated molar flows for the material balance streams.

This application of the tee operations caused the three streams connected to each tee operation to share the same composition calculated by the preceding main solution pumps. Consequently, additional adjust operations were required to obtain the desired CO_2 loading for the lean solution by manipulating the user-specified reboiler steam mass flows.

Two alternative methods to the above tee operations were also considered. The first method replaced the tee operations with recycle operations, which made the lean solution stream properties specifiable and eliminated the need for the material balance streams. However, this approach was not undertaken as it was not recommended that recycle operations be attached to streams which have variables determined by an adjust operation (Hyprotech Ltd, 2001c).

In the second option, the tee operations were replaced by mixer operations which combined the pressurised solution and material balance streams to produce the lean solution streams. As with the tee operations, the reboiler steam adjust operations were required to obtain the desired lean solution CO_2 loading, and manual adjustment of the makeup water flow was needed to ensure negligible flow

for the material balance streams. However with the mixer operations, multiple set operations were also necessary in order to set the temperature and composition of each lean solution stream equal to that for its corresponding pressurised solution stream. Due to its additional complexity, this approach was rejected in favour of the one with the tee operations.

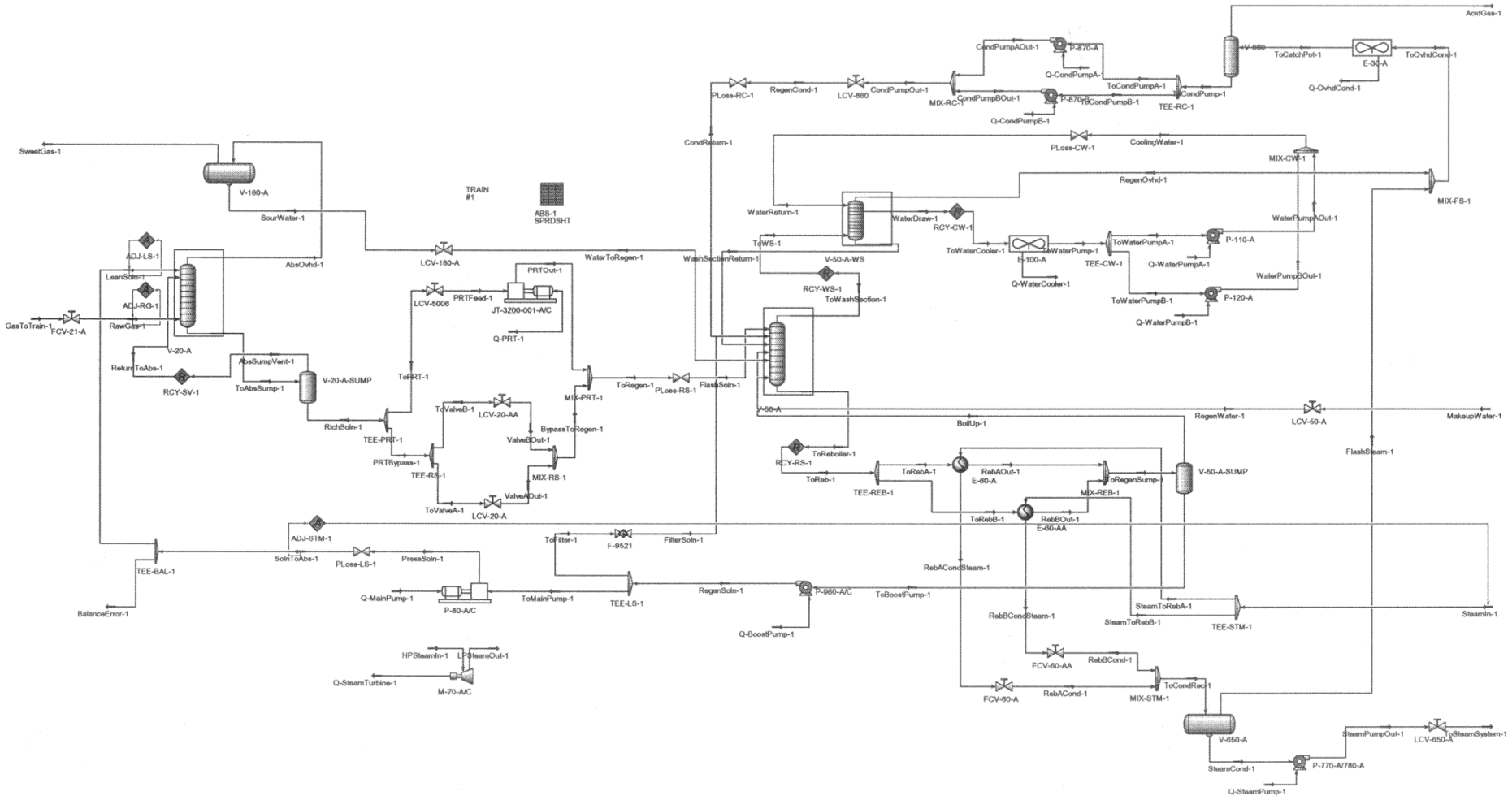

Figure 8.2.1: Process flow diagram for the steady-state HYSYS® model of CO_2 train #1.

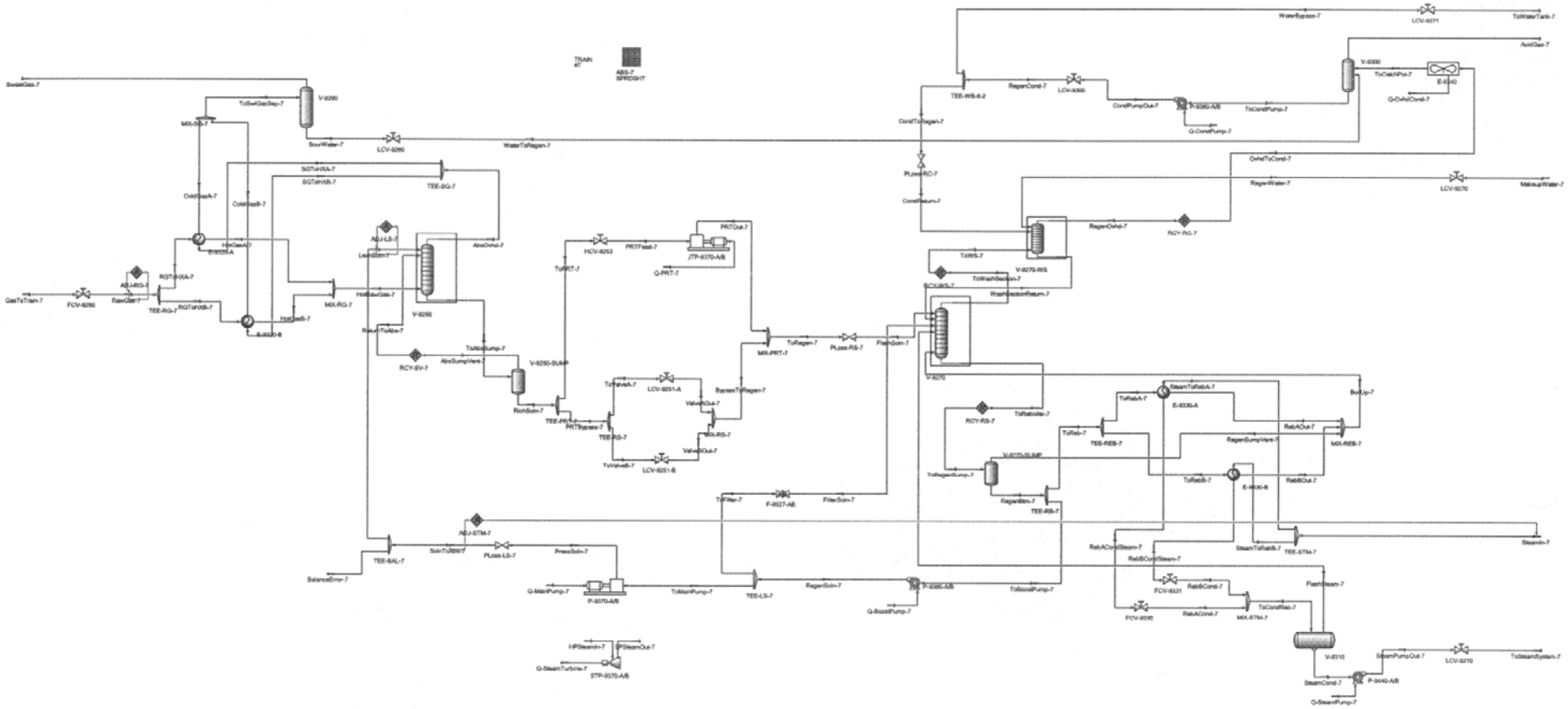

Figure 8.2.2: Process flow diagram for the steady-state HYSYS® model of CO_2 train #7.

8.3 Model Validation

The performance of the above steady-state HYSYS® CO_2 train process models was compared against both sets of typical operating data in Table 2.1.2. It should be noted that the first data set was used in the development of the Aspen Custom Modeler® absorber and regenerator column models, while the second set of data was used solely for model validation purposes.

The resulting vapour and liquid phase composition profiles for the absorber and regenerator columns in CO_2 trains #1 and #7 are given in Figures 8.3.1 and 8.3.2, and the column temperature profiles are shown in Figure 8.3.3. The corresponding profiles for the other five CO_2 trains are very similar to these, and are included as Figures H.3.1 to H.3.6 in Appendix H. Values for the operating parameters calculated by the CO_2 train models are provided in Tables 8.3.1 and 8.3.2, along with their percentage deviation from the data values listed in Table 2.1.2.

For all seven CO_2 trains, the CO_2 and H_2S vapour phase concentrations were seen to decrease up the absorber columns, with the acid gas content initially declining at a slightly faster rate near the bottom of the columns. The reverse trend was observed for the liquid phase acid gas loading. These HYSYS® absorber composition profiles agreed well with their corresponding Aspen Custom Modeler® profiles from Chapter 4, with the exception of the CO_2 curves for CO_2 train #7 and the extent of H_2S removal predicted for the seven CO_2 trains.

In the Aspen Custom Modeler® model of CO_2 train #7, there was a sharp decrease in the rates at which the CO_2 levels changed in the lower third of the absorber column due to the very high CO_2 loading in this part of the column which reduced the solution capacity for further CO_2 absorption. The absence of this behaviour in the corresponding HYSYS® model was an indication of the limitations of the stage efficiency approach in representing the solution chemistry in HYSYS®. This suggested that caution must be taken when considering the results for simulations with high raw gas to lean solution flow ratios. In particular, the predicted rich solution CO_2 loading should be checked to ensure it does not exceed 1 (mol CO_2)·(mol K_2CO_3)$^{-1}$.

Another sign of the limitations associated with the stage efficiency approach was that the sweet gas H_2S concentrations predicted by the HYSYS® models were found to exceed those for the Aspen Custom Modeler® models by approximately 95%. This resulted from the stage efficiency correlations being based solely on the sweet gas CO_2 content, due to the inability to use separate component efficiencies. However, it should be noted that the HYSYS® values for the sweet gas H_2S content were still within the range specified by the plant data.

The general shape of the HYSYS® regenerator composition profiles matched that of the corresponding Aspen Custom Modeler® profiles. CO_2 was rapidly removed from the rich solution near the bottom of the regenerator columns due to contact with the stripping steam, whereas the desorption of H_2S occurred swiftly near the top of the columns. As for the Aspen Custom Modeler® profiles, a

comparison of the HYSYS® absorber and regenerator liquid phase profiles in Figures 8.3.1 and 8.3.2 showed that a sizeable fraction of the absorbed acid gases was flashed off due to the depressurisation of the rich solution. The HYSYS® models predicted that up to 43% of the absorbed CO_2 and up to 58% of the absorbed H_2S were flashed off, which were considerably less than the Aspen Custom Modeler® model predictions of up to 64% and 86%, respectively, for CO_2 and H_2S. However, both predictions for the quantity of CO_2 flashed off during the solution depressurisation were within the literature range of one- to two-thirds of the absorbed CO_2 (Kohl and Nielson, 1997).

The observed discrepancies for the quantities of flashed acid gas were most likely due to the poorer thermodynamic representation of the CO_2-K_2CO_3-H_2O system by the enhanced PR equation of state compared to the Electrolyte NRTL model. However, despite the higher levels of residual acid gas in the low pressure rich solution for the HYSYS® models, there was good agreement (within ±10%) between the quantities of reboiler steam required by the HYSYS® and Aspen Custom Modeler® models to regenerate the solution.

The absorber and regenerator temperature profiles also corresponded well with the equivalent Aspen Custom Modeler® profiles in Chapter 4. The absorber profiles showed characteristic temperature bulges near the bottom of the columns that were similar in shape to those in the Aspen Custom Modeler® profiles, except for CO_2 train #7. The HYSYS® profiles for this CO_2 train closely resembled those for the other six CO_2 trains, unlike the corresponding Aspen Custom Modeler® profiles. This reflected the above-mentioned differences between the HYSYS® and Aspen Custom Modeler® absorber composition profiles for CO_2 train #7. As for the Aspen Custom Modeler® process models, temperature drops between 7 and 15°C accompanied the depressurisation of the rich solution, and the regenerator temperatures increased down the columns, reaching a maximum at the solution reboilers and a minimum at the overhead condensers.

For all seven CO_2 trains, good agreement was observed between the HYSYS® model results and the two sets of plant data. The model and data values for most of the operating parameters were within ±6%, with larger deviations of up to ±10% for the reboiler steam flows. The model values for the sweet gas H_2S content, the rich solution H_2S loading and the column pressure drops were found to be within the given range, while the predicted lean solution H_2S loading values were effectively zero like the plant data, being of the order of 10^{-8} to 10^{-25}. The most significant deviations were associated with the predicted acid gas temperatures for CO_2 train #4, which were up to 30% lower than the data values. However, as mentioned in Section 4.4, the data values were unexpectedly high, and since the HYSYS® temperature values were within ±1% of the values predicted by the Aspen Custom Modeler® models, these deviations were considered to be acceptable.

In conclusion, the agreement between the model results and the plant data was deemed sufficiently close that the HYSYS® process models of the Moomba CO_2 trains were regarded as suitable for the steady-state simulation of the actual CO_2 trains, within the range of operating parameters considered

during the model development process. To demonstrate a potential application of these HYSYS® CO_2 train process models, the steady-state models for CO_2 trains #1 and #7 are converted into dynamic process models in the next chapter.

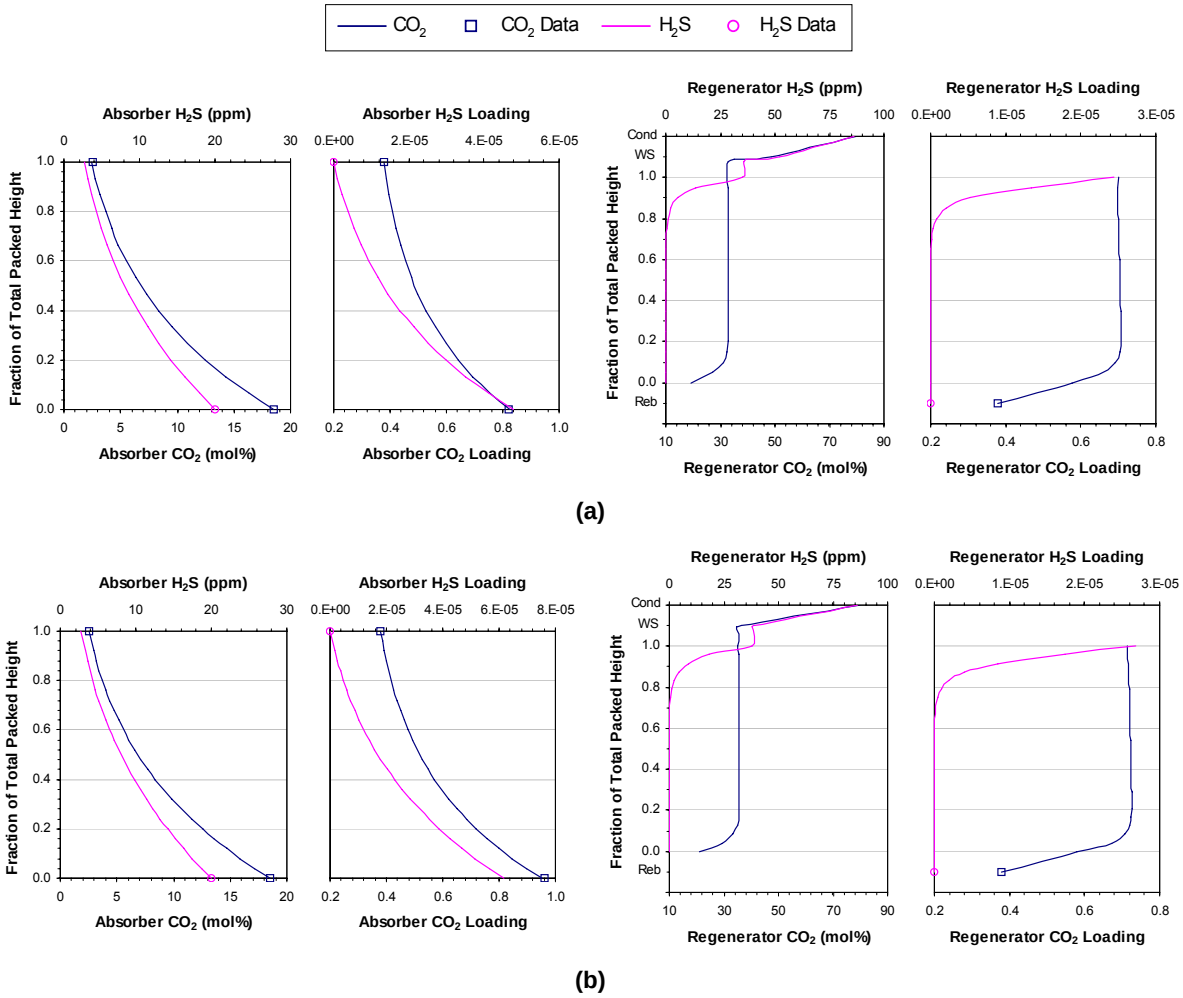

Figure 8.3.1: CO_2 and H_2S vapour and liquid phase profiles for the first set of data. (a) CO_2 train #1. (b) CO_2 train #7. (Cond = condenser, WS = wash section, Reb = reboiler)

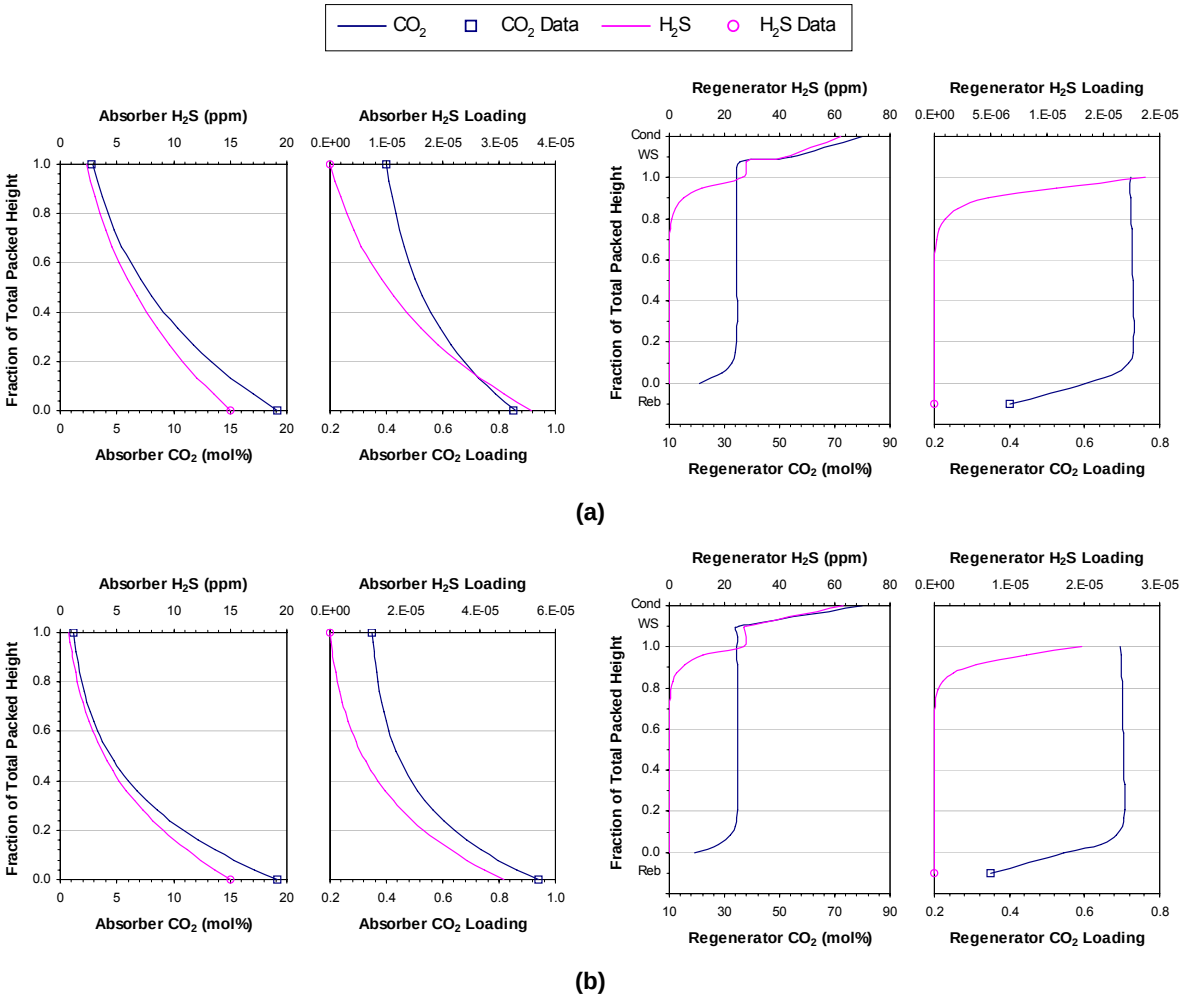

Figure 8.3.2: CO_2 and H_2S vapour and liquid phase profiles for the second set of data. (a) CO_2 train #1. (b) CO_2 train #7. (Cond = condenser, WS = wash section, Reb = reboiler)

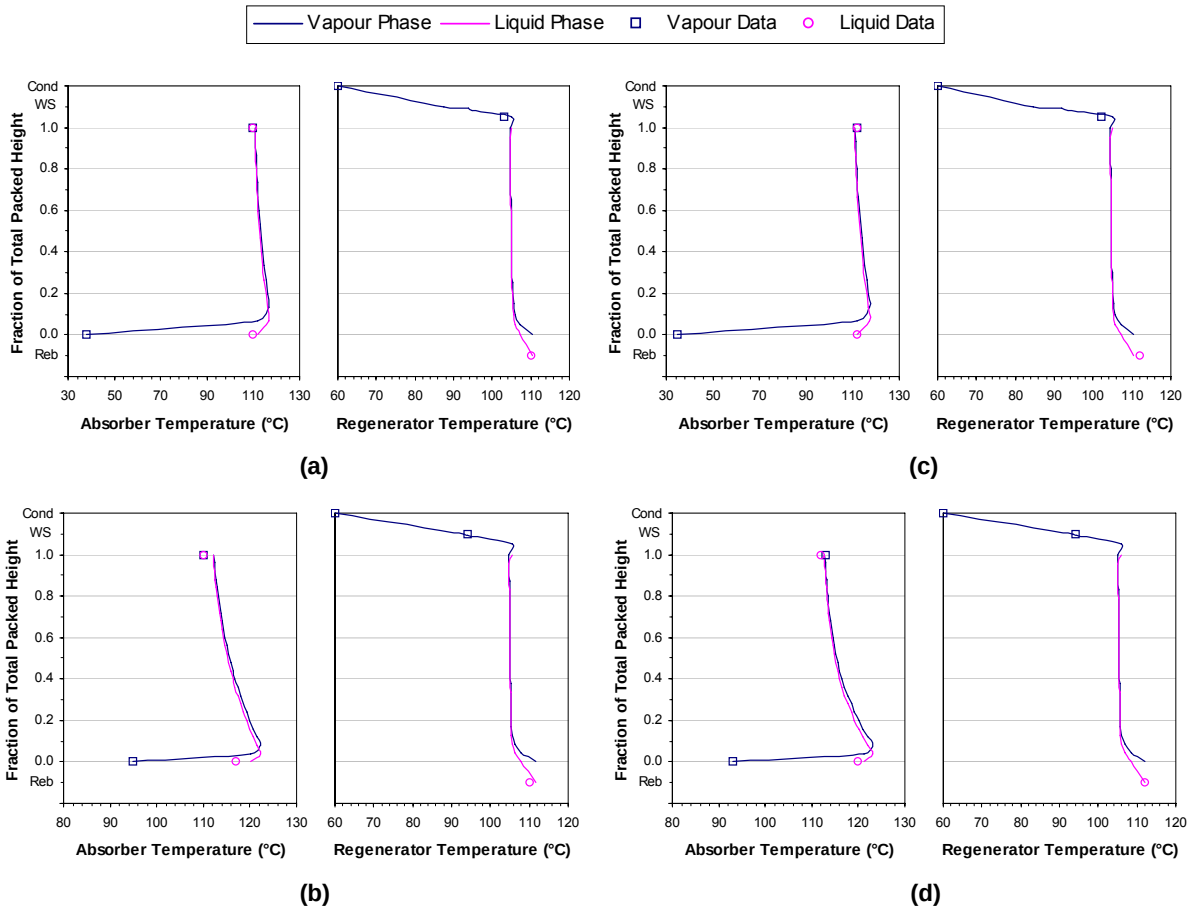

Figure 8.3.3: Vapour and liquid phase temperature profiles for the two sets of plant data. (a) CO_2 train #1 and (b) CO_2 train #7 profiles for the first set of data. (c) CO_2 train #1 and (d) CO_2 train #7 profiles for the second set of data. (Cond = condenser, WS = wash section, Reb = reboiler)

Table 8.3.1: CO_2 train simulation results for the first set of plant data in Table 2.1.2. The bracketed values are the percentage deviations from the data.

CO_2 Train	#1	#2	#3	#4	#5	#6	#7
Sweet Gas							
mol% CO_2 [a]	2.51 (0.4%)	2.51 (0.4%)	2.53 (1.2%)	2.53 (1.2%)	2.52 (0.8%)	2.53 (1.2%)	2.55 (2.0%)
ppm H_2S	2.80 (- [f])	2.70 (- [f])	2.66 (- [f])	2.63 (- [f])	2.54 (- [f])	2.62 (- [f])	2.76 (- [f])
Temperature (°C)	110.9 (0.8%)	110.8 (0.7%)	111.9 (1.7%)	112.0 (1.8%)	112.3 (2.1%)	112.1 (1.9%)	112.2 (2.0%)
Acid Gas							
CO_2 (10^6 sm^3/d) [b]	0.320 (0.0%)	0.270 (0.0%)	0.479 (-0.2%)	0.549 (-0.2%)	0.549 (-0.2%)	0.669 (-0.2%)	0.907 (-0.3%)
Temperature (°C) [c]	104.5 (1.5%)	105.3 (2.2%)	78.8 (-1.5%)	76.9 (-25.4%)	95.1 (0.1%)	94.4 (0.4%)	93.3 (-0.7%)
Lean Solution							
CO_2 loading [d]	0.380 (0.0%)	0.380 (0.0%)	0.380 (0.0%)	0.380 (0.0%)	0.380 (0.0%)	0.380 (0.0%)	0.380 (0.0%)
H_2S loading ($\times 10^{-16}$) [d]	4572.2 (- [g])	4835.1 (- [g])	174.9 (- [g])	184.7 (- [g])	85.1 (- [g])	6.0 (- [g])	0.2 (- [g])
wt% K_2CO_3 [e]	27.0 (0.0%)	27.0 (0.0%)	30.0 (0.0%)	30.0 (0.0%)	30.0 (0.0%)	30.0 (0.0%)	30.0 (0.0%)
Flow (m^3/h)	550.0 (0.0%)	550.0 (0.0%)	670.0 (0.0%)	812.0 (0.0%)	1000.0 (0.0%)	1000.0 (0.0%)	1068.0 (0.0%)
Temperature (°C)	110.8 (0.7%)	110.8 (0.7%)	111.9 (1.7%)	112.0 (1.8%)	112.2 (2.0%)	112.1 (1.9%)	112.1 (1.9%)
Rich Solution							
CO_2 loading [d]	0.825 (0.6%)	0.756 (0.7%)	0.861 (0.1%)	0.834 (-0.7%)	0.749 (-0.1%)	0.830 (-0.1%)	0.951 (-0.9%)
H_2S loading ($\times 10^{-5}$) [d]	4.8 (- [f])	4.1 (- [f])	5.2 (- [f])	4.9 (- [f])	4.0 (- [f])	4.9 (- [f])	6.2 (- [f])
Flow (m^3/h)	564.6 (-0.9%)	562.4 (-0.8%)	693.3 (-1.0%)	838.8 (-0.7%)	1026.8 (-0.7%)	1032.6 (-0.7%)	1112.0 (-0.7%)
Temperature (°C)	111.9 (1.7%)	111.7 (1.6%)	118.8 (1.5%)	118.5 (1.3%)	117.5 (0.5%)	118.6 (1.3%)	120.2 (2.7%)
Makeup Water							
Flow (m^3/h)	1.51 (- [f])	1.18 (- [f])	1.54 (- [f])	1.72 (- [f])	1.59 (- [f])	2.14 (- [f])	3.41 (- [f])
Sour Water							
Flow (m^3/h)	0.00 (- [g])	0.00 (- [g])	1.28 (-1.7%)	1.46 (-2.6%)	1.45 (-3.3%)	1.78 (-0.9%)	2.48 (-4.5%)
Absorber							
Pressure drop (bar)	0.03 (- [f])	0.02 (- [f])	0.02 (- [f])	0.03 (- [f])	0.02 (- [f])	0.04 (- [f])	0.04 (- [f])
Regenerator							
Pressure drop (bar)	0.04 (- [f])	0.04 (- [f])	0.04 (- [f])	0.04 (- [f])	0.04 (- [f])	0.04 (- [f])	0.04 (- [f])
Solution Reboiler							
Steam flow (t/h)	29.4 (1.3%)	26.3 (7.7%)	35.5 (2.0%)	41.5 (-2.0%)	43.7 (-1.2%)	49.8 (1.1%)	61.5 (-5.3%)

[a] This refers to the CO_2 content in the dry gas. [b] sm^3/d refers to m^3/d at standard conditions (dry gas at 15°C and 1 atm). [c] This is the vapour temperature entering the regenerator wash sections in CO_2 trains #1 and #2 and leaving the wash sections in trains #3 to #7. [d] The CO_2 and H_2S loading refer to the moles of CO_2 and H_2S per equivalent mole of K_2CO_3 in the solution. The equivalent moles of K_2CO_3 are defined as the total number of moles of K_2CO_3 in the solution if all the $KHCO_3$, KHS and K_2S in the solution are converted back into K_2CO_3. [e] This refers to the equivalent weight percent of K_2CO_3 in the solution. [f] No percentage deviation was calculated as the corresponding data value was not given. [g] No percentage deviation was calculated as the data value was zero.

Table 8.3.2: CO_2 train simulation results for the second set of plant data in Table 2.1.2. The bracketed values are the percentage deviations from the data.

CO_2 Train	#1	#2	#3	#4	#5	#6	#7
Sweet Gas							
mol% CO_2 [a]	2.95 (5.3%)	2.82 (0.8%)	3.01 (3.7%)	3.00 (3.4%)	3.10 (-0.1%)	2.48 (-0.7%)	1.19 (-0.7%)
ppm H_2S	2.33 (- [f])	2.18 (- [f])	2.31 (- [f])	2.34 (- [f])	2.28 (- [f])	1.84 (- [f])	0.79 (- [f])
Temperature (°C)	111.1 (-0.8%)	111.1 (-0.8%)	111.7 (-1.2%)	111.5 (-0.5%)	111.3 (-0.6%)	113.1 (0.1%)	112.8 (-0.2%)
Acid Gas							
CO_2 (10^6 sm^3/d) [b]	0.301 (0.5%)	0.261 (0.4%)	0.466 (-0.9%)	0.531 (0.2%)	0.542 (0.3%)	0.684 (0.6%)	0.831 (0.1%)
Temperature (°C) [c]	104.3 (2.2%)	104.9 (1.9%)	75.4 (0.6%)	72.6 (-29.5%)	94.0 (-1.0%)	94.4 (0.4%)	93.6 (-0.4%)
Lean Solution							
CO_2 loading [d]	0.400 (0.0%)	0.400 (0.0%)	0.400 (0.0%)	0.400 (0.0%)	0.440 (0.0%)	0.350 (0.0%)	0.350 (0.0%)
H_2S loading ($\times 10^{-16}$) [d]	3314.6 (- [g])	3366.4 (- [g])	117.7 (- [g])	47.4 (- [g])	343.2 (- [g])	6.2 (- [g])	2.1E-13 (- [g])
wt% K_2CO_3 [e]	28.0 (0.0%)	28.0 (0.0%)	30.0 (0.0%)	29.0 (0.0%)	30.0 (0.0%)	31.0 (0.0%)	30.0 (0.0%)
Flow (m^3/h)	481.0 (0.0%)	475.0 (0.0%)	638.0 (0.0%)	758.0 (0.0%)	922.9 (0.0%)	940.1 (0.1%)	946.1 (0.0%)
Temperature (°C)	111.0 (-0.9%)	111.0 (-0.9%)	111.6 (-0.4%)	111.4 (-0.5%)	111.3 (-0.6%)	113.1 (1.9%)	112.8 (0.7%)
Rich Solution							
CO_2 loading [d]	0.859 (1.1%)	0.803 (0.4%)	0.891 (0.2%)	0.892 (0.2%)	0.836 (-0.5%)	0.819 (-0.2%)	0.939 (-0.1%)
H_2S loading ($\times 10^{-5}$) [d]	3.6 (- [f])	3.2 (- [f])	3.8 (- [f])	3.8 (- [f])	3.1 (- [f])	3.7 (- [f])	4.6 (- [f])
Flow (m^3/h)	494.8 (-0.8%)	487.0 (-0.6%)	660.7 (-0.9%)	783.8 (-0.7%)	949.4 (-0.6%)	973.4 (-0.7%)	986.7 (-0.8%)
Temperature (°C)	112.0 (0.0%)	112.0 (0.0%)	118.5 (0.4%)	118.0 (-0.8%)	116.9 (-0.9%)	120.0 (0.0%)	121.2 (1.0%)
Makeup Water							
Flow (m^3/h)	1.51 (- [f])	1.24 (- [f])	1.56 (- [f])	1.72 (- [f])	1.84 (- [f])	2.15 (- [f])	2.99 (- [f])
Sour Water							
Flow (m^3/h)	0.00 (- [g])	0.00 (- [g])	1.22 (1.3%)	1.40 (-0.1%)	1.38 (-1.4%)	1.79 (-0.8%)	2.06 (-1.9%)
Absorber							
Pressure drop (bar)	0.03 (- [f])	0.02 (- [f])	0.02 (- [f])	0.03 (- [f])	0.03 (- [f])	0.04 (- [f])	0.04 (- [f])
Regenerator							
Pressure drop (bar)	0.04 (- [f])	0.04 (- [f])	0.04 (- [f])	0.04 (- [f])	0.04 (- [f])	0.04 (- [f])	0.04 (- [f])
Solution Reboiler							
Steam flow (t/h)	25.9 (9.6%)	23.4 (8.1%)	33.2 (-5.0%)	38.7 (7.6%)	38.1 (2.7%)	51.3 (3.4%)	57.4 (5.8%)

[a] This refers to the CO_2 content in the dry gas. [b] sm^3/d refers to m^3/d at standard conditions (dry gas at 15°C and 1 atm). [c] This is the vapour temperature entering the regenerator wash sections in CO_2 trains #1 and #2 and leaving the wash sections in trains #3 to #7. [d] The CO_2 and H_2S loading refer to the moles of CO_2 and H_2S per equivalent mole of K_2CO_3 in the solution. The equivalent moles of K_2CO_3 are defined as the total number of moles of K_2CO_3 in the solution if all the $KHCO_3$, KHS and K_2S in the solution are converted back into K_2CO_3. [e] This refers to the equivalent weight percent of K_2CO_3 in the solution. [f] No percentage deviation was calculated as the corresponding data value was not given. [g] No percentage deviation was calculated as the data value was zero.

8.4 Summary

In summary, this chapter concluded the development of steady-state process models of the Moomba CO_2 trains in the HYSYS® simulation environment. Particular focus was given to the expansion of the absorber and regenerator column models from Chapter 7 into process models of the absorption and regeneration circuits that comprise the CO_2 trains.

Since the absorber and regenerator columns form the central components of the absorption and regeneration circuits for the CO_2 trains, process models of these circuits were developed by extending the column process models to include various ancillary operations. Of particular importance were the solution pumpsets, which consisted of the main solution pumps, steam turbines and power recovery turbines. Due to the lack of a hydraulic turbine operation in HYSYS®, pump operations were used to represent the power recovery turbines, and a spreadsheet operation was used to perform the necessary pumpset calculations for the steady-state simulations. This spreadsheet operation was not necessary in the dynamic simulation mode due to the ability of the HYSYS® pump operations to act as hydraulic turbines in dynamic simulations.

The steady-state HYSYS® process models of the CO_2 trains were completed by linking the resulting absorption and regeneration circuit models. This required the addition of a number of adjust logical operations to facilitate the user-specification of the raw gas and lean solution streams entering the absorber columns. Tee operations were included to split each lean solution stream so that their flow rates could be user-specified. This modelling approach necessitated the manual adjustment of the makeup water streams to ensure negligible flow for the resulting material balance streams.

The performance of the completed steady-state HYSYS® CO_2 train models was generally found to agree well with that of the corresponding Aspen Custom Modeler® CO_2 train models and with the plant data used in the development of the Aspen Custom Modeler® models. Some discrepancies, primarily concerning the absorption of H_2S, were observed due to the limitations of the HYSYS® models in representing the solution chemistry for the potassium carbonate system. However, these deviations were deemed to be acceptable since the primary focus of the CO_2 trains is to remove CO_2.

Good agreement was also observed between the HYSYS® process models and a second independent set of plant data, thereby validating the HYSYS® models. The HYSYS® CO_2 trains process models were therefore considered to be suitable for the steady-state simulation of the Moomba CO_2 trains, albeit within the range of operating parameters considered during the model development process.

In the following chapter, the steady-state models for CO_2 trains #1 and #7 are converted into dynamic process models in order to demonstrate a potential application of the HYSYS® CO_2 train process models.

CHAPTER 9

DYNAMIC HYSYS® SIMULATIONS OF CO_2 REMOVAL TRAINS #1 AND #7

Detailed steady-state process models of the Moomba CO_2 trains were successfully developed in the HYSYS® simulation environment in the previous chapter. However, these process models do not provide any information on the dynamic behaviour of the CO_2 trains, which limits the potential applications of the HYSYS® models. As a result, this chapter focuses on the conversion of the steady-state models for the two most dissimilar CO_2 trains, CO_2 trains #1 and #7, into dynamic process models.

Particular attention is given to the various process model modifications required when transitioning between steady-state and dynamic simulations in HYSYS®. The fundamental differences between the two simulation modes necessitate several key changes to the steady-state CO_2 train models in order to perform dynamic simulations for the CO_2 trains.

The development of the dynamic CO_2 train process models is followed by a series of process case studies, in which the dynamic behaviour of CO_2 trains #1 and #7 is examined. Simple FOPDT process transfer functions are derived to describe the observed behaviour of the two CO_2 trains. These will be used in the next chapter to analyse the multivariable controllability of the two CO_2 trains and to develop suitable diagonal control structures.

9.1 Dynamic CO_2 Train Models

The detailed HYSYS® process models developed in Chapter 8 enable the steady-state simulation of the Moomba CO_2 trains and can be used for a variety of purposes, such as to evaluate the effects of different operating conditions for process optimisation. While these steady-state HYSYS® models are particularly useful, they do not provide any insight into the dynamic behaviour of the CO_2 trains. As a result, the steady-state models can not be utilised in potentially useful applications like controllability analyses or control strategy development.

In order to simulate the dynamic behaviour of the CO_2 trains, the steady-state HYSYS® models have to be converted into dynamic process models. The following sections concentrate on the development of dynamic process models of the two most dissimilar CO_2 trains: CO_2 trains #1 and #7. Dynamic models of the other five CO_2 trains were not considered in this work, but are anticipated to exhibit dynamic behaviour somewhere in between that of these two CO_2 trains.

9.1.1 Model Configuration

Process model modifications are required when switching between steady-state and dynamic simulations in HYSYS®. These necessary changes are due to the inherent differences between the two simulation modes.

In the steady-state simulations, the unit operations are modular and a non-sequential calculation algorithm is applied to the material, energy and composition balances (Hyprotech Ltd, 2001b). Consequently, the results of any calculation are automatically propagated both backwards and forwards throughout the steady-state process model. This approach enables the properties of internal streams to be user-specified where necessary, as well as those of the boundary streams.

In contrast, the dynamic simulation mode utilises a sequential algorithm for the energy and composition balances, while the material (or pressure-flow) balances are calculated simultaneously in a pressure-flow matrix (Hyprotech Ltd, 2001b). The temperatures and compositions of the boundary feed streams must therefore be specified so that the temperatures and compositions can be calculated sequentially for each downstream unit operation and material stream. These calculations are based on the HYSYS® holdup model, which is described in detail in the HYSYS® Dynamic Modelling manual (Hyprotech Ltd, 2001b).

The pressures for the boundary material streams must also be specified in the dynamic simulation mode to enable the calculation of the internal pressures and flows based on the sizes and resistances of the model unit operations. The pressure gradients across the entire process model and across each unit operation have to be carefully considered since they act as the driving force for flow in the dynamic simulation mode.

The process flow diagrams for the dynamic process models of CO_2 trains #1 and #7 are included as Figures 9.1.1 and 9.1.2. These are based on simplified forms of the steady-state process models in Figures 8.2.1 and 8.2.2, in which all parallel items were modelled by single units that were sized accordingly. This model simplification was implemented in order to reduce the computation time for the dynamic simulations since the calculation speed decreased with increasing model complexity.

To satisfy the above requirements for the dynamic simulation mode, all the pressure and flow specifications for the internal material streams were removed, while pressure specifications were set for the boundary material streams. Similarly, temperature and composition specifications were set for the boundary feed streams, but not for the remaining material streams. Sufficient sizing information had been provided in the steady-state process models to satisfy the holdup calculations. Consequently, only the dynamic specifications recommended by the HYSYS® Dynamic Modelling manual (Hyprotech Ltd, 2001b) were needed for the various unit operations.

For the valve operations, the recommended dynamic specifications entailed replacing the fixed pressure drops with pressure-flow relations. Similarly, the “overall K value” specification was used for the heat transfer operations instead of fixed pressure drops. For the mixer operations, the pressure specification was set to the “Equalise All” option, while the “Remove Use Splits” option was activated for the tee operations. As in the steady-state process models, characteristic pump curves were used as the operating specifications for the various pump operations. For the hydraulic turbine models, the “Pump is acting as turbine” and the “Use Curves“ options were activated, while the corresponding spreadsheet calculations were deactivated.

Due to the sequential nature of the dynamic calculations, the recycle operations were redundant in dynamic mode and were therefore removed. The recycle operations could have been retained in the dynamic models since they had no effect on the simulation results: the recycle operations simply acted as throughputs without any holdup or pressure gradient. The adjust operations similarly did not function in dynamic mode. Being the steady-state equivalent of the dynamic HYSYS® control operations, the adjust operations for the raw gas, lean solution and reboiler steam flows were instead replaced with PID control operations. These were configured to control the raw gas flow via the raw gas inlet valve, the lean solution flow via the main solution pump speed, and the reboiler steam flow via the steam condensate flow valve.

PID control operations were added to control the temperatures of the regenerator overhead condensers by manipulating the overhead condenser duties. This approach was equivalent to the actual practice of manually switching the condenser fans on and off as required. These temperature control loops replaced the temperature specifications on the material streams leaving the overhead condensers. PID control operations were also included to control the liquid levels in the column sumps and separator vessels. It should be noted that for CO_2 train #7, a split-range controller was implemented for the regenerator liquid level controller, as specified by the technical drawings in the

Santos TIMS database. The tuning of the above flow, level and temperature controllers will be discussed in the next section.

The final modification to the process models was the removal of the material balance streams and the tee operations for the lean solution streams. The replacement of the adjust operations with PID controllers made these streams and tee operations redundant: they were no longer required to control the lean solution flow.

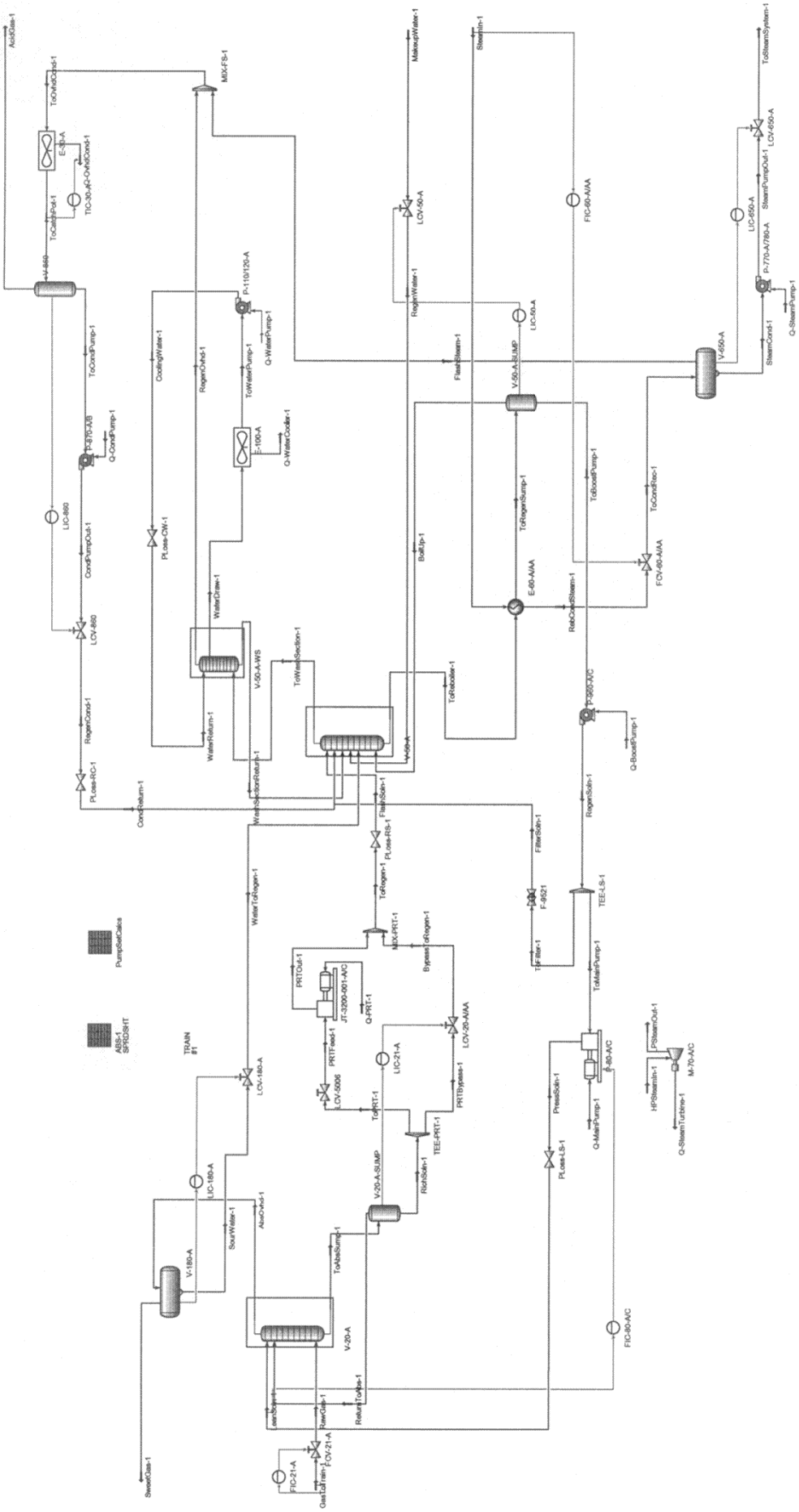

Figure 9.1.1: Process flow diagram of the simplified dynamic HYSYS® model for CO_2 train #1.

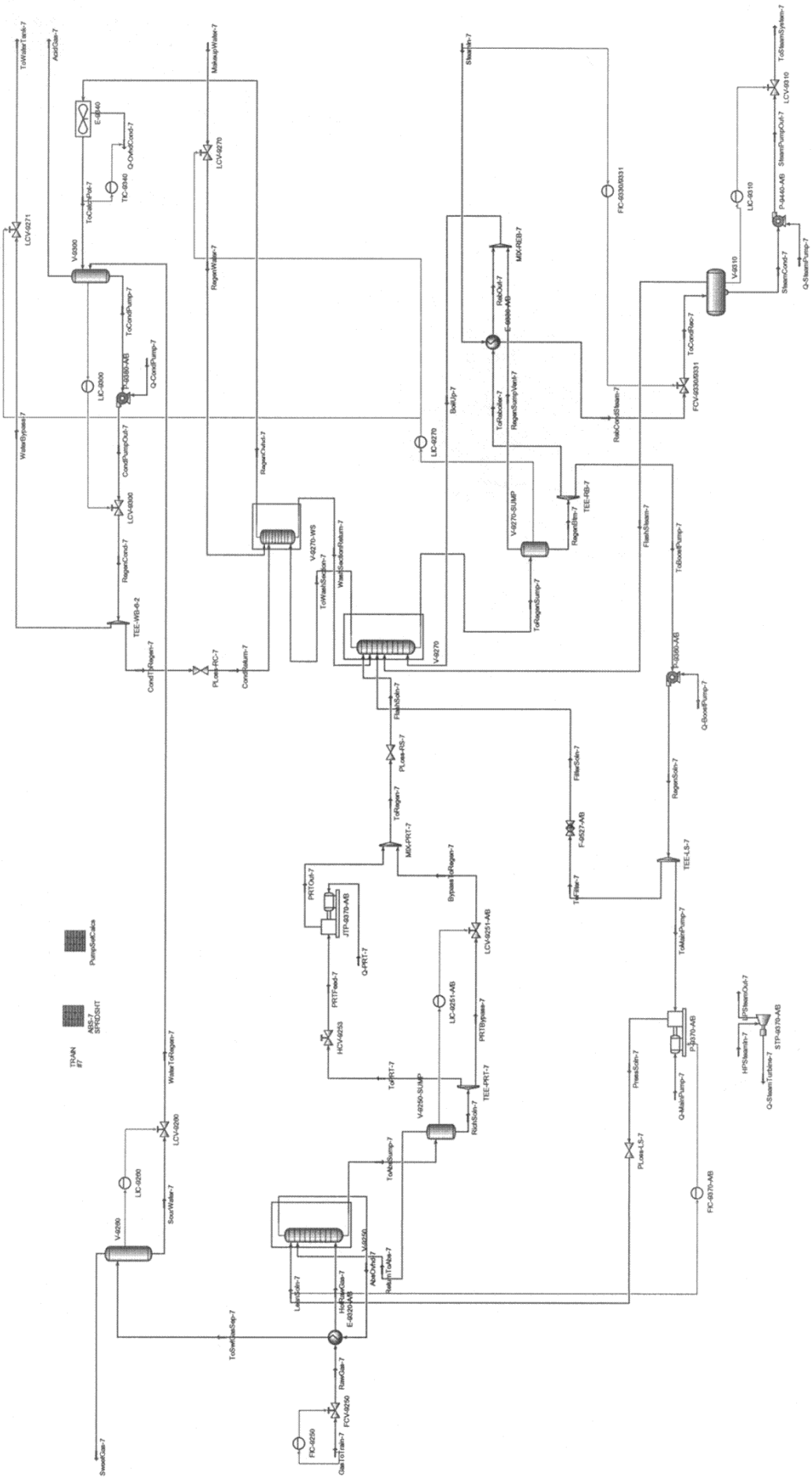

Figure 9.1.2: Process flow diagram of the simplified dynamic HYSYS® model for CO_2 train #7.

9.1.2 Flow, Temperature and Level Control Loops

While some controller settings were available from Santos for the flow and liquid level control loops illustrated in Figures 9.1.1 and 9.1.2, none were available for the temperature control loops since the overhead condenser temperatures are currently under manual control. For the purposes of this work, the flow, temperature and level control loops were tuned according to the PID tuning rules presented in Tables 2.5.2 and 2.5.3.

For the flow control loops, only PI controller settings were used; derivative action was not applied due to the extremely rapid dynamic nature of the flow control loops. Due to the insignificant dead time associated with these flow loops, the Ziegler-Nichols frequency domain method was used to determine their ultimate gains and ultimate periods. These parameters were then used to calculate the controller settings via the Zeigler-Nichols and Tyreus-Luyben tuning rules in Table 2.5.2.

Table 9.1.1 presents the resulting flow loop characteristics and controller settings, while Figure 9.1.3 compares the loop responses to setpoint and load step changes for the two controller tuning rules. As expected, more conservative controller settings were produced by the Tyreus-Luyben tuning rules, thereby resulting in slower responses to the step changes in setpoint and load. Since the Ziegler-Nichols settings were not observed to be overly aggressive for these flow loops (i.e. no oscillatory loop responses), they were utilised for this work.

The Ziegler-Nichols frequency domain method was also used to determine the process characteristics for the temperature control loops, which are given in Table 9.1.2. Since derivative action is often in temperature control loops (Svrcek et al., 2006), Table 9.1.2 also compares the PI and PID controller settings derived from the Ziegler-Nichols and Tyreus-Luyben tuning rules in Table 2.5.2. The resulting loop responses to setpoint and load step changes are provided in Figure 9.1.4.

As for the flow control loops, the Ziegler-Nichols controller settings resulted in more aggressive loop responses compared to the Tyreus-Luyben settings. It was also observed that the loop responses corresponding to the PID settings for both sets of tuning rules were faster than those for the PI settings, but were also more oscillatory for the setpoint step change. Consequently, the Tyreus-Luyben PI controller settings were selected for this work as they still provided a reasonable response time, as well as the least underdamped response.

For the liquid level control loops, the equipment sizing information and process specifications were used to calculate the PID controller settings from the critically damped, minimum IAE and QDR correlations provided in Table 2.5.3. The resulting settings are given in Table 9.1.3, while Figure 9.1.5 compares the corresponding loop responses to setpoint and load step changes. The QDR controller settings produced the most oscillatory loop responses, which were far too aggressive in some cases, whereas the critically damped settings gave the slowest and least underdamped responses. The

minimum IAE controller settings offered the best compromise between response speed and response quality, and were therefore employed for this work.

It should be noted that the flow controllers were all reverse-acting, while the temperature and level controllers were all direct-acting, with the exception of the reverse split-range action for manipulating the makeup water flow to CO_2 train #7.

Table 9.1.1: Flow control loop characteristics and controller settings for CO_2 trains #1 and #7.

Flow Loop	Raw Gas		Lean Solution		Reboiler Steam	
CO_2 Train	#1	#7	#1	#7	#1	#7
Loop Characteristics						
K_u	0.34	0.37	0.74	0.45	0.35	0.30
P_u (min/cycle)	0.02	0.02	0.03	0.03	0.02	0.02
Controller Settings						
Ziegler-Nichols						
K_c	0.15	0.17	0.34	0.20	0.16	0.14
τ_I (min)	0.01	0.01	0.03	0.03	0.01	0.01
Tyreus-Luyben						
K_c	0.11	0.12	0.23	0.14	0.11	0.09
τ_I (min)	0.04	0.04	0.07	0.07	0.04	0.04

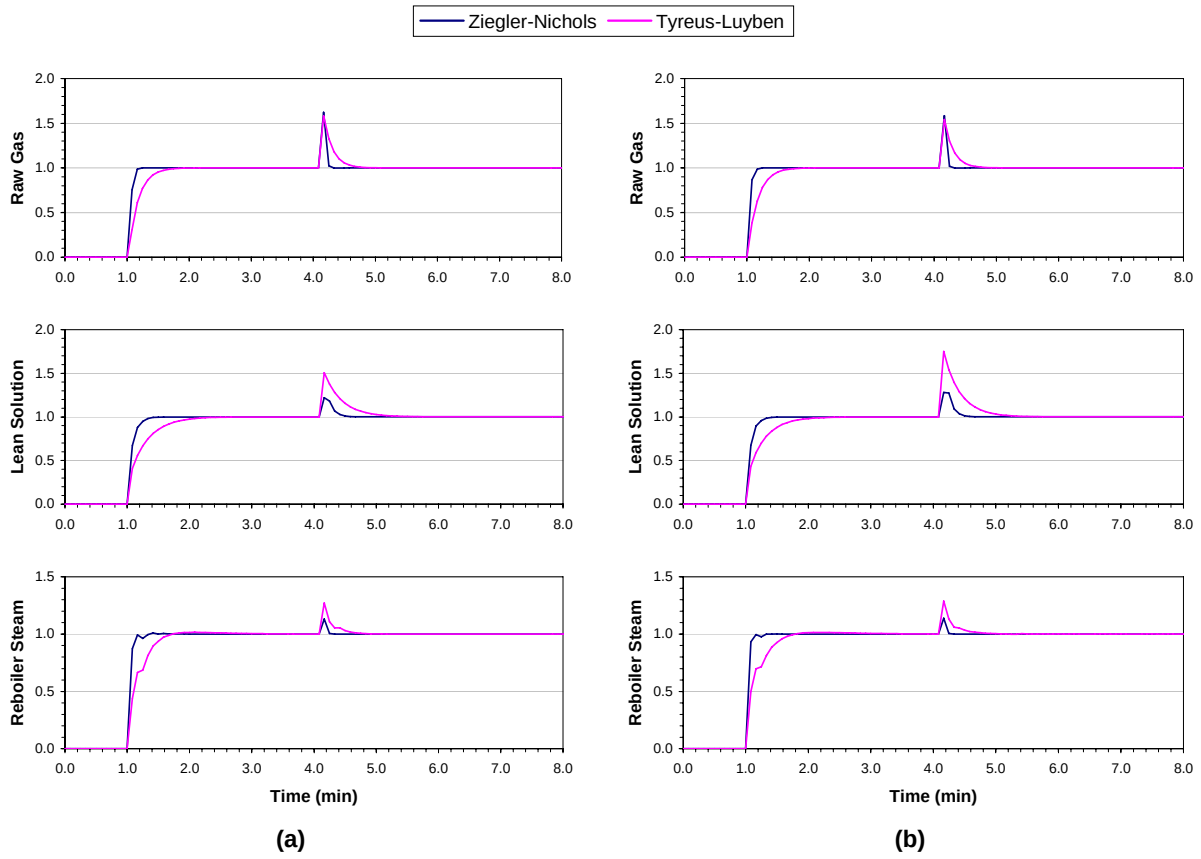

Figure 9.1.3: Flow control loop responses. (a) CO_2 train #1. (b) CO_2 train #7. A 2% magnitude setpoint step change occurred at 1 min, followed by a 2% magnitude load step change at 4 min.

Table 9.1.2: Temperature control loop characteristics and controller settings for CO_2 trains #1 and #7.

CO_2 Train	#1		#7	
Loop Characteristics				
K_u	5.00		4.00	
P_u (min/cycle)	0.17		0.17	
Controller Settings	PI	PID	PI	PID
Ziegler-Nichols				
K_c	2.27	3.00	1.82	2.40
τ_I (min)	0.14	0.08	0.14	0.08
τ_D (min)	–	0.02	–	0.02
Tyreus-Luyben				
K_c	1.56	2.30	1.25	1.84
τ_I (min)	0.37	0.37	0.37	0.37
τ_D (min)	–	0.03	–	0.03

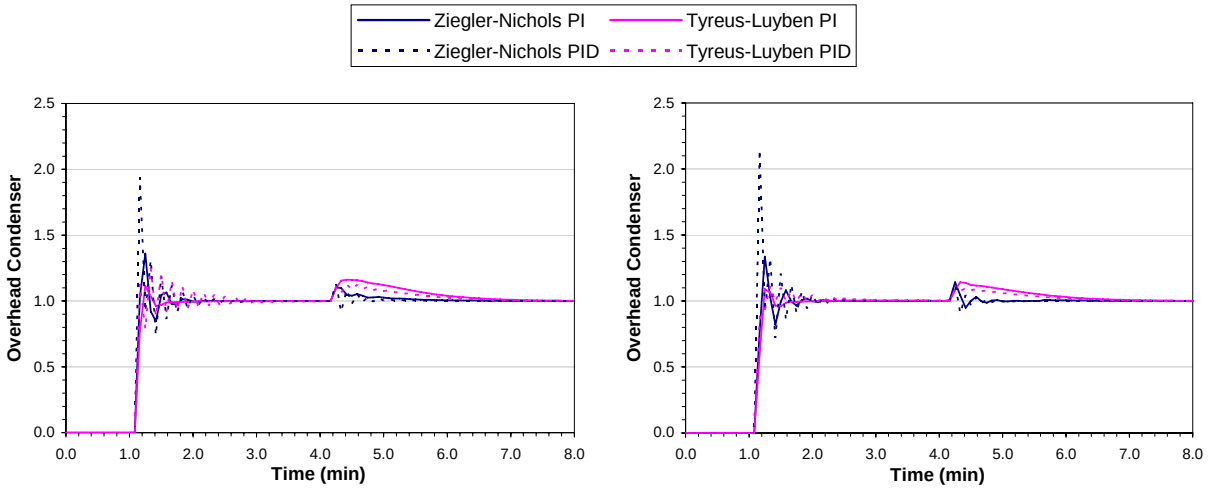

Figure 9.1.4: Temperature control loop responses. (a) CO_2 train #1. (b) CO_2 train #7. A 2% magnitude setpoint step change occurred at 1 min, followed by a 2% magnitude load step change at 4 min.

Table 9.1.3: Liquid level controller settings for CO_2 trains #1 and #7.

Liquid Level Loop	Absorber		Sweet Gas Separator		Overhead Catchpot		Steam Receiver		Regenerator	
CO_2 Train	#1	#7	#1	#7	#1	#7	#1	#7	#1	#7
Critically damped										
K_c	2.96	2.96	2.96	2.96	2.96	2.96	2.96	2.96	2.96	2.96
τ_I (min)	4.01	6.32	34.20	68.70	9.38	4.78	2.25	2.85	19.47	46.74
Minimum IAE										
K_c	1.28	1.28	1.28	1.28	1.28	1.28	1.28	1.28	1.28	1.28
τ_I (min)	0.44	0.69	3.76	7.55	1.03	0.53	0.25	0.31	2.14	5.13
QDR										
K_c	2.00	2.00	2.00	2.00	2.00	2.00	2.00	2.00	2.00	2.00
τ_I (min)	1.10	1.73	9.36	18.81	2.57	1.31	0.62	0.78	5.33	12.80

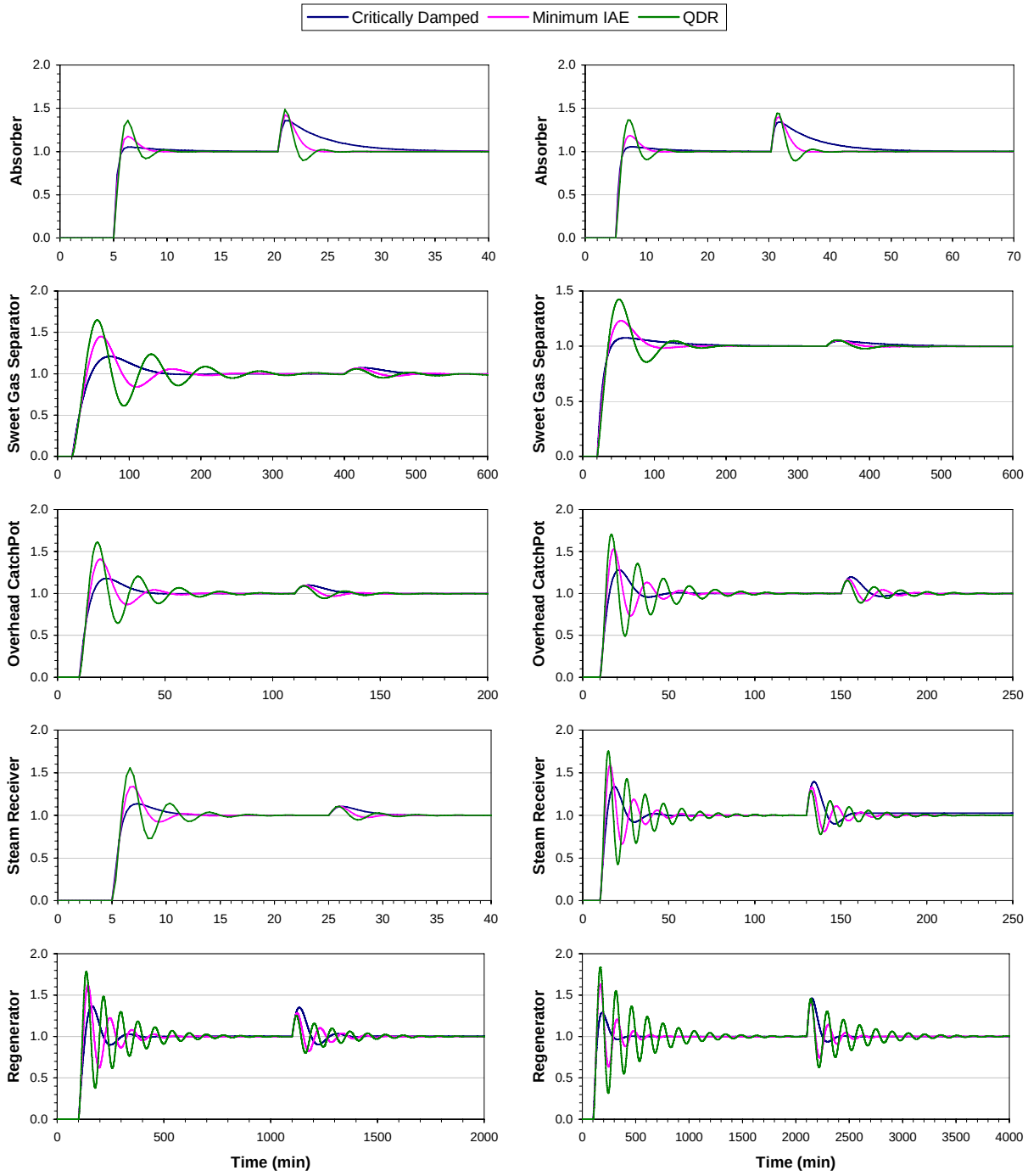

Figure 9.1.5: Liquid level control loop responses. (a) CO_2 train #1. (b) CO_2 train #7. 2% magnitude setpoint and load step changes were implemented at the following times: For the absorber level loop, the setpoint was changed at 5 min, followed by the load at 20 min for CO_2 train #1 and at 30 min for CO_2 train #7. For the sweet gas separator level loop, the setpoint was changed at 10 mins, followed by the load at 400 min for CO_2 train #1 and at 340 min for CO_2 train #7. For the overhead catchpot level loop, the setpoint was changed at 10 min, followed by the load at 110 min for CO_2 train #1 and at 150 min for CO_2 train #7. For the steam condensate receiver level loop, the setpoint was changed at 5 min for CO_2 train #1, followed by the load at 25 min; for CO_2 train #7, the setpoint was changed at 10 min, followed by the load at 130 min. Finally, for the regenerator level loop, the setpoint was changed at 100 min, followed by the load at 1100 min for CO_2 train #1 and at 2100 min for CO_2 train #7.

9.2 Process Case Studies

After implementing the controller parameters derived in the previous section, the dynamic HYSYS® process models of CO_2 trains #1 and #7 were used to investigate the transient process behaviour of the two CO_2 trains. It should be noted that these dynamic simulations were strictly theoretical case studies as the CO_2 train dynamic process models were not validated against plant data due to difficulties with obtaining sufficient online plant data. Online measurements were not available for the solution composition[1] and the online CO_2 analysers for the raw and sweet gas streams were not always reliable (Barber, 2007).

Based on an inspection of the CO_2 train plant data from 2002 to 2005, three different operating regions were considered in the dynamic simulations: high, medium and low gas throughputs. These regions corresponded respectively to 100, 80 and 60% of the raw gas flow rates from the first set of plant data in Table 2.1.2, and 100, 90 and 70% of the equivalent raw gas to lean solution flow ratio data. All other process conditions were taken to be the same as for the set of plant data; the exception was the reboiler steam flow rates, which were adjusted to give the desired lean solution CO_2 loading.

The control of the CO_2 trains is primarily focussed on controlling three process variables: the sweet gas CO_2 content, the raw gas throughput and the sweet gas pressure to the LRP Plant (Santos Ltd, 1998). These were consequently identified as the three primary process outputs (controlled variables) for each CO_2 train. However, since the latter two variables are directly related to the flow rate of the sweet gas, the sweet gas CO_2 content and flow rate were instead taken to be the two key CO_2 train process outputs for this work.

An examination of the CO_2 trains identified four main process inputs (manipulated variables) for each CO_2 train: the raw gas flow rate, the lean solution flow rate, the lean solution CO_2 loading and the lean solution strength. In the parametric studies in Chapter 5, the lean solution CO_2 loading was shown to be dependent on the reboiler steam flow rate, while the lean solution strength was dependent on the flow rates of makeup water and water bypass, which are both used to control the regenerator liquid level. Consequently, the key process inputs for the CO_2 trains were taken to be the raw gas flow rate, the lean solution flow rate, the reboiler steam flow rate and the regenerator liquid level. The examination of the CO_2 trains also identified the raw gas CO_2 content as the primary process disturbance.

[1] A potential improvement to the Moomba CO_2 trains is the implementation of online monitoring of the solution composition. While direct online measurement is not feasible, the solution composition could be monitored indirectly using a more easily measured property such as pH or conductivity. For example, pH was used to monitor the CO_2 loading in the amine solution for the Imperial College CO_2-MEA pilot plant (Albrecht et al., 1980), whereas van der Lee and co-workers (2003, 2004) used conductivity in their CO_2-amine pilot plant. However, for this approach to succeed, rigorous calibration studies are required to accurately correlate the solution concentration with the alternate measurable property.

In order to determine the effect of the above process inputs and disturbance on the process outputs for CO_2 trains #1 and #7, process step response curves for the two trains were obtained for each operating region. Based on the observed process variable fluctuations in the historical plant data, ±2% step changes were applied to the process inputs and disturbance, and the resulting averaged step response curves for the process outputs are shown in Figures 9.2.1 to 9.2.5. The vertical axes for these figures are dimensionless and are equivalent to those for the response curves depicted in Table 2.5.1. To achieve this, the process outputs were expressed in perturbation form and were scaled by dividing each output variable by its allowed range and then by the similarly scaled step change.

Most of the step response curves depicted in Figures 9.2.1 to 9.2.5 were relatively non-oscillatory and were readily described by the simple FOPDT model. The corresponding model parameters were obtained by fitting the FOPDT model step response function from Table 2.5.1 to these response curves via a least squares method. However, distinctly underdamped response curves were observed for the step changes in the regenerator liquid level. This was most likely the result of interactions arising from the various control loops in the process model, such as the regenerator liquid level control loop. For these underdamped responses, USOPDT model parameters were fitted graphically using the method shown in Table 2.5.1. These parameters were then used to determine the approximate FOPDT model parameters from equation (2.5.1), as suggested by Panda and co-workers (2004), since the quality of the validating data for the CO_2 Removal Trains did not justify the use of more complex models than the FOPDT model. The resulting set of FOPDT process transfer functions for CO_2 trains #1 and #7 are given in Tables 9.2.1 and 9.2.2.

Despite their dissimilar configurations, the two CO_2 trains were generally seen to follow the same behavioural trends over the three different operating regions, as indicated by the similarity between their step response curves. The observed steady-state relationships between the process inputs and outputs were also found to be consistent with the results of the parametric studies performed in Chapter 5. While this was insufficient for validation purposes, it did indicate that the dynamic process models were producing reasonable results.

It should be noted that one process output was not previously considered in Chapter 5: the sweet gas flow rate. In the dynamic case studies, it was observed to follow the same trends as the sweet gas CO_2 content for the changes in the process inputs. This was not unexpected since the flow rate of the sweet gas is directly related to its CO_2 content for a constant CO_2 content in the raw gas. In contrast, the sweet gas flow rate was observed to be inversely related to the sweet gas CO_2 content for changes in the raw gas CO_2 content, as it compensated for the changing volume of CO_2 removed.

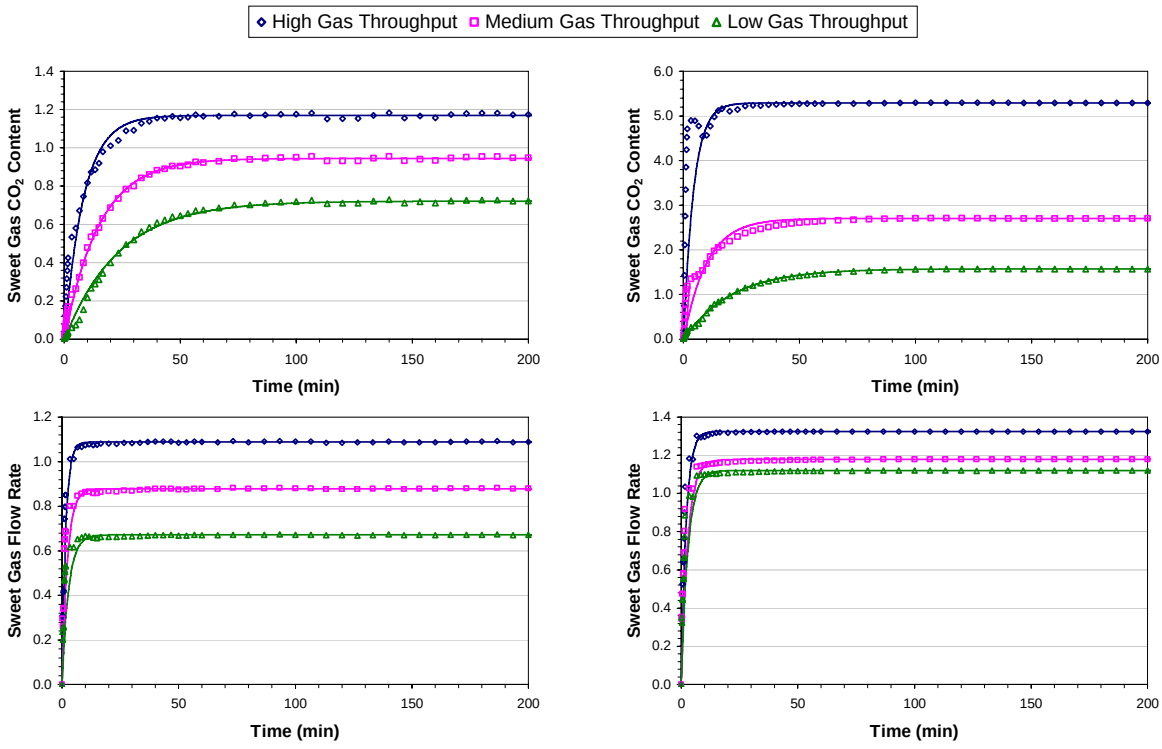

Figure 9.2.1: Process response curves for a 2% magnitude step change in the raw gas flow rate at 0 min. (a) CO_2 train #1. (b) CO_2 train #7. The points represent the process response, while the lines represent the FOPDT model predictions.

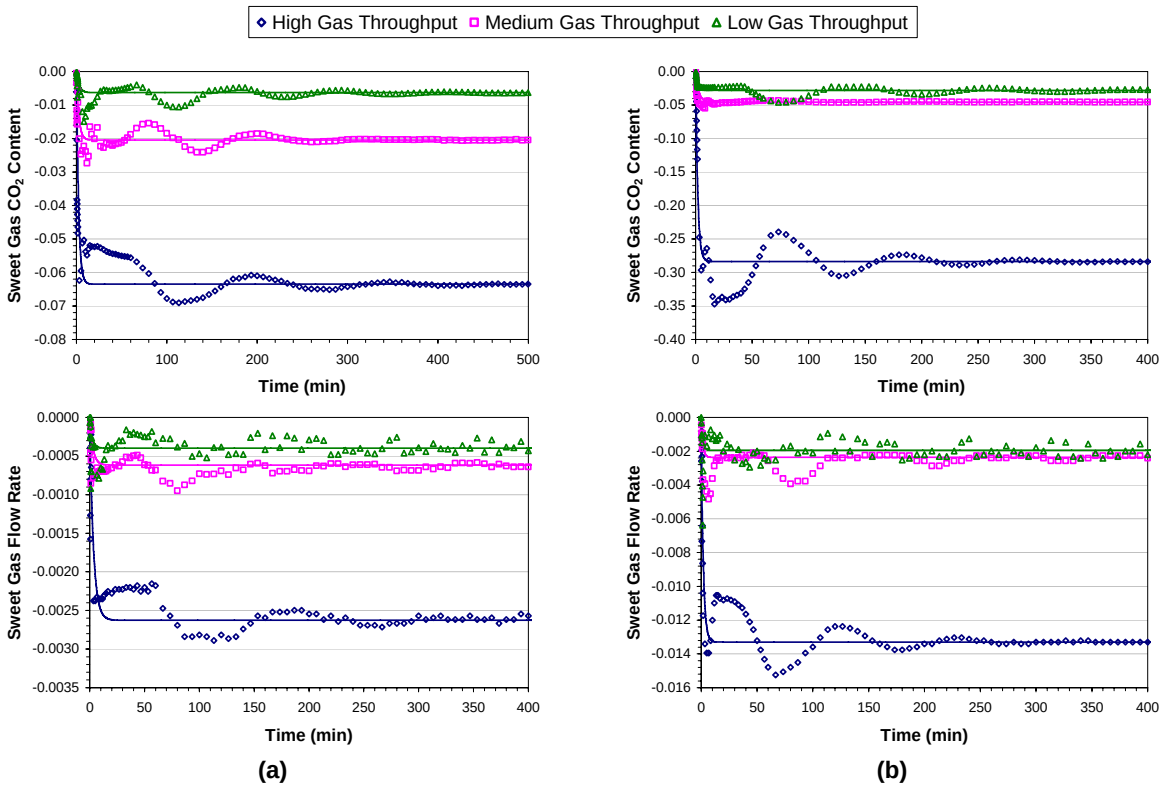

Figure 9.2.2: Process response curves for a 2% magnitude step change in the lean solution flow rate at 0 min. (a) CO_2 train #1. (b) CO_2 train #7. The points represent the process response, while the lines represent the FOPDT model predictions.

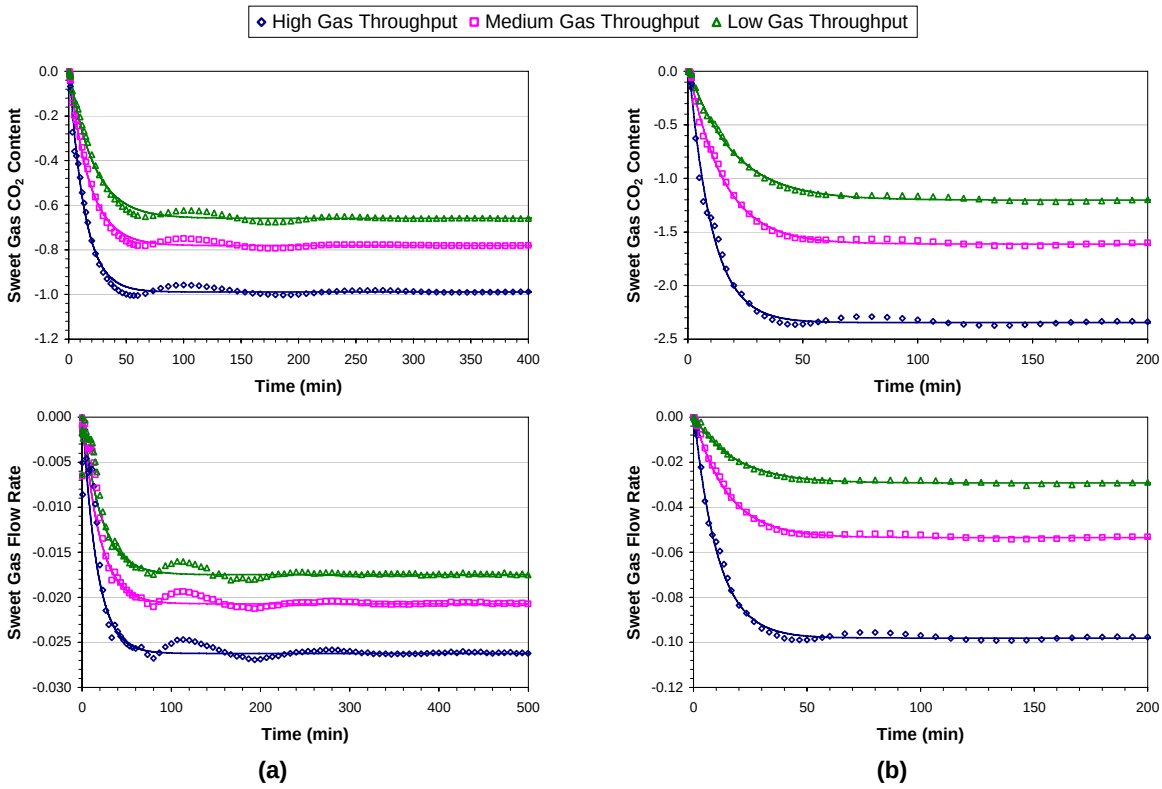

Figure 9.2.3: Process response curves for a 2% magnitude step change in the reboiler steam flow rate at 0 min. (a) CO_2 train #1. (b) CO_2 train #7. The points represent the process response, while the lines represent the FOPDT model predictions.

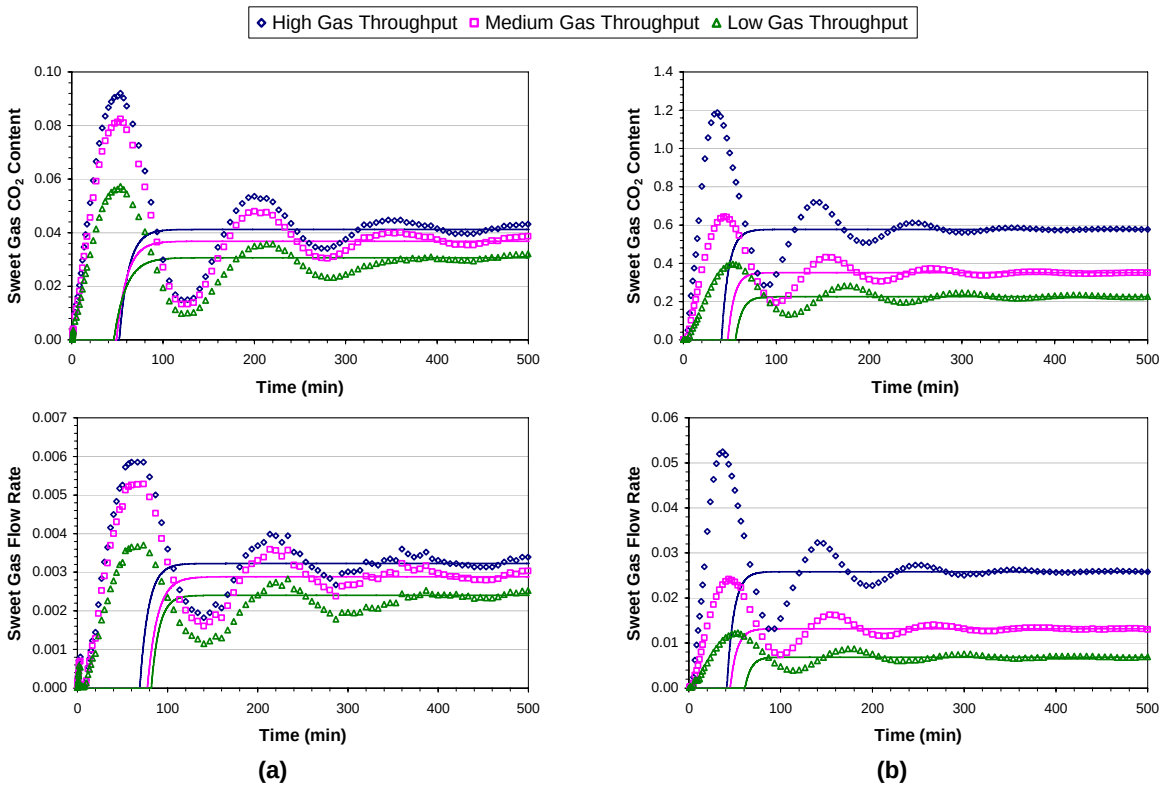

Figure 9.2.4: Process response curves for a 2% magnitude step change in the regenerator liquid level at 0 min. (a) CO_2 train #1. (b) CO_2 train #7. The points represent the process response, while the lines represent the FOPDT model predictions.

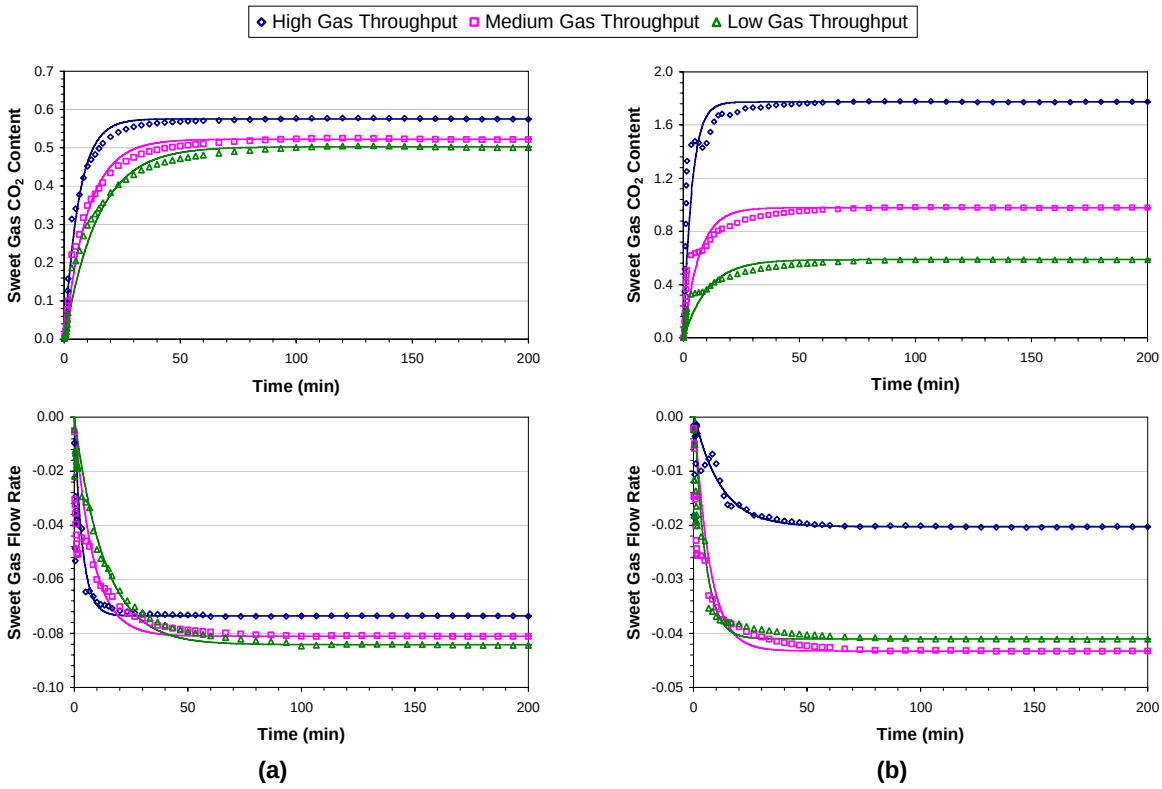

Figure 9.2.5: Process response curves for a 2% magnitude step change in the raw gas CO_2 content at 0 min. (a) CO_2 train #1. (b) CO_2 train #7. The points represent the process response, while the lines represent the FOPDT model predictions.

Table 9.2.1: Process transfer functions for CO_2 train #1. The time constants and dead times are given in minutes.

	Raw Gas Flow	Lean Solution Flow	Reboiler Steam Flow	Regenerator Liquid Level	Raw Gas CO_2 Content
High Gas Throughput					
Sweet Gas CO_2 Content	$\frac{1.17 \cdot e^{-0.17 \cdot s}}{8.22 \cdot s + 1}$	$\frac{-0.0635 \cdot e^{-0.17 \cdot s}}{2.28 \cdot s + 1}$	$\frac{-0.989 \cdot e^{-0.67 \cdot s}}{13.17 \cdot s + 1}$	$\frac{0.0412 \cdot e^{-51.94 \cdot s}}{10.24 \cdot s + 1}$	$\frac{0.576 \cdot e^{-0.17 \cdot s}}{6.12 \cdot s + 1}$
Sweet Gas Flow	$\frac{1.09 \cdot e^{-0.17 \cdot s}}{1.62 \cdot s + 1}$	$\frac{-0.00263 \cdot e^{-0.17 \cdot s}}{3.37 \cdot s + 1}$	$\frac{-0.0262 \cdot e^{-0.83 \cdot s}}{16.02 \cdot s + 1}$	$\frac{0.00323 \cdot e^{-69.15 \cdot s}}{9.50 \cdot s + 1}$	$\frac{-0.0735 \cdot e^{-0.17 \cdot s}}{3.44 \cdot s + 1}$
Medium Gas Throughput					
Sweet Gas CO_2 Content	$\frac{0.945 \cdot e^{-0.17 \cdot s}}{14.90 \cdot s + 1}$	$\frac{-0.0204 \cdot e^{-0.17 \cdot s}}{2.53 \cdot s + 1}$	$\frac{-0.781 \cdot e^{-0.67 \cdot s}}{17.31 \cdot s + 1}$	$\frac{0.0368 \cdot e^{-48.87 \cdot s}}{11.33 \cdot s + 1}$	$\frac{0.523 \cdot e^{-0.17 \cdot s}}{9.94 \cdot s + 1}$
Sweet Gas Flow	$\frac{0.879 \cdot e^{-0.17 \cdot s}}{2.34 \cdot s + 1}$	$\frac{-0.000617 \cdot e^{-0.17 \cdot s}}{2.90 \cdot s + 1}$	$\frac{-0.0207 \cdot e^{-0.83 \cdot s}}{18.73 \cdot s + 1}$	$\frac{0.00288 \cdot e^{-77.51 \cdot s}}{11.10 \cdot s + 1}$	$\frac{-0.08108 \cdot e^{-0.17 \cdot s}}{8.12 \cdot s + 1}$
Low Gas Throughput					
Sweet Gas CO_2 Content	$\frac{0.721 \cdot e^{-0.17 \cdot s}}{23.39 \cdot s + 1}$	$\frac{-0.00603 \cdot e^{-0.17 \cdot s}}{3.02 \cdot s + 1}$	$\frac{-0.659 \cdot e^{-0.67 \cdot s}}{21.11 \cdot s + 1}$	$\frac{0.0307 \cdot e^{-46.01 \cdot s}}{13.28 \cdot s + 1}$	$\frac{0.503 \cdot e^{-0.17 \cdot s}}{14.30 \cdot s + 1}$
Sweet Gas Flow	$\frac{0.671 \cdot e^{-0.17 \cdot s}}{2.80 \cdot s + 1}$	$\frac{-0.000398 \cdot e^{-0.17 \cdot s}}{2.22 \cdot s + 1}$	$\frac{-0.0175 \cdot e^{-0.83 \cdot s}}{20.85 \cdot s + 1}$	$\frac{0.00240 \cdot e^{-81.88 \cdot s}}{8.65 \cdot s + 1}$	$\frac{-0.0842 \cdot e^{-0.17 \cdot s}}{13.31 \cdot s + 1}$

Table 9.2.2: Process transfer functions for CO_2 train #7. The time constants and dead times are given in minutes.

	Raw Gas Flow	Lean Solution Flow	Reboiler Steam Flow	Regenerator Liquid Level	Raw Gas CO_2 Content
High Gas Throughput					
Sweet Gas CO_2 Content	$\frac{5.29 \cdot e^{-0.17 \cdot s}}{4.30 \cdot s + 1}$	$\frac{-0.284 \cdot e^{-0.17 \cdot s}}{1.80 \cdot s + 1}$	$\frac{-2.35 \cdot e^{-0.67 \cdot s}}{9.98 \cdot s + 1}$	$\frac{0.577 \cdot e^{-41.10 \cdot s}}{7.58 \cdot s + 1}$	$\frac{1.77 \cdot e^{-0.17 \cdot s}}{3.52 \cdot s + 1}$
Sweet Gas Flow	$\frac{1.32 \cdot e^{-0.17 \cdot s}}{2.10 \cdot s + 1}$	$\frac{-0.0133 \cdot e^{-0.17 \cdot s}}{1.84 \cdot s + 1}$	$\frac{-0.0981 \cdot e^{-0.33 \cdot s}}{10.52 \cdot s + 1}$	$\frac{0.0258 \cdot e^{-41.27 \cdot s}}{7.58 \cdot s + 1}$	$\frac{-0.0203 \cdot e^{-0.50 \cdot s}}{11.66 \cdot s + 1}$
Medium Gas Throughput					
Sweet Gas CO_2 Content	$\frac{2.70 \cdot e^{-0.17 \cdot s}}{9.93 \cdot s + 1}$	$\frac{-0.0456 \cdot e^{-0.17 \cdot s}}{2.60 \cdot s + 1}$	$\frac{-1.61 \cdot e^{-0.67 \cdot s}}{14.97 \cdot s + 1}$	$\frac{0.351 \cdot e^{-47.95 \cdot s}}{6.82 \cdot s + 1}$	$\frac{0.978 \cdot e^{-0.17 \cdot s}}{6.70 \cdot s + 1}$
Sweet Gas Flow	$\frac{1.18 \cdot e^{-0.17 \cdot s}}{2.80 \cdot s + 1}$	$\frac{-0.00237 \cdot e^{-0.17 \cdot s}}{1.48 \cdot s + 1}$	$\frac{-0.0535 \cdot e^{-0.33 \cdot s}}{14.68 \cdot s + 1}$	$\frac{0.0132 \cdot e^{-44.99 \cdot s}}{7.23 \cdot s + 1}$	$\frac{-0.0433 \cdot e^{-0.50 \cdot s}}{6.66 \cdot s + 1}$
Low Gas Throughput					
Sweet Gas CO_2 Content	$\frac{1.58 \cdot e^{-0.17 \cdot s}}{20.66 \cdot s + 1}$	$\frac{-0.0281 \cdot e^{-0.17 \cdot s}}{2.99 \cdot s + 1}$	$\frac{-1.20 \cdot e^{-0.67 \cdot s}}{19.23 \cdot s + 1}$	$\frac{0.226 \cdot e^{-56.10 \cdot s}}{6.96 \cdot s + 1}$	$\frac{0.588 \cdot e^{-0.17 \cdot s}}{10.54 \cdot s + 1}$
Sweet Gas Flow	$\frac{1.12 \cdot e^{-0.17 \cdot s}}{2.91 \cdot s + 1}$	$\frac{-0.00195 \cdot e^{-0.17 \cdot s}}{1.38 \cdot s + 1}$	$\frac{-0.0292 \cdot e^{-0.33 \cdot s}}{17.88 \cdot s + 1}$	$\frac{0.00687 \cdot e^{-61.08 \cdot s}}{6.63 \cdot s + 1}$	$\frac{-0.0410 \cdot e^{-0.5 \cdot s}}{4.71 \cdot s + 1}$

To demonstrate the potential application of the HYSYS® CO_2 train process models in the analysis and design of control strategies for the CO_2 trains, the simple FOPDT process transfer functions derived in this section are used in the next chapter to analyse the multivariable controllability of the two CO_2 trains, and to develop suitable diagonal control structures for them. As discussed in Section 2.5, the application of diagonal control structures to the hot potassium carbonate process has not been previously documented in literature, despite the diagonal control structure being the simplest and most widely used form of multivariable control.

For this reason, only simple PID controllers were considered in the development of the diagonal control structures for CO_2 trains #1 and #7 for this work. However, both CO_2 trains demonstrated distinctly non-linear dynamic behaviour, as illustrated by the variation in the process transfer functions and step response curves over the different operating regions. This observed process non-linearity suggested that more complex adaptive controller algorithms, such as gain scheduling, may provide more effective control of the CO_2 trains than simple PID controllers. It is therefore recommended that the application of more complex controller algorithms to the CO_2 trains be investigated in any future work.

9.3 Summary

In summary, this chapter presented simplified dynamic HYSYS® process models of CO_2 trains #1 and #7 and investigated the dynamic relationships between the key process outputs and inputs for the two CO_2 trains.

The dynamic HYSYS® models were developed from the detailed steady-state models presented in Chapter 4. Due to the inherent differences between the dynamic and steady-state simulation modes in HYSYS®, a number of process model modifications were required to convert the steady-state models into dynamic ones. These changes included the amendment of various stream and unit operation specifications, the replacement of the adjust operations with PID control operations, and the addition of level control loops for all vessels.

The inclusion of the PID control operations necessitated the specification of suitable controller parameters in order to complete the dynamic process models. Only some of the required parameters were available from Santos due to various control loops being under manual control. Consequently, for the purposes of this work, the model control loops were tuned according to the methods discussed in Section 2.5.

Using the completed dynamic process models, the dynamic behaviour of CO_2 trains #1 and #7 was examined in a series of theoretical process case studies. Three different operating regions were considered in these studies: high, medium and low gas throughputs. The resulting process response curves were used to derive simple FOPDT process transfer functions which adequately described the relationships between the key process outputs (the sweet gas CO_2 content and flow rate) and the primary process inputs (the raw gas flow rate, the lean solution flow rate, the lean solution CO_2 loading and the lean solution strength) and disturbance (the raw gas CO_2 content). The two CO_2 trains were observed to behave quite similarly, despite the differences in their configurations.

The FOPDT process transfer functions are used in the next chapter to demonstrate the potential application of the HYSYS® CO_2 train process models in the analysis and development of suitable diagonal control structures for the CO_2 trains. As determined in the literature review in Chapter 2, the application of this simple form of multivariable control has not been previously documented for hot potassium carbonate process operations, thereby constituting a gap in the current literature.

CHAPTER 10

PROCESS CONTROL STUDIES FOR CO_2 TRAINS #1 AND #7

Simplified dynamic HYSYS® process models of Moomba CO_2 trains #1 and #7 were developed in the previous chapter, and were used to derive FODPT process transfer functions to describe the dynamic behaviour of the two CO_2 trains. In this chapter, these process transfer functions are used to analyse the multivariable controllability of the two CO_2 trains in order to develop potentially suitable diagonal control structures for the overall automatic control of each CO_2 train.

The analysis methods discussed in Chapter 2 are applied to the process transfer functions to evaluate the possible diagonal control structures and structure configurations arising from the different combinations and permutations of the key process inputs and outputs. The effect of the primary process disturbance on the performance of the potential diagonal control structures is also examined.

Finally, controller parameters for the optimal diagonal control structures are determined using the BLT tuning approach, and the selected diagonal control structures are tested via dynamic MATLAB® simulations to determine their applicability to the two CO_2 trains.

The simple case studies discussed in this chapter demonstrate a potentially useful application of the HYSYS® process models of the Moomba CO_2 trains. Further work is required in order to develop a viable control strategy for the CO_2 trains.

10.1 Selection of Diagonal Control Structure

In the previous chapter, four manipulated variables (process inputs) were identified for the CO_2 trains, in contrast to two controlled variables (process outputs). Consequently, six alternative diagonal control structures were proposed for each train, one for each of the six possible combinations of manipulated variables. However, three of these were immediately eliminated as they excluded the raw gas flow rate, which is required for the effective control of the sweet gas flow rate.

The remaining sets of manipulated variable were denoted as RGF-LSF, RGF-RSF and RGF-RLL, with RGF referring to the raw gas flow rate, LSF referring to the lean solution flow rate, RSF referring to the reboiler steam flow rate, and RLL referring to the regenerator liquid level. The process transfer function matrices for the resulting three potential control structures were derived from the simple process transfer functions in Table 9.2.1 and 9.2.2, and are given in Table 10.1.1. These matrices corresponded to a 2×2 system of the form:

$$\begin{bmatrix} y_1 \\ y_2 \end{bmatrix} = \begin{bmatrix} \mathbf{G_p}_{,11}(s) & \mathbf{G_p}_{,12}(s) \\ \mathbf{G_p}_{,21}(s) & \mathbf{G_p}_{,22}(s) \end{bmatrix} . \begin{bmatrix} m_1 \\ m_2 \end{bmatrix} \qquad (10.1.1)$$

where y_1 is the sweet gas CO_2 content, y_2 is the sweet gas flow rate, m_1 is the raw gas flow rate, and $\mathbf{G_p}_{,11}(s)$ to $\mathbf{G_p}_{,21}(s)$ are the process transfer functions relating the controlled variables y to the manipulated variables m. The manipulated variable m_2 varies depending on the control structure. For the RGF-LSF structure, m_2 is the lean solution flow rate; for the RGF-RSF structure, it refers to the reboiler steam flow rate; and it is the regenerator liquid level for the RGF-RLL structure.

To identify the optimal set of manipulated variables, and therefore the optimal diagonal control structure for CO_2 trains #1 and #7, the MRI, CN, DCN and DC sensitivity indices were used to investigate the sensitivity of the alternative diagonal control structures to process uncertainties and disturbances. The necessary calculations were performed in the MATLAB® 5.2 numerical computing environment, using equations (2.5.4) to (2.5.6). The dead times could not be directly implemented in the MATLAB® calculations, and were instead specified as rational transfer functions using the third-order Padé approximation. An example MATLAB® script for determining the sensitivity indices is provided in Section I.1 of Appendix I.

The resulting values of the four sensitivity indices at steady-state (s=0 or ω=0 rad/min) are summarised in Table 10.1.2, while the corresponding frequency plots are given in Figures 10.1.1 to 10.1.3. Of particular interest was the frequency range between 0.01 and 1 rad/min, due to the importance of this frequency range to feedback control (Skogestad et al., 1990).

From Table 10.1.2 and Figure 10.1.1, it was observed that the MRI values for the three different diagonal control structures were quite small (<1) over the examined frequency range. This indicated that the three structures were relatively sensitive to process uncertainties. The RGF-RSF structure was found to have the largest MRI values, making it the preferred option of the three. This preference

was confirmed by the CN values provided in Table 10.1.2 and Figure 10.1.1. The RGF-LSF and RGF-RLL structures were quite ill-conditioned, having CN values that were generally substantially larger than 10. In contrast, the RGF-RSF structure was reasonably well-conditioned, since most of its CN values were below 10, with the exception of the CN values associated with CO_2 train #7 at high gas throughput. However, these were still considerably less than the corresponding CN values for the other two control structures.

Unit magnitude changes in the raw gas CO_2 content and in the setpoints for the sweet gas CO_2 content and flow rate were considered for the DCN and DC calculations. From Table 10.1.2 and Figures 10.1.2 and 10.1.3, it was evident that the DCN values for the RGF-LSF and RGF-RLL control structures were considerably larger than the corresponding values for the RGF-RSF structure over the examined frequency range. The same trend was observed for the DC values. This indicated that, of the three potential control structures, the RGF-RSF structure was the least sensitive to process disturbances and setpoint changes.

Consequently, from the above sensitivity analyses, the RGF-RSF structure was identified as the optimal diagonal control structure for CO_2 trains #1 and #7. It was therefore selected for the interaction and stability analyses, which are discussed in the following section.

Table 10.1.1: Process transfer function matrices for the diagonal control structures. The time constants and dead times are given in minutes.

	RGF-LSF	RGF-RSF	RGF-RLL
CO_2 Train #1			
High Gas Throughput	$\begin{bmatrix} \frac{1.17 \cdot e^{-0.17 \cdot s}}{8.22 \cdot s + 1} & \frac{-0.0635 \cdot e^{-0.17 \cdot s}}{2.28 \cdot s + 1} \\ \frac{1.09 \cdot e^{-0.17 \cdot s}}{1.62 \cdot s + 1} & \frac{-0.00263 \cdot e^{-0.17 \cdot s}}{3.37 \cdot s + 1} \end{bmatrix}$	$\begin{bmatrix} \frac{1.17 \cdot e^{-0.17 \cdot s}}{8.22 \cdot s + 1} & \frac{-0.989 \cdot e^{-0.67 \cdot s}}{13.17 \cdot s + 1} \\ \frac{1.09 \cdot e^{-0.17 \cdot s}}{1.62 \cdot s + 1} & \frac{-0.0262 \cdot e^{-0.83 \cdot s}}{16.02 \cdot s + 1} \end{bmatrix}$	$\begin{bmatrix} \frac{1.17 \cdot e^{-0.17 \cdot s}}{8.22 \cdot s + 1} & \frac{0.041 \cdot e^{-51.94 \cdot s}}{10.24 \cdot s + 1} \\ \frac{1.09 \cdot e^{-0.17 \cdot s}}{1.62 \cdot s + 1} & \frac{0.00323 \cdot e^{-69.15 \cdot s}}{9.50 \cdot s + 1} \end{bmatrix}$
Medium Gas Throughput	$\begin{bmatrix} \frac{0.945 \cdot e^{-0.17 \cdot s}}{14.90 \cdot s + 1} & \frac{-0.0204 \cdot e^{-0.17 \cdot s}}{2.53 \cdot s + 1} \\ \frac{0.879 \cdot e^{-0.17 \cdot s}}{2.34 \cdot s + 1} & \frac{-0.000617 \cdot e^{-0.17 \cdot s}}{2.90 \cdot s + 1} \end{bmatrix}$	$\begin{bmatrix} \frac{0.945 \cdot e^{-0.17 \cdot s}}{14.90 \cdot s + 1} & \frac{-0.781 \cdot e^{-0.67 \cdot s}}{17.31 \cdot s + 1} \\ \frac{0.879 \cdot e^{-0.17 \cdot s}}{2.34 \cdot s + 1} & \frac{-0.0207 \cdot e^{-0.83 \cdot s}}{18.73 \cdot s + 1} \end{bmatrix}$	$\begin{bmatrix} \frac{0.945 \cdot e^{-0.17 \cdot s}}{14.90 \cdot s + 1} & \frac{0.0368 \cdot e^{-48.87 \cdot s}}{11.33 \cdot s + 1} \\ \frac{0.879 \cdot e^{-0.17 \cdot s}}{2.34 \cdot s + 1} & \frac{0.00288 \cdot e^{-77.51 \cdot s}}{11.10 \cdot s + 1} \end{bmatrix}$
Low Gas Throughput	$\begin{bmatrix} \frac{0.721 \cdot e^{-0.17 \cdot s}}{23.39 \cdot s + 1} & \frac{-0.00603 \cdot e^{-0.17 \cdot s}}{3.02 \cdot s + 1} \\ \frac{0.671 \cdot e^{-0.17 \cdot s}}{2.80 \cdot s + 1} & \frac{-0.000398 \cdot e^{-0.17 \cdot s}}{2.22 \cdot s + 1} \end{bmatrix}$	$\begin{bmatrix} \frac{0.721 \cdot e^{-0.17 \cdot s}}{23.39 \cdot s + 1} & \frac{-0.659 \cdot e^{-0.67 \cdot s}}{21.11 \cdot s + 1} \\ \frac{0.671 \cdot e^{-0.17 \cdot s}}{2.80 \cdot s + 1} & \frac{-0.0175 \cdot e^{-0.83 \cdot s}}{20.85 \cdot s + 1} \end{bmatrix}$	$\begin{bmatrix} \frac{0.721 \cdot e^{-0.17 \cdot s}}{23.39 \cdot s + 1} & \frac{0.0307 \cdot e^{-46.01 \cdot s}}{13.28 \cdot s + 1} \\ \frac{0.671 \cdot e^{-0.17 \cdot s}}{2.80 \cdot s + 1} & \frac{0.00240 \cdot e^{-81.88 \cdot s}}{8.65 \cdot s + 1} \end{bmatrix}$
CO_2 Train #7			
High Gas Throughput	$\begin{bmatrix} \frac{5.29 \cdot e^{-0.17 \cdot s}}{4.30 \cdot s + 1} & \frac{-0.284 \cdot e^{-0.17 \cdot s}}{1.80 \cdot s + 1} \\ \frac{1.32 \cdot e^{-0.17 \cdot s}}{2.10 \cdot s + 1} & \frac{-0.0133 \cdot e^{-0.17 \cdot s}}{1.84 \cdot s + 1} \end{bmatrix}$	$\begin{bmatrix} \frac{5.29 \cdot e^{-0.17 \cdot s}}{4.30 \cdot s + 1} & \frac{-2.35 \cdot e^{-0.67 \cdot s}}{9.98 \cdot s + 1} \\ \frac{1.32 \cdot e^{-0.17 \cdot s}}{2.10 \cdot s + 1} & \frac{-0.0981 \cdot e^{-0.33 \cdot s}}{10.52 \cdot s + 1} \end{bmatrix}$	$\begin{bmatrix} \frac{5.29 \cdot e^{-0.17 \cdot s}}{4.30 \cdot s + 1} & \frac{0.577 \cdot e^{-41.10 \cdot s}}{7.58 \cdot s + 1} \\ \frac{1.32 \cdot e^{-0.17 \cdot s}}{2.10 \cdot s + 1} & \frac{0.0258 \cdot e^{-41.27 \cdot s}}{7.58 \cdot s + 1} \end{bmatrix}$
Medium Gas Throughput	$\begin{bmatrix} \frac{2.70 \cdot e^{-0.17 \cdot s}}{9.93 \cdot s + 1} & \frac{-0.0456 \cdot e^{-0.17 \cdot s}}{2.60 \cdot s + 1} \\ \frac{1.18 \cdot e^{-0.17 \cdot s}}{2.80 \cdot s + 1} & \frac{-0.00237 \cdot e^{-0.17 \cdot s}}{1.48 \cdot s + 1} \end{bmatrix}$	$\begin{bmatrix} \frac{2.70 \cdot e^{-0.17 \cdot s}}{9.93 \cdot s + 1} & \frac{-1.61 \cdot e^{-0.67 \cdot s}}{14.97 \cdot s + 1} \\ \frac{1.18 \cdot e^{-0.17 \cdot s}}{2.80 \cdot s + 1} & \frac{-0.0535 \cdot e^{-0.33 \cdot s}}{14.68 \cdot s + 1} \end{bmatrix}$	$\begin{bmatrix} \frac{2.70 \cdot e^{-0.17 \cdot s}}{9.93 \cdot s + 1} & \frac{0.351 \cdot e^{-47.95 \cdot s}}{6.82 \cdot s + 1} \\ \frac{1.18 \cdot e^{-0.17 \cdot s}}{2.80 \cdot s + 1} & \frac{0.0132 \cdot e^{-44.99 \cdot s}}{7.23 \cdot s + 1} \end{bmatrix}$
Low Gas Throughput	$\begin{bmatrix} \frac{1.58 \cdot e^{-0.17 \cdot s}}{20.66 \cdot s + 1} & \frac{-0.0281 \cdot e^{-0.17 \cdot s}}{2.99 \cdot s + 1} \\ \frac{1.12 \cdot e^{-0.17 \cdot s}}{2.91 \cdot s + 1} & \frac{-0.00195 \cdot e^{-0.17 \cdot s}}{1.38 \cdot s + 1} \end{bmatrix}$	$\begin{bmatrix} \frac{1.58 \cdot e^{-0.17 \cdot s}}{20.66 \cdot s + 1} & \frac{-1.20 \cdot e^{-0.67 \cdot s}}{19.23 \cdot s + 1} \\ \frac{1.12 \cdot e^{-0.17 \cdot s}}{2.91 \cdot s + 1} & \frac{-0.0292 \cdot e^{-0.33 \cdot s}}{17.88 \cdot s + 1} \end{bmatrix}$	$\begin{bmatrix} \frac{1.58 \cdot e^{-0.17 \cdot s}}{20.66 \cdot s + 1} & \frac{0.266 \cdot e^{-56.10 \cdot s}}{6.96 \cdot s + 1} \\ \frac{1.12 \cdot e^{-0.17 \cdot s}}{2.91 \cdot s + 1} & \frac{0.00687 \cdot e^{-61.08 \cdot s}}{6.63 \cdot s + 1} \end{bmatrix}$

Table 10.1.2: Sensitivity analysis indices at steady-state.

	CO_2 Train #1			CO_2 Train #7		
	RGF-LSF	RGF-RSF	RGF-RLL	RGF-LSF	RGF-RSF	RGF-RLL
High Gas Throughput						
MRI	0.041	0.585	0.026	0.056	0.437	0.115
CN	38.67	3.05	62.13	97.79	13.56	47.92
DCN - d	29.70	2.11	47.73	24.80	3.18	12.11
DCN - y_1	26.33	1.86	42.31	23.72	3.04	11.58
DCN - y_2	28.34	2.62	45.51	94.88	13.25	46.51
DC - d	10.79	0.69	17.34	8.05	0.95	3.92
DC - y_1	16.47	1.04	26.48	4.34	0.51	2.11
DC - y_2	17.73	1.47	28.48	17.37	2.24	8.48
Medium Gas Throughput						
MRI	0.014	0.465	0.023	0.016	0.529	0.127
CN	95.88	3.09	56.26	184.19	6.28	23.32
DCN - d	75.29	2.20	44.17	80.95	2.46	10.19
DCN - y_1	65.31	1.89	38.31	73.56	2.23	9.26
DCN - y_2	70.21	2.64	41.21	168.87	5.96	21.43
DC - d	30.86	0.81	18.10	26.88	0.73	3.36
DC - y_1	50.62	1.32	29.69	24.94	0.67	3.12
DC - y_2	54.42	1.84	31.93	57.26	1.79	7.22
Low Gas Throughput						
MRI	0.004	0.383	0.019	0.015	0.592	0.125
CN	246.40	2.93	51.46	131.16	3.72	15.56
DCN - d	195.34	2.067	40.79	83.27	2.08	9.84
DCN - y_1	167.85	1.75	35.05	76.02	1.89	8.98
DCN - y_2	180.38	2.55	37.70	106.89	3.35	12.75
DC - d	101.07	0.94	21.10	25.38	0.56	2.98
DC - y_1	170.35	1.56	35.56	39.33	0.86	4.62
DC - y_2	183.08	2.27	38.25	55.30	1.52	6.57

Notation: d is the raw gas CO_2 content, y_1 is the sweet gas CO_2 content, and y_2 is the sweet gas flow rate.

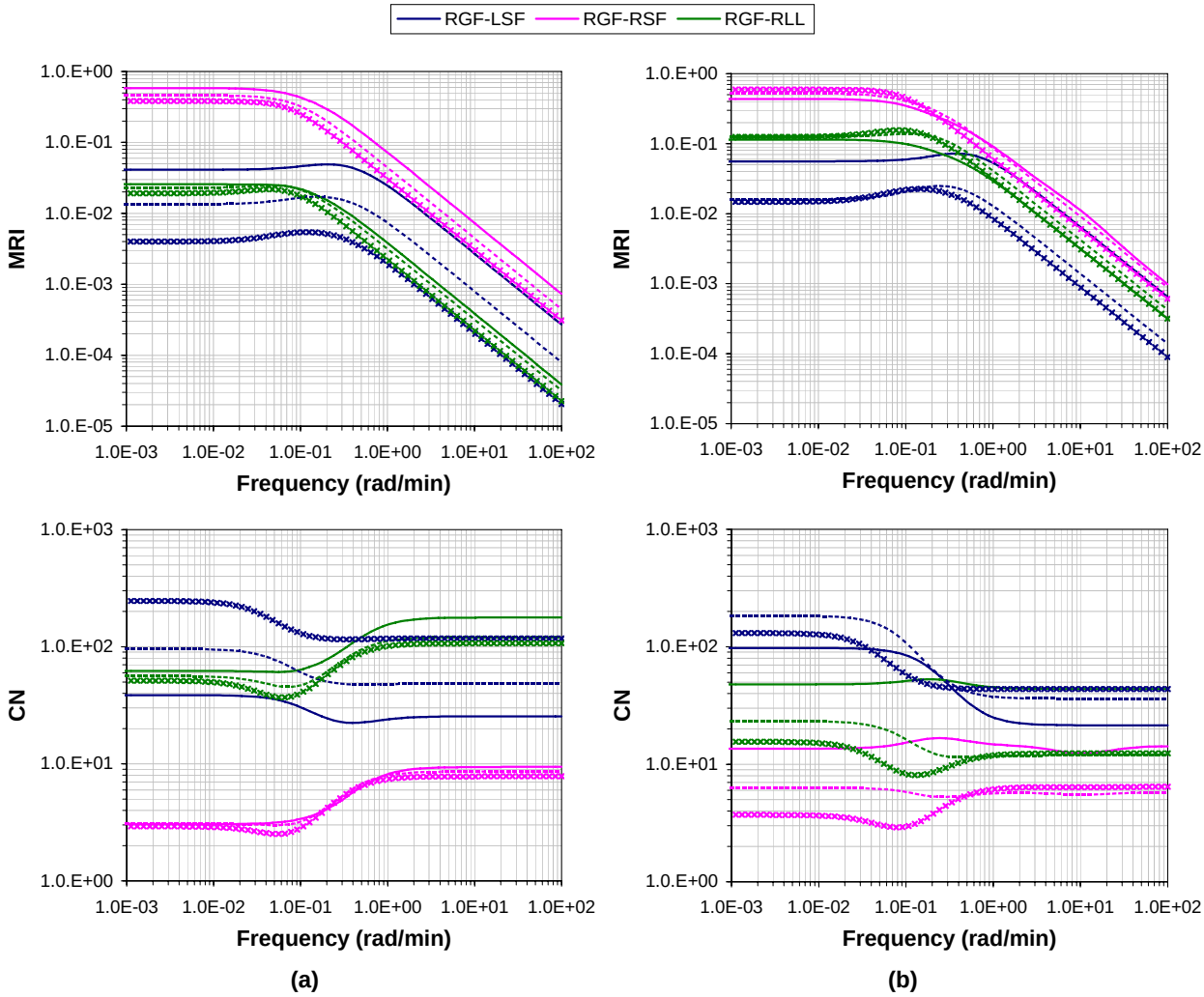

Figure 10.1.1: Frequency plots of the MRI and CN. (a) CO_2 train #1. (b) CO_2 train #7. The solid lines (––) represent the high gas throughput conditions, the dashed lines (---) represent the medium gas throughput conditions, and the crosses (×××) represent the low gas throughput conditions.

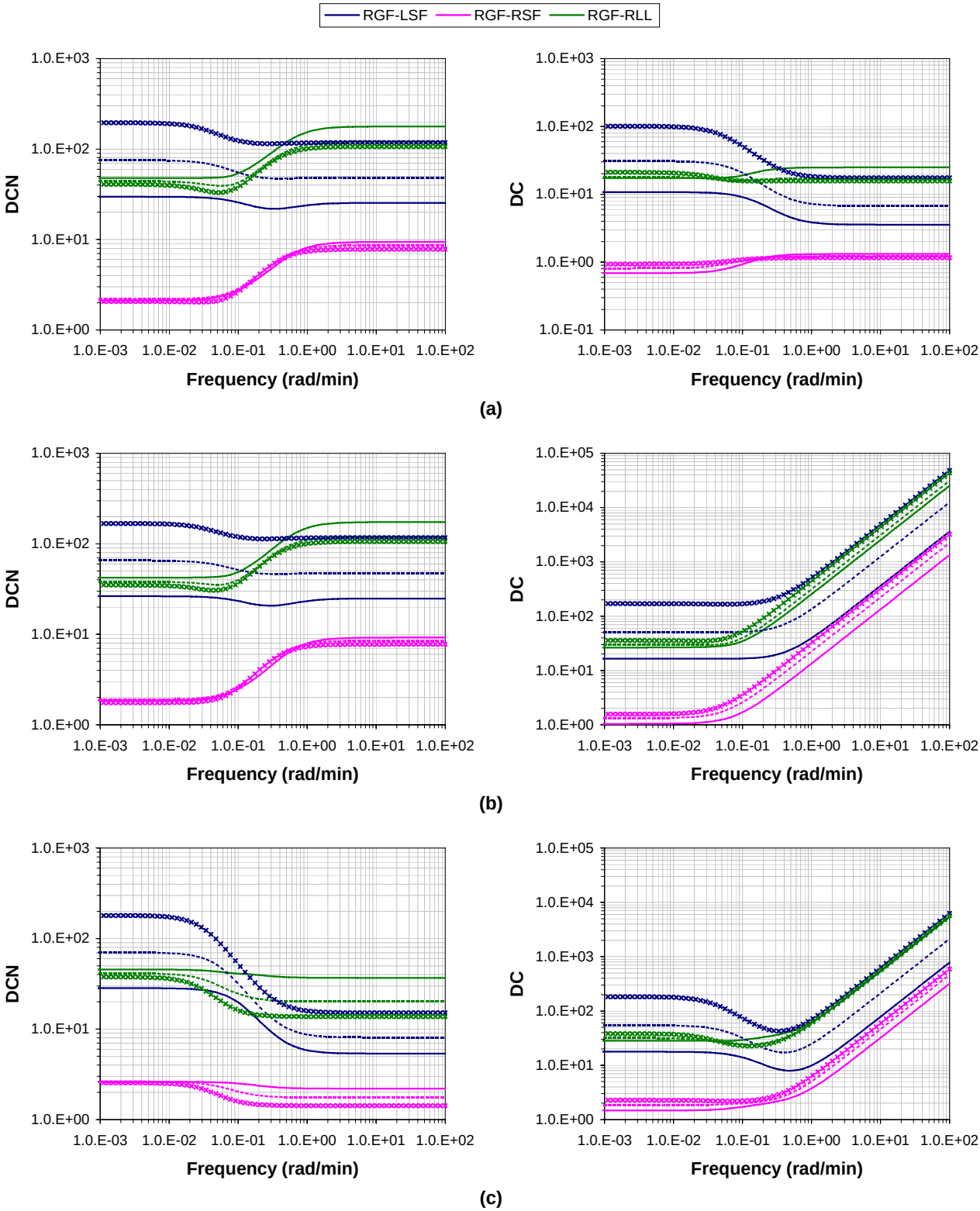

Figure 10.1.2: Frequency plots of DCN and DC for CO_2 train #1. Unit magnitude change in (a) the raw gas CO_2 content, (b) the sweet gas CO_2 content setpoint and (c) the sweet gas flow rate setpoint. The solid lines (––) represent the high gas throughput conditions, the dashed lines (---) represent the medium gas throughput conditions, and the crosses (×××) represent the low gas throughput conditions.

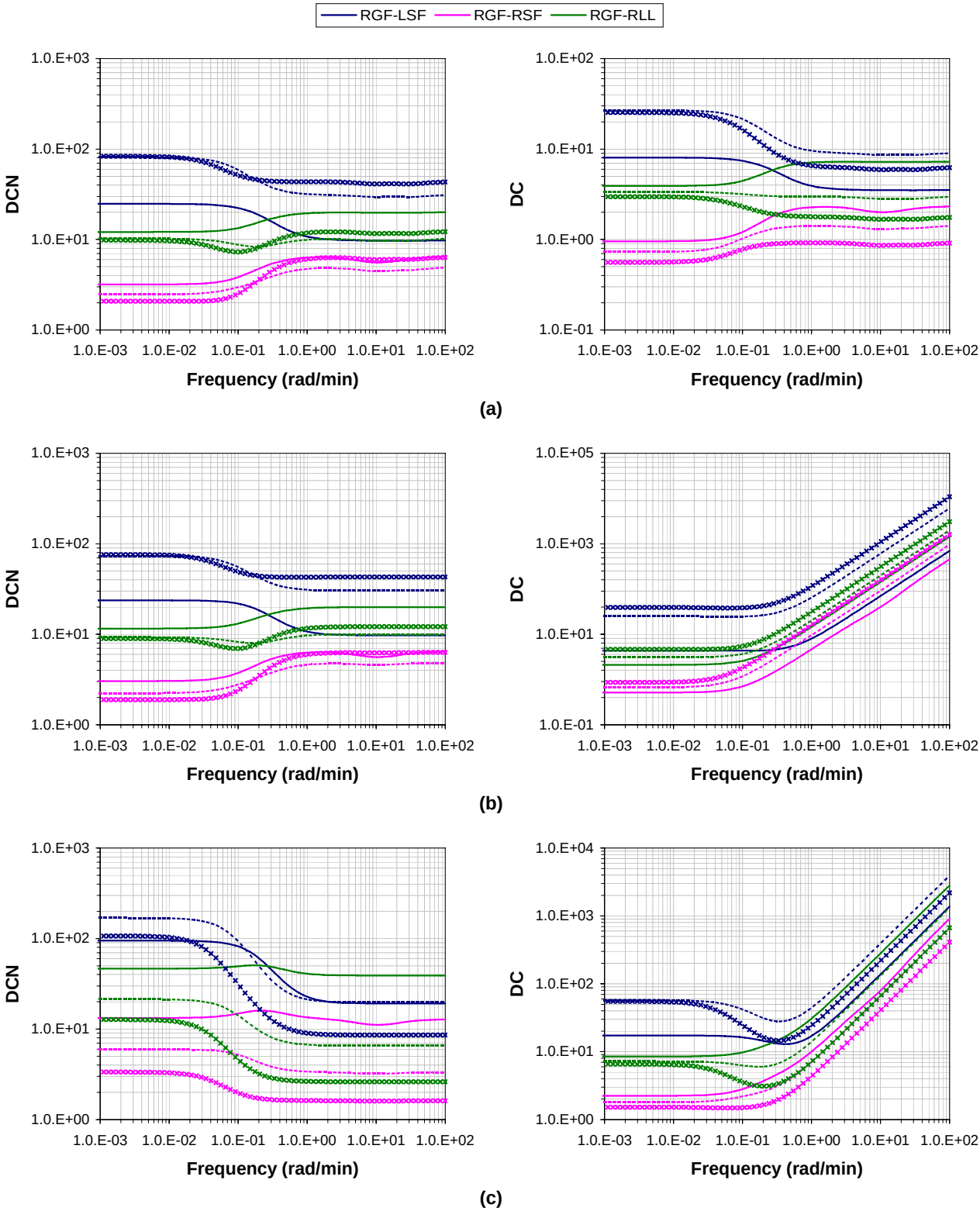

Figure 10.1.3: Frequency plots of DCN and DC for CO_2 train #7. Unit magnitude change in (a) the raw gas CO_2 content, (b) the sweet gas CO_2 content setpoint and (c) the sweet gas flow rate setpoint. The solid lines (––) represent the high gas throughput conditions, the dashed lines (---) represent the medium gas throughput conditions, and the crosses (×××) represent the low gas throughput conditions.

10.2 Selection of Diagonal Control Structure Configuration

Based on the sensitivity analyses performed in the previous section, the RGF-RSF diagonal control structure was identified as the optimal control structure for CO_2 trains #1 and #7. In this section, the loop interactions and system stability are evaluated in order to determine the best configuration for this control structure. As in the previous section, all necessary calculations were performed in the MATLAB® 5.2 numerical computing environment.

As an initial analysis, the process stability and controllability were checked by determining the system poles and zeros. An example of the MATLAB® scripts for performing these calculations is provided in Section I.2.1 in Appendix I. For the purpose of brevity, the calculated poles and zeros for the RGF-RSF control structure have not been included in the main body of this thesis, but are instead provided in Table I.2.1 in Appendix I.

No right-hand-plane (RHP) poles were identified, which indicated that the control structure was stable (Skogestad and Postlethwaite, 1996) for both CO_2 trains over the different operating regions. Due to the third-order Padé approximations for the dead times, several RHP zeros were identified for each system, which indicated that the systems would have inverse response behaviour. However, these RHP zeros were not located near the origin, which would have otherwise implied poor control performance (Skogestad and Postlethwaite, 1996).

To determine the loop interactions, the **RGA** was derived as a function of frequency using equation (2.5.7). An example of the MATLAB® scripts used to perform these calculations is included in Section I.2.2 in Appendix I. The steady-state values for the diagonal and off-diagonal elements λ_{11} and λ_{12}, respectively, are given in Table 10.2.1, while the corresponding frequency plots are depicted in Figure 10.2.1. It should be noted that for 2×2 systems, $\lambda_{11}=\lambda_{22}$ and $\lambda_{12}=\lambda_{21}$ since the elements of each row and column of the **RGA** sum to 1 (Skogestad and Postlethwaite, 1996).

It was observed that the diagonal elements of the **RGA** were small and negative, whereas the off-diagonal elements were positive and close to 1 over the examined frequency range. This strong off-diagonal dominance favoured the off-diagonal variable pairings for minimising the loop interactions. However, some degree of interaction was still expected, especially for CO_2 train #7, since the off-diagonal elements were greater than 1 (Svrcek et al., 2006). The off-diagonal pairings were also preferred due to their positive values, which ensured the systems corresponding to the off-diagonal pairings were decentralised integral controllable (Skogestad and Postlethwaite, 1996). This indicated that a diagonal control structure with integral action in each loop could be implemented such that the feedback system was stable and each loop could be detuned independently without introducing instability.

To confirm the suitability of the off-diagonal variable pairings, the process transfer function matrices were reordered such that the paired variables were along the diagonal, as shown in Table 10.2.2.

Using these reordered transfer function matrices, the NI and MIC were calculated from equations (2.5.8) and (2.5.9). An example MATLAB® script for these calculations is included in Section I.2.3 in Appendix I, while the resulting values are given in Table 10.2.1. For both CO_2 trains, the NI and MIC values were positive. This signified that the RGF-RSF systems described by the process transfer function matrices in Table 10.2.2 were definitely closed-loop stable.

As a result of the above analyses, the optimal configuration for the RGF-RSF diagonal control structure for CO_2 trains #1 and #7 was identified as the one in which the raw gas and reboiler steam flow rates were used to control the sweet gas flow rate and CO_2 content, respectively, corresponding to the y_1-m_2 and y_2-m_1 variable pairings from equation (10.1.1). This was not unexpected since the sweet gas flow rate is directly dependent on the raw gas flow rate.

The performance of the optimal diagonal control structure configuration is analysed in the next section.

Table 10.2.1: Steady-state results for the interaction and stability analyses for the RGF-RSF control structure. The NI and MIC values correspond to the off-diagonal RGA pairings.

	λ_{11}, λ_{12}	NI	MIC
CO_2 Train #1			
High Gas Throughput	-0.03, 1.03	0.97	0.86, 1.22
Medium Gas Throughput	-0.03, 1.03	0.97	0.68, 0.98
Low Gas Throughput	-0.03, 1.03	0.97	0.55, 0.78
CO_2 Train #7			
High Gas Throughput	-0.20, 1.20	0.83	2.72, 0.95
Medium Gas Throughput	-0.08, 1.08	0.92	1.83, 0.96
Low Gas Throughput	-0.04, 1.04	0.97	1.38, 0.94

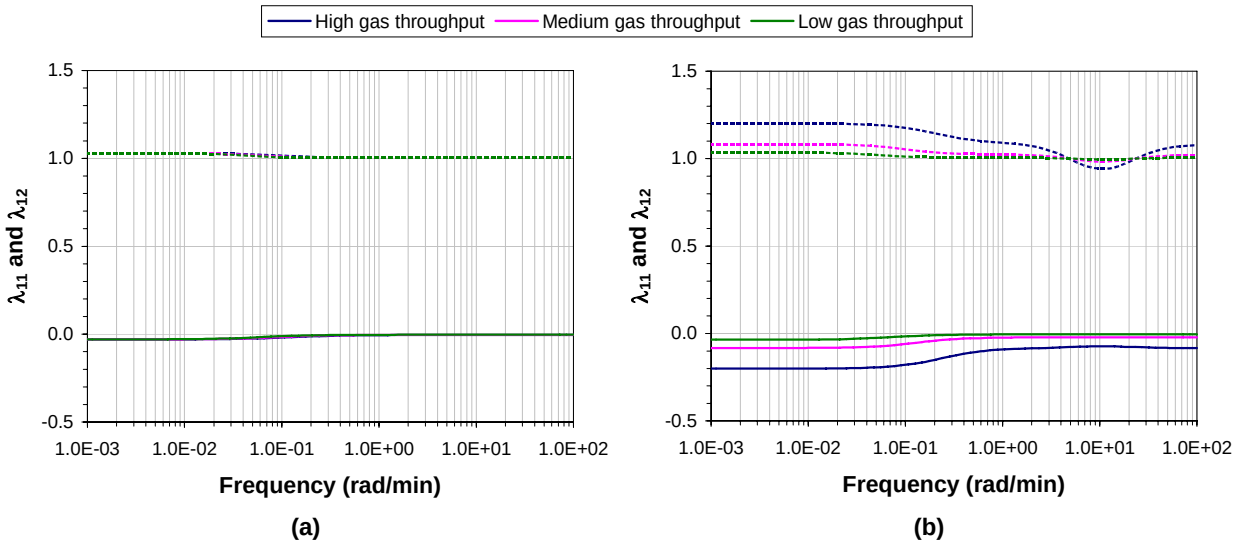

Figure 10.2.1: Frequency plots for the RGA elements. (a) CO_2 train #1. (b) CO_2 train #7. The solid lines (––) represent the diagonal elements λ_{11}, while the dashed lines (---) represent the off-diagonal elements λ_{12}.

Table 10.2.2: Reordered process transfer function matrices for the RGF-RSF diagonal control structure. The time constants and dead times are given in minutes.

	CO_2 Train #1	CO_2 Train #7
High Gas Throughput	$\begin{bmatrix} \frac{-0.989 \cdot e^{-0.67 \cdot s}}{13.17 \cdot s + 1} & \frac{1.17 \cdot e^{-0.17 \cdot s}}{8.22 \cdot s + 1} \\ \frac{-0.0262 \cdot e^{-0.83 \cdot s}}{16.02 \cdot s + 1} & \frac{1.09 \cdot e^{-0.17 \cdot s}}{1.62 \cdot s + 1} \end{bmatrix}$	$\begin{bmatrix} \frac{-2.35 \cdot e^{-0.67 \cdot s}}{9.98 \cdot s + 1} & \frac{5.29 \cdot e^{-0.17 \cdot s}}{4.30 \cdot s + 1} \\ \frac{-0.0981 \cdot e^{-0.33 \cdot s}}{10.52 \cdot s + 1} & \frac{1.32 \cdot e^{-0.17 \cdot s}}{2.10 \cdot s + 1} \end{bmatrix}$
Medium Gas Throughput	$\begin{bmatrix} \frac{-0.781 \cdot e^{-0.67 \cdot s}}{17.31 \cdot s + 1} & \frac{0.945 \cdot e^{-0.17 \cdot s}}{14.90 \cdot s + 1} \\ \frac{-0.0207 \cdot e^{-0.83 \cdot s}}{18.73 \cdot s + 1} & \frac{0.879 \cdot e^{-0.17 \cdot s}}{2.34 \cdot s + 1} \end{bmatrix}$	$\begin{bmatrix} \frac{-1.61 \cdot e^{-0.67 \cdot s}}{14.97 \cdot s + 1} & \frac{2.70 \cdot e^{-0.17 \cdot s}}{9.93 \cdot s + 1} \\ \frac{-0.0535 \cdot e^{-0.33 \cdot s}}{14.68 \cdot s + 1} & \frac{1.18 \cdot e^{-0.17 \cdot s}}{2.80 \cdot s + 1} \end{bmatrix}$
Low Gas Throughput	$\begin{bmatrix} \frac{-0.659 \cdot e^{-0.67 \cdot s}}{21.11 \cdot s + 1} & \frac{0.721 \cdot e^{-0.17 \cdot s}}{23.39 \cdot s + 1} \\ \frac{-0.0175 \cdot e^{-0.83 \cdot s}}{20.85 \cdot s + 1} & \frac{0.671 \cdot e^{-0.17 \cdot s}}{2.80 \cdot s + 1} \end{bmatrix}$	$\begin{bmatrix} \frac{-1.20 \cdot e^{-0.67 \cdot s}}{19.23 \cdot s + 1} & \frac{1.58 \cdot e^{-0.17 \cdot s}}{20.66 \cdot s + 1} \\ \frac{-0.0292 \cdot e^{-0.33 \cdot s}}{17.88 \cdot s + 1} & \frac{1.12 \cdot e^{-0.17 \cdot s}}{2.91 \cdot s + 1} \end{bmatrix}$

10.3 Analysis of Diagonal Control Structure Performance

Having identified a suitable configuration for the RGF-RSF diagonal control structure for CO_2 trains #1 and #7, the performance of the resulting control systems are analysed in this section using the frequency-dependent **PRGA** and **CLDG** described by equations (2.5.10) and (2.5.11). The steady-state values for the **PRGA** and **CLDG** are provided in Table 10.3.1, while the corresponding frequency plots are given in Figure 10.3.1. An example of the MATLAB® scripts used to perform the necessary calculations is included in Section I.3 in Appendix I.

It was observed that the **PRGA** and **CLDG** elements were larger for CO_2 train #7 than for CO_2 train #1. This implied that the former CO_2 train was more difficult to control than the latter, which was consistent with the greater degree of interaction indicated by the larger off-diagonal **RGA** elements for CO_2 train #7 in Table 10.2.1. It was also noted that the **PRGA** and **CLDG** elements decreased with decreasing gas throughput, which indicated that the trains, more notably CO_2 train #7, became more difficult to control with increasing gas throughput. This corresponded well with the observed trend for the off-diagonal **RGA** elements in Figure 10.2.1.

To achieve acceptable diagonal control structure performance for the two trains, condition (2.5.12) for the open loop transfer functions $\mathbf{G_{OL,i}}(s)$ had to be satisfied for each control loop. For the sweet gas CO_2 content loop (denoted as Loop 1), $|\mathbf{PRGA}_{11}|$ and $|\mathbf{PRGA}_{12}|$ were considered for setpoint tracking, while $|\mathbf{CLDG}_{11}|$ was considered for disturbance rejection. In the case of the sweet gas flow rate loop (denoted as Loop 2), $|\mathbf{PRGA}_{22}|$ and $|\mathbf{PRGA}_{21}|$ were considered for setpoint tracking, while $|\mathbf{CLDG}_{21}|$ was considered for disturbance rejection.

For CO_2 train # 1, both $|\mathbf{PRGA}_{11}|$ and $|\mathbf{PRGA}_{12}|$ were larger than $|\mathbf{CLDG}_{11}|$ over the examined frequency range. This implied that changes in the setpoints for the sweet gas CO_2 content and flow rate had a greater effect on the sweet gas CO_2 content than any changes in the raw gas CO_2 content. At low frequencies (up to 0.01, 0.03 and 0.04 rad/min respectively for the low, medium and high gas throughput conditions), $|\mathbf{PRGA}_{12}|$ was marginally larger than $|\mathbf{PRGA}_{11}|$, which remained relatively constant over the frequency range. Consequently, to ensure satisfactory performance for Loop 1 for CO_2 train #1 over the three operating regions, $|1+\mathbf{G_{OL,1}}(s)|$ had to be greater than the high gas throughput $|\mathbf{PRGA}_{12}|$ values at frequencies below 0.04 rad/min. For higher frequencies at which setpoint tracking was still required, $|1+ \mathbf{G_{OL,1}}(s)|$ had to be greater than the corresponding $|\mathbf{PRGA}_{11}|$ values.

For CO_2 train #7, it was observed that $|\mathbf{CLDG}_{11}|$ was greater than 1 for frequencies up to 0.05 and 0.25 rad/min respectively for the medium and high gas throughput conditions. This implied that control was needed in Loop 1 for disturbance rejection for frequencies up to 0.25 rad/min. Even so, tracking the sweet gas flow rate setpoint was still more difficult due to the larger values of $|\mathbf{PRGA}_{12}|$ over the entire frequency range. However, the sweet gas CO_2 content setpoint became the more difficult setpoint to track ($|\mathbf{PRGA}_{12}|<|\mathbf{PRGA}_{11}|$) for the low and medium gas throughput conditions at

frequencies above 0.04 and 0.19 rad/min respectively. Nevertheless, to ensure acceptable control performance for Loop 1 for CO_2 train #7 over the three operating regions, $|1+\mathbf{G}_{\mathbf{OL},1}(s)|$ had to be greater than the high gas throughput $|\mathbf{PRGA}_{12}|$ values over the frequency range required for setpoint tracking.

For both CO_2 trains, $|\mathbf{CLDG}_{21}|$ was observed to be less than 1 over the examined frequency range, indicating that changes in the raw gas CO_2 content had little effect on the sweet gas flow rate. The $|\mathbf{PRGA}_{22}|$ values were considerably larger than those for $|\mathbf{PRGA}_{21}|$ and $|\mathbf{CLDG}_{21}|$, which unsurprisingly implied that changes in the sweet gas flow rate setpoint had the most significant effect on the sweet gas flow rate. Consequently, to ensure satisfactory performance for Loop 2 for CO_2 trains #1 and #7 over the three operating regions, $|1+\mathbf{G}_{\mathbf{OL},2}(s)|$ had to be greater than the high gas throughput $|\mathbf{PRGA}_{22}|$ values over the frequency range required for setpoint tracking.

To test the validity of the above findings, BLT tuning was applied to tune the SISO controllers for the RGF-RSF diagonal control structures for the two CO_2 trains. This is discussed in the following section.

Table 10.3.1: Steady-state values for the PRGA and CLDG for the selected configuration for the RGF-RSF diagonal control structure.

	CO_2 Train #1		CO_2 Train #7	
	PRGA	**CLDG**	**PRGA**	**CLDG**
High Gas Throughput	$\begin{bmatrix} 1.03 & -1.11 \\ -0.03 & 1.03 \end{bmatrix}$	$\begin{bmatrix} 0.67 \\ -0.09 \end{bmatrix}$	$\begin{bmatrix} 1.20 & -4.80 \\ -0.05 & 1.20 \end{bmatrix}$	$\begin{bmatrix} 2.23 \\ -0.11 \end{bmatrix}$
Medium Gas Throughput	$\begin{bmatrix} 1.03 & -1.11 \\ -0.03 & 1.03 \end{bmatrix}$	$\begin{bmatrix} 0.63 \\ -0.10 \end{bmatrix}$	$\begin{bmatrix} 1.08 & -2.48 \\ -0.04 & 1.08 \end{bmatrix}$	$\begin{bmatrix} 1.17 \\ -0.08 \end{bmatrix}$
Low Gas Throughput	$\begin{bmatrix} 1.03 & -1.11 \\ -0.03 & 1.03 \end{bmatrix}$	$\begin{bmatrix} 0.61 \\ -0.10 \end{bmatrix}$	$\begin{bmatrix} 1.04 & -1.46 \\ -0.03 & 1.04 \end{bmatrix}$	$\begin{bmatrix} 0.67 \\ -0.06 \end{bmatrix}$

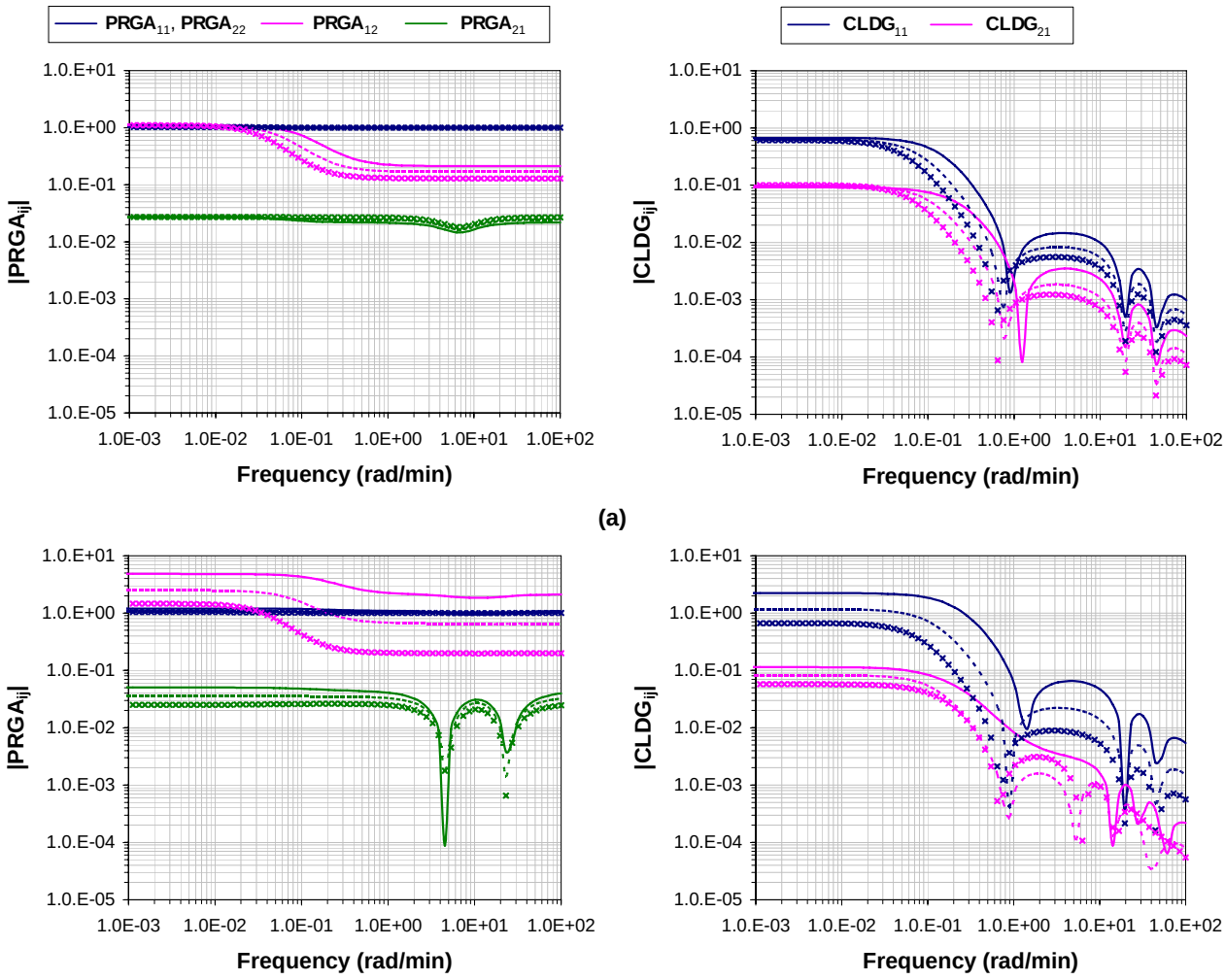

Figure 10.3.1: Frequency plots for $|PRGA_{ij}|$ and $|CLDG_{ij}|$. (a) CO_2 train #1. (b) CO_2 train #7. The solid lines (––) represent the high gas throughput conditions, the dashed lines (---) represent the medium gas throughput conditions, and the crosses (×××) represent the low gas throughput conditions.

10.4 BLT Tuning

As described in Section 2.5.6, BLT tuning is a well-known and simple method for tuning diagonal control structures. This section discusses the application of this method to determine the controller settings for the RGF-RSF diagonal control structure defined in Table 10.2.2 for CO_2 trains #1 and #7. These controller settings were required in order to perform dynamic simulations of the diagonal control structure so that its performance could be assessed, as described in the next section.

Using equation (2.5.14), the cross-over frequency ω_{co} was obtained with the Microsoft Excel® Solver tool. This parameter was used to calculate the ultimate gain K_u and period P_u via equations (2.5.15) and (2.5.16). The resulting values for ω_{co}, K_u and P_u are given in Table 10.4.1, along with the corresponding Ziegler-Nichols controller gain K_c^{ZN} and integral time constant τ_I^{ZN}. The Ziegler-Nichols settings were obtained using the PI tuning rules provided in Table 2.5.2. Derivative action was not considered for the RGF-RSF diagonal control structure since the SISO loops were not slow enough, as indicated by their moderate time constants, to require derivative action to tighten the dynamic response. Additionally, signal noise is expected in practice for the CO_2 trains, which precludes the use of derivative action (Svrcek et al., 2006).

Following the method outlined in Section 2.5.6, detuning factors F were determined for each CO_2 train and operating region. An example MATLAB® script for BLT tuning is provided in Section I.4 of Appendix I. The resulting F factors and SISO controller settings for the diagonal control structures are included in Table 10.4.1, while plots of the corresponding W functions, as defined by equation (2.5.19), are provided as Figure 10.4.1. According to these plots, the BLT tuned control systems were closed-loop stable since the W curves did not encircle the critical point (-1, 0). The controller settings obtained from the BLT tuning procedure were therefore considered valid.

It was also observed that the CO_2 train #7 loops were significantly more detuned by the BLT tuning method, compared to their equivalent loops in CO_2 train #1. Consequently, more conservative controller settings (i.e. smaller K_c and larger τ_I values) were required for CO_2 train #7 in order to achieve a similar level of compromise between robustness and performance as for CO_2 train #1. This reflected the more difficult control problem posed by the former CO_2 train, which was implied in the previous sections by the **PRGA**, **CLDG** and **RGA**.

Table 10.4.1: BLT tuning parameters for the RGF-RSF diagonal control structures for CO_2 trains #1 and #7.

		Process Parameters			Controller Parameters				
		ω_{co} (rad/min)	K_u	P_u (min)	K_c^{ZN}	τ_I^{ZN} (min)	F	K_c	τ_I (min)
CO_2 Train #1									
High Gas Throughput	Loop 1	2.40	-31.67	2.61	-14.39	1.19	2.14	-6.76	2.53
	Loop 2	9.80	15.88	0.64	7.22	0.29		3.39	0.62
Medium Gas Throughput	Loop 1	2.40	-41.43	2.63	-18.83	1.19	2.52	-7.50	3.00
	Loop 2	9.69	22.67	0.65	10.31	0.29		4.11	0.74
Low Gas Throughput	Loop 1	2.39	-50.37	2.63	-22.90	1.20	2.82	-8.15	3.36
	Loop 2	9.65	27.06	0.65	12.30	0.30		4.38	0.83
CO_2 Train #7									
High Gas Throughput	Loop 1	2.42	-24.16	2.60	-10.98	1.18	4.02	-2.73	4.75
	Loop 2	9.72	20.43	0.65	9.29	0.29		2.31	1.18
Medium Gas Throughput	Loop 1	2.40	-35.92	2.62	-16.33	1.19	3.85	-4.25	4.57
	Loop 2	9.65	26.99	0.65	12.27	0.30		3.20	1.14
Low Gas Throughput	Loop 1	2.39	-45.94	2.63	-20.88	1.20	3.29	-6.33	3.95
	Loop 2	9.64	28.09	0.65	12.77	0.30		3.87	0.98

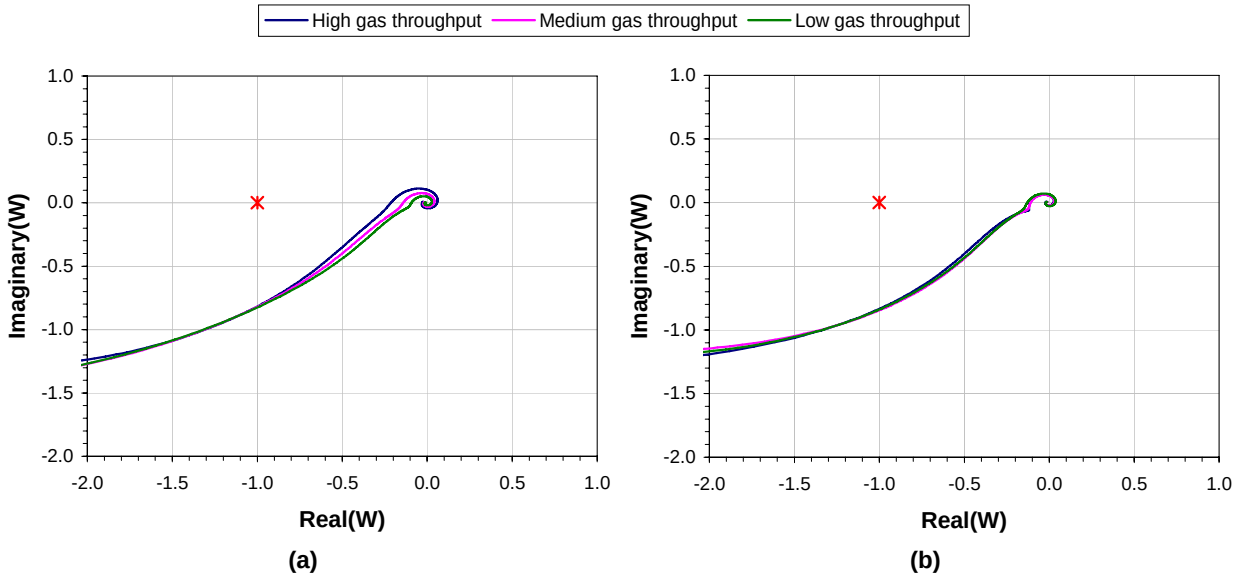

Figure 10.4.1: Plots of the scalar function W. (a) CO_2 train #1. (b) CO_2 train #7. The critical point (-1, 0) is highlighted in red.

10.5 Diagonal Control Structure Dynamic Simulations

Having obtained suitable controller settings from the BLT tuning method, a series of dynamic simulations were performed to analyse the dynamic performance of the RGF-RSF diagonal control structure for CO_2 trains #1 and #7. The necessary calculations were performed in MATLAB® 5.2, and an example MATLAB® script is provided in Section I.5 in Appendix I.

As a matter of interest, each set of controller settings was applied to all three operating regions for their respective CO_2 train. The purpose of this comparison was to determine whether it was possible to achieve acceptable control performance for the two CO_2 trains using the same set of controller settings across the different operating regions.

For each simulation case, the open-loop transfer functions $\mathbf{G_{OL,i}}(s)$ were first determined to verify if condition (2.5.12) for achieving acceptable disturbance rejection and setpoint performance was satisfied over the relevant frequency ranges identified in Section 10.3. Figure 10.5.1 compares the resulting frequency-dependent $|1+\mathbf{G_{OL,i}}(s)|$ curves against the relevant **PRGA** elements identified in Section 10.3. It was observed that the $|1+\mathbf{G_{OL,i}}(s)|$ values were greater than the corresponding **PRGA** elements at frequencies below approximately 0.1 to 1 rad/min. These frequencies corresponded to the frequency range usually needed for setpoint tracking, as required to satisfy condition (2.5.12) for the **PRGA** elements. This indicated that the controller settings obtained from the BLT tuning method could produce a reasonable control performance for both CO_2 trains, regardless of operating region.

However, a comparison of Figures 10.3.1 and 10.5.1 showed that for CO_2 train #7, the $|1+\mathbf{G_{OL,1}}(s)|$ values were not always larger than the corresponding **CLDG** elements for which control was required for disturbance rejection ($|\mathbf{CLDG}_{ik}|>1$). This implied that the Loop 1 controller settings for CO_2 train #7 may not provide adequate disturbance rejection at higher frequencies.

In order to test the control performance of the BLT tuned controller settings for the RGF-RSF diagonal control structure, the servo and regulator closed-loop transfer function matrices $\mathbf{G_{CLS}}(s)$ and $\mathbf{G_{CLR}}(s)$ for setpoint tracking and disturbance rejection, respectively, were defined as follows:

$$\mathbf{G_{CLS}}(s) = \left[\mathbf{I} + \mathbf{G_p}(s) \cdot \mathbf{G_c}(s)\right]^{-1} \cdot \mathbf{G_p}(s) \cdot \mathbf{G_c}(s) \tag{10.5.1}$$

$$\mathbf{G_{CLR}}(s) = \left[\mathbf{I} + \mathbf{G_p}(s) \cdot \mathbf{G_c}(s)\right]^{-1} \cdot \mathbf{G_d}(s) \tag{10.5.2}$$

where $\mathbf{I}$ is the identity matrix, $\mathbf{G_p}(s)$ is the process transfer function matrix, $\mathbf{G_c}(s)$ is the controller transfer function matrix, and $\mathbf{G_d}(s)$ is the disturbance transfer function matrix.

Unit magnitude disturbance and setpoint changes were applied separately to $\mathbf{G_{CLS}}(s)$ and $\mathbf{G_{CLR}}(s)$ for each case to obtain the closed-loop step response curves for each controlled variable. The resulting response curves were observed to be quite similar for the three operating conditions. Consequently for brevity, the closed-loop step response curves for the high gas throughput conditions are given in

Figures 10.5.2 and 10.5.3, while the corresponding curves for the medium and low gas throughput conditions are included as Figures I.5.1 to I.5.4 in Appendix I. The vertical axes for these figures are dimensionless and are equivalent to those for the response curves depicted in Table 2.5.1. To achieve this, the process outputs were expressed in perturbation form and were scaled by dividing each output variable by its allowed range and then by the similarly scaled step change.

It was observed that the closed-loop step responses for all the simulation cases were reasonably rapid with regard to the process time constants for the two CO_2 trains, as steady-state was achieved within one hour. The controlled variables responded most quickly at the high gas throughput conditions, while the low gas throughput conditions produced the slowest closed-loop responses. It was also noted that the closed-loop step responses for Loop 2 tended to be much faster than the corresponding Loop 1 responses. These findings were consistent with the observed trends for the process time constants given in Table 10.2.2. The process time constants for Loop 1 were much larger than those for Loop 2, and the process time constants for both loops increased with increasing gas throughput. No offset was observed at steady-state due to the integral action of the controllers.

For CO_2 train #1, the effect of a unit magnitude change in the raw gas CO_2 content on the closed-loop response for the different controller settings are illustrated in the leftmost plots in Figures 10.5.2, I.5.1 and I.5.3. The corresponding step responses for unit magnitude changes in the sweet gas CO_2 content and flow rate setpoints are depicted in the middle and rightmost plots in these three figures. For both disturbance rejection and setpoint tracking, it was observed that the most rapid responses with the largest overshoots were produced by the controller settings derived for the high gas throughput conditions. In contrast, the low gas throughput controller settings generated the most damped step responses.

This observed trend was consistent with the high gas throughput controller settings having the smallest integral time constants, while the largest integral time constants were associated with the low gas throughput controller settings. It should be noted that despite its slightly more aggressive nature, the high gas throughput controller settings still produced relatively damped closed-loop step responses for the three operating regions. Each of the three sets of controller settings for CO_2 train #1 in Table 10.4.1 therefore generated acceptable control performances for the RGF-RSF diagonal control structure, regardless of the operating region, which was consistent with the earlier analysis of the **PRGA** elements and $|1+\mathbf{G}_{\mathbf{OL},i}(s)|$ values.

For CO_2 train #7, the leftmost plots in Figures 10.5.3, I.5.2 and I.5.4 show the closed-loop step responses for a unit magnitude change in the raw gas CO_2 content, while the centre and rightmost plots illustrate the corresponding effects of unit magnitude changes in the two setpoints. In contrast to CO_2 train #1, the high gas throughput controller settings were found to generate the most damped closed-loop step responses for the disturbance rejection and setpoint tracking cases. The corresponding responses produced by the low gas throughput controller settings were the least

damped, and in the case of the high gas throughput conditions, the responses were distinctly under-damped.

This observed control behaviour was consistent with the high gas throughput controller settings having the smallest controller gains and largest integral time constants, while the low gas throughput settings were the most aggressive with the largest controller gains and the integral time constants. Since none of the controller settings for CO_2 train #7 produced overly oscillatory or unstable closed-loop responses, the three sets of controller settings were each applicable to the RGF-RSF diagonal control structure, regardless of the operating region. While this agreed with the earlier analysis of the **PRGA** elements and $|1+\mathbf{G}_{\mathbf{OL},i}(s)|$ values, it also contrasted with the analysis of the **CLDG** elements and $|1+\mathbf{G}_{\mathbf{OL},i}(s)|$ values since reasonable disturbance rejection was achieved with the different controller settings over the three operating regions.

The results of the above-discussed process control studies therefore indicated that the implementation of the RGF-RSF diagonal control structure identified in this work could potentially enable the automatic control of the two key process outputs, the sweet gas CO_2 content and flow rate, for the two most dissimilar CO_2 trains, CO_2 trains #1 and #7. These studies demonstrated a potential application for the HYSYS® process models of the Moomba CO_2 trains, in that they could be used to facilitate the development of a fully automated control strategy for the CO_2 trains.

As the above described control studies were purely for demonstrative purposes, and not a key focus of this work, the diagonal control structures were not rigorously tested for performance in the presence of process noise. Neither were they implemented in HYSYS® to investigate the model mismatch between the HYSYS® and MATLAB® process models. It should be noted that these measures are highly recommended for any future work as they are essential to the development of a viable control scheme for the CO_2 trains. However, before such work can proceed, the dynamic process models need to be validated against detailed high quality step-test data from the CO_2 trains, which was not accessible at the time.

A final point to note, the reasonable control performances observed in the dynamic process control studies indicated that the simple PID controllers in the diagonal control structure provided sufficient control action, despite the non-linear behaviour of the CO_2 trains. This justified the exclusion of more advanced controllers from this work, and suggested that more complex multivariable controllers may not be necessary in order to achieve reasonable control of the Moomba CO_2 trains.

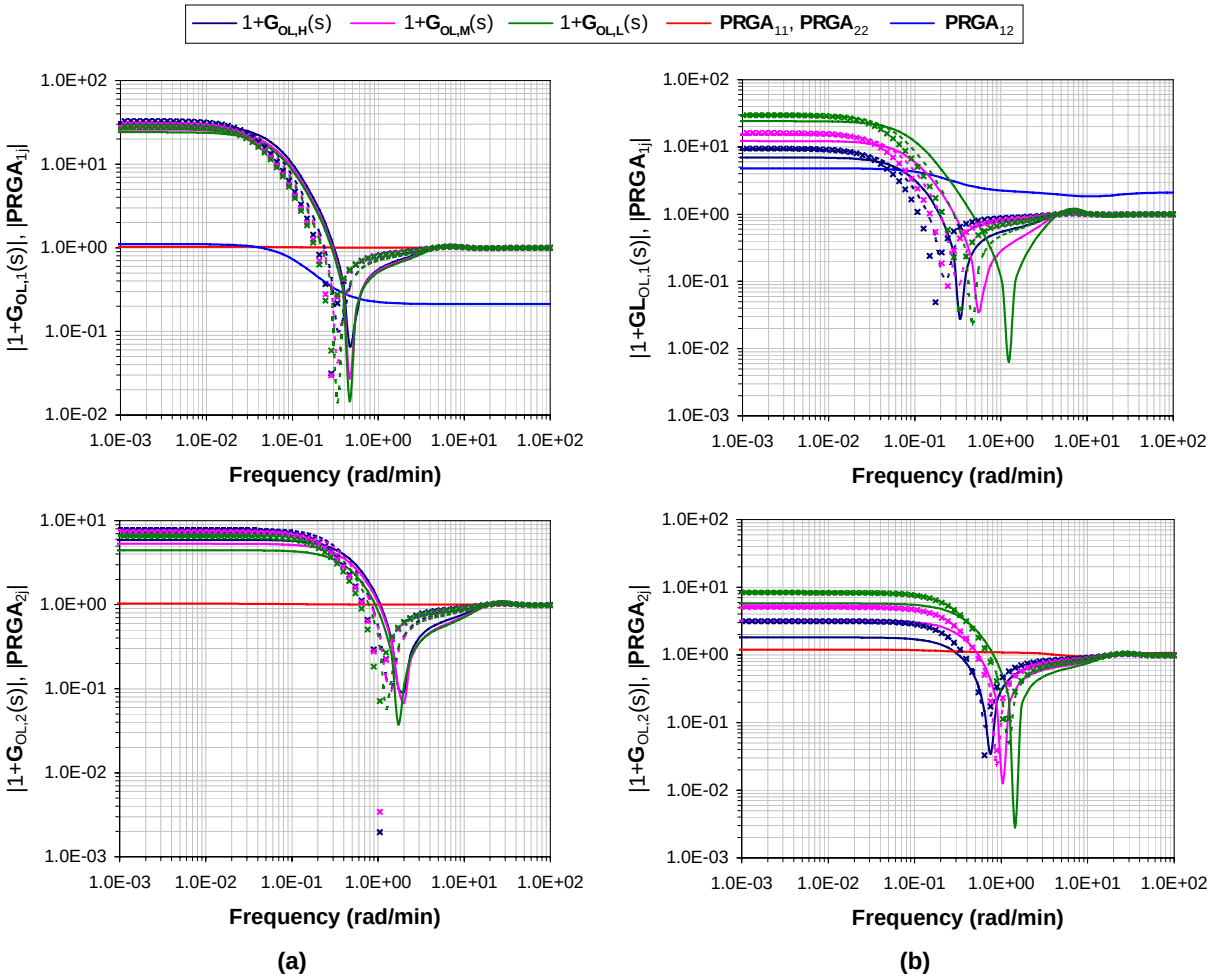

Figure 10.5.1: Frequency plots of $|1+G_{OL,i}(s)|$ and $|PRGA_{ij}|$. (a) CO_2 trains #1. (b) CO_2 train #7. The solid lines (––) represent the high gas throughput conditions, the dashed lines (---) represent the medium gas throughput conditions, and the crosses (×××) represent the low gas throughput conditions. The subscripts H, M and L respectively denote the controller settings corresponding to the high, medium and low gas throughput conditions.

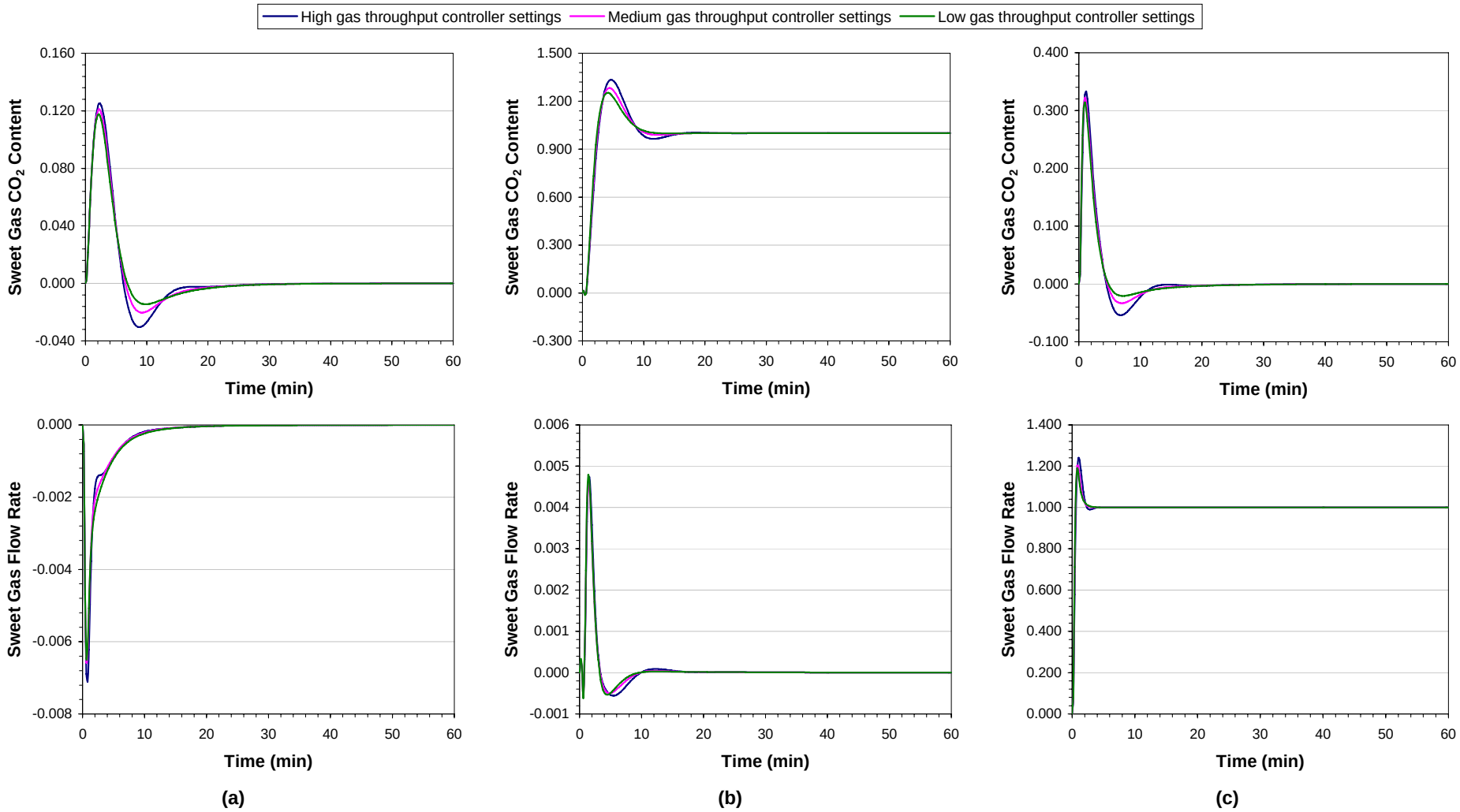

Figure 10.5.2: CO_2 train #1 closed-loop step response curves at the high gas throughput conditions. (a) Unit magnitude change in the raw gas CO_2 content at 0 min. (b) Unit magnitude change in the sweet gas CO_2 content setpoint at 0 min. (c) Unit magnitude change in the sweet gas flow rate setpoint at 0 min.

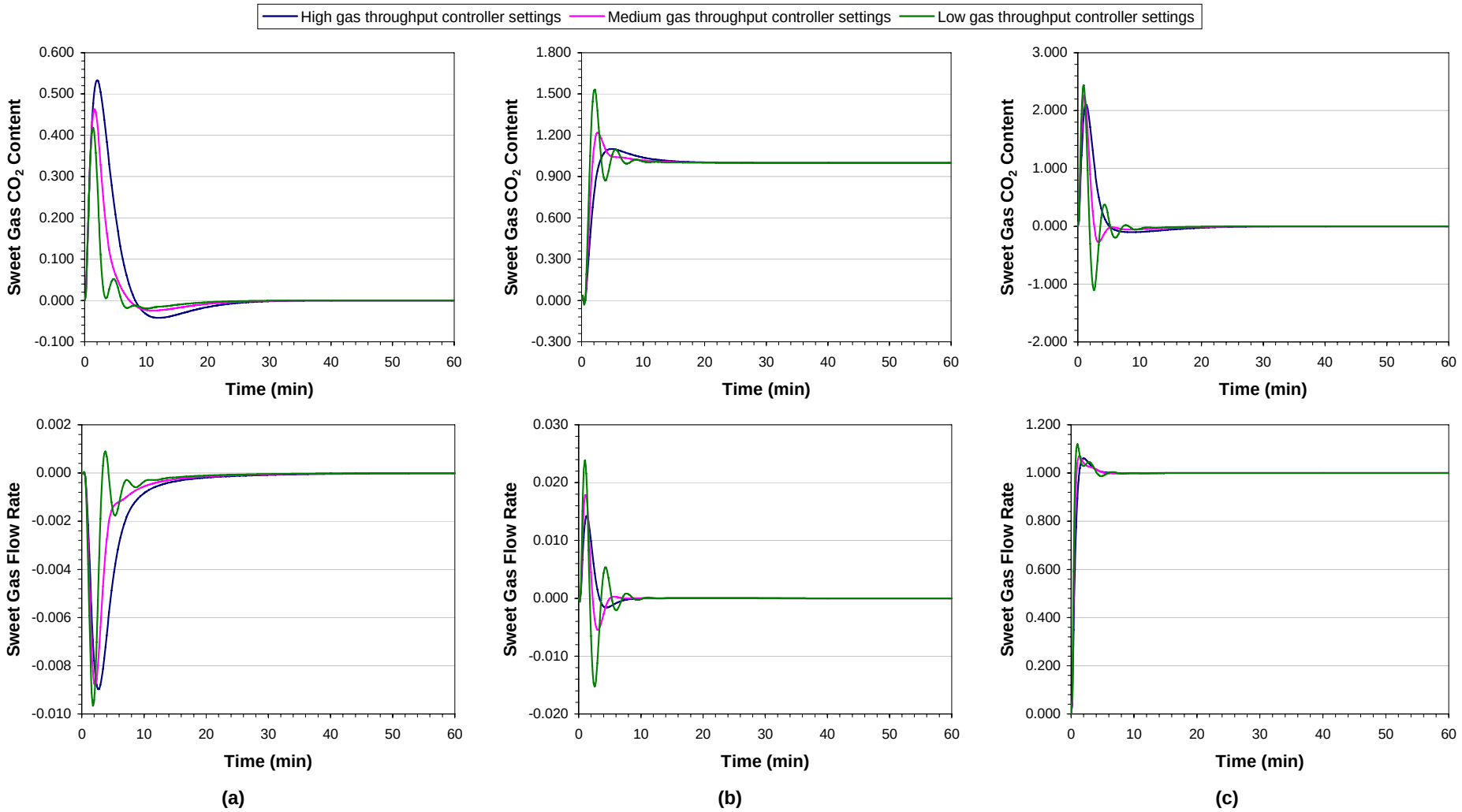

Figure 10.5.3: CO_2 train #7 closed-loop step response curves at the high gas throughput conditions. (a) Unit magnitude change in the raw gas CO_2 content at 0 min. (b) Unit magnitude change in the sweet gas CO_2 content setpoint at 0 min. (c) Unit magnitude change in the sweet gas flow rate setpoint at 0 min.

10.6 Summary

In summary, a simple and fully automatic control strategy was developed in this chapter for each of the two most dissimilar CO_2 trains, CO_2 trains #1 and #7, to control the two key process outputs: the sweet gas flow rate and CO_2 content. This demonstrated the potential application of the HYSYS® process models of the Moomba CO_2 trains in facilitating the development of a fully automated control system for the CO_2 trains.

As previously mentioned, the diagonal control structure is the simplest and most widely used form of multivariable control. However, its application to hot potassium carbonate process operations, like the CO_2 trains, has not been documented in the literature. Consequently, this chapter focussed on the development of diagonal control structures for the two CO_2 trains, based on the simple FOPDT process transfer functions derived in the previous chapter. All the necessary calculations for this exercise were performed in the MATLAB® 5.2 numerical computing environment.

Due to the different possible combinations of the process inputs and outputs, a number of alternative diagonal control structures had to be considered for each CO_2 train. Their sensitivity to process uncertainties and disturbances was evaluated, and the optimal set of process inputs was found to comprise of the raw gas flow rate and the reboiler steam flow rate, which corresponded to the RGF-RSF diagonal control structure. The optimal control structure configuration was then identified from the possible variable pairing permutations by analysing the system stability and loop interactions. It was determined that for the RGF-RSF structure, the raw gas flow rate should be paired with the sweet gas flow rate, while the sweet gas CO_2 content should be paired with the reboiler steam flow rate.

Dynamic MATLAB® simulations were performed to test the performance of the RGF-RSF diagonal control structure for the two CO_2 trains. The relevant controller parameters were obtained using the BLT tuning method, and the frequency ranges of interest were determined from the analysis of the control performance of the RGF-RSF structure. It was observed that acceptable disturbance rejection and setpoint tracking was achieved with the selected diagonal control structure for both CO_2 trains. This indicated that the RGF-RSF diagonal control structure could potentially be used to facilitate the fully automatic control of the Moomba CO_2 trains. However, further work is required to confirm this.

CHAPTER 11

CONCLUSIONS AND RECOMMENDATIONS

11.1 Conclusions

In this thesis, a new rigorous non-equilibrium rate-based model for chemical absorption and desorption was developed, and was successfully applied to the hot potassium carbonate process CO_2 Removal Trains at the Santos Moomba Processing Facility. Unlike previous rate-based models for the hot potassium carbonate process, the model presented in this work included rigorous electrolyte thermodynamics for both the absorber and regenerator columns. This model also differed in that it considered the use of reaction rate expressions for representing the effect of chemical reactions. However, enhancement factors were used instead in the final form of the model as preliminary simulations showed that minimal improvement was obtained with the more rigorous rate expressions, despite the greater associated computing time and model accuracy.

The non-equilibrium rate-based process models of the CO_2 trains were implemented in the equation-based Aspen Custom Modeler® simulation platform. This simulation environment enabled rigorous thermodynamic and physical property calculations via the Aspen Properties® software package. Literature data were used to determine the parameters for the relevant Aspen Properties® property models. Where these were found to be inadequate, the data were instead used to regress the parameters for alternative property models from literature or to develop empirical correlations.

Preliminary simulations identified the need for correction factors in order to achieve closer agreement between the model predictions for the absorber columns and the plant data. In contrast, the results for the regenerator column model agreed well with the plant data. A liquid phase enthalpy correction was developed for the absorber column model to generate a more reasonable temperature profile, while adjustment factors for the absorber effective interfacial area were derived to provide closer agreement between the predicted and data values for the sweet gas CO_2 content. Following the application of these model adjustments, the CO_2 train process models were successfully validated against an independent set of steady-state plant data.

The validation of these Aspen Custom Modeler® process models demonstrated that the non-equilibrium rate-based model presented in this work was suitable for modelling the hot potassium carbonate process. However, this approach could not be easily implemented in HYSYS®, Santos's preferred simulation environment, due to the lack of electrolyte components and property models and the limitations of the HYSYS® column operations in accommodating chemical reactions and non-equilibrium column behaviour. Importation of the Aspen Custom Modeler® process models into HYSYS® was considered, but was disregarded due to the significant associated computation time. Instead, a novel approach involving hypothetical HYSYS® components and the HYSYS® column stage efficiencies was developed to compensate for the restricted capabilities of this simulation platform.

Hypothetical K_2CO_3* and H_2O* components were created to facilitate the simulation of the hot potassium carbonate system in HYSYS®. In addition, the standard Peng-Robinson property package

model was modified to include tabular physical property models to accommodate the properties of this electrolyte system. Literature data were used to derive parameters for the relevant thermodynamic and physical property models. To compensate for the limitations of the standard Peng-Robinson property package, stage efficiency correlations were derived from parametric studies performed on the Aspen Custom Modeler® CO_2 train process models. These correlations related various operating parameters to the column performance, and were used to represent the effects of the non-equilibrium column behaviour and the liquid phase chemistry for the hot potassium carbonate process. Preliminary simulations indicated that the stage efficiency correlations were only necessary for the absorber columns as the regenerator columns were satisfactorily represented using the default equilibrium stages.

The combination of the stage efficiency correlations and the hypothetical components was found to enable the reasonable representation of the potassium carbonate system in HYSYS®. Consequently, detailed steady-state process models of the CO_2 trains were created in this simulation environment using technical data from the Santos TIMS controlled documentation database. As for the Aspen Custom Modeler® process models, the HYSYS® CO_2 train process models were successfully validated against an independent set of steady-state plant data. It was noted that HYSYS® process models predicted a considerably higher H_2S content for the sweet gas, compared to the Aspen Custom Modeler® process models. However, this discrepancy was deemed acceptable for this work since the primary focus of the Moomba CO_2 trains is the removal of CO_2, and in that regard, the HYSYS® CO_2 train process models were found to produce excellent results.

To demonstrate a potential application of the HYSYS® process models, dynamic process models of CO_2 trains #1 and #7, the two most dissimilarly configured trains, were created by modifying the steady-state HYSYS® process models. These changes to the model configuration and specifications were necessary due to the fundamental differences between the two simulation modes. The dynamic process models were used to investigate the transient behaviour of the two CO_2 trains over a range of operating conditions. Particular attention was given to the key process outputs (the sweet gas CO_2 content and flow rate), inputs (the raw gas flow rate, the lean solution flow rate, the reboiler steam flow rate and the regenerator liquid level) and disturbance (the raw gas CO_2 content). Simple first-order plus dead time process transfer functions relating these variables were derived from the results of the dynamic process case studies.

The process transfer functions were used to develop individual diagonal control structures to fully automate the control of CO_2 trains #1 and #7. This simple form of multivariable control was considered in this work because despite its wide usage, its application to hot potassium carbonate process operations has not been documented in literature. A number of analysis techniques were applied to evaluate the sensitivity, stability and controllability of the potential diagonal control structures. The two CO_2 trains were found to share the same optimal diagonal control structure, in

which the sweet gas CO_2 content was controlled by the reboiler steam flow rate while the sweet gas flow rate was controlled by the raw gas flow rate.

The results of the controllability analyses were confirmed by dynamic simulations in the MATLAB® numerical computing environment, which showed that effective disturbance rejection and setpoint tracking were achieved for both CO_2 trains with this control structure. This suggested that the identified control system was independent of the CO_2 train configuration, and could potentially be applied to the remaining five CO_2 trains to enable the fully automatic control of all seven CO_2 trains. The process control studies performed in this work therefore demonstrated a possible useful application for the HYSYS® process models of the Moomba CO_2 trains, in that they could be used to facilitate the development of a fully automated control strategy for the Moomba CO_2 Removal Trains.

In conclusion, a new rigorous non-equilibrium rate-based model was developed in this work for the hot potassium carbonate process. To demonstrate this model, it was implemented in the Aspen Custom Modeler® simulation platform and was successfully used to simulate the CO_2 Removal Trains at the Santos Moomba Processing Facility. However, this model could not be readily applied in HYSYS®, the preferred simulation environment for Santos, so a novel approach was followed to develop detailed CO_2 train process models in HYSYS® using the Aspen Custom Modeler® process models. A potential use for the resulting HYSYS® process models was then demonstrated through the development of diagonal control structures to facilitate the fully automatic control of the CO_2 trains.

Further work is recommended to extend the application and improve the modelling accuracy of the Aspen Custom Modeler® and HYSYS® CO_2 train process models. It is also suggested that work be performed on the process control of the CO_2 trains to investigate the effectiveness of more complex control algorithms compared to the simple diagonal control structure. These recommendations are listed in the next section.

11.2 Recommendations

The recommendations for future work are divided into the three categories:

1. Recommendations for further Aspen Custom Modeler® simulation work:
   (a) Validate the Aspen Custom Modeler® column models against a larger set of plant data, including data for the current conditions at the Moomba Processing Facility and data for start-up and shut-down conditions;
   (b) Investigate the effects of different types of random packing on the hydrodynamic behaviour and performance of the column models; and
   (c) Extend the model process chemistry to include the effects of amine activators, such as MEA, DEA and ACT-1, and other solution additives like anti-foaming agents and corrosion inhibitors.

2. Recommendations for further HYSYS® simulation work:
   (a) Extend the operating range over which the HYSYS® column stage efficiency correlations are valid to include a wider range of conditions, such as start-up and shut-down;
   (b) Incorporate the effect of different types of random packing into the column stage efficiency correlations;
   (c) Extend the model component system to include amine activators and other solution additives;
   (d) Adjust the physical and thermodynamic properties of the hypothetical K_2CO_3* component to enable the entrainment of the potassium carbonate solution, as observed in practice;
   (e) Convert the steady-state process models for CO_2 trains #2 to #6 into dynamic models; and
   (f) Validate the dynamic CO_2 train process models against online plant data.

3. Recommendations for further process control studies:
   (a) Derive process transfer functions for CO_2 trains #2 to #6 and, following the procedure described in this work for CO_2 trains #1 and #7, develop a diagonal control structure for each of these CO_2 trains which could facilitate the fully automatic control of the Moomba CO_2 trains; and
   (b) Develop alternative control systems for the CO_2 trains using more complex control algorithms, such as multivariable controllers and model predictive control, and compare their effectiveness against the simple diagonal control structure.

References

Abrams, D. S. and Prausnitz, J. M. (1975). "Statistical thermodynamics of liquid mixtures: a new expression for the Gibbs energy of partly or completely miscible systems." The American Institute of Chemical Engineers Journal **21**: 116 - 128.

Alatiqi, I. M., Sabri, M. F. and Alper, E. (1993). "Multivariable control system design of CO_2/amine absorber/desorber units by using a rigorous steady-state model." Gas Separation and Purification **7**(2): 119 - 121.

Albrecht, J. J., Kershenbaum, L. S. and Pyle, D. L. (1980). "Identification and linear multivariable control in an absorption-desorption pilot plant." AIChE Journal **26**(3): 496 - 504.

Al-Ramdhan, H. A. (2001). A Rate-Based Model for the Design and Simulation of a Carbon Dioxide Absorber Using the Hot Potassium Carbonate Process. PhD Thesis. Golden, Colorado School of Mines

Anderko, A., Wang, P. and Rafal, M. (2002). "Electrolyte solutions: from thermodynamic and transport property models to the simulation of industrial processes." Fluid Phase Equilibria **194 -197**: 123 - 142.

Armand Products Company (1998). Potassium Carbonate Handbook. Princeton NJ, Armand Products Company.

Aseyev, G. G. and Zaytsev, I. D. (1996). Volumetric Properties of Electrolyte Solutions: Estimation Methods and Experimental Data. New York, Begell House.

Aspen Technology Inc. (2003). Aspen Physical Property System: Physical Property Methods and Models. v12.1. Cambridge MA, Aspen Technology Inc.

Aspen Technology Inc. (2006). Solution ID: 118492. Available from http://support.aspentech.com. Accessed: 10 August 2006.

Astarita, G., Savage, D. W. and Bisio, A. (1983). Gas Treating with Chemical Solvents. New York, John Wiley and Sons.

Astarita, G., Savage, D. W. and Longo, J. M. (1981). "Promotion of CO_2 mass transfer in carbonate solutions." Chemical Engineering Science **36**(3): 581 - 588.

Åström, K. J. and Hagglünd, T. (1984). "Automatic tuning of simple regulators with specifications on phase and amplified margins." Automatica **20**(5): 645 - 651.

Åström, K. J. and Hagglünd, T. (1995). PID Controllers: Theory, Design and Tuning. 2nd ed. Research Triangle Park, Instrument Society of America.

Austgen, D. M., Rochelle, G. T., Peng, X. and Chen, C.-C. (1989). "Model of vapour-liquid equilibria for aqueous acid gas-alkanolamine systems using the Electrolyte-NRTL equation." Industrial and Engineering Chemistry Research **28**(7): 1060 - 1073.

Barber, C. (2007). Personal communication. 6 June.

Baroncini, C., Filippo, P. D., Latini, G. and Pacetti, M. (1980). "An improved correlation for the calculation of liquid thermal conductivity." International Journal of Thermophysics **1**(2): 159 - 175.

Bartoo, R. K. (1984). "Removing acid gas by the Benfield Process." Chemical Engineering Progress **80**(10): 35 - 39.

Bedekar, S. G. (1955). "Properties of sodium carbonate-sodium bicarbonate solutions." Journal of Applied Chemistry **5**(2): 72 - 75.

Benson, H. E. and Field, J. H. (1959). Method for Separating CO_2 and H_2S from Gas Mixtures. Patent No. 2,886,405. United States.

Benson, H. E., Field, J. H. and Jimeson, R. M. (1954). "CO_2 absorption employing hot potassium carbonate solutions." Chemical Engineering Progress **50**(7): 356 - 364.

Benson, H. E. and McCrea, D. H. (1979). Removal of acid gases from hot gas mixtures. Patent No. 4,160,810. United States.

Benson, H. E. and Parrish, R. W. (1974). "HiPure process removes CO_2/H_2S." Hydrocarbon Processing **53**(4): 81 - 82.

Bergman, D. F. (1976). Predicting the Phase Behaviour of Natural Gas in Pipelines. PhD Thesis. Ann Arbor, University of Michigan

Bergman, D. F., Tek, M. R. and Katz, D. L. (1975). Retrograde Condensation in Natural Gas Pipelines. New York, American Gas Association.

Billet, R. and Schultes, M. (1999). "Prediction of mass transfer columns with dumped and arranged packings: Updated summary of the calculation method of Billet and Schultes." Chemical Engineering Research and Design : Transactions of the Institution of Chemical Engineers **A 77**: 498 - 504.

Bingham, E. C. (1922). Fluidity and Plasticity. New York, McGraw-Hill.

Bird, R. B., Stewart, W. E. and Lightfoot, E. N. (1960). Transport Phenomena. New York, John Wiley and Sons.

Bocard, J. P. and Mayland, B. J. (1962). "New charts for hot carbonate process." Hydrocarbon Processing and Petroleum Refiner **41**(4): 128 - 132.

Bravo, J. L. and Fair, J. R. (1982). "Generalised correlation for mass transfer in packed distillation columns." Industrial and Engineering Chemistry Process Design and Development **21**: 162 - 170.

Brelvi, S. W. and O'Connell, J. P. (1972). "Corresponding states correlations for liquid compressibility and partial molal volumes of gases at infinite dilution in liquids." AIChE Journal **18**(6): 1239 - 1243.

Breslau, B. R. and Miller, I. F. (1972). "On the viscosity of concentrated aqueous electrolyte solutions." Journal of Physical Chemistry **74**(5): 1056 - 1061.

Breslau, B. R., Welsh, P. B. and Miller, I. F. (1974). "Estimating the viscosities of aqueous electrolytic solutions." Chemical Engineering **81**(8): 112 - 113.

Bristol, E. H. (1966). "On a new measure of interactions for multivariable process control." IEEE Transactions on Automatic Control **AC-11**: 133 -134.

Britt, H. I. and Luecke, R. H. (1973). "The estimation of parameters in nonlinear, implicit models." Technometrics **15**(2): 223 - 247.

Brock, J. R. and Bird, R. B. (1955). "Surface tension and the principle of corresponding states." AIChE Journal **1**: 174 - 177.

Cavett, R. H. (1964). Physical data for distillation calculations: vapour-liquid equilibria. 27th Midyear Meeting, API Division of Refining, San Francisco, USA.

Chakravarty, T., Phukan, U. K. and Weiland, R. H. (1985). "Reaction of acid gases with mixtures of amines." Chemical Engineering Progress **81**(4): 32 - 36.

Charpentier, J.-C. (1981). "Mass-transfer rates in gas-liquid absorbers and reactors." Advances in Chemical Engineering **11**: 1 - 133.

Chase, M. W., Jr. (1998). NIST-JANAF Thermochemical Tables. 4th ed. Woodbury, American Institute of Physics.

Chen, C.-C. (1980). Computer Simulation of Chemical Processes with Electrolytes. Sc. D. Thesis. Cambridge, Massachusetts Institute of Technology

Chen, C. C., Britt, H. I., Boston, J. F. and Clarke, W. M. (1983). "Thermodynamic property evaluation in computer-based flowsheet simulation for aqueous electrolyte systems." AIChE Symposium Series **79**(229): 126 - 134.

Chen, C.-C., Britt, H. I., Boston, J. F. and Evans, L. B. (1982). "Local composition model for excess Gibbs energy of electrolyte systems." The American Institute of Chemical Engineers Journal **28**(4): 588 - 596.

Chen, C.-C. and Evans, L. B. (1986). "A local composition model for the excess Gibbs energy of aqueous electrolyte systems." The American Institute of Chemical Engineers Journal **32**(3): 444 - 454.

Chernen'kaya, E. I. and Revenko, S. S. (1975). "Viscosity and density of K_2CO_3 and $KHCO_3$ solutions." Zhurnal Prikladnoi Khimii **48**(1): 126 - 130.

Chernen'kaya, E. I. and Vernigora, G. A. (1973). "Thermal conductivities of solutions of Na_2CO_3, K_2CO_3, KCl and K_2SO_4 at various temperatures." Zhurnal Prikladnoi Khimii **46**(7): 1603 - 1605.

Chung, T. H., Ajlan, M., Lee, L. L. and Starling, K. E. (1988). "Generalised multiparameter correlation for nonpolar and polar fluid transport properties." Industrial and Engineering Chemistry Research **27**(4): 671 - 679.

Correia, R. J. and Kestin, J. (1980). "Viscosity and density of aqueous Na_2CO_3 and K_2CO_3 solutions in the temperature range 20-90°C and the pressure range 0-30 MPa." Journal of Chemical and Engineering Data **25**: 201 - 206.

Criss, C. M. and Cobble, J. W. (1964a). "The thermodynamic properties of high temperature aqueous solutions. IV. Entropies of the ions up to 200° and the correspondence principle." Journal of the American Chemical Society **86**(12): 5385 - 5390.

Criss, C. M. and Cobble, J. W. (1964b). "The thermodynamic properties of high temperature aqueous solutions. V. The calculation of ionic heat capacities up to 200°, entropies and heat capacities above 200°." Journal of the American Chemical Society **86**(12): 5390 - 5393.

Cullinane, J. T. and Rochelle, G. T. (2004). "Carbon dioxide absorption with aqueous potassium carbonate promoted by piperazine." Chemical Engineering Science **59**: 3619 - 3630.

Danckwerts, P. V. (1951). "Significance of liquid film coefficients in gas absorption." Industrial and Engineering Chemistry **43**(6): 1460 - 1467.

Danckwerts, P. V. (1970). Gas-Liquid Reactions. New York, McGraw-Hill Book Company.

Danckwerts, P. V. and Kennedy, A. M. (1954). "Kinetics of liquid-film process in gas absorption. Part I: Models of the absorption process." Transactions of the Institution of Chemical Engineers **32**(Supplement No 1): S49 - S53.

Danckwerts, P. V. and Sharma, M. M. (1966). "The absorption of carbon dioxide into solutions of alkalis and amines (with some notes on hydrogen sulfide and carbonyl sulfide)." The Chemical Engineer (202): 244 - 280.

de Hemptinne, J.-C., Dhima, A. and Shakir, S. (2000). The Henry constant for 20 hydrocarbons, CO_2, H_2S in water as a function of pressure and temperature. 14th Symposium on Thermophysical Properties, Boulder, Colorado, USA.

de Leye, L. and Froment, G. F. (1986). "Rigorous simulation and design of columns for gas absorption and chemical reaction - I." Computers and Chemical Engineering **10**(5): 493 - 504.

Dean, D. E. and Stiel, L. I. (1965). "The viscosity of nonpolar gas mixtures at moderate and high pressure." AIChE Journal **11**(3): 526 - 532.

Drummond, S. E. (1981). Boiling and mixing of hydrothermal fluids: chemical effects on mineral precipitation. PhD Thesis. University Park, Pennsylvania State University

Ebrahimi, S., Picioreanu, C., Kleerebezem, R., Heijnen, J. J. and van Loosdrecht, M. C. M. (2003). "Rate-based modelling of SO_2 absorption into aqueous $NaHCO_3/Na_2CO_3$ solutions accompanied by the desorption of CO_2." Chemical Engineering Science **58**: 3589 - 3600.

Ely, J. F. and Hanley, H. J. M. (1981). "Prediction of transport properties. 1. Viscosity of fluids and mixtures." Industrial and Engineering Chemistry Fundamentals **20**(4): 323 - 332.

Ely, J. F. and Hanley, H. J. M. (1983). "Prediction of transport properties. 2. Thermal conductivity of pure fluids and mixtures." Industrial and Engineering Chemistry Fundamentals **22**(1): 90 - 97.

Fernández-Prini, R., Alvarez, J. L. and Harvey, A. H. (2003). "Henry's constants and vapour-liquid distribution constants for gaseous solutes in H_2O and D_2O at high temperatures." Journal of Physical and Chemical Reference Data **32**(2): 903 - 916.

Ferrell, R. T. and Himmelblau, D. M. (1967). "Diffusion coefficients of nitrogen and oxygen in water." Journal of Chemical and Engineering Data **12**(1): 111 - 115.

Field, J. H., Benson, H. E., Johnson, G. E., Tosh, J. S. and Forney, A. J. (1962). Pilot-Plant Studies of the Hot-Carbonate Process for Removing Carbon Dioxide and Hydrogen Sulfide. Bulletin 597. Washington, United States Department of the Interior, Bureau of Mines

Fortescue, T. R., Kershenbaum, L. S. and Ydstie, B. E. (1981). "Implementation of self-tuning regulators with variable forgetting factors." Automatica **17**(6): 831 - 835.

Fürst, W. and Renon, H. (1993). "Representation of excess properties of electrolyte solutions using a new equation of state." The American Institute of Chemical Engineers Journal **39**(2): 335 - 343.

Garcia, C. E., Prett, D. M. and Morari, M. (1989). "Model predictive control: Theory and practice - a survey." Automatica **25**(3): 335 - 348.

Golub, G. H. and Kahan, W. (1965). "Calculating the singular values and pseudo-inverse of a matrix." Journal of the Society for Industrial and Applied Mathematics: Series B, Numerical Analysis **2**(2): 205 - 224.

Gonçalves, F. A. and Kestin, J. (1981). "The viscosity of Na_2CO_3 and K_2CO_3 aqueous solutions in the range 20 - 60°C." International Journal of Thermophysics **2**(4): 315 - 322.

Graboski, M. S. and Daubert, T. E. (1978). "A modified Soave equation of state for phase equilibrium calculations. 1. Hydrocarbon systems." Industrial and Engineering Chemistry Process Design and Development **17**(4): 443 - 448.

Grosdidier, P., Morari, M. and Holt, B. R. (1985). "Closed-loop properties from steady-state gain information." Industrial and Engineering Chemistry Fundamentals **24**: 221 - 235.

Grover, B. S. (1987). Process for the removal of acid gases from gas mixtures. Patent No. 4,702,898. United States.

Haar, L., Gallagher, J. S. and Kell, G. S. (1984). NBS/NRC Steam Tables: Thermodynamic and Transport Properties and Computer Programs for Vapour and Liquid States of Water in SI Units. Washington, Hemisphere Publishing Corporation.

Hankinson, R. W. and Thomson, G. H. (1979). "A new correlation for saturated densities of liquids and their mixtures." AIChE Journal **25**(4): 653 - 663.

Harned, H. S. and Owen, B. B. (1958). The Physical Chemistry of Electrolytic Solutions. 3rd ed. New York, Reinhold Publishing Corporation.

Hayduk, W. and Laudie, H. (1974). "Prediction of diffusion coefficients for nonelectrolytes in dilute aqueous solutions." AIChE Journal **20**(3): 611 - 615.

Higbie, R. (1935). "The rate of absorption of a pure gas into a still liquid during short periods of exposure." Transactions of the American Institute of Chemical Engineers **31**: 365 - 383.

Hilliard, M. D. (2005). Thermodynamics of Aqueous Piperazine/Potassium Carbonate/Carbon Dioxide Characterised by the Electrolyte NRTL Model within Aspen Plus. M.S. Thesis. Austin, The University of Texas

Horvath, A. L. (1985). Handbook of Aqueous Electrolyte Solutions: Physical Properties, Estimation and Correlation Methods. Chichester, Ellis Horwood Limited.

Huang, H.-P., Jeng, J.-C., Chiang, C.-H. and Pan, W. (2003). "A direct method for multi-loop PI/PID controller design." Journal of Process Control **13**: 769 - 786.

Hudson Products Corporation (2002). Hudson Products Corporation website. http://www.hudsonproducts.com. Accessed: 10 October 2005.

Hyprotech Ltd (2001a). HYSYS Simulation Basis. Calgary, Hyprotech Ltd.

Hyprotech Ltd (2001b). HYSYS Dynamic Modelling. Calgary, Hyprotech Ltd.

Hyprotech Ltd (2001c). HYSYS Steady State Modelling. Calgary, Hyprotech Ltd.

Joback, K. G. (1984). A Unified Approach to Physical Property Estimation Using Multivariate Statistical Techniques. M.S. Thesis. Cambridge, Massachusetts Institute of Technology

Jones, G. and Dole, M. (1929). "The viscosity of aqueous solutions of strong electrolytes with special reference to barium chloride." Journal of the American Chemical Society **51**(10): 2950 - 2964.

Joseph, B. (1999). A tutorial on inferential control and its applications. 1999 American Control Conference, San Diego, USA.

Joshi, S. V., Astarita, G. and Savage, D. W. (1981). "Prediction of pilot plant performance for a chemical gas absorption process." The American Institute of Chemical Engineers Symposium Series **77**(202): 63 - 77.

Kenig, E. Y., Schneider, R. and Górak, A. (1999). "Rigorous dynamic modelling of complex reactive absorption processes." Chemical Engineering Science **54**: 5195 - 5203.

Kenig, E. Y., Schneider, R. and Górak, A. (2001). "Reactive absorption: Optimal process design via optimal modelling." Chemical Engineering Science **56**: 343 - 350.

Kent, R. L. and Eisenberg, B. (1976). "Better Data for Amine Treating." Hydrocarbon Processing **55**(2): 87 - 90.

Kershenbaum, L. S. (2000). "Experimental testing of advanced algorithms for process control." Chemical Engineering Research and Design : Transactions of the Institution of Chemical Engineers **78**(A4): 509 - 521.

Kershenbaum, L. S. and Pérez-Correa, J. R. (1989). "An extended horizon feedback/feedforward self-tuning controller." AIChE Journal **35**(11): 1835 - 1844.

Kesler, M. G. and Lee, B. I. (1976). "Improve prediction of enthalpy of fractions." Hydrocarbon Processing **55**(3): 153 - 158.

Kister, H. Z. (1992). Distillation Design. Boston, McGraw-Hill.

Koch-Glitsch (2003a). Intalox Packed Tower Systems: Metal Random Packing. Bulletin KGMRP-1 2M0303B.

Koch-Glitsch (2003b). Intalox Packed Tower Systems: IMTP® High Performance Packing. Bulletin KGIMTP-2 2MI303E.

Kohl, A. L. and Nielson, R. B. (1997). Alkaline Salt Solutions for Acid Gas Removal. Gas Purification. Houston, Gulf Publishing Company**:** 330 - 414.

Kolev, N. (1976). "Operation of randomly packed columns." Chemie Ingenieur Technik **48**(12): 1105 - 1112.

Krishnamurthy, R. and Taylor, R. (1985). "Simulation of packed distillation and absorption columns." Industrial and Engineering Chemistry Process Design and Development **24**(3): 513 - 524.

Kucka, L., Kenig, E. Y. and Górak, A. (2002). "Kinetics of the gas-liquid reaction between carbon dioxide and hydroxide ions." Industrial and Engineering Chemistry Research **41**: 5952 - 5957.

Kucka, L., Müller, I., Kenig, E. Y. and Górak, A. (2003). "On the modelling and simulation of sour gas absorption by aqueous amine solutions." Chemical Engineering Science **58**: 3571 - 3578.

Lee, J. H. and Cooley, B. (1997). Recent advances in model predictive control and other related areas. 5th International Conference on Chemical Process Control, AICHE and CACHE, Tahoe City, USA.

Letsou, A. and Stiel, L. I. (1973). "Viscosity of saturated nonpolar liquids at elevated pressures." AIChE Journal **19**(2): 153 - 158.

Lewin, D. R. (1996). "A simple tool for disturbance resiliency diagnosis and feedforward control design." Computers and Chemical Engineering **20**(1): 13 - 25.

Lewis, W. K. and Whitman, W. G. (1924). "Principles of gas absorption." Industrial and Engineering Chemistry **16**(1215 - 1220).

Loehe, J. R. and Donohue, M. D. (1997). "Recent advances in modelling thermodynamic properties of aqueous strong electrolyte systems." The American Institute of Chemical Engineers Journal **43**(1): 180 - 195.

Luyben, W. L. (1986). "Simple method for tuning SISO controllers in multivariable systems." Industrial and Engineering Chemistry: Process Design and Development **25**: 654 - 660.

Luyben, W. L. (1996). "Tuning proportional-integral-derivative controllers for integrator/dead time processes." Industrial and Engineering Chemistry Research **35**(3480 - 3483).

Luyben, W. L. and Luyben, M. L. (1997). Essentials of Process Control. New York, McGraw-Hill.

Marini, L., Clement, K., Georgakis, C. and Suenson, M. M. (1985). "Experimental and theoretical investigation of an absorber-stripper pilot plant under nonequilibrium conditions." Industrial and Engineering Chemistry Fundamentals **24**(3): 296 - 301.

Mason, E. A. and Saxena, S. C. (1958). "Approximate formula for the thermal conductivity of gas mixtures." Physics of Fluids **1**: 361 - 369.

Mayer, J. (2002). Experimentelle und theoretische Untersuchungen zur chemischen Absorption am Biespiel der Koksofengasreinigung. Berlin, Logos Verlag.

Misic, D. and Thodos, G. (1961). "The thermal conductivity of hydrocarbon gases at normal pressures." AIChE Journal **7**(2): 264 - 267.

Misic, D. and Thodos, G. (1963). "Atmospheric thermal conductivities for gases of simple molecular structure." Journal of Chemical and Engineering Data **8**(4): 540 - 544.

Mock, B., Evans, L. B. and Chen, C. C. (1986). "Thermodynamic representation of phase equilibria of mixed-solvent electrolyte systems." AIChE Journal **32**(10): 1655 - 1664.

Monica, T. J., Yu, C. C. and Luyben, W. L. (1988). "Improved multiloop single-input/single-output (SISO) controllers for multivariable processes." Industrial and Engineering Chemistry Research **27**: 969 - 973.

Morari, M. (1983). "Design of resilient processing plants. III. A general framework for the assessment of dynamic resilience." Chemical Engineering Science **38**: 1881 - 1891.

Murphree, E. V. (1925). "Rectifying column calculations with particular reference to N component mixtures." Industrial and Engineering Chemistry **17**(7): 747 - 750.

Niederlinski, A. (1971). "A heuristic approach to the design of linear multivariable interacting control systems." Automatica **7**(6): 691 - 701.

Noeres, C., Kenig, E. Y. and Górak, A. (2003). "Modelling of reactive separation processes: reactive absorption and reactive distillation." Chemical Engineering and Processing **42**: 157 - 178.

O'Dwyer, A. (2006). Handbook of PI and PID Controller Tuning Rules. 2nd ed. London, Imperial College Press.

Onda, K., Kobayashi, T., Fujine, M. and Takahashi, M. (1971). "Concentration profile of sodium ion in gas absorption." Chemical Engineering Science **26**: 2027 - 2035.

Onda, K., Sada, E. and Takeuchi, H. (1968b). "Gas absorption with chemical reaction in packed columns." Journal of Chemical Engineering of Japan **1**(1): 62 - 66.

Onda, K., Takeuchi, H. and Okumoto, Y. (1968a). "Mass transfer coefficients between gas and liquid phases in packed columns." Journal of Chemical Engineering of Japan **1**(1): 56 - 62.

Onsager, L. and Samaras, N. N. T. (1934). "The surface tension of Debye-Hückel electrolytes." The Journal of Chemical Physics **2**(8): 528 - 536.

Ooi, S. M., Colby, C. B., Humphris, K., King, K. D. and O'Neill, B. K. (2005). The evaluation of different electrolyte thermodynamic models for simulating the hot potassium carbonate process. 7th World Congress of Chemical Engineering, Glasgow, Scotland.

Panda, R. C., Yu, C.-C. and Huang, H.-P. (2004). "PID tuning rules for SOPDT systems: Review and some new results." ISA Transactions **43**: 283 - 295.

Park, K. Y. and Edgar, T. F. (1984). "Simulation of the hot carbonate process for removal of CO_2 and H_2S from medium Btu gas." Energy Progress **4**(3): 174 - 180.

Peng, D. Y. and Robinson, D. B. (1976). "A two constant equation of state." Industrial and Engineering Chemistry Fundamentals **15**: 59 - 64.

Perry, R. H. and Green, D. W. (1997). Perry's Chemical Engineers' Handbook. 7th ed. New York, McGraw-Hill.

Pitzer, K. S. (1973). "Thermodynamics of electrolytes. I. Theoretical basis and general equations." The Journal of Physical Chemistry **77**(2): 268 - 277.

Pitzer, K. S. (1980). "Electrolytes. From dilute solutions to fused salts." Journal of American Chemical Society **102**(9): 2902 - 2906.

Pitzer, K. S., Lippmann, D. Z., Curl, R. F., Jr., Huggins, C. M. and Petersen, D. E. (1955). "Volumetric and thermodynamic properties of fluids. II. Compressibility factor, vapour pressure and enthalpy of vaporization." Journal of American Chemical Society **77**(13): 3433 - 3440.

Pohorecki, R. and Kucharski, E. (1991). "Desorption with chemical reaction in the system CO_2-aqueous solution of potassium carbonate." The Chemical Engineering Journal **46**: 1 - 7.

Pohorecki, R. and Moniuk, W. (1988). "Kinetics of reactions between carbon dioxide and hydroxyl ions in aqueous electrolyte solutions." Chemical Engineering Science **43**(7): 1677 - 1684.

Poling, B. E., Prausnitz, J. M. and O'Connell, J. P. (2001). The Properties of Gases and Liquids. 5th ed. New York, McGraw-Hill.

Popolizio, B. (2005). Personal communication. 27 October.

Puranik, S. S. and Vogelpohl, A. (1974). "Effective interfacial area in irrigated packed columns." Chemical Engineering Science **29**(2): 501 - 507.

Qin, S. J. and Badgwell, T. A. (2003). "A survey of industrial model predictive control technology." Control Engineering Practice **11**: 733 - 764.

Rahimpour, M. R. and Kashkooli, A. Z. (2004). "Enhanced carbon dioxide removal by promoted hot potassium carbonate in a split-flow absorber." Chemical Engineering and Processing **43**: 857 - 865.

Rao, D. P. (1990). "Design of a packed column for absorption of carbon dioxide in DEA promoted hot K_2CO_3 solution." Gas Separation and Purification **4**: 58 - 61.

Rao, D. P. (1991). "Design of packed towers for absorption and desorption of carbon dioxide using hot promoted K_2CO_3 solution." Gas Separation and Purification **5**(9): 177 - 180.

Ratcliff, G. A. and Holdcroft, J. G. (1963). "Diffusivities of gases in aqueous electrolyte solutions." Transactions of the Institution of Chemical Engineers **41**: 315 - 319.

Redlich, O. and Kwong, J. N. S. (1949). "On the thermodynamics of solutions. V. An Equation of State. Fugacities of gaseous solutions." Chemical Reviews **44**: 233 - 245.

Reid, R. C., Prausnitz, J. M. and Sherwood, T. K. (1977). The Properties of Gases and Liquids. 3rd ed. New York, McGraw-Hill.

Renon, H. (1996). "Models for excess properties of electrolyte solutions: molecular bases and classification, needs and trends for new developments." Fluid Phase Equilibria **116**: 217 - 224.

Renon, H. and Prausnitz, J. M. (1968). "Local compositions in thermodynamic excess functions for liquid mixtures." The American Institute of Chemical Engineers Journal **14**: 135 - 144.

Riedel, L. (1951). "The thermal conductivity of aqueous solutions of strong electrolytes." Chemie Ingenieur Technik **23**: 59 - 64.

Riedel, L. (1954). "A new universal vapour-pressure equation. I. The extension of the theorem of corresponding states." Chemie Ingenieur Technik **26**: 83 - 89.

Robinson, R. A. and Stokes, R. H. (1965). Electrolyte Solutions. 2nd (Revised) ed. London, Butterworths.

Rosenbrock, H. H. (1974). Computer Aided Control System Design. London, Academic Press.

Rowley, R. L., Wilding, W. V., Oscarson, J. L. and Yang, Y. (1998). DIPPR® Project 801 Database of Evaluated Process Design Data. http://dippr.byu.edu. Brigham Young University. Accessed: 2005.

Sander, B., Fredenslund, A. and Rasmussen, P. (1986a). "Calculation of vapour-liquid equilibria in mixed solvent/salt systems using an extended UNIQUAC equation." Chemical Engineering Science **41**(5): 1171 - 1183.

Sander, B., Rasmussen, P. and Fredenslund, A. (1986b). "Calculation of vapour-liquid equilibria in nitric acid-water-nitrate salt systems using an extended UNIQUAC equation." Chemical Engineering Science **41**(5): 1185 - 1195.

Santos Ltd (1997). South Australian Operations: Moomba Processing Facilities, Santos Ltd.

Santos Ltd (1998). Section 4.0: CO_2 Removal (Benfield) Plants. Moomba Gas Plant Technical Manual, Santos Ltd**:** 4.10.

Sanyal, D., Vasishtha, N. and Saraf, D. N. (1988). "Modelling of carbon dioxide absorber using hot carbonate process." Industrial and Engineering Chemistry Research **27**(11): 2149 - 2156.

Schneider, R. and Górak, A. (2001). "Model optimization for the dynamic simulation of reactive absorption processes." Chemical Engineering and Technology **24**(10): 979 - 989.

Seader, J. D. and Henley, E. J. (1998). Separation Process Principles. New York, John Wiley and Sons.

Seborg, D. E., Edgar, T. F. and Mellichamp, D. A. (1989). Process Dynamics and Control. New York, John Wiley and Sons.

Seborg, D. E., Edgar, T. F. and Shah, S. L. (1986). "Adaptive control strategies for process control: A survey." AIChE Journal **32**(6): 881 - 913.

Sherwood, T. K. and Holloway, F. A. L. (1940a). "Performance of packed towers - Experimental studies of absorption and desorption." Transactions of the American Institute of Chemical Engineers **36**(1): 21 -37.

Sherwood, T. K. and Holloway, F. A. L. (1940b). "Performance of packed towers - Liquid-film data for several packings." Transactions of the American Institute of Chemical Engineers **36**(1-2): 39 - 90.

Shinskey, F. G. (1979). Process Control Systems : Application, Design, Adjustment. 2nd ed. New York, McGraw-Hill.

Shulman, H. L., Ullrich, C. F., Proulx, A. Z. and Zimmerman, J. O. (1955). "Performance of packed columns. 1. Total, static, and operating holdups." AIChE Journal **1**(2): 247 - 253.

Skogestad, S. (2003). "Simple analytic rules for model reduction and PID controller tuning." Journal of Process Control **13**: 291 - 309.

Skogestad, S., Jacobsen, E. W. and Morari, M. (1990). "Inadequacy of steady-state analysis for feedback control: distillate-bottom control of distillation columns." Industrial and Engineering Chemistry Research **29**(12): 2339 - 2346.

Skogestad, S. and Morari, M. (1987). "Effect of disturbance direction on closed-loop performance." Industrial and Engineering Chemistry Research **26**(10): 2029 - 2035.

Skogestad, S. and Postlethwaite, I. (1996). Multivariable Feedback Control: Analysis and Design. Chichester, John Wiley and Sons.

Soave, G. (1972). "Equilibrium constants from a modified Redlich-Kwong equation of state." Chemical Engineering Science **27**: 1197 - 1203.

Spencer, C. F. and Danner, R. P. (1972). "Improved equation for prediction of saturated liquid density." Journal of Chemical and Engineering Data **17**(2): 236 - 241.

Stanley, G., Marino-Galarraga, M. and McAvoy, T. J. (1985). "Shortcut operability analysis. 1. The relative disturbance gain." Industrial and Engineering Chemistry Process Design and Development **24**: 1181 - 1188.

Staton, J. S. (1985). Performance and Modelling of a Hot Potassium Carbonate Acid Gas Removal System in Treating Coal Gas. PhD Thesis. Raleigh, North Carolina State University

Stephanopoulos, G. (1984). Chemical Process Control: An Introduction to Theory and Practice. Englewood Cliffs, Prentice-Hall.

Stephanopoulos, G. and Han, C. (1996). "Intelligent systems in process engineering: A review." Computers and Chemical Engineering **20**(6/7): 743 - 791.

Stichlmair, J., Bravo, J. L. and Fair, J. R. (1989). "General model for prediction of pressure drop and capacity of countercurrent gas/liquid packed columns." Gas Separation and Purification **3**: 19 - 28.

Stichlmair, J. and Fair, J. R. (1998). Distillation: Principles and Practice. New York, Wiley-VCH.

Stiel, L. I. and Thodos, G. (1964). "The thermal conductivity of nonpolar substances in the dense gaseous and liquid regions." AIChE Journal **10**(1): 26 - 30.

Stone, D. (2005). Personal communication. 23 January.

Stryjek, R. and Vera, J. H. (1986a). "PRSV: An improved Peng-Robinson equation of state for pure compounds and mixtures." Canadian Journal of Chemical Engineering **64**(2): 323 - 333.

Stryjek, R. and Vera, J. H. (1986b). "PRSV: An improved Peng-Robinson equation of state with new mixing rules for strongly non-ideal mixtures." Canadian Journal of Chemical Engineering **64**(2): 334 - 340.

Stumm, W. and Morgan, J. J. (1996). Aquatic Chemistry: Chemical Equilibria and Rates in Natural Waters. 3rd ed. New York, John Wiley and Sons.

Suenson, M. M., Georgakis, C. and Evans, L. B. (1985). "Steady-state and dynamic modelling of a gas absorber-stripped system." Industrial and Engineering Chemistry Fundamentals **24**(3): 288 - 295.

Sulzer Chemtech (2006). Metal Random Packing: Superior random packings combined with innovative mass transfer technology. Brochure 22.64.06.40 - VI.06 - 50.

Svrcek, W. Y., Mahoney, D. P. and Young, B. R. (2006). A Real-Time Approach to Process Control. 2nd ed. Chichester, John Wiley and Sons.

Tamimi, A., Rinker, E. B. and Sandall, O. C. (1994). "Diffusion coefficients for hydrogen sulfide, carbon dioxide, and nitrous oxide in water over the temperature range 293 - 368 K." Journal of Chemical and Engineering Data **39**(2): 330 - 332.

Taylor, R. and Krishna, R. (1993). Multicomponent Mass Transfer. New York, John Wiley and Sons.

Thiele, R. (2007). Selektive Absorption innerhalb der Kokereigasreinigung. PhD Thesis. Berlin, Technischen Universität Berlin

Thiele, R., Repke, J.-U., Diekjakobs, B., Thielert, H. and Wozny, G. (2005a). A general rate-based model for industrial reactive absorption and desorption processes in sour gas treatment. 2005 AIChE Spring National Meeting, Atlanta, USA.

Thiele, R., Repke, J.-U., Diekjakobs, B., Thielert, H. and Wozny, G. (2005b). Rate-based modelling of reactive absorption and desorption processes in sour gas treatment. 7th World Congress of Chemical Engineering, Glasgow, Scotland.

Thomsen, K. and Rasmussen, P. (1999). "Modelling of vapour-liquid-solid equilibrium in gas-aqueous electrolyte systems." Chemical Engineering Science **54**: 1787 - 1802.

Todinca, T. (1994). "Mathematical model for the gas desorber used for carbon dioxide desorption from DEA-promoted hot potassium carbonate." Chemical Bulletin of the Technical University of Timisoara **39**(53): 127 - 134.

Todinca, T. (1995). "Mathematical modelling of absorption-desorption processes: Carbon dioxide removing plants using diethanolamine promoted hot potassium carbonate." Chemical Bulletin of the Technical University of Timisoara **40**(54): 11 - 20.

Todinca, T., Moszkowicz, P., Târnoveanu, M. and Benadda, B. (1997). "Absorption of carbon dioxide in diethanolamine promoted hot potassium carbonate processes." International Chemical Engineering Symposium Series **142**: 429 - 437.

Tosh, J. S., Field, J. H., Benson, H. E. and Anderson, R. B. (1960). Equilibrium Pressures of Hydrogen Sulfide and Carbon Dioxide over Solutions of Potassium Carbonate. Report of Investigations 5622. Washington, United States Department of the Interior, Bureau of Mines

Tosh, J. S., Field, J. H., Benson, H. E. and Haynes, B. S. (1959). Equilibrium Study of the System Potassium Carbonate, Potasstium Bicarbonate, Carbon Dioxide, and Water. Report of Investigations 5484. Washington, United States Department of the Interior, Bureau of Mines

Twu, C. H. (1985). "Internally consistent correlation for predicting liquid viscosities of petroleum fractions." Industrial and Engineering Chemistry Process Design and Development **24**(4): 1287 -1293.

Tyreus, B. D. and Luyben, W. L. (1992). "Tuning PI controllers for integrator/dead time processes." Industrial and Engineering Chemistry Research **31**: 2625 - 2628.

UOP Gas Processing (1998). UOP Benfield ACT-1 Activator Operating Manual. Des Plaines, UOP

UOP Gas Processing (2000). Benfield Process Technical Sheet. Des Plaines, UOP

van der Lee, J. H., Swallow, J. A. and Young, B. R. (2003). "CO_2 loading measurement and control in an amine absorption/stripping pilot plant." Technical Papers of ISA **444**: 59 - 65.

van der Lee, J. H., Young, B. R. and Svrcek, W. Y. (2001). Model predictive control of a pilot amine absorption/stripping plant. 51st Canadian Chemical Engineering Conference, Halifax, Canada.

van der Lee, J. H., Young, B. R., Swallow, J. A. and Svrcek, W. Y. (2004). Monitoring CO_2 loading of rich and lean streams in an amine absorption/stripping pilot plant. 49th Annual ISA Analysis Division Symposium, Cincinnati, USA.

van Krevelen, D. W. and Hoftijzer, P. J. (1948). "Kinetics of simultaneous absorption and chemical reaction." Chemical Engineering Progress **44**: 529 - 536.

van Swaaij, W. P. M. and Versteeg, G. F. (1992). "Mass transfer accompanied with complex reversible chemical reactions in gas-liquid systems: An overview." Chemical Engineering Science **47**(13 - 14): 3181 - 3195.

Wade, H. L. (2004). Basic and Advanced Regulatory Control: System Design and Application. 2nd ed. Research Triangle Park, The Instrumentation, Systems and Automation Society.

Wang, G. Q., Yuan, X. G. and Yu, K. T. (2005). "Review of mass-transfer correlations for packed columns." Industrial and Engineering Chemistry Research **44**: 8715 - 8729.

Wang, J. H. (1965). "Self-diffusion coefficients of water." Journal of Physical Chemistry **69**(12): 4412.

Wilke, C. R. (1950). "A viscosity equation for gas mixtures." The Journal of Chemical Physics **18**(4): 517 - 519.

Willcocks, L. (2008). Personal communication. 26 May.

Wilson, G. M. (1980). A New Correlation of Ammonia, Carbon Dioxide, and Hydrogen Sulfide Volatility Data from Aqueous Sour Water Systems. Washington DC, American Petroleum Institute

Witcher, M. and McAvoy, T. J. (1977). "Interacting control systems: Steady state and dynamic measurement of interaction." ISA Transactions **16**: 35 - 41.

Witherspoon, P. A. and Saraf, D. N. (1965). "Diffusion of methane, ethane, propane and n-butane in water from 25 to 43°." Journal of Physical Chemistry **69**(11): 3752 - 3755.

Wittenmark, B. (1997). A survey of adaptive control applications. Dynamic Modelling Control Applications for Industry Workshop, IEEE Industry Applications Society, Vancouver, Canada.

Ydstie, B. E., Kershenbaum, L. S. and Sargent, R. W. H. (1985). "Theory and application of an extended horizon self-tuning controller." AIChE Journal **31**(11): 1771 - 1780.

Yen, L. C. and Woods, S. S. (1966). "A generalised pressure correlation for gas-solvent-reservoir oil systems." AIChE Journal **12**(1): 95 - 99.

Yih, S.-M. and Lai, H.-C. (1987). "Simultaneous absorption of carbon dioxide and hydrogen sulfide in hot carbonate solutions in a packed absorber-stripper unit." Chemical Engineering Communications **51**(1-6): 277 - 290.

Yu, C. C. and Luyben, W. L. (1986). "Design of multiloop SISO controllers in multivariable processes." Industrial and Engineering Chemistry: Process Design and Development **25**: 498 - 503.

Zemaitis, J. F., Jr, Clark, D. M., Rafal, M. and Scrivner, N. C. (1986). Handbook of Aqueous Electrolyte Thermodynamics: Theory and Application. New York, Design Institute for Physical Property Data.

Ziegler, J. G. and Nichols, N. B. (1942). "Optimum settings for automatic controllers." Transactions of the ASME **64**: 759 - 768.

Ziegler, J. G. and Nichols, N. B. (1943). "Process lags in automatic control circuits." Transactions of the ASME **65**: 433 - 444.